ELECTRICAL CONTACTS AND SURFACE EFFECTS ON SEMICONDUCTING CHALCOGENIDE GLASSES

BY

ANDREW M. WALLACE

A THESIS SUBMITTED FOR THE DEGREE OF DOCTOR OF PHILOSOPHY

AT THE UNIVERISTY OF EDINBURGH

IN

NOVEMBER 1975

PREFACE

This thesis has been composed by myself and is the result of my own work except when otherwise indicated.

I am indebted to Dr. A.E. Owen and Dr. J.M. Robertson for their guidance and encouragement throughout the course of this work. In addition, I should like to thank Dr. C. Main, Dr. J.M. Marshall and Mr. B.W. Flynn for critical advice and discussion.

Finally, I am grateful to the Science Research Council for financial assistance, and to all others, both within and without the department, who have helped me over the past three years.

ABSTRACT

The electrical contact and surface properties of thin amorphous films of $Ge_{10}As_{40}Te_{50}$ and $Si_{12}Te_{48}As_{30}Ge_{10}$ have been investigated. A preliminary study of the variation of the conductivity of thin films of $Ge_{10}As_{40}Te_{50}$ showed behaviour typical of a wide range of similar materials. Measurements of the steady-state current-voltage and capacitance-voltage characteristics of thin-film sandwich devices of $Ge_{10}As_{40}Te_{50}$ with a variety of metal electrodes indicated the absence of blocking contacts, except when an oxidising electrode such as aluminium was used, but photovoltaic data suggests that space charge layers do exist at the metal-amorphous semiconductor contact.

A study of the field-effect modulated conductance of thin films of $Ge_{10}As_{40}Te_{50}$ and $Si_{12}Te_{48}As_{30}Ge_{10}$ indicated that a high density of localised states was present within the gap, at and/or near the semiconductor surface, giving rise to very narrow ($<100\text{Å}$) space charge layers. Existing theories for transport through narrow Schottky barriers have been modified to fit the amorphous case, and the non-blocking nature of the metal-amorphous semiconductor contact has been explained in terms of a series/parallel combination of recombination/generation and tunnelling mechanisms.

Current-voltage, capacitance-voltage and photo-electric data were obtained on heterojunctions formed between thin-films of $Ge_{10}As_{40}Te_{50}$ and both p- and n-type silicon substrates. Junctions of this type were strongly rectifying, but n-type devices showed a much "softer" reverse

characteristic. Qualitative models of the two types of device have been presented, and the various transport mechanisms discussed.

TABLE OF CONTENTS page no

CHAPTER 1 CHALCOGENIDE GLASSES

1.1 Definition

Amorphous semiconducting glasses are materials in which the characteristic three-dimensional periodicity of the crystalline state is absent. In principle it should be possible to prepare any solid in an amorphous form, but in practice the ease with which this can be achieved varies greatly from one material to another. In chemical terms these materials can be divided conveniently into three main categories. The chalcogenide glasses are formed by the combination of one or more of the group VI elements beneath oxygen, that is S, Se or Te, with various other elements, such as Si, Ge, As, P, Sb, Bi etc., but do not contain oxide constituents. The transition metal oxides are glasses in which a transition metal oxide is the major constituent, e.g. V_2O_5, MnO_2, Fe_2O_3 etc. In particular, the V_2O_5 - P_2O_5 system has been extensively studied. The third group contains principally amorphous Si and Ge, which can only be obtained in the amorphous form by deposition from the vapour. The subject matter of this thesis is concerned with materials in the chalcogenide group.

A distinction must be made between the terms 'vitreous' or 'glassy' and 'amorphous'. A vitreous solid or glass is prepared in bulk form by quenching the melt without crystallisation, and the structure of the liquid is generally, though not always, retained. An amorphous film is prepared by sputtering or evaporation of the resultant glass on to a suitable substrate, and although in many cases

the thin amorphous films have similar properties to the parent glass, they are rarely identical. The composition and properties of the film can be strongly dependent on the preparation conditions; such factors as substrate temperature, ambient atmosphere and evaporation or sputtering rate being particularly important.

1.2 Glass Forming Systems

Chalcogenide glasses can be prepared from liquid elements; e.g. S or Se, from binary systems; e.g. As-Se, As-S, As-Te, from ternary systems; e.g. Ge-As-Te, Si-As-Te, from quaternary systems; e.g. Si-Te-As-Ge, and so on. However, for any given grouping of the above elements, there is a limited compositional range of vitreous materials, referred to as the 'glass forming region'. Figure (1.1) illustrates the glass forming regions of the binary As-Te and Ge-Te systems[3], and the ternary Ge-As-Te system[4-7], the differences apparent in the extent of the latter regions being very much dependent on the preparation techniques of the authors concerned. Thus compound glasses can be prepared in stoichiometric; e.g. As_2Se_3, As_2Te_3 or non-stoichiometric proportions; e.g. $As_{45}Te_{55}$, $Ge_{10}As_{40}Te_{50}$. Stable glasses such as As_2Se_3 can be prepared by cooling the melt at a very low rate, but less stable glasses such as As_2Te_3 must be cooled very rapidly to avoid devitrification. As an example of a material intermediate between these two extremes, differential scanning calorimetric (DSC) and resistance data on $Ge_{10}As_{40}Te_{50}$[8] is illustrated in Figure (1.2). On heating a sample of the

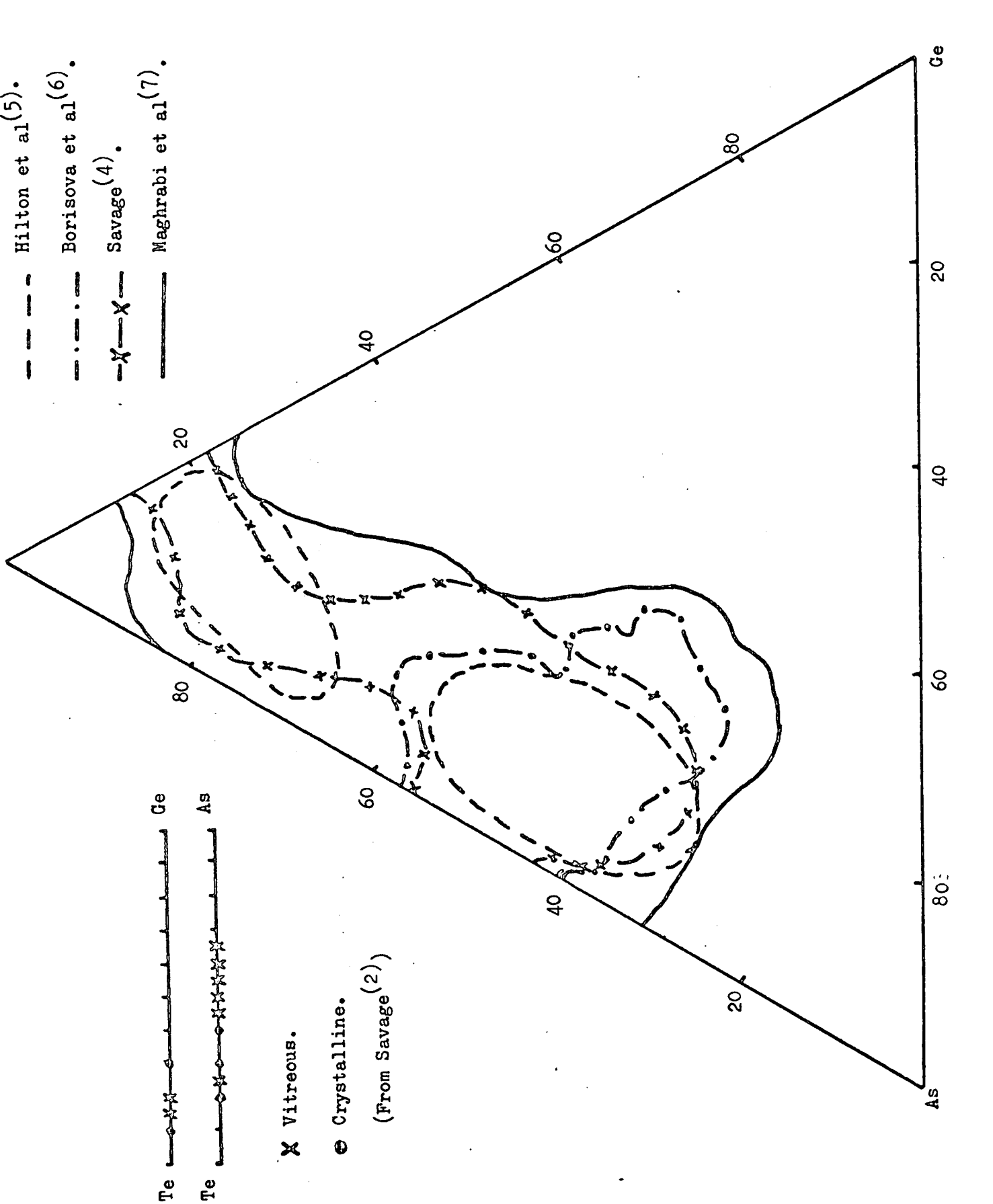

Figure 1.1 Regions of glass formation in the binary Te – Ge and Te – As systems, and the ternary Ge – As – Te system.

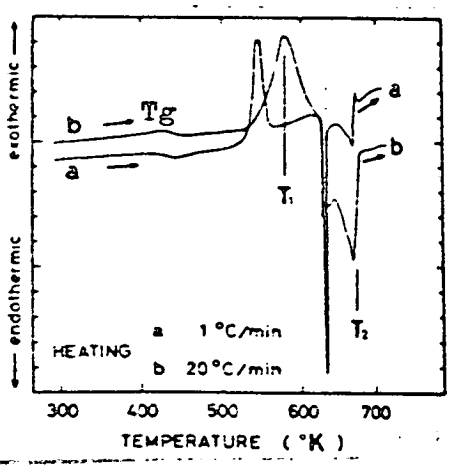

(a) DSC analysis for different heating rates.

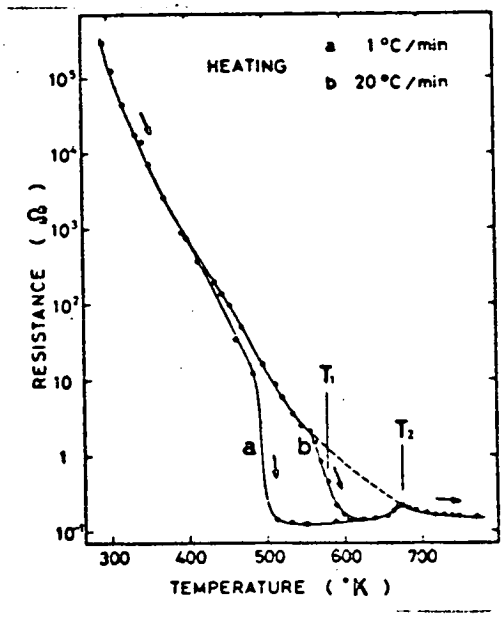

(b) Resistance vs. temperature characteristic for different heating rates.

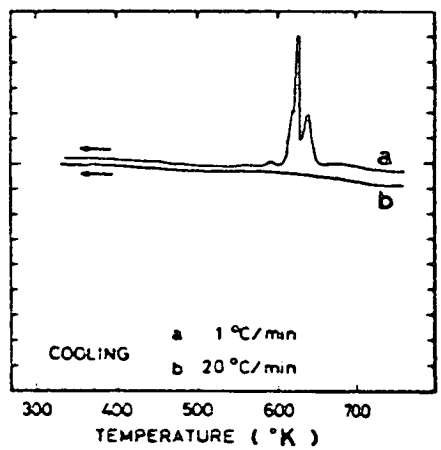

(c) DSC analysis for different cooling rates.

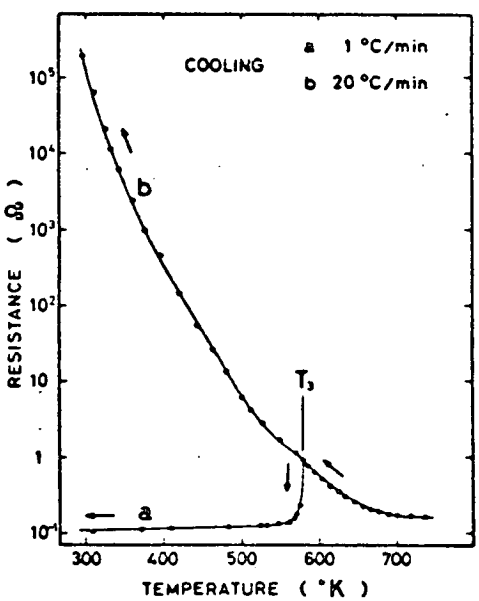

(d) Resistance vs. temperature characteristi for different cooling rates.

Figure 1.2 Differential scanning calorimetric (DSC) and resistance data for $Ge_{10}As_{40}Te_{50}$ (From Tanaka et al[8]).

bulk glass, the material undergoes a second-order phase transition at the glass transition temperature, Tg. This marks the onset of softening and is accompanied by an increase of heat capacity and thermal expansion coefficent. At T_1, the crystallisation point, an exothermic peak is evident, occurring at a significantly lower temperature for the slower heating rate. This is accompanied by a sharp drop in the measured resistance. Between T_1 and the melting point, T_2, the material is in a crystalline phase, and if cooled from this state will not return to its amorphous form, but if the material is cooled from the subsequent molten state, the resulting solid form is strongly dependent on cooling rate, as illustrated by the data of Figures (2(c)) and (2(d)). If the melt is cooled slowly, curve (a), a liquid-to-crystalline phase transition occurs at T_3, indicated by the DSC exothermic peak and the sudden drop in resistance. However, if the melt is cooled rapidly, curve (b), no corresponding transition occurs and the vitreous form is obtained.

1.3 Structural Aspects

Although chalcogenide glasses lack the long-range order (LRO) of the crystalline state, the arrangement of atoms is not entirely random and a high degree of short range order (SRO) is retained. Thus the first few "co-ordination shells" around any particular atom are usually in some well-defined orientation with respect to that atom, but beyond the nearest neighbours the periodicity becomes more and more blurred. This is

usually demonstrated experimentally by X-ray absorption fine structure (EXAFS) techniques, from which a radial distribution function (RDF) can be derived.

Most of the research into the structural aspects of chalcogenide glasses has naturally concentrated on the elemental glasses such as Se, and on those binary chalcogenides with direct crystalline counterparts, such as As_2Se_3 and As_2Te_3, rather than on the more complex non-stoichiometric alloys. Crystalline Se, for example, exists in two main forms, trigonal Se (hellicoidal chain structure) and monoclinic Se (8-fold ring structure). Figure (1.3) compares the RDF's of crystalline hexagonal Se and amorphous Se in the bulk glass and vapour deposited forms[9]. The first two peaks of the amorphous data are about as sharp as the corresponding crystalline hexagonal peaks, although the data indicates that the nearest neighbours are slightly farther out than in the hexagonal structure, 2.34Å and 3.75Å as against 2.32Å and 3.55Å, but at larger radial distances the two sets of data differ radically. Although the structure of amorphous Se is not completely resolved, it is generally thought to consist of a mixture of trigonal chains and 8-fold rings.[9,10,11]

X-ray diffraction studies of bulk, glassy As_2Se_3[12-14] show that the first and second interatomic spacings are very close to those in the crystal, and that the co-ordination numbers are the same, indicating the preservation of short range order. However, studies of glassy As_2Te_3[12,15] indicate that the local co-ordination in the amorphous material is different from that in the crystalline. In

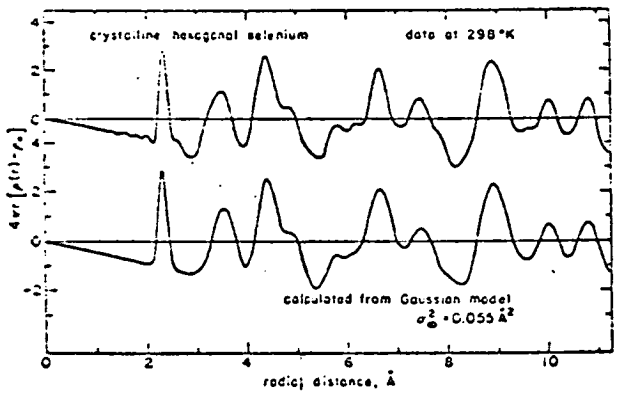

Figure 1.3(a) Reduced radial distribution function and calculated function from Gaussian model of crystalline hexagonal selenium.
(From Kaplow et al[9]).

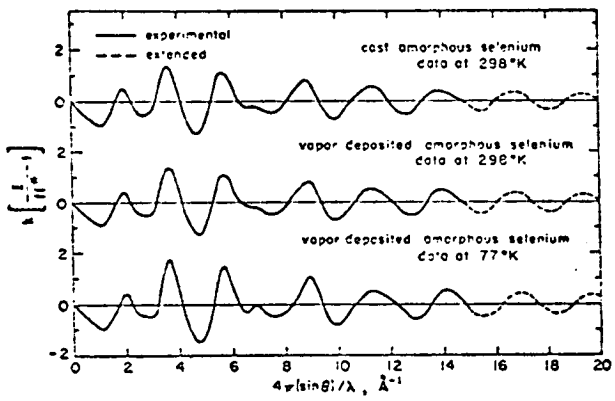

Figure 1.3(b) Reduced-intensity functions for amorphous selenium.
(From Kaplow et al[9]).

order to explain this perhaps surprising data, some knowledge of the crystal structures is required. Crystalline As_2Se_3,[16,17] illustrated schematically in Figure (1.4(a)), is known to have a pronounced layered structure[16,17], each layer being composed of puckered rings in which each As atom is bonded to three Se atoms and each Se atom is bonded to two As atoms. The interlayer separation is large, the layers held together weakly by Van der Waals bonding. Crystalline As_2Te_3[15], illustrated schematically in Figure (1.4(b)), manifests a structure which consists of zig-zag chains in which the As atoms are octahedrally and trigonally bound to the Te atoms, such that the As atoms have co-ordination numbers of 6 or 3, and the Te atoms have co-ordination numbers of 3 or 2.

Models for glassy As_2Se_3, and for amorphous As_2Se_3 in thin film form, have been obtained by Renninger et al[18] by fitting the computed RDF's of these theoretical configurations to very accurate experimental data. The cross-sections illustrated in Figure (1.4(c)) show the proposed group structure, a group being defined as a collection of four or more atoms connected through nearest neighbour bonds. Fitzpatrick and Maghrabi[15] have suggested that glassy As_2Te_3 might be arranged in a three dimensional network made up of random, covalently bonded As $Te_{3/2}$ groupings, thus having a structure not dissimilar to glassy As_2Se_3.

Comparatively little data is available for the more complex glasses, such as those of the Ge-As-Te system. Can these materials be interpreted in terms of a glassy,

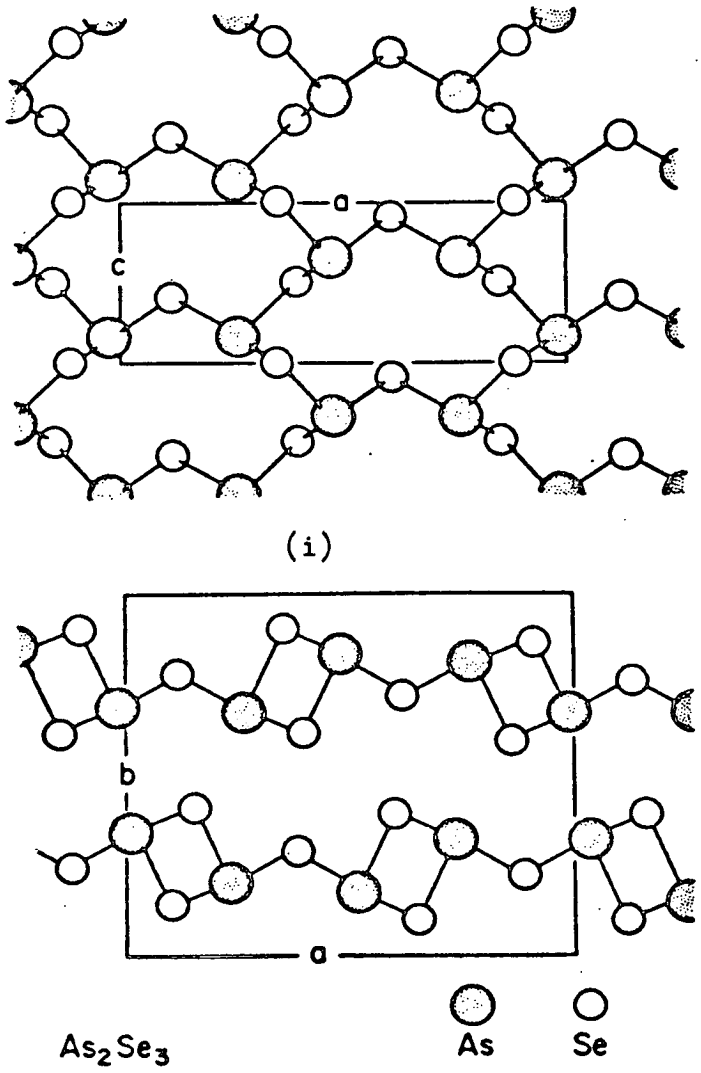

Figure 1.4(a) Crystal Structure of As_2Se_3.

(i) Atomic arrangement in layers.

(ii) Inter-layer configuration.

(From Thornburg[17]).

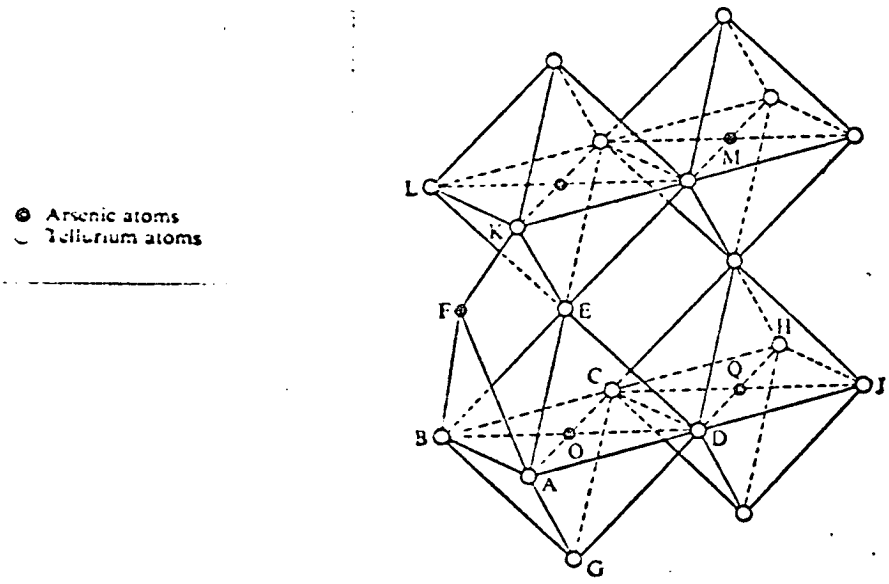

Figure 1.4(b) Crystal structure of As_2Te_3.
(From Fitzpatrick et al[15]).

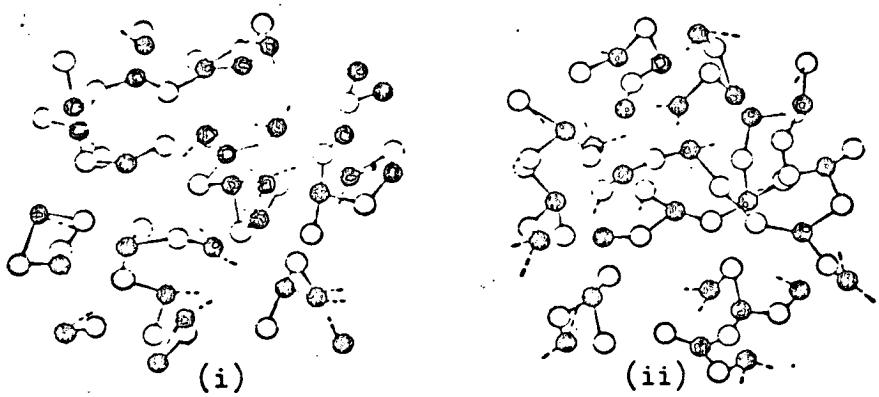

Figure 1.4(c) Cross sections of models for 40 As (dark circles)–60Se (open circles).

(i) Bulk.

(ii) Film.

(From Renninger et al[18]).

random structure of As $Te_{3/2}$ groupings with Ge atoms incorporated in some way? Hilton et al[7] have observed the first two peaks of the RDF in glassy $Ge_{15}As_{45}Te_{40}$ to be at 2.50Å and 4.02Å respectively. As the first peak contains all interatomic distances ranging from Ge-Ge= 2.43Å to Te-Te=2.86Å, it is difficult to make definite pronouncements about the short range order.

X-ray analysis and transmission electron microscopy on chalcogenide ternary and quaternary systems have shown the importance of annealing at elevated temperatures with regard to structural transformation and phase separation.[19-21] Amorphous thin films prepared from glasses in the Ge-As-Te system have a strong tendency to phase separate, compared to the Ge-As-Se system for example, as can be seen by the appearance of crystalline peaks on EXAFS data, and by the poly-crystalline structure of electron diffraction patterns. The vast majority of the work presented here was carried out at temperatures well below the point where phase-separation occurs, so that the thin films retain the true amorphous form.

1.4 Choice of Glass Composition

The principal chalcogenide alloy used for this work was the ternary compound, $Ge_{10}As_{40}Te_{50}$. This was chosen for various reasons:-

(a) Fabrication is relatively easy, lying well within the glass forming region of the Ge-As-Te system.

(b) It has a suitable conductivity and activation energy to allow experimental work at a wide range of

temperatures.

(c) The thermal and electrical properties of the alloy are fairly well documented in the literature.[2,4,22,23]

(d) Use of this glass provided a convenient link with the work of Main[24] in the same laboratory on switching in glasses of the Ge-As-Te system.

In addition, much of the experimental work on $Ge_{10}As_{40}Te_{50}$ has been repeated for the quaternary composition $Si_{12}Te_{48}As_{30}Ge_{10}$, another potentially useful switching glass whose thermal and electrical properties are well categorised.[19,25,26] This data provides a useful comparison with data on the ternary composition, as well as the work of Marshall[26-28] on $Si_{12}Te_{48}As_{30}Ge_{10}$, also resident in the same laboratory.

2.1 The Effect of Disorder on Band Structure

The band theory of crystalline solids is now very well established, and numerous reviews are available in the literature[1], and so it is not necessary to present one here. Rather it is desirable to consider how the same arguments and principles can be extended to arrive at a theory for electronic conduction in glassy materials. In a perfect crystalline material, the solution of the Schrödinger equation is facilitated by the periodic structure, and it is found that there are certain states (wave functions) in which the electron can propagate unhindered through the material. States of specifiable energy are available to an electron, but only in certain well defined bands, separated from each other by 'forbidden gaps'. The precise nature of the band structure depends on the geometry of the crystal, and the presence of particular impurities or defects in the crystal lattice can result in discrete energy levels within the forbidden gap, as illustrated in Figure (2.1(a)).

The distribution of electrons amongst the allowed energy states is governed by the Fermi-Dirac distribution,[1] illustrated in Figure (2.1(b)), and expressed,

$$F(E) = \frac{1}{1 + \exp\left((E-E_F)/kT\right)} \qquad (2.1.1)$$

where E_F is a constant known as the Fermi level or Fermi energy, k is Boltzmann's constant, and T the absolute temperature. When considering states at energies well

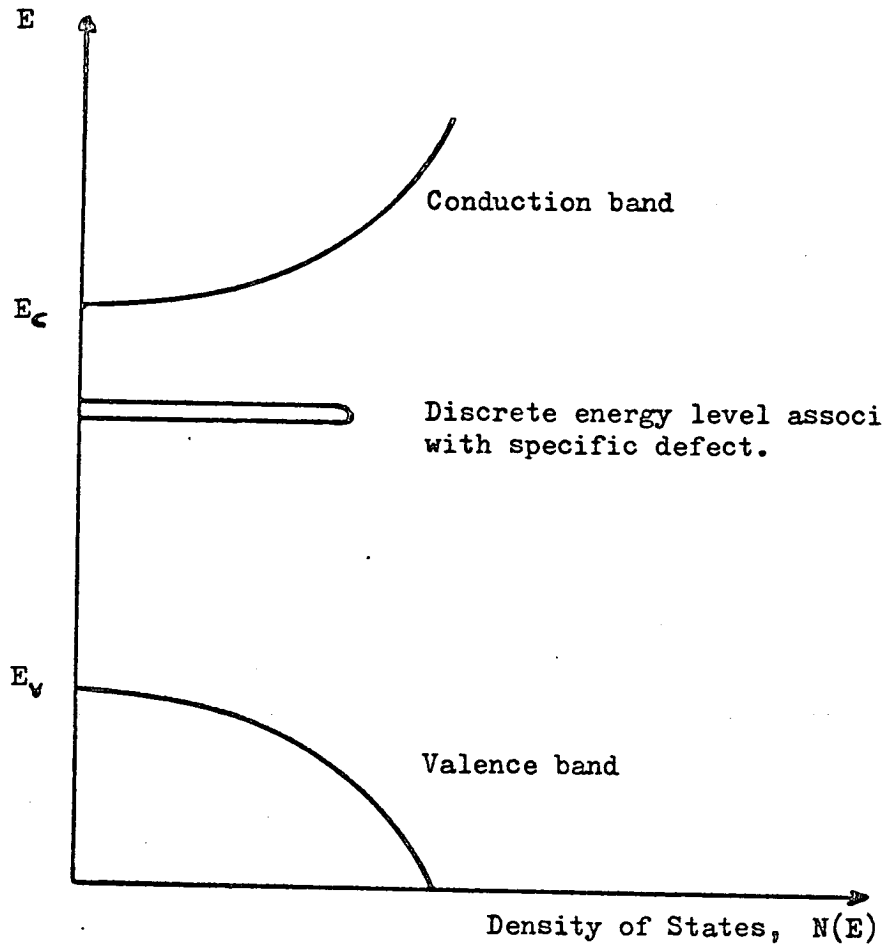

Figure 2.1(a) Schematic band structure for crystalline material with specific defect.

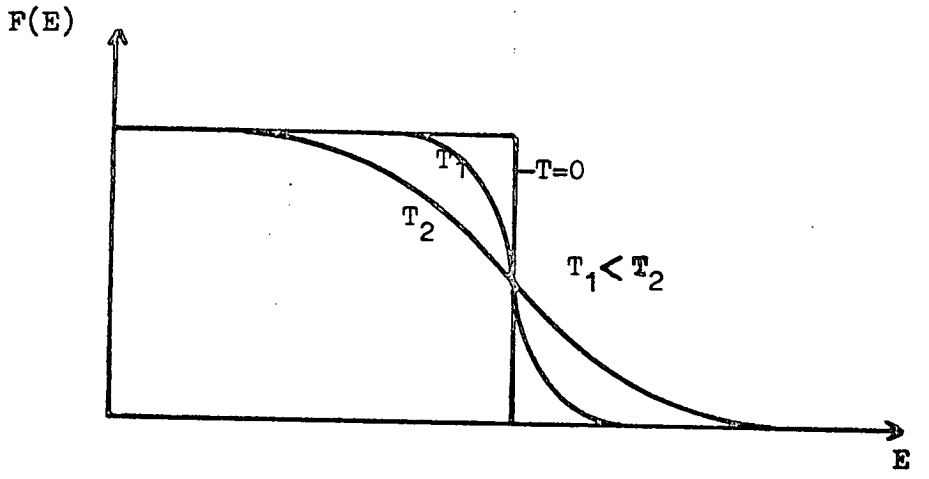

Figure 2.1(b) Schematic representation of Fermi function for three different temperatures.

above E_F, the Maxwell-Boltzmann approximation can be used,

$$F(E) = \exp(-(E-E_F)/kT) \qquad (2.2.2)$$

Thus knowing the Fermi level and the density of states at a particular energy, E, it is possible to calculate the number of electrons, n(E), occupying these states at any given temperature.

The preservation of short range order in the amorphous chalcogenides allows a theoretical treatment in terms of band theory,[2,3] analogous to the crystalline case, subject to certain modifications. An essential factor in all such models is the presence of localised states within the hitherto "forbidden" gap of the material. Localised defect states are formed, both from states which previously belonged to the valence band, and from states which previously belonged to the conduction band, the energy separation of such states from the parent band being related to the degree of distortion responsible. It is reasonable to suppose that there is a high probability of small atomic distortions and that larger distortions are less frequent, introducing the concept of a "tail" of localised states extending into the forbidden gap. Localised states in the conduction band tail are normally empty, and become negatively charged when occupied by a trapped electron, whereas states in the valence band tail are normally occupied by electrons, and become positively charged when a hole is trapped; i.e. the absence of an electron.

In addition to the "tails" of states, it is also possible that there may be sets of localised states at more or less discrete energies within the gap, characteristic of some particular structural characteristic of the material.

The exact nature and distribution of localised states in these materials is still a matter for conjecture, but it is probable that there is no single band model for all amorphous semiconductors, or even for all chalcogenides, but that rather each separate composition must be considered in its own right . On the basis of these considerations, several authors have proposed various band models for chalcogenide alloys. Qualitatively, complex chalcogenide compounds of non-stoichiometric proportions are expected to have larger band tails, possibly with some degree of overlap, and are perhaps best represented by the model of Cohen, Fritzsche and Ovshinsky[4] (CFO model) illustrated in Figure (2.2(a)). The density of states at the Fermi level may be as high as 10^{25}-10^{26} $m^{-3}.eV^{-1}$.

For elements and simple stoichiometric compounds such as Se, As_2Se_3 and As_2Te_3, in which a high degree of short range order has been demonstrated, one might expect much shorter band tails and peaks of localised states at reasonably well-defined levels within the gap, associated with particular structural defects. The Marshall-Owen model[5] for vitreous As_2Se_3, shows considerably less extensive band tails than the CFO model, and has two well defined sets of localised states within the forbidden gap:- a density of 10^{25}-10^{26} $m^{-3}.eV^{-1}$ of "acceptor-like" states in the lower half of the gap, compensated by an almost equal concentration of "donor-like" states in the upper half of the gap, necessary to explain the apparent intrinsic behaviour of As_2Se_3.

A common feature of these and other widely used

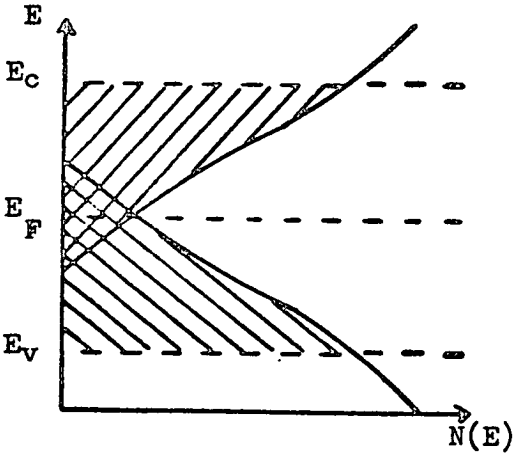

Figure 2.2(a) Cohen-Fritzsche-Ovshinsky model (From Ref. 4)

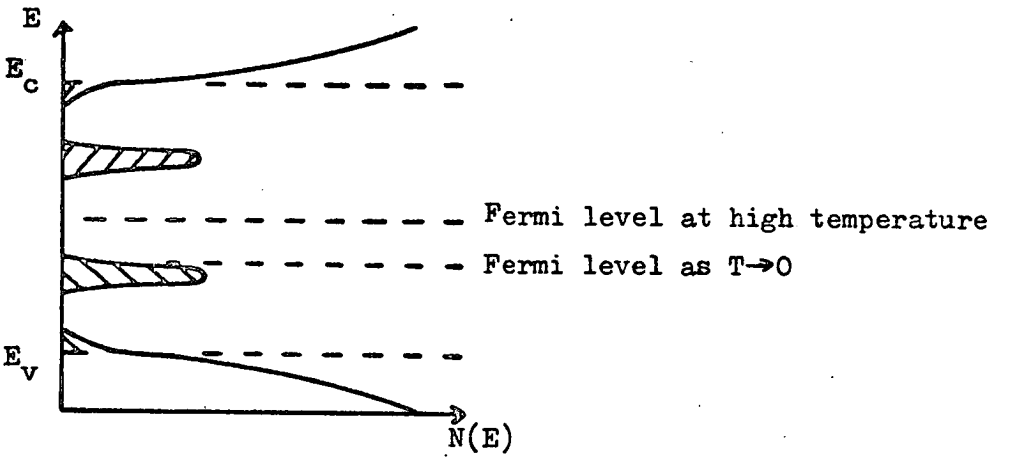

Figure 2.2(b) Marshall-Owen model (From Ref. 5)

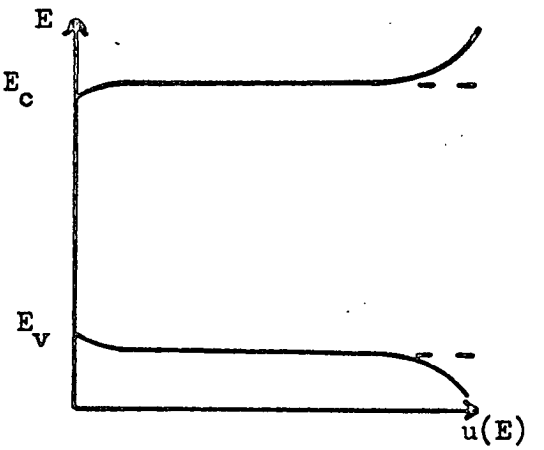

Figure 2.2(c) Schematic representation of mobility gap.

models[6,7] is the existence of the 'mobility gap', illustrated in Figure (2.2(c)). This implies a sharp drop in the mobility of the charge carriers, of the order of a factor $\triangleq 1000$[8], at the 'mobility edges', E_c and E_v.

Before considering charge transport in the bulk of the amorphous chalcogenides, it is convenient to mention here two recurring problems concerned with band theory which arise in the study of electrical contacts and surfaces on these alloys. In a perfect crystalline semiconductor, surface states have been shown to exist within the forbidden gap due to the interruption of the periodic lattice structures at the surface of the crystal,[9] generally classified into fast and slow states. The fast states exchange charge with the conduction or valence band very rapidly, whereas slow states require a longer period for charge exchange. In a real semiconductor, additional surface states may be present due to the absorption of impurities on the surface. On the other hand, in an amorphous semiconductor, the presence of a high density of localised states throughout the material may be combined, at the surface, with surface states of this nature. Thus in a variety of experiments (e.g. field effect, tunnelling), it is not entirely clear whether the localised states under investigation are peculiar to the surface, or an extension of bulk localised states into the surface layer, or a combination of both.

A second problem is indicated by the schematic three-dimensional model for an amorphous semiconductor proposed by Fritzche[10], illustrated in Figure (2.3), to explain

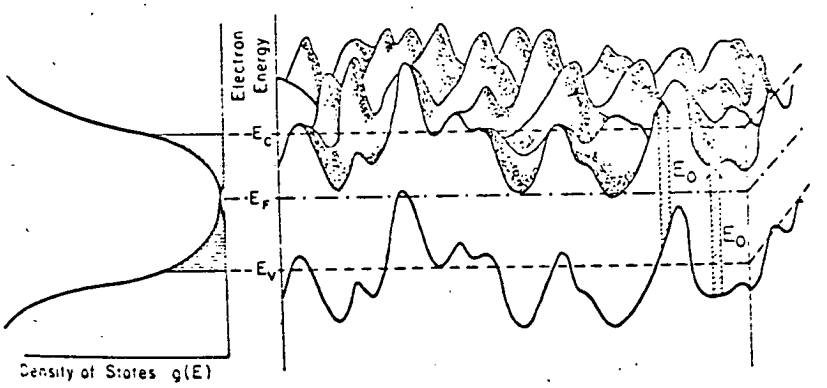

Figure 2.3 Illustration of the three-dimensional model of Fritzsche[10], considering long-wavelength potential fluctuations. E_c and E_v are the mobility edges or percolation thresholds and E_α corresponds to an average optical gap.

the discrepancy between the optical absorption edge and the electrical gap in a Ge-As-Te-S alloy. This model predicts irregular spatial potential fluctuations throughout the bulk of the semiconductor, and has important consequences as regards charge transport theory (Section 2.2). The model can plausibly be represented in two dimensions by the familiar CFO model, as is also illustrated in Figure (2.3). The presence and possible enhancement of these potential fluctuations by discrete localised charges in the barrier region, may invalidate the conventional description of contacts, assuming a uniform charge distribution and equipotential surfaces parallel to the interface. Thus, while many of the theoretical aspects of this work are considered in terms of two dimensional models, the alternative or accompanying explanation in three dimensions must also be considered.

2.2 Electronic Transport

Charge transport in an amorphous semiconductor can be thought of as a combination of several parallel contributions, though normally one particular mechanism predominates. Consider the model shown in Figure (2.4), based on that of a review paper by Spear[11]. At energies well removed from the mobility edges, the effect of random potential fluctuations on transport is slight. Hence, carriers may propagate freely, subject to the usual scattering processes, and a Bloch-type wave function is applicable. The mobility, μ, is given by a standard expression[1],

$$\mu = {}^{q}/_{m^*}.\tau \geq 10^{-2} m^{-2}.V^{-1}.s^{-1} \qquad (2.2.1)$$

where q is electronic charge, m* the effective mass and τ

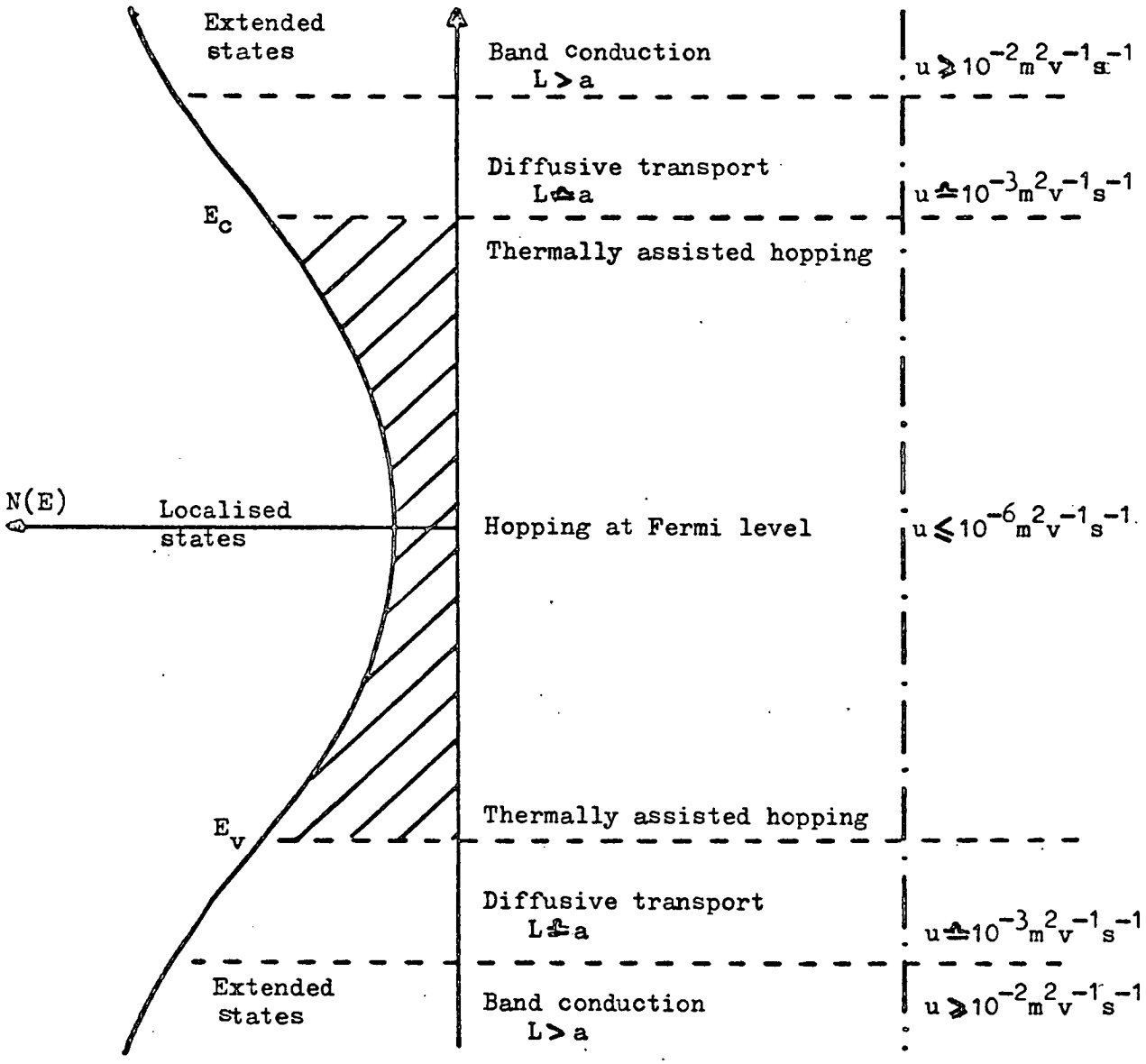

Figure 2.4 Illustration of the various transport processes in an amorphous semiconductor of arbitrary localised state distribution.

(From Spear[11]).

L mean free path

a inter-atomic separation

the mean free time between collisions.

At energies close to the mobility edges, various effects associated with the absence of long range order begin to dominate the transport. The mean free path and the coherence length of the electron wave functions approach the interatomic separation, and the assumptions leading to free propagation with Bloch type wave functions cease to be valid. Within this region, Cohen[3] argues that carrier transport is essentially diffusive, similar to Brownian motion. By considering the carrier jumping from site to site, with an atomic frequency, $\nu_c \simeq 10^{15} s^{-1}$, an estimate of the drift mobility can be obtained from the expression,

$$\mu = {}^{1}/_{6} \cdot \frac{qa^2}{kT} \cdot \nu_c \simeq 10^{-3} m^2 . V^{-1} . s^{-1} \qquad (2.2.2)$$

where k is Boltzmann's constant, T the absolute temperature and a the interatomic distance.

The mobility edge can also be considered as a "percolation threshold" at E_c (or E_v).[10,12] Two dimensional constant energy cross-sections can be taken through the potential fluctuation model of Figure (2.3), as illustrated in Figure (2.5). Thus, below E_c, there are "lakes" of allowed localised regions, L_1 - L_5, separated by potential barriers, while above E_c, there is a finite possibility of a continuous path through the material, represented by the "ocean", O_1. At energies far above E_c, the "ocean" extends almost throughout the entire cross-sectional area.

In the region of localised states just below E_c, transport is achieved by a thermally activated hopping

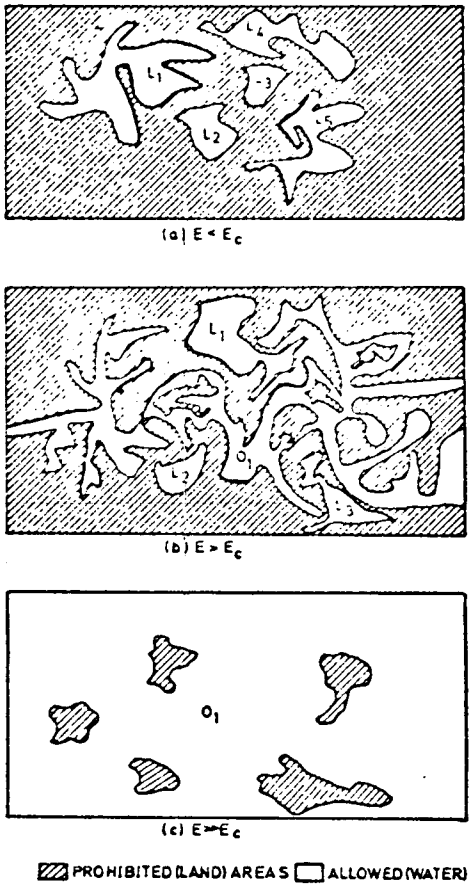

Figure 2.5 Percolation model (from Brenig[12]).

process,[6,8] with the mobility given by[11]

$$\mu = \frac{qR^2}{kT} \cdot \nu_{ph} \cdot \exp(-2\alpha R) \cdot \exp(-W/_{kT}) \qquad (2.2.3)$$

where R is the average hopping distance and ν_{ph} the phonon frequency. The term $\exp(-2\alpha R)$ is a measure of the overlap of the wave functions on neighbouring hopping sites, and the term $\nu_{ph}.\exp(-W/_{kT})$ represents the probability that a localised carrier will hop to a new site at an energy W above the original site. From this expression the hopping mobility is estimated to be $10^{-6}m^2.V^{-1}.s^{-1}$ or less; i.e. considerably smaller than in the region above the mobility edge.

Conduction may also occur by carriers hopping between localised states at the Fermi level,[13] according to the expression for the conductivity,

$$\sigma = \sigma_o.\exp(\frac{-\Delta W}{kT}) \qquad (2.2.4)$$

where σ_o is a constant and ΔW is half the width of the defect band at E_F. This process has an even lower mobility than those already mentioned. However, this expression only applies to hopping between nearest neighbours and Mott[8] further argues that at very low temperatures hopping to more distant sites is probable, and ultimately the conductivity behaves as,

$$\ln \sigma = A - BT^{-\frac{1}{4}} \qquad (2.2.5)$$

The total conductivity in a given material is the sum of all these contributions, and is obtained as an integral over all the available energy states.

$$\sigma = q\int N(E).\mu(E).F(E).dE. \qquad (2.2.6)$$

The effect of temperature on the relative magnitudes of the

various types of conduction is illustrated in Figure (2.6), using the Mott-Davis model[6] which shows a single deep level of localised states centred at the Fermi level. At high temperature, T_1, the thermal equilibrium densities of electrons and holes in extended states are sufficiently large for "band-type" conduction to predominate. At an intermediate temperature, T_2, the occupancy in extended states is negligible, and thermally activated hopping in the band tails is the most important mechanism, while at a very low temperature, T_3, hopping between localised states at the Fermi level becomes dominant, despite the very low mobility.

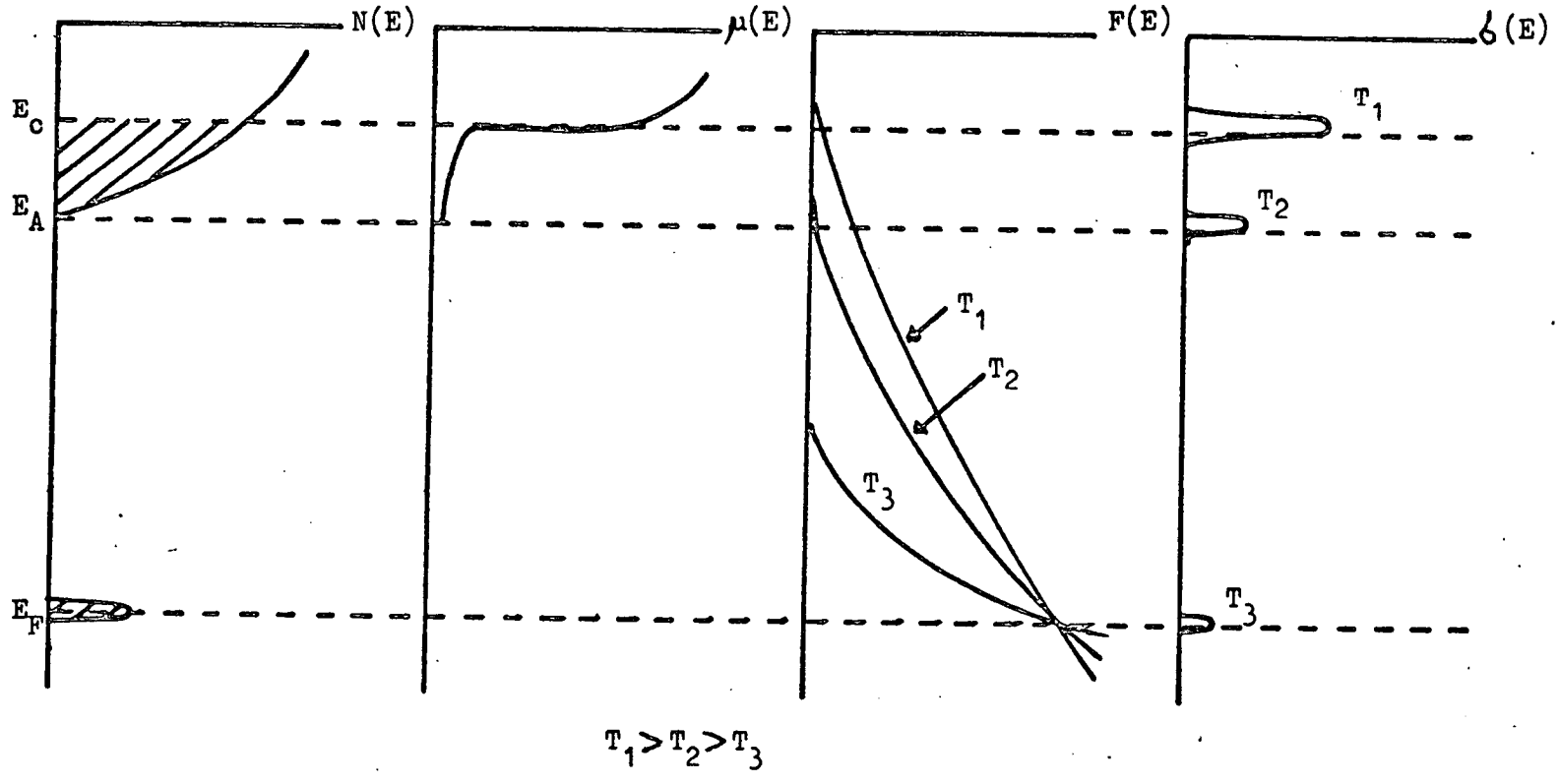

Figure 2.6 Illustration of the effect of temperature on the mode of conduction (From Mott and Davis[8]).

CHAPTER 3 SEMICONDUCTOR JUNCTIONS

3.1 Introduction

It has been demonstrated in the previous chapters that the existence of short-range order in the chalcogenide glasses allows a discussion of their properties in terms of conventional band theory, subject to certain modifications. Thus it is reasonable to suppose that the junctions between amorphous semiconducting glasses and other materials can be treated in a manner analogous to crystalline semiconductor junctions, although the dominant transport processes may be radically different. Many fine references exist,[1-6] covering the whole spectrum of crystalline semiconductor junction phenomena, thus the purpose of this chapter is to provide a brief resume of conventional theory, as a point of reference in the development of the energy band relations and transport processes in chalcogenide glass devices, presented in subsequent chapters.

3.2 The Metal-Crystalline Semiconductor Junction

The energy band relation at a metal-semiconductor contact is generally determined by both the respective metal and semiconductor work functions, and the surface states. However, two limiting cases can be defined. In the absence of interface states, as illustrated in Figure (3.1(a)), charge flows from the semiconductor to the metal as the two materials are brought into contact, such that electronic equilibrium is established and the Fermi levels coincide. Where the metal work function, ϕ_m, is greater than that of the semiconductor, ϕ_s, the Fermi level in the

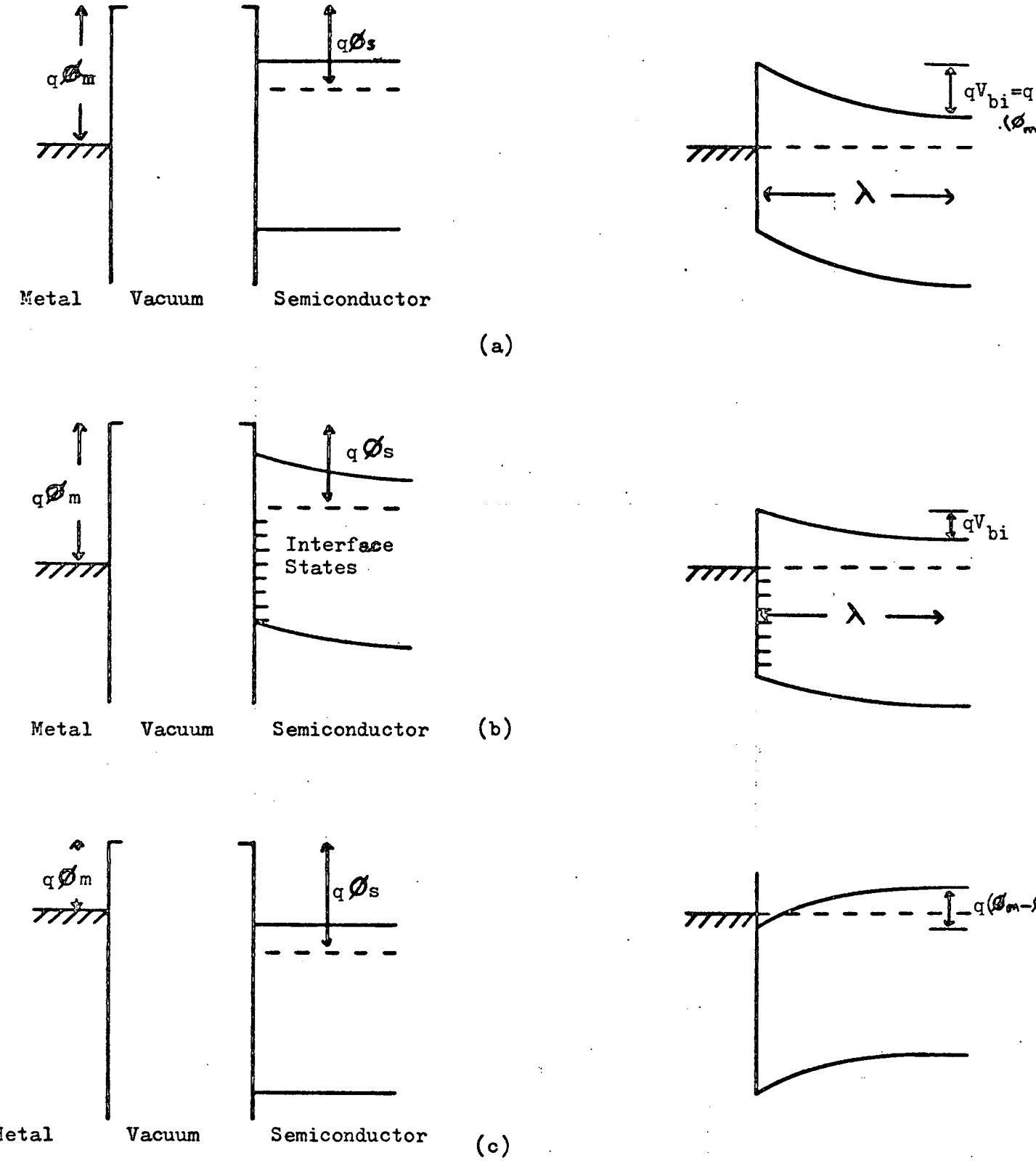

Figure 3.1 Energy band relations at metal-semiconductor contacts.

(a) Blocking contact: no interface states.
(b) Blocking contact in presence of interface states.
(c) Ohmic contact.

semiconductor is lowered relative to the metal Fermi level by an amount equal to the difference in the two work functions, creating a contact potential difference,

$$q\,V_{bi} = q(\phi_m - \phi_s) \qquad (3.2.1)$$

A negative charge is built up at the metal surface, while an equal and opposite positive charge exists within the semiconductor. The resulting depletion region adjacent to the contact constitutes an effective blocking barrier to the majority carriers in the semiconductor, in this case electrons, and is referred to as a Schottky barrier.[7]

The width of the resultant space charge region, , can be deduced from a solution of Poisson's equation, subject to a 'square' shape approximation for the charge distribution in the depletion region. Under zero bias conditions, this can be expressed[1]

$$\lambda = \left[\frac{2\varepsilon_s(V_{bi} - kT/q)}{qN_D}\right]^{\frac{1}{2}} \qquad (3.2.2)$$

where ε_s is the semiconductor permittivity, and N_D the donor concentration.

The second limiting case is illustrated in Figure (3.1(b)). Here, the barrier height is determined by the surface properties of the semiconductor rather than the respective work functions. The metal and the semiconductor come into equilibrium with the interface layer essentially independently, the density of surface states being large enough to accommodate any additional charges arising from the contact of the two materials.

Finally, in Figure (3.1(c)), the case where $\phi_m < \phi_s$ in the absence of surface states is considered. It is

evident that under these circumstances the preservation of electronic equilibrium leads to the formation of an accumulation region adjacent to the interface, and the contact is "injecting" or "ohmic" rather than "blocking". The space charge region provides no barrier to majority carrier flow, the current through the system generally being controlled by the semiconductor bulk resistance.

What are the main transport mechanisms in metal-semiconductor blocking contacts, and how are these affected by the relevant bias conditions? Figure (3.2) illustrates the influence of forward and reverse bias on the Schottky barrier formed between an n-type, non-degenerate, crystalline semiconductor and a metal. The principal mechanisms of current transport are summarised;[8]

(a) Thermionic emission of electrons over the top of the barrier.

(b) Quantum mechanical tunnelling through the barrier.

(c) Recombination/generation in the space charge region.

(d) Recombination/generation in the neutral region.

In practice, in nearly ideal Schottky diodes, process (a) is by far the most important (though not, as shall be seen, in amorphous semiconductor-metal junctions), while processes (b), (c) and (d) cause departures from ideal behaviour.

The classical isothermal thermionic emission theory of Bethe[9] and the isothermal diffusion theory of Schottky[8] have been combined recently into a more general thermionic emission-diffusion theory by Crowell and Sze.[10] Briefly,

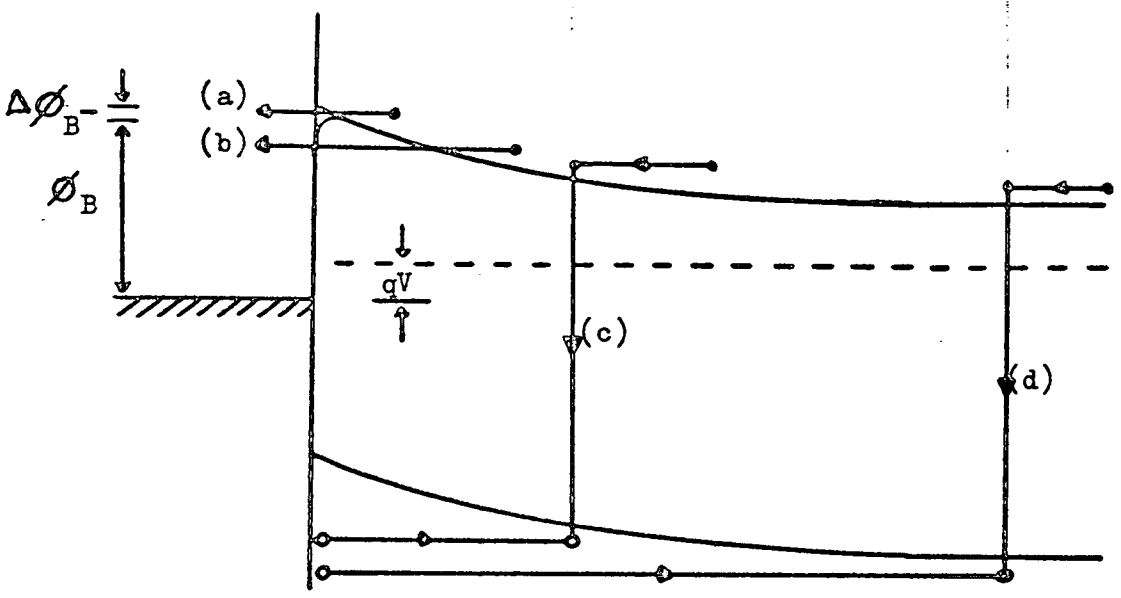

Forward bias

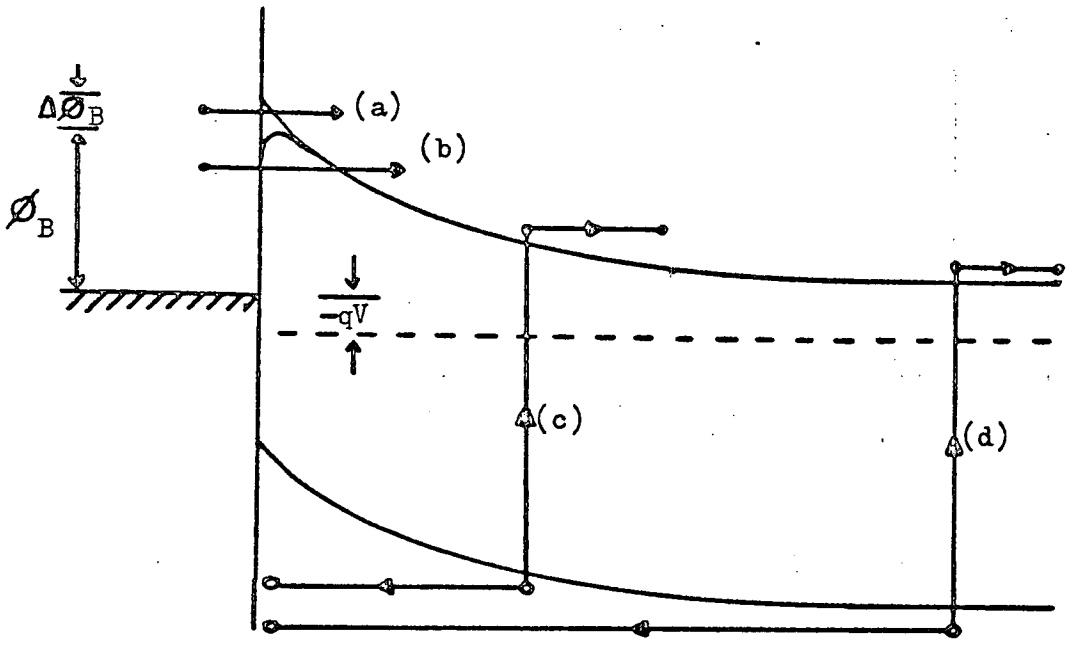

Reverse bias

Figure 3.2 Transport processes in a Schottky barrier under forward and reverse bias conditions.

(a) Thermionic emission over the barrier.
(b) Quantum mechanical tunnelling through the barrier.
(c) Recombination(forward bias)/ generation (reverse bias)in the space charge region.
(d) Recombination/generation in the neutral region.

the thermionic emission theory neglects the effect of electron collisions within the depletion region, assuming the thickness of the barrier layer to be small in comparison with the mean free path of the carriers. Thus the limiting process is emission over the potential barrier. In contrast, the diffusion theory considers the effect of electron collisions in the space charge region; i.e. the limiting process is drift and diffusion through the depletion region, which is large compared with the mean free path.

In either theory, the current density J can be expressed in terms of the applied bias, V,

$$J = J_o(\exp(\frac{qV}{kT}) - 1) \qquad (3.2.3)$$

where J_o is the saturation current density. This implies a highly rectifying characteristic, illustrated schematically in Figure (3.3(a)). The expression for J depends on the applicable theory. For the thermionic emission case,

$$J_o = A^{**}T^2 \exp\left[\frac{-q\phi_B}{kT}\right] \qquad (3.2.4)$$

where A** is the effective Richardson constant and ϕ_B the barrier height. In the diffusion case,

$$J_o = q.N_c.\ \mu.E_m.\ \exp\left[\frac{-q\phi_B}{kT}\right] \qquad (3.2.5)$$

where N_c is the effective density of states in the conduction band, μ the electron mobility, and E_m the maximum field strength, which is expressed,

$$E_m = \left[\frac{2qN_D}{\epsilon_s}\ (V_{bi} - V - kT/q)\right]^{\frac{1}{2}}. \qquad (3.2.6)$$

The application of an electrical field across the depletion region lowers the effective barrier height by an

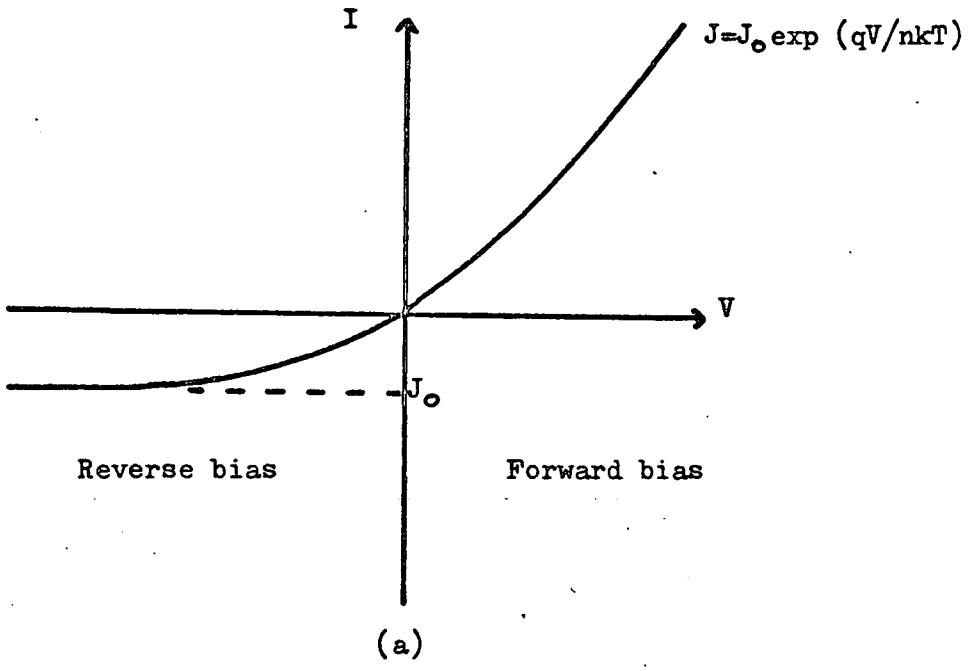

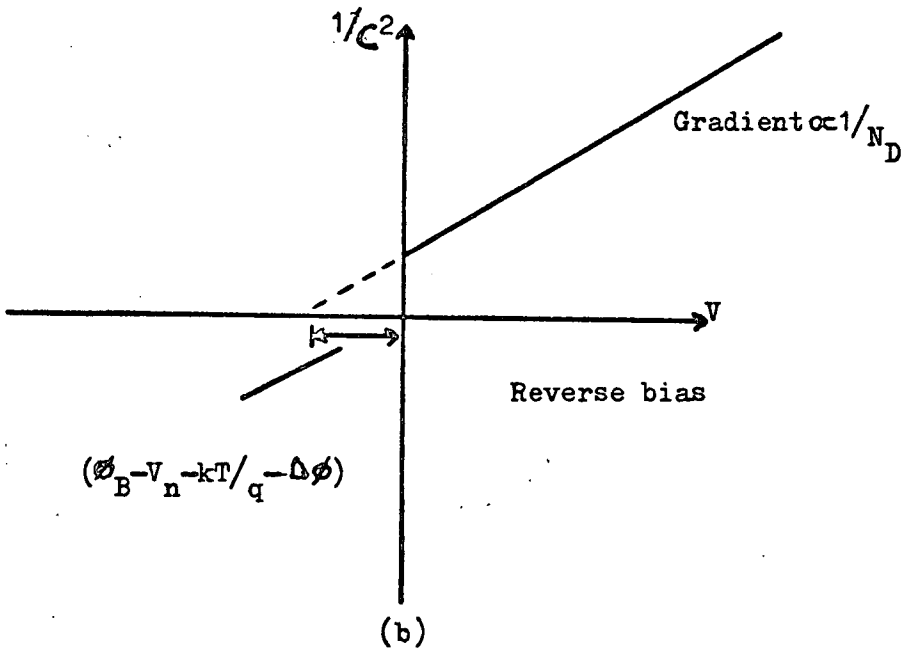

Figure 3.3 (a) Schematic I-V characteristic of Schottky barrier.
(b) Schematic $1/C^2$ - V characteristic of Schottky barrier.

amount $\Delta\phi_B$, due to image force lowering,

$$\Delta\phi_B = q\cdot\left[\frac{q}{4\pi\varepsilon_D}\right]^{\frac{1}{2}}\cdot\left[\frac{2qN_D}{\varepsilon_s}\right]^{\frac{1}{4}}\cdot(V_{bi}-V-kT/q)^{\frac{1}{4}} \qquad (3.2.7)$$

where ε_D is the image force permittivity, which is usually considered equal to ε_s. Image force lowering affects both the forward and reverse characteristics. Under forward bias, when $V > 3kT/q$, the characteristic can be represented by,

$$J \triangleq \exp(\frac{qV}{nkT}) \qquad (3.2.8)$$

where n is generally slightly above unity and can be representative of the 'idealness' of the diode. As an example, Crowell et al[11] report values of n=1.02 and n=1.04 for tungsten-silicon and tungsten-gallium arsenide diodes respectively.

The principal effect of image force lowering on the reverse characteristic is to 'soften' it. Where $V > 3kT/q$, equation (3.2.3) reduces to

$$J \triangleq J_o \qquad (3.2.9)$$

However, J_o is no longer constant with applied reverse bias, as the effective barrier height is voltage dependent. For the thermionic emission theory, the reverse current can be expressed

$$J_o = A^{**}T^2\exp\left[\frac{-q\phi_{BO}}{kT}\right].\exp\left[\frac{q(qE_m/4\pi\varepsilon_s)^{\frac{1}{2}}}{kT}\right] \qquad (3.2.10)$$

from a consideration of equations (3.2.4), (3.2.6) and (3.2.7). ϕ_{BO} is the asymptotic, zero-bias barrier height. As E_m is proportional to $(N_D)^{\frac{1}{2}}$ the presence of a large number of impurities can lead to appreciable softening of the reverse characteristic.[12]

The barrier region parameters can generally be determined from both current-voltage, capacitance-voltage and photo-electric measurements. For thermionic emission, the height of the barrier can be found by rearranging equation (3.2.4) to obtain,

$$\phi_B = kT/q \ln\left[\frac{A^{**}T^2}{J_s}\right] \qquad (3.2.11)$$

The capacitance of the semiconductor depletion region can be expressed as a function of reverse bias,

$$C = \left[\frac{q \varepsilon_s N_D}{2(V_{bi}-V-kT/q)}\right]^{\frac{1}{2}} \qquad (3.2.12)$$

Thus a plot of $1/C^2$ v. V is linear, of gradient proportional to the inverse of the semiconductor dopant density, and from whose intercept on the voltage axis, V_i, confirmation of the barrier height can be obtained from

$$\phi_B = V_i + V_n + kT/q - \Delta\phi_B \qquad (3.2.13)$$

where V_n is the depth of the semiconductor Fermi level below the conduction band. A schematic characteristic is illustrated in Figure (3.3(b)).

The third, most accurate and direct technique for determining the barrier height, by measuring the photovoltage or photocurrent of a metal-semiconductor contact when a monochromatic light is incident upon the metal surface, is discussed in the chapter on optical measurements.

3.3 Homojunctions

Homojunctions are formed in a semiconductor single crystal when an extrinsic p-type region and an extrinsic n-type region are in close contact, separated by a

relatively narrow transition zone, as illustrated in Figure (3.4(a)). An 'abrupt' junction is one in which the p-type region has a uniform concentration of acceptors, N_a, extending to the interface, where it adjoins an n-type region with a uniform concentration of donors, N_D, by a step function transition, illustrated in Figure (3.4(b)). A 'graded' junction is one in which N_A and N_D vary relatively slowly with distance normal to the junction, before reaching their bulk values at some distance into the semiconductor, as illustrated in Figure (3.4(c)). In practice, the abrupt junction is easier to analyse mathematically, and often provides a good approximation to the real situation.

The application of an external bias to a p-n junction causes rectification, as depletion regions are present on either side of the junction similar to the depletion region present in the blocking semiconductor-metal contact. These depletion regions are usually the most resistive part of the crystal, and hence most of the voltage drop occurs across these regions except under high forward bias. In this case, Figure (3.5(a)), the barrier is reduced, and a large current flows due to the injection of majority carriers into the region of opposite polarity. Under reverse bias, the barrier is raised, and a considerably smaller current flows due entirely to the diffusion of minority carriers towards the junction, as illustrated in Figure (3.5(b)). The ideal current-voltage characteristic is, not surprisingly, similar to that of the metal-semiconductor diode in form,

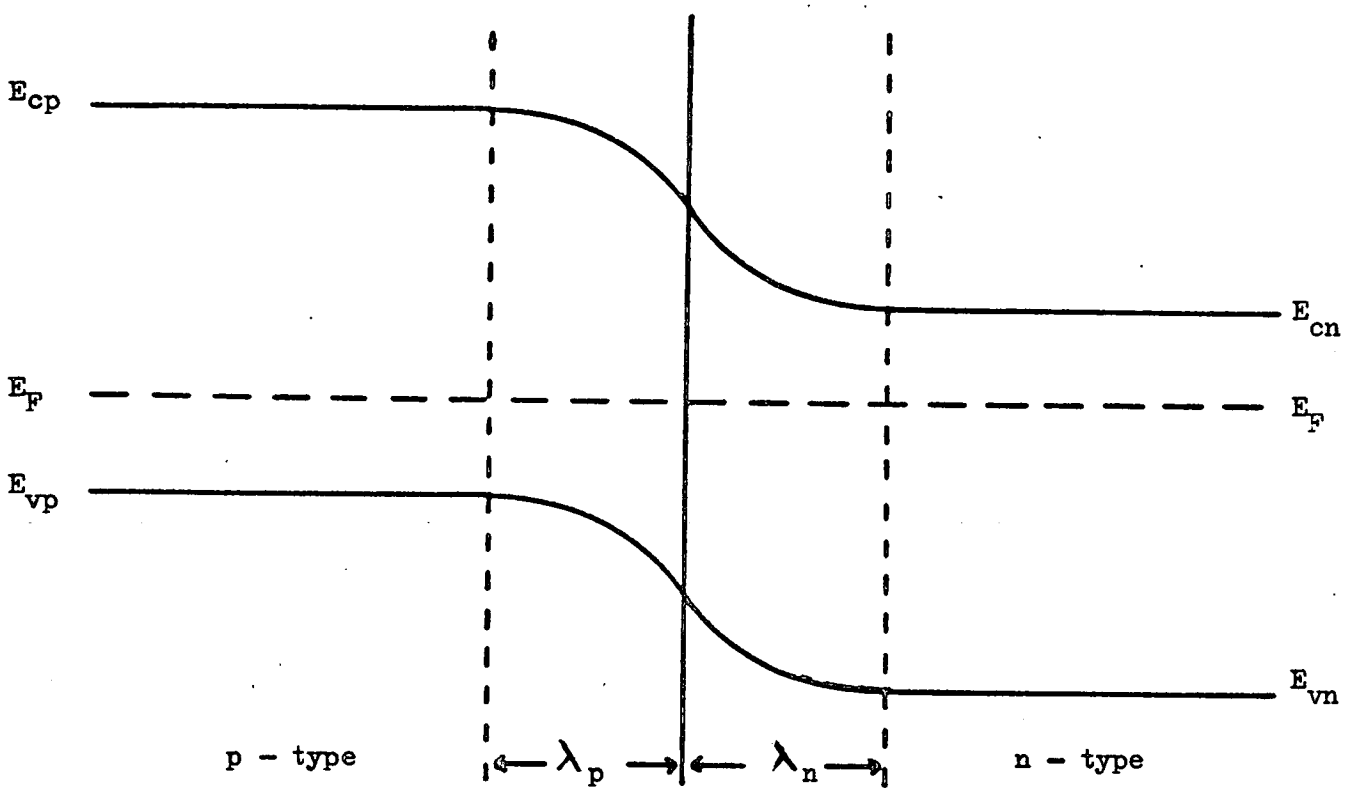

Figure 3.4(a) Energy band relation for a p–n homojunction.

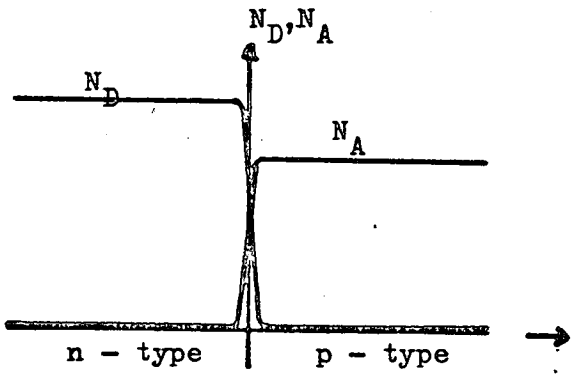

Figure 3.4(b) Impurity atom concentration for an abrupt junction.

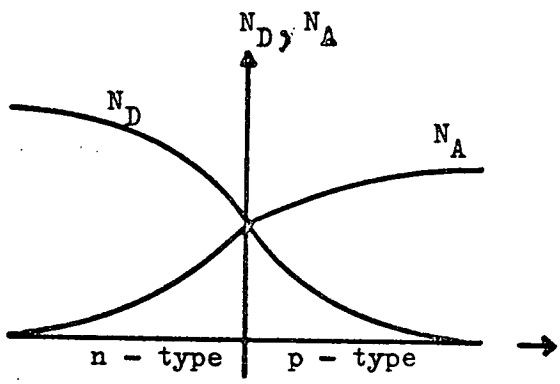

Figure 3.4(c) Impurity atom concentration for a graded junction.

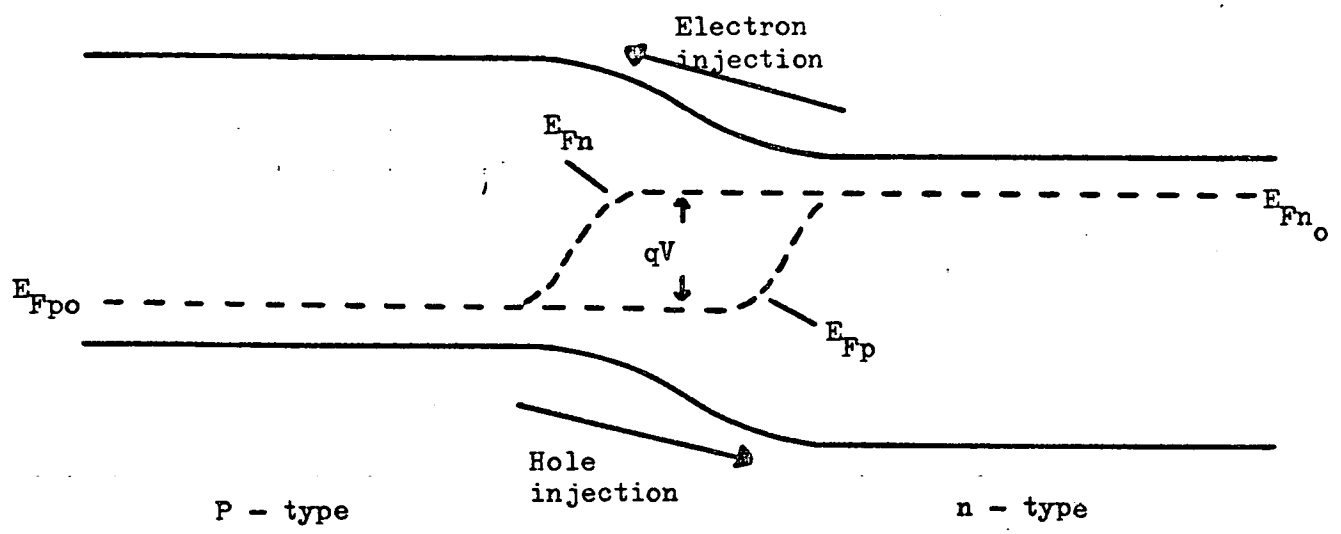

Figure 3.5(a) Homojunction under forward bias.

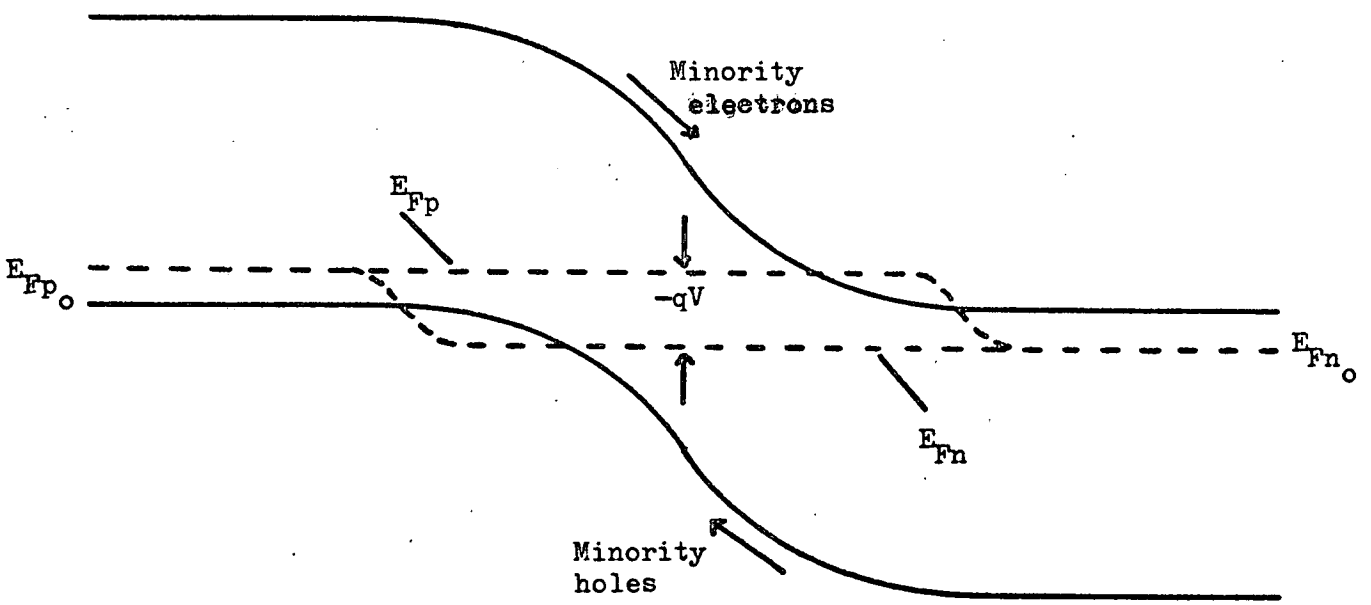

Figure 3.5(b) Homojunction under reverse bias.

E_{Fp} Quasi-Fermi level for holes.

E_{Fn} Quasi-Fermi level for electrons.

E_{Fp_o}, E_{Fn_o} Bulk Fermi levels.

$$J = J_s \left(\exp\left(\frac{qV}{kT}\right)-1\right) \qquad (3.3.1)$$

However, the reverse saturation current, J_s, is now expressed,

$$J_s = \frac{qD_p}{L_p} \cdot p_n + \frac{qD_n}{L_n} \cdot n_p \qquad (3.3.2)$$

where D_p and D_n are the hole and electron diffusion constants, L_p and L_n are the hole and electron diffusion lengths respectively and p_n and n_p are the minority carrier concentrations in the n and p regions. As the minority carrier concentrations are exponentially dependent on temperature, it follows that J_s is also exponentially temperature-dependent.

The reverse saturation current is dependent on applied bias for two reasons. Firstly, with increasing voltage across the junction, the depletion regions widen and the minority carriers are collected from a wider area, leading to a slight increase of J_s with reverse bias. Secondly, at much higher reverse bias, the relatively high electric field intensity in the depletion layers can lead to 'avalanching' of minority carriers, until eventual junction breakdown is reached. Minority carriers crossing the depletion layer attain relatively high energies per free path, and in subsequent collisions may break covalent bonds forming electron-hole pairs. The multiplication of minority carriers by this effect is represented by the Miller factor,[13]

$$M = \frac{1}{1-\left[\frac{V}{V_B}\right]^m} \qquad (3.3.3)$$

where V_B, the breakdown voltage, and m are constants for the particular junction concerned.

A plot of $1/C^2$ vs. V is linear, as in the case of metal-semiconductor diodes, although the capacitive contribution of both depletion regions must be considered,

$$C = \left[\frac{q\varepsilon_s . N_A . N_D}{2(V_{bi}-V).(N_A+N_D)}\right]^{\frac{1}{2}} \qquad (3.3.4)$$

In many cases, either N_A or N_D can be determined, depending on the relevant doping concentrations, and the intercept on $1/C^2 = 0$ yields the diffusion voltage, V_{bi}.

Under bias conditions, the minority carrier concentrations in both n- and p-type regions contiguous to the space charge layers are greatly disturbed from the equilibrium values, while the concentration of majority carriers, relative to the equilibrium values, is not much affected. This leads to the introduction of the concept of quasi-Fermi levels, (Q.F.L's). Under forward bias, the injection of majority carriers into the region of opposite polarity, increases the concentration of minority carriers on the opposite side, shifting the relevant Q.F.L's, as illustrated in Figure (3.5(a)). Under reverse bias, majority carrier injection is prevented, but the presence of the potential barrier encourages the flow of minority carriers, reducing their concentration and shifting the Q.F.L's, as illustrated in Figure (3.5(b)). Within the barrier region, the difference between the two Q.F.L's is proportional to the applied bias, while at distances far from the interface the minority carrier concentrations revert to their equilibrium values.

3.4 Heterojunctions

The heterojunction is defined as a junction formed between two semiconductors having different energy band gaps, and like the homojunction can further be classified as abrupt if the charge density in the depletion regions can be approximated to a square function. They can also be classified as isotype, where the semiconductors in contact are of the same conductivity type, p-p or n-n, or anisotype for semiconductors of opposite conductivity type, p-n.

The energy band diagram of the ideal p-n heterojunction proposed by Anderson[14] is illustrated in Figure (3.6(a)). The two semiconductors in contact have different band gaps (E_g), different permittivities (ϵ), different work functions (ϕ) and different electron affinities (χ), and the energy discontinuities at the conduction and valence band edges (ΔE_c and ΔE_v) are a consequence of the abrupt charges in these parameters. The case of the n-n heterojunction illustrated in Figure (3.6(b)) [15,16] is somewhat different; as the work function in the wide gap semiconductor is the smaller, the energy bands are bent oppositely to the previous case. If, however, interface states are present, the energy bands at the interface are free to move up or down with the necessary charge being supplied by electrons(or their absence) in these states, as illustrated in Figure (3.6(c)), in a manner analogous to the metal-semiconductor contact, Figure (3.1(b)).

Returning to the anisotype model of Anderson, the widths of the respective depletion regions can be calculated

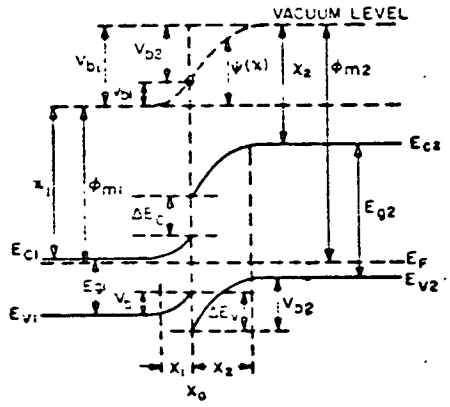

Figure 3.6(a) n–p heterojunction
(From Anderson[14])

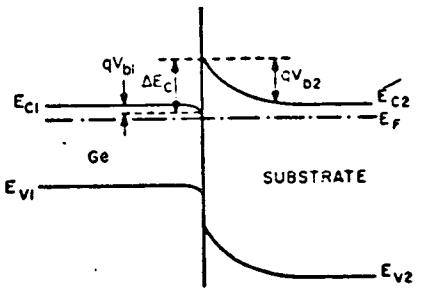

Figure 3.6(b) n–n heterojunction
(From Chang[15])

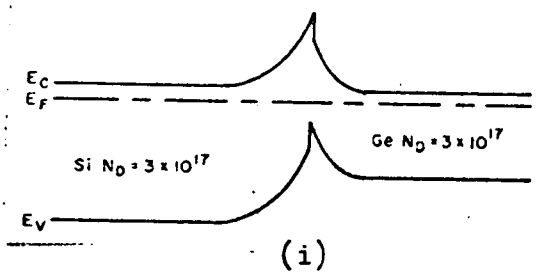

(i)

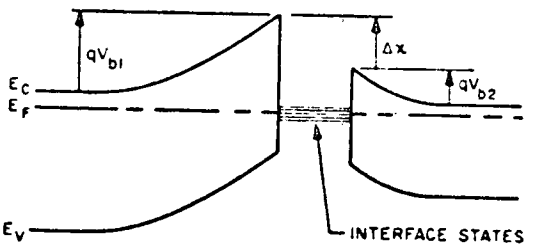

(ii)

Figure 3.6(c) (i) n–n heterojunction with interface states.
(ii) Magnified interface region.
(From Oldham and Milnes[16]).

using Poisson's equation in the usual manner,[14,17]

$$\lambda_1 = \left[\frac{2N_{A2}\varepsilon_1\varepsilon_2(V_{bi}-V)}{qN_{D1}(\varepsilon_1 N_{D1}+\varepsilon_2 N_{A2})}\right]^{\frac{1}{2}} \qquad (3.4.1)$$

$$\lambda_2 = \left[\frac{2N_{D1}\varepsilon_1\varepsilon_2(V_{bi}-V)}{qN_{A2}(\varepsilon_1 N_{D1}+\varepsilon_2 N_{A2})}\right]^{\frac{1}{2}} \qquad (3.4.2)$$

and the capacitance is expressed,

$$C = \left[\frac{qN_{D1}N_{A2}\,\varepsilon_1\varepsilon_2}{2(\varepsilon_1 N_{D1}+\varepsilon_2 N_{A2})(V_{bi}-V)}\right]^{\frac{1}{2}} \qquad (3.4.3)$$

whichevidently reduces to the equivalent homojunction Equation (3.4.2) where the semiconductors are identical. Thus a graph of $1/C^2$ against V can again be plotted to yield either N_{A1} or N_{D2}, and the diffusion voltage, V_{bi}. However, where a large density of interface states is present, a decrease in slope with increasing reverse bias has been observed.[18]

The mechanisms for current flow across heterojunctions are more complex than for homojunctions, or metal-semiconductor diodes. The characteristics can be influenced by various factors depending on the band discontinuities, ΔE_c and ΔE_v, and the density of interface states. If the density of interface states is very high, then the dominant mechanism may be generation/recombination current from the interface. Furthermore, if either or both of the barriers is very thin, then tunnelling current may predominate. The n-n isotype heterojunction of Figure (3.6(b)) is interesting, as the dominant conduction mechanism is thermionic emission, and the current-voltage

characteristic can be expressed,[1,15]

$$J = J_s \left(1 - V/V_{bi}\right) \cdot \exp\left[\left(\frac{qV}{kT}\right) - 1\right] \qquad (3.4.4)$$

where,

$$J_s = \frac{qA^{**}TV_{bi}}{k} \cdot \exp\left[\frac{-qV_{bi}}{kT}\right] \qquad (3.4.5)$$

The reverse current does not saturate, but increases linearly with voltage at large V. At very high voltages an avalanching process, similar to the homojunction case, might occur.

3.5 The Metal-Insulator-Semiconductor (MIS) Device

The metal-insulator-semiconductor (MIS) device is a particularly powerful tool in the study of semiconductor surfaces. The energy band diagram of the ideal MIS system is illustrated in Figure (3.7(a)), in which

(i) the flat band condition is present at zero bias.

(ii) interface states are neglected; the only charges which are present under any biasing conditions are those in the semiconductor, and those with equal magnitude but opposite polarity on the metal surface adjacent to the insulator.

(iii) the insulator has infinite resistance.

On application of a D.C. bias normal to the surface of the semiconductor, charge of the opposite polarity is attracted into the surface region, resulting in the accumulation, depletion, or inversion situation as shown in Figures (3.7(b)-(d)). For instance, the application of a positive voltage normal to the n-type semiconductor illustrated produces an accumulation of electrons on the

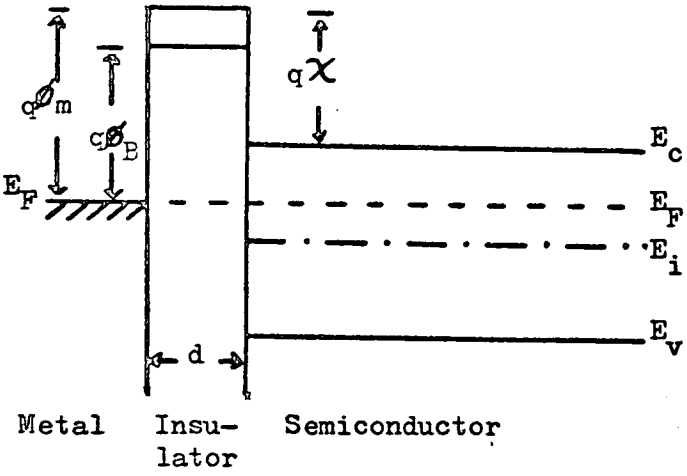

(a) Equilibrium.

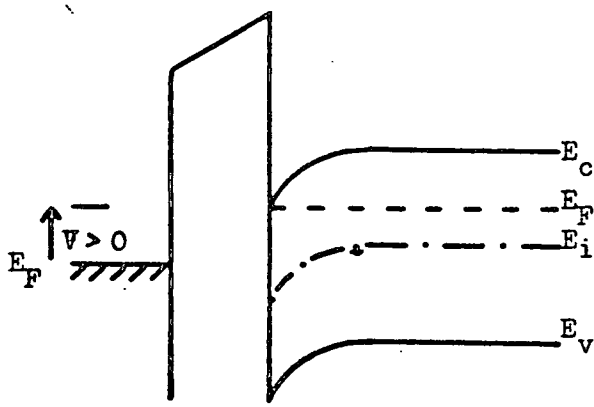

(b) Accumulation

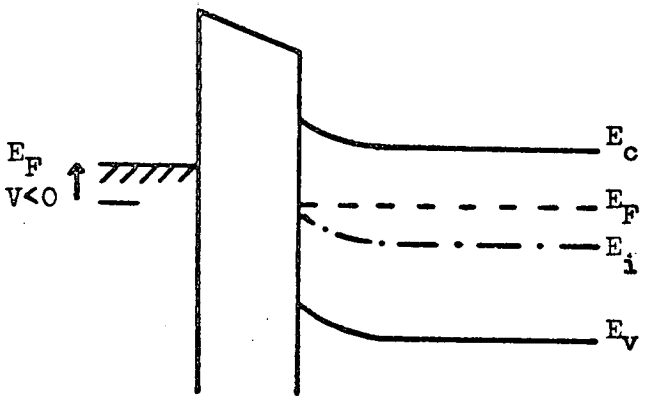

(c) Depletion.

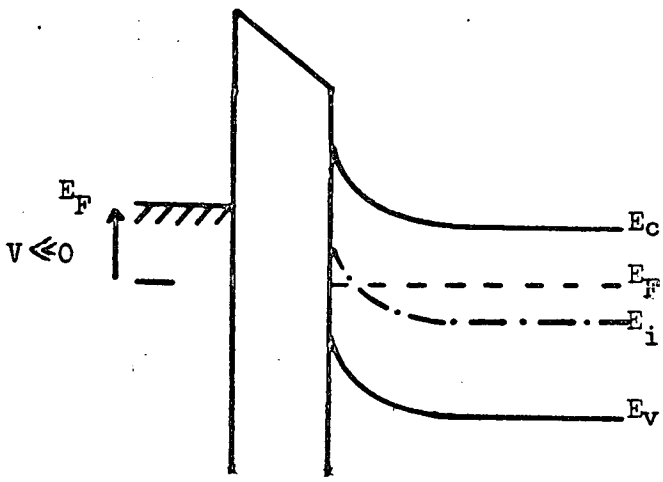

(d) Inversion.

Figure 3.7 The Metal-insulator-semiconductor device under various bias conditions.

semiconductor surface, and the bands are bent downwards by an amount ψ_s, the surface potential. Thus the concentration of electrons at the surface is increased,

$$n_s = n_o.\exp\left[\frac{q\psi_s}{kT}\right] \qquad (3.5.1)$$

whereas the concentration of holes is decreased,

$$p_s = p_o.\exp\left[\frac{-q\psi_s}{kT}\right] \qquad (3.5.2)$$

where n_o and p_o are the zero-bias electron and hole concentrations. Evidently, for application of a negative voltage, the reverse situation occurs.

The alteration of the equilibrium charge concentrations at the semiconductor surface is reflected by a change in both the conductance and the capacitance of that same surface layer. Thus measurement of these parameters as a function of applied normal voltage yields valuable information about the semiconductor surface.[4] However, the application of field-effect modulated conductance and field-effect modulated capacitance techniques to amorphous materials presents certain interesting problems and is discussed in detail in subsequent chapters.

CHAPTER 4 EXPERIMENTAL METHODS

4.1 Introduction

The purpose of this work is to investigate the surface properties and contact phenomena associated with chalcogenide glass thin films. To this end, junctions have been formed between $Ge_{10}As_{40}Te_{50}$ (GAT) and other materials, such that a critical investigation of the device characteristics will yield information about the properties of the surface region. In addition, a number of the experiments have been repeated on $Si_{12}Te_{48}As_{30}Ge_{10}$ (STAG). The first part of this chapter deals with the preparation of the bulk materials, the fabrication of the various thin film device configurations, and the thin film analysis. The latter part describes the various experimental techniques employed to obtain information from these samples, with particular regard to the layout of apparatus, often specific to a particular sample configuration. Finally, a brief section on the measurement of the thermal time constant of the substrate is included.

4.2 Sample Preparation and Analysis

4.2.1 Preparation of the Bulk Glasses

The GAT and STAG alloys were prepared in an identical manner. A silica ampule was prepared by sealing a cylindrical tube at one end and pulling out the other end to form a bottle neck. This was cleansed in acetone, rinsed in distilled water and thoroughly dried in a warm oven immediately before use. Accurately weighed amounts

of the constituent elements (99.999% pure-Koch Lite Laboratories Ltd.) were placed in the ampule, which was immediately evacuated to a pressure $<10^{-5}$ Torr and sealed at the bottle neck, using a silica plug. The ampule was next placed inside a horizontal rocking furnace for 24 hours, maintained at a temperature of 900°C by an automatic controller, ensuring complete mixing of the melt. At the end of this period, the tube was drawn out of the furnace with tongs and immediately quenched in cold water in order to obtain the vitreous solid form. The weight of the melts prepared in this manner was generally between 45g. and 50g.

4.2.2 Evaporating and Sputtering Techniques

With the exception of the heterojunction samples (Section 4.2.7) either microscope glass slides, or corning '7059' glass slides were used as substrates throughout. The optimum size was 1" square, though some 1" x ½" slides were used for field effect structures. The most successful method of cleaning consisted of ultrasonic vibration in a solution of 'Decom', a commercially available detergent, followed by rinsing and further ultrasonic vibration in de-ionised water. Finally the slides were blown dry in filtered N_2.

For most purposes in the present experiments, thin glass films in the range 0.1 um to 10 um were prepared by R.F. sputtering in a Nordiko sputtering plant. The various thin metal electrodes used were generally either electron beam evaporated from molybdenum or carbon crucibles, or thermally evaporated in quartz crucibles

surrounded by a tungsten filament. Molybdenum cannot be easily evaporated, however, as very high temperatures are necessary, so this was always sputtered from a solid circular disc. The evaporating and R.F. sputtering systems are conceptually similar, as illustrated schematically in Figure (4.1). A two-stage pumping system utilising a mechanical rotary pump followed by an oil diffusion pump is used to evacuate the chamber to a pressure $<10^{-5}$ Torr. Within the chamber there is a target or source from which the material is sputtered or evaporated on to the substrate a fixed distance above. Between the target and the substrate, there is a movable radiation shield which can be controlled from outside the system.

When sputtering, the clean substrates were placed in a specially designed circular brass holder, capable of handling nine 1" x 1" slides simultaneously, which was then bolted on to the top assembly of the sputterer ensuring good thermal contact. When in position, the substrates could be liquid-cooled by a continuous flow of water through a spiral copper pipe, or heated by a ring heater, according to the preparation conditions required. In view of the relatively low transition temperature of these materials, 180°C - 190°C for $Ge_{10}As_{40}Te_{50}$,[1,2] water cooling was generally used. The bulk glass was powdered with a mortar and pessel for use as a target, and the sputtering was carried out in an atmosphere of argon at a pressure between 5 and 8. 10^{-3} Torr. The R.F. power level was usually 100W, but in some cases lower power

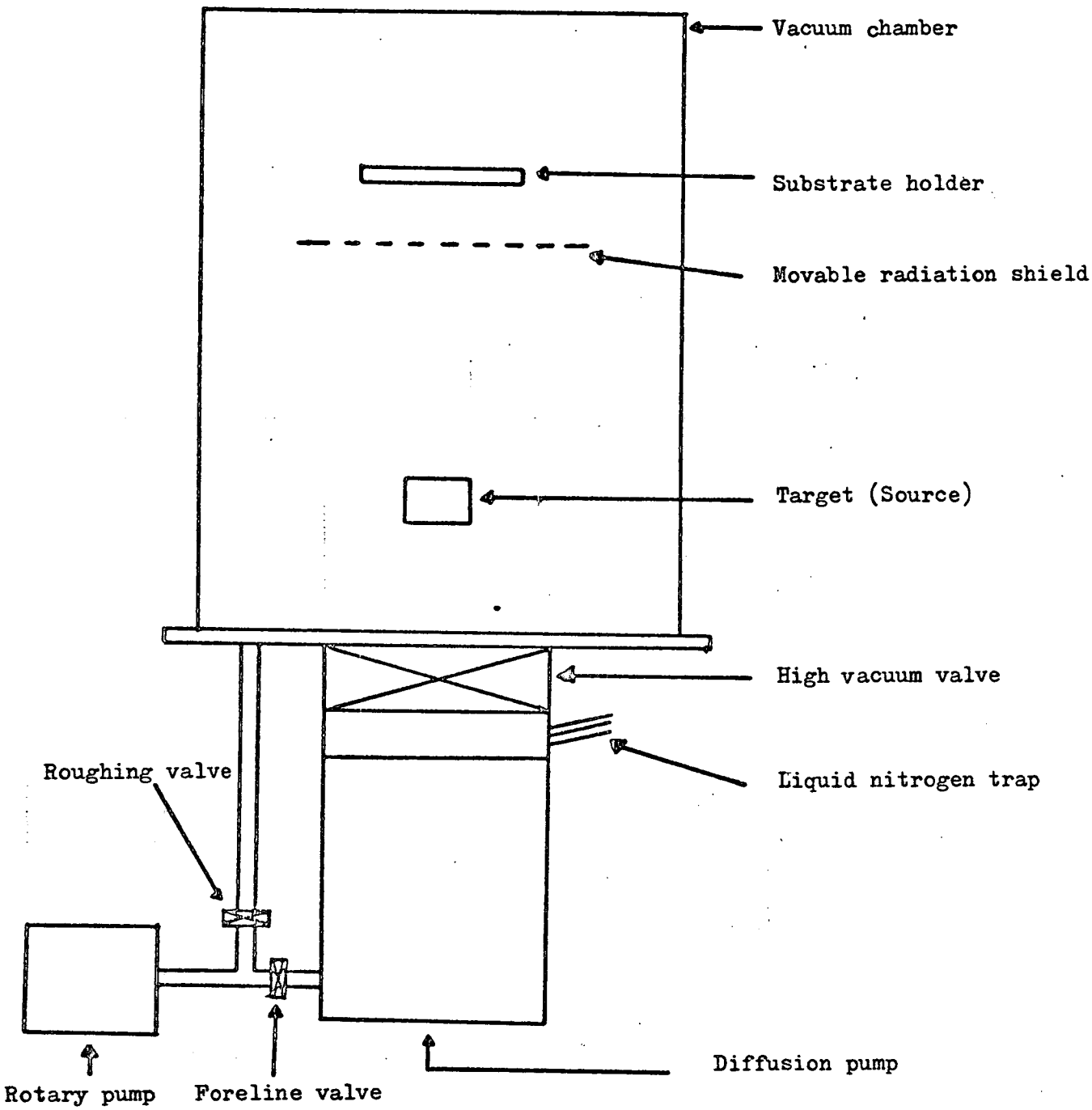

Figure 4.1 Schematic diagram of Evaporating/Sputtering System.

levels were used. The radiation shield was used for a period of 10-15 minutes at the start of every run, the "pre-sputtering" phase, in order to eliminate any non-equilibrium factors related to initial power and pressure fluctuations, surface contamination on the target, preferential sputtering of one element etc.

When evaporating, similar precautions were observed, but it is relevant to mention an important difference in the operation of the two systems. An advantage of the filamentary system over the electron beam process is that the substrate remains much cooler, thus when electrode deposition on to a previously sputtered chalcogenide film was required, the former system was invariably used.

4.2.3 Sample Classification and Analysis

The advantage of R.F. sputtering over evaporation as a method of preparation of thin films of multicomponent glass alloys is that sputtering yields do not vary widely from element to element, whereas the various constituents may evaporate at greatly different temperatures. Thus sputtered thin films are normally closer to the original composition of the target source. This is evident from Table (4.1) which summarises the chemical compositions of several representative sputtered GAT films and a single evaporated film, analysed by spectrophotometer colorimetry techniques.[3] The deviations in composition of the sputtered films from the target composition are minor compared to those of the evaporated film (the boiling point of Ge is much higher than those of Te and As), and the data is reasonably self consistent.

Table 4.1

Analyses of sputtered films, $Ge_{10}As_{40}Te_{50}$.

Atomic %	Ge	As	Te
(i)	15	26	59
(ii)	13.5	27.2	59.3
(iii)	20.1	19.6	60.3
(iv)	18.0	25.3	56.7
(v)	20.6	25.2	54.2

Analysis of thermally evaporated film, $Ge_{10}As_{40}Te_{50}$.

Atomic %	Ge	As	Te
	0.7	59.8	39.6

The variation in composition of a sputtered film as a function of time, and hence as a function of depth in the resultant layer, was checked for a film of STAG. A sliding shield attached to the substrate holder was used to obtain three thin glass films ($\simeq$0.2 um.) prepared at successive 15-minute intervals from the start of the sputtering run. An analysis by X-ray fluorescence techniques[4] showed no significant variation in composition with film thickness within the experimental accuracy of the method ($\pm$ 5 at %).

The thicknesses of the sputtered thin films were determined by a Taylor-Hobson 'Tallysurf 3', accurate to $\pm$ 0.02 um. The instrument consists of a stylus and skid arrangement; as the stylus is drawn across the surface under investigation, the 'step' at the edge of the thin film is registered by a zero-drift A.C. technique. Variations in thickness over the surface of a 1" x 1" glass slide were generally $<$ 5% and thus would not be expected to introduce significant errors in the much smaller area samples used in the experimental work.

4.2.4 Preparation of Bulk Samples

Specimens of the bulk glass of a size and shape suitable for resistivity measurements were obtained by grinding large pieces of the prepared glass on a conventional glass plate using a mixture of alcohol and alumina powder as a "grinding paste". Large area samples about 1mm. in thickness were prepared, and the opposite faces were checked for parallelism by taking micrometer measurements

of the thickness at several points. Gold electrodes were then evaporated over the whole area of the opposite flat faces, and care was taken to ensure that no "shorting" path existed down the sides of the sample.

The resistances of the samples were obtained from low-field, room-temperature, current-voltage characteristics, and using the formula,

$$\rho = R.A/t$$

where R is the device resistance, A the device area and t the device thickness, values for the resistivity, ρ, were calculated. Typical results are shown in Table (4.2). The values are reasonably consistent, and in good agreement with those quoted by Tanaka[1] for identical compositions, $1.55.10^3$ Ohm-m and 2.10^3 Ohm.m. The differences are probably attributable either to a temperature difference between the two sets of data, or to a difference in the method of bulk glass preparation.

4.2.5 Sandwich and Coplanar Devices

The two principal thin film device configurations are illustrated in Figure (4.2). In practice, the coplanar electrode arrangement was seldom used, most of the basic conductivity and capacitance measurements being carried out on sandwich devices. Thin copper plate masks were prepared by standard photo-lithographic techniques,[5] and placed in intimate contact with the substrate during evaporation or sputtering to produce the desired configuration. However, the 20 um gaps in the coplanar devices were etched as much greater accuracy was required.

Table 4.2

Bulk Samples of $Ge_{10}As_{40}Te_{50}$ - Resistivity Data.

	Area(A)	Thickness(d)	Resistivity(ρ)
Sample 1	$27mm^2$	1.04mm	$3.34.10^3 \Omega$-m.
Sample 2	$53mm^2$	1.75mm	$3.35.10^3 \Omega$-m.
Sample 3	$92mm^2$	1.81mm	$3.10.10^3 \Omega$-m.

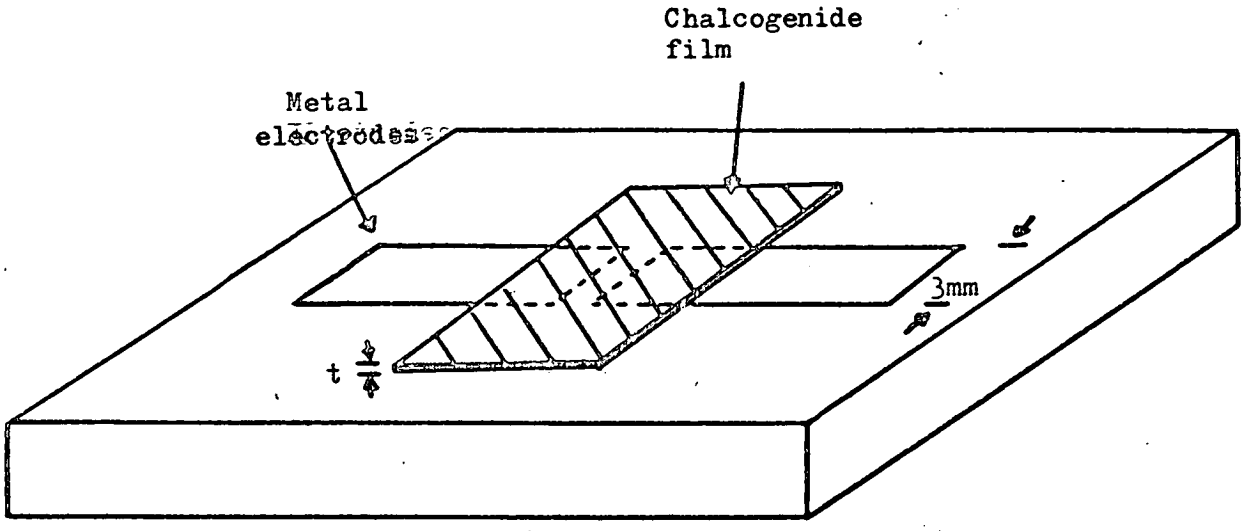

Figure 4.2(a) Coplanar thin-film device; gap width = 20um.

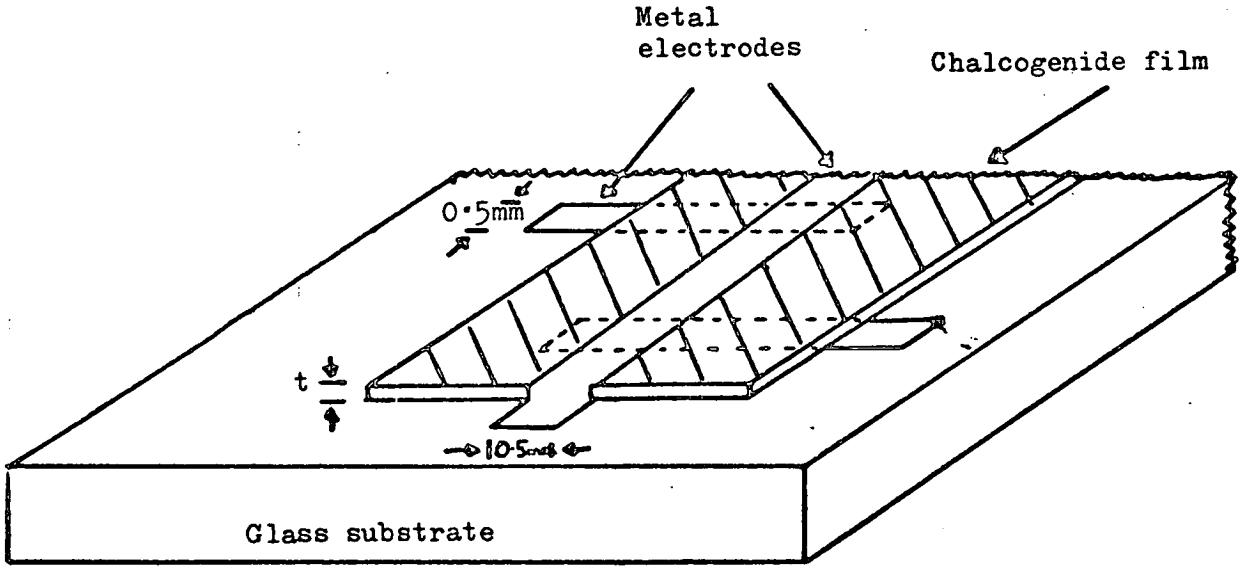

Figure 4.2(b) Sandwich thin-film device; 10 devices on each slide.

A standard optical microscope was available for inspection of the completed devices.

When the bottom electrode of the sandwich devices was an oxidising metal, particularly in the case of aluminium, the breaking of the vacuum previous to deposition of the thin glass film resulted in the formation of a thin oxide layer between the metal and the glass. However, no oxide layer was formed at the metal-glass interface when an oxidising metal was deposited onto a pre-sputtered chalcogenide film. This is discussed more fully in Section (6.5).

Photovoltaic measurements were also performed on sandwich samples using semi-tranpsarent metal electrodes. The approximate thickness of the evaporated metal during preparation was determined by monitoring the resistance of the metal as it was deposited onto an accompanying 1" x 1" slide in the vacuum system. A digital multimeter (DMM) was connected across two ceramic lead throughs in the base of the evaporating chamber, from which thin insulated wires were attached to two opposite edges of the glass slide. The measured resistance on the DMM in Ohms. square.$^{-1}$ was thus inversely proportional to the metal film thickness. A second glass slide was also included for subsequent electrode transmission measurements on the electrode material. For sputtered Mo electrodes, a similar set-up was used in the sputtering chamber. The majority of GAT and STAG samples from which photovoltaic data were obtained had a Au/Mo system of electrodes, though some data was also obtained on sandwich devices with Al, Sb and

S_nO_2 electrodes.

4.2.6 Field-Effect Device Structure

The specimen configuration for measurement of the field-effect modulated conductance is illustrated in Figure (4.3). A coplanar structure with an etched 20 um. gap similar to that described above was used, but the area of the sputtered glass film was reduced. The GAT or STAG film was generally thin, between 0.5 and 1.0 um, so that any increase in surface conductivity was as large as possible relative to the total measured conductivity. An evaporated insulating layer of As_2S_3 covered the chalcogenide film at all points, of thickness $\simeq$5 um, which was thin enough to provide a high field strength normal to the chalcogenide, yet thick enough to ensure a reasonably continuous layer. Finally, a narrow gold field electrode was evaporated directly over the coplanar gap, producing the classical field effect device. It was important to keep the area of the top electrode as small as possible, to minimise the possibility of dielectric failure due to "pinholing".

4.2.7 Heterojunction Structure

Heterojunctions were formed between thin glassy films of $Ge_{10}As_{40}Te_{50}$ and n and p-type silicon substrates of various resistivities, in the device structure illustrated schematically in Figure (4.4). The silicon substrates, of thicknesses ranging between 175 um. and 475 um. were cut into approximate 1" squares by a diamond scribe, then cleansed in a solution of 70% H_20, 20% H_20_2, 10% HCl by volume at a temperature of 80°C for 20 minutes to remove

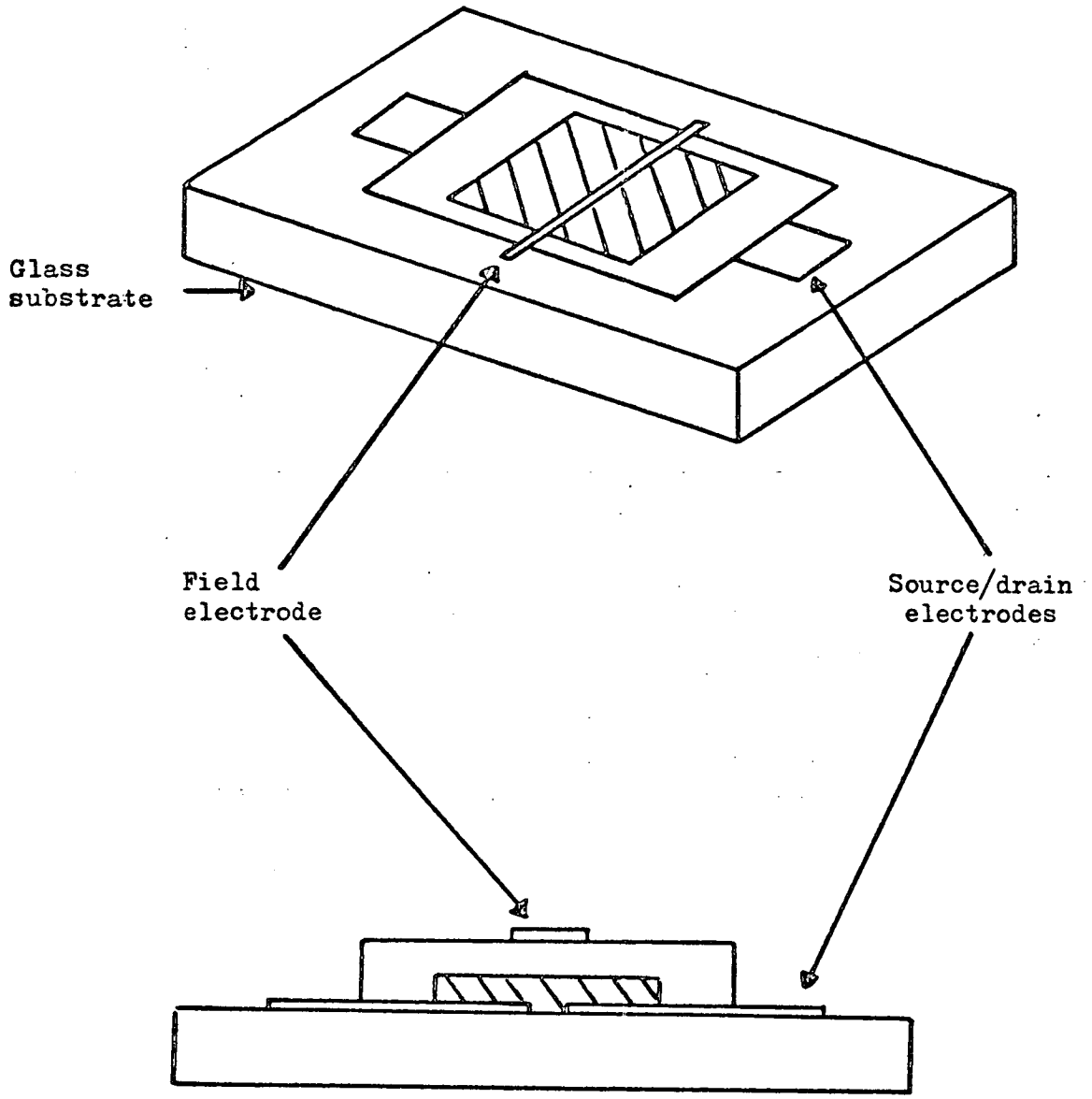

Chalcogenide film.

As_2S_3 insulator.

Figure 4.3 Field effect device.

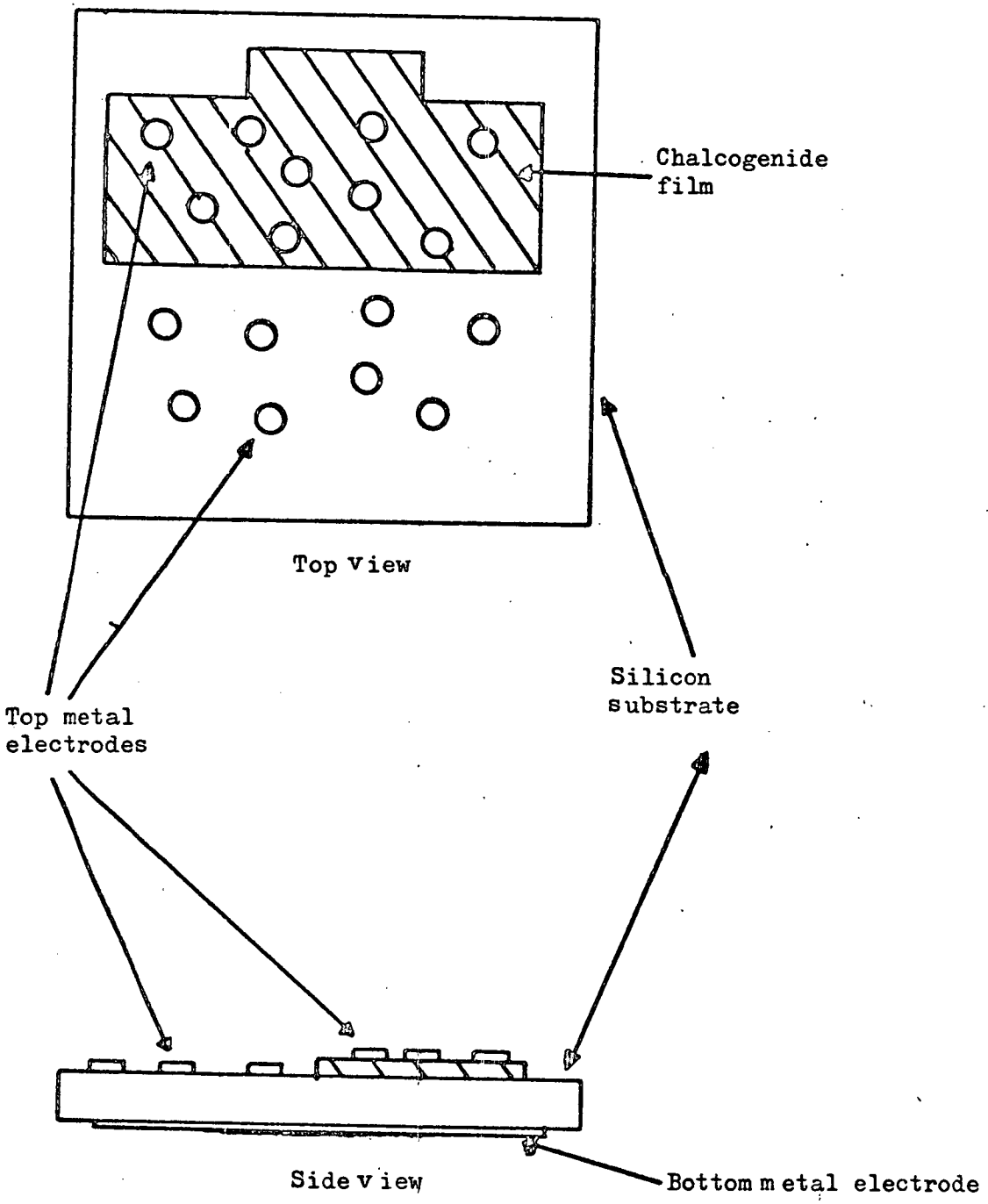

Figure 4.4 Heterojunction structure; several devices on each slide.

any metallic impurities. This was followed by a rinse in continuously flowing distilled water and a drying process in a jet of filtered N_2. The surface oxide was next etched in an HF solution, prior to a further washing and drying procedure and immediate transfer of the uncontaminated substrates to an evaporating system for deposition of the back metal electrode. On p-type substrates an Al electrode was evaporated and then sintered in an N_2 atmosphere at 450°C for 20 minutes, while an Sb-doped Au electrode was used for n-type substrates, sintered in N_2 at 350°C for 20 minutes. This procedure was necessary to produce good ohmic contacts on the back surface. Following the sputtering of the glass film on to the front surface of the silicon, a series of small circular gold electrodes was evaporated on to the glass. The active device area was thus defined by the area of the top electrode. For photo-electric measurements, thin sputtered Mo contacts were used, as the thickness was easier to control. A number of metal-silicon-metal devices were also fabricated on each substrate in order to check the non-blocking nature of the back contact.

4.3 Experimental Procedure

4.3.1 Environmental Chamber

Most of the experiments described in this work were carried out within an evacuated chamber, using a small aluminium sample mounting whose temperature was controlled by a 'coldfinger' assembly illustrated schematically in Figure (4.5). The 4" x 4½" x 5" chamber is constructed

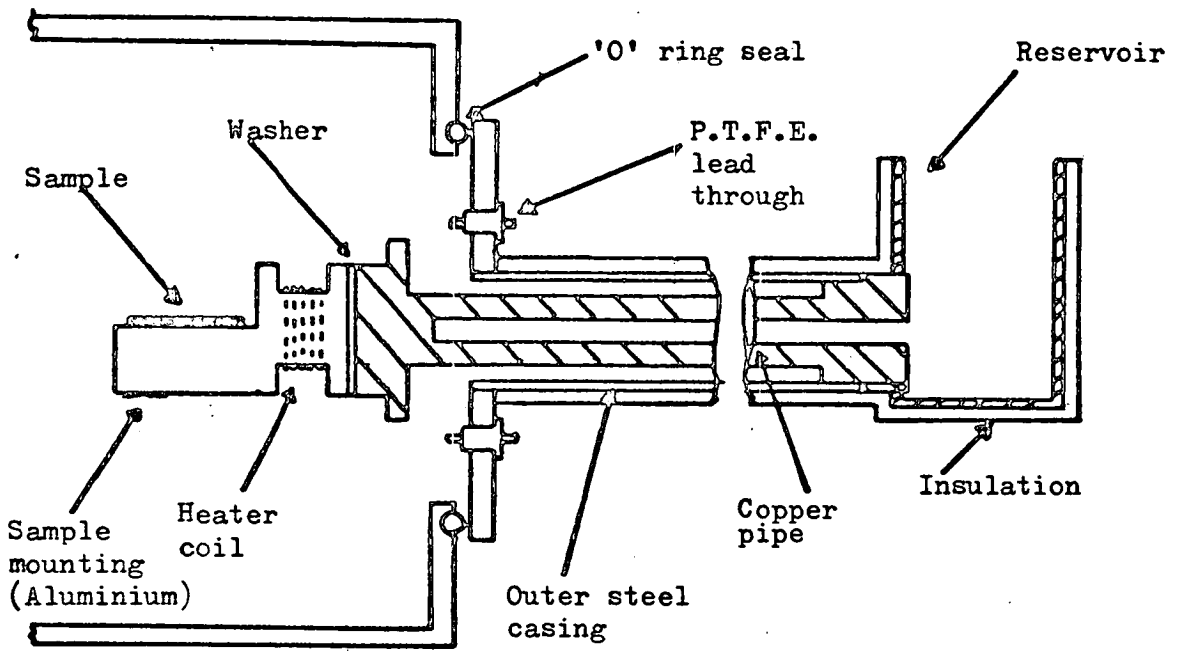

Figure 4.5 Environmental Chamber:-"Coldfinger" apparatus.

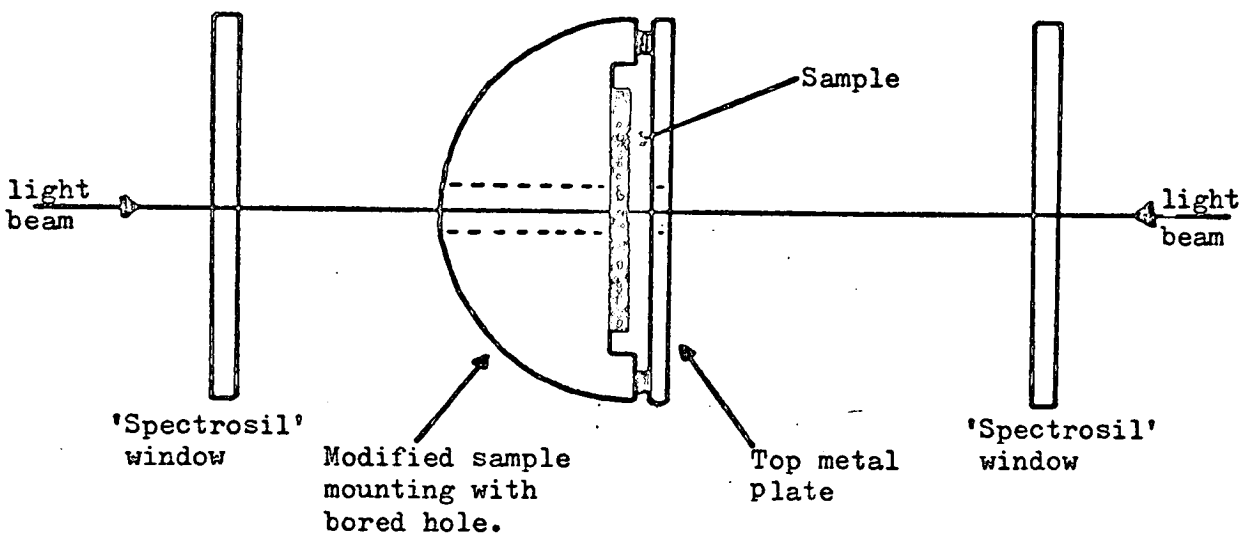

Figure 4.6 Modified configuration for optical measurements.

from 3/16" brass plates, welded together to ensure vacuum-tight seams. The vacuum was maintained in operation by a small rotary pump which drew air out of the chamber through a small gas valve mounted on top of the box. Three circular holes are present, two on the sides of the box and one on the front face. For 'dark' measurements the two diametrically opposite holes, radius ½", were sealed by small circular brass plates in intimate contact with rubber 'O' rings which fitted into grooves surrounding the holes, held in place by flanges bolted to the exterior wall. For optical measurements, the plates were replaced by windows of "Spectrosil", a fused silica glass with a quasi-uniform transmission characteristic over the range 180nm. to 2000nm. The third hole of radius 1¼" was designed to receive the cold finger assembly, and has a groove for a third 'O' ring around its circumference.

The standard sample mounting was fabricated from a 2" length of 1¼" diameter aluminium rod, cut to provide a 1¼" x 1¾" platform suitable for the glass substrates, and a recess for the heater coil. The substrates were adhered to the platform using silicon grease, which provided a good thermal contact. The heater coil was manufactured from alternate layers of wound tungsten wire and insulating tape, set in Araldite glue. The temperature of the sample mounting was monitored by a chromel-alumel thermocouple embedded in the aluminium rod. For optical measurements, a modified mounting was used, in which a thin slot was cut right through the metal, so that the light beam could pass through the entire system

unobstructed, as illustrated in Figure (4.6), but the heat transfer properties were not too adversely affected. As a further improvement a rectangular aluminium plate with a corresponding slot was bolted over the sample.

The temperature of the aluminium sample mounting could be varied continuously from 100K to 500K by balancing the energy supplied from the heater coil against the heat flow from the mounting to the end plate of the copper pipe, maintained at the temperature of the reservoir ambient. The copper pipe leading from the reservoir was thermally insulated from the box walls by the vacuum; hence the outer chamber assembly remained at the approximate temperature of the atmosphere during operation. For low temperature measurements, the reservoir was filled with liquid N_2 at 77K, while for high temperature measurements the reservoir was either left empty or filled with an ice-water mixture at 273K. By varying the current supplied to the heater, an accuracy of $\pm$ 0.25K was achieved. The accuracy of the thermocouple, and the possibility of a heat gradient across the glass substrate, was checked by comparing the reading with that obtained from a calibrated thermistor mounted on a glass slide. At temperatures as low as 110K, a deviation of less than 2K was observed.

Finally, electrical connections to the sample, the thermocouple, and the heater inside the vacuum chamber were made by means of insulated P.T.F.E. "barb" lead throughs, inserted in holes bored in the coldfinger flange assembly. Within the chamber thin wire strands were attached to the sample electrodes with a silver 'DAG'

solution. Outside the chamber the lead throughs were screened from electrical interference by a small metal box bolted to the front face of the chamber, and fitted with BNC sockets. Co-axial BNC cables were used for all the exterior connections.

4.3.2 Apparatus for Current-Voltage Measurements

The experimental arrangement for plotting current-voltage characteristics at various temperatures, and the variation of conductivity as a function of temperature, is illustrated in Figure (4.7(a)). A voltage was applied across the sample placed within the coldfinger chamber, and the resultant current was measured by a Keighley 610C electrometer. The digital voltmeter recorded the total voltage across the sample and the electrometer, therefore it was necessary to ensure that the internal resistance of the electrometer was a small fraction of the total resistance. The series resistor provided a current limit through the sample, in the event of switching or investigation of the negative resistance region.

In order to extend the range of current-voltage data on these devices to cover temperatures above room temperature, a pulsed technique was used. This made it possible to obtain conductivity-field characteristics to much higher fields, by eliminating Joule heating effects. The apparatus for high temperature pulsed current-voltage measurements, illustrated schematically in Figure (4.7(b)), had previously been designed and used in the same laboratory by J.M. Marshall. A pulse of variable width and magnitude was obtained by triggering the output of a

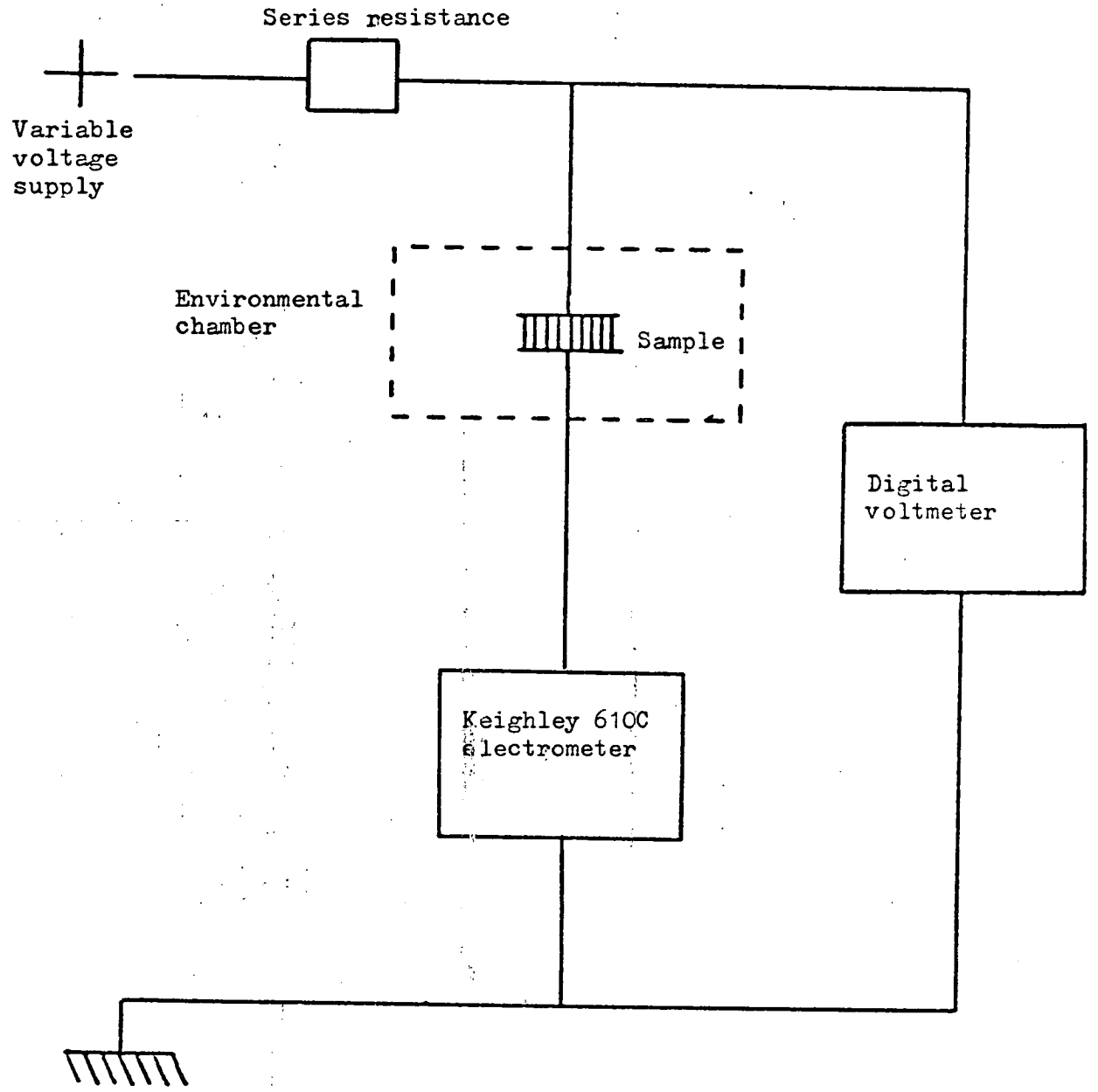

Figure 4.7(a) Circuit configuration for steady-state current-voltage measurements.

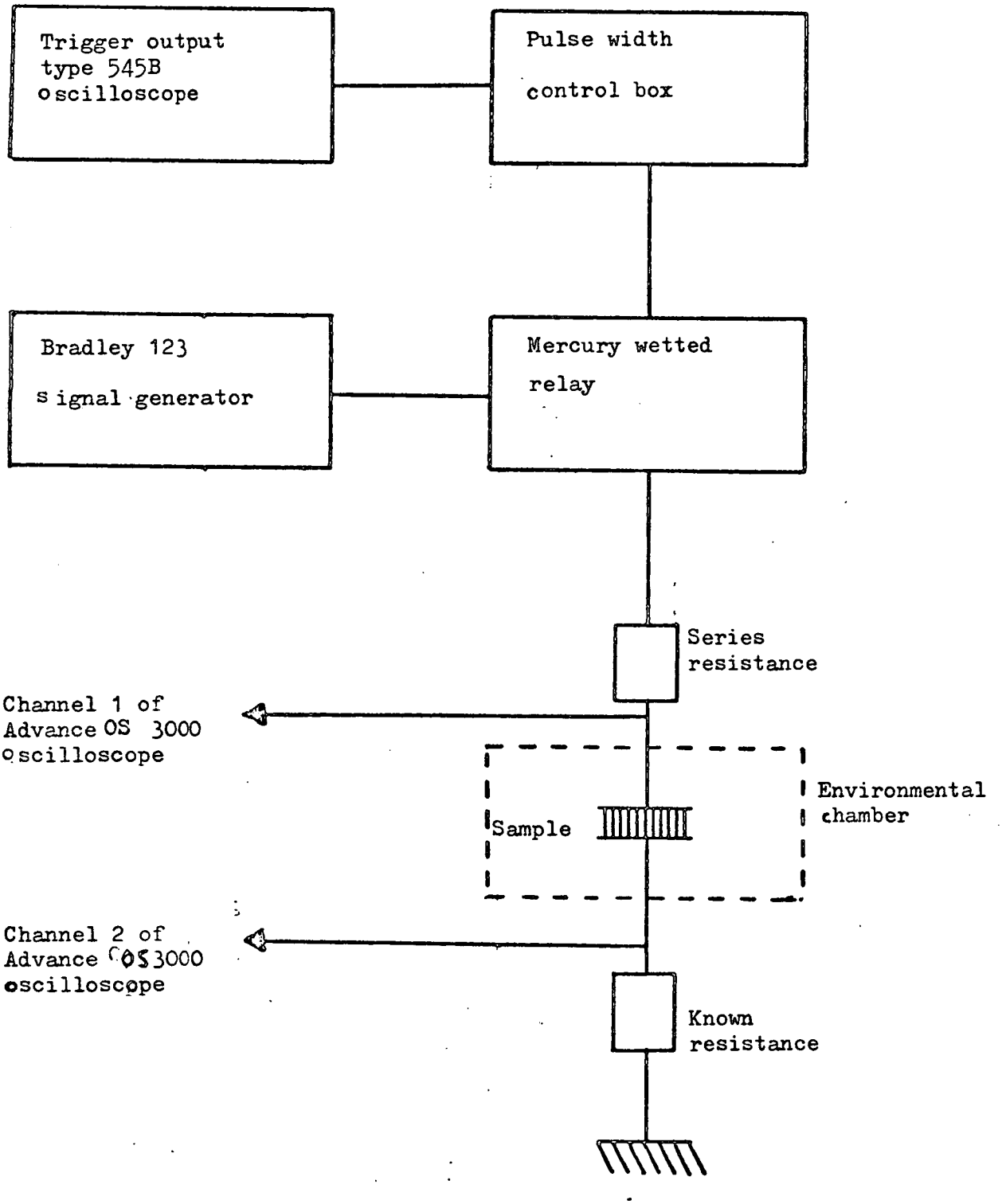

Figure 4.7(b) Circuit configuration for pulsed current-voltage measurements.

The typical range of pulse widths used was from 0.1 to 1 μs, the pulse separation being kept much greater than the pulse width, so that no sample heating was observed.

Bradley 123 signal generator, and displayed across one channel of an Advance OS3000 oscilliscope. The current through the device was monitored by displaying the voltage across a known series resistor across the second channel of the oscilloscope. The accuracy of this method was of course severely limited by the accuracy of the oscilloscope display.

In some cases, a Phillips PH6507 curve tracer was also used to display complete current-voltage characteristics prior to more meticulous measurement using the apparatus of Figure (4.7(a)). This technique was extensively employed on the heterojunction samples, and the results were recorded with a polaroid camera.

4.3.3 Apparatus for Capacitance-Voltage Measurements

The apparatus layout illustrated schematically in Figure (4.8(a)) allowed the automatic measurement of both the D.C. current-voltage and the capacitance-voltage characteristics of thin film sandwich devices. The voltage supply was a 0 - 250V variable speed ramp, obtained by amplifying the 10V ramp output of an Advance OS3000 oscilloscope by the simple high voltage amplifying circuit illustrated in Figure (4.8(b)). The speed of the ramp was controlled by the time base of the oscilloscope, while the peak voltage was best controlled by the 5MΩ potentiometer. The high series resistance between the sample and the voltage source not only served as a current limiter, but also blocked off the stray capacitance of the supply. The sample voltage was monitored by a high impedance

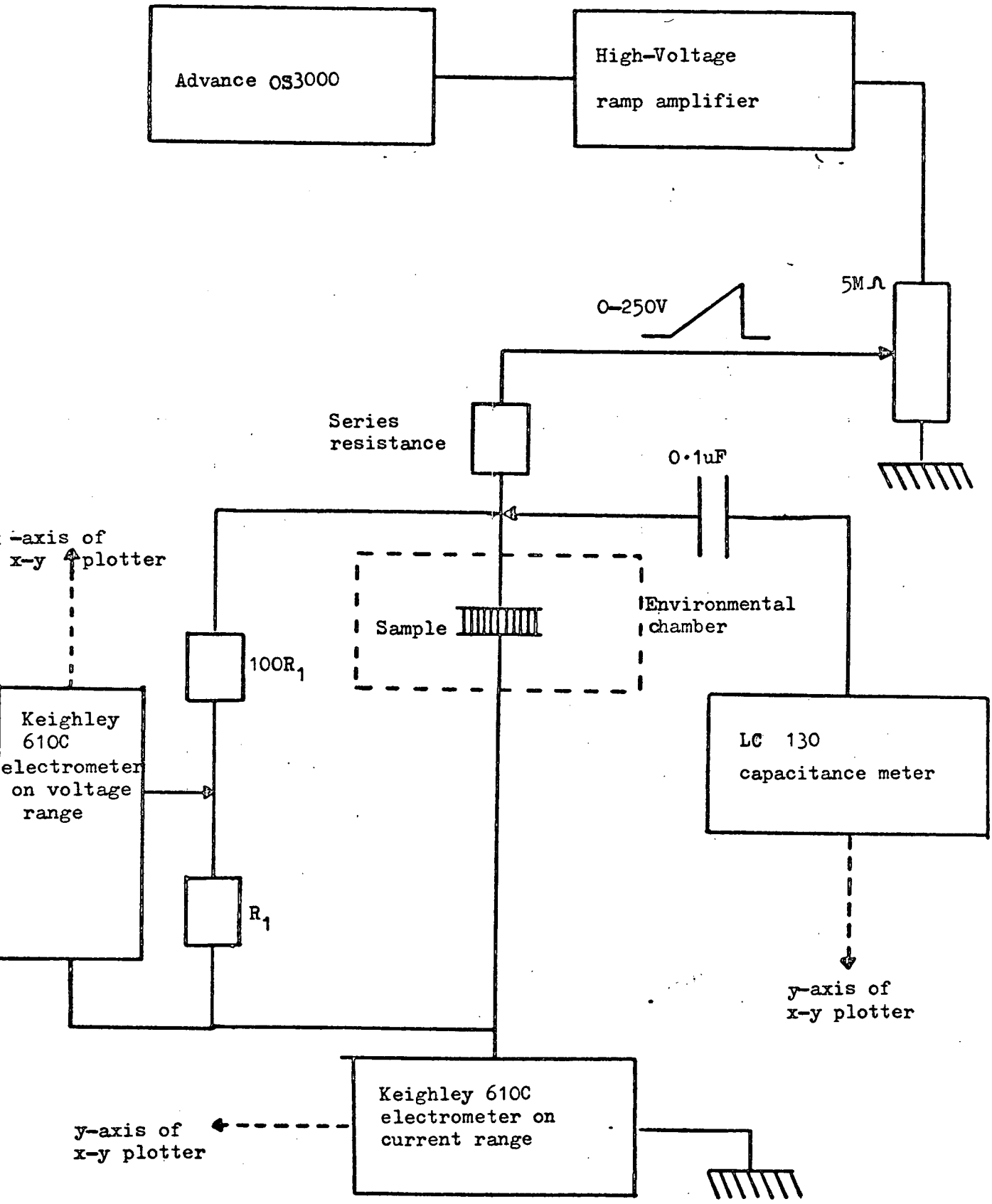

Figure 4.8(a) Circuit configuration for automatic measurement of I-V and C-V characteristics.

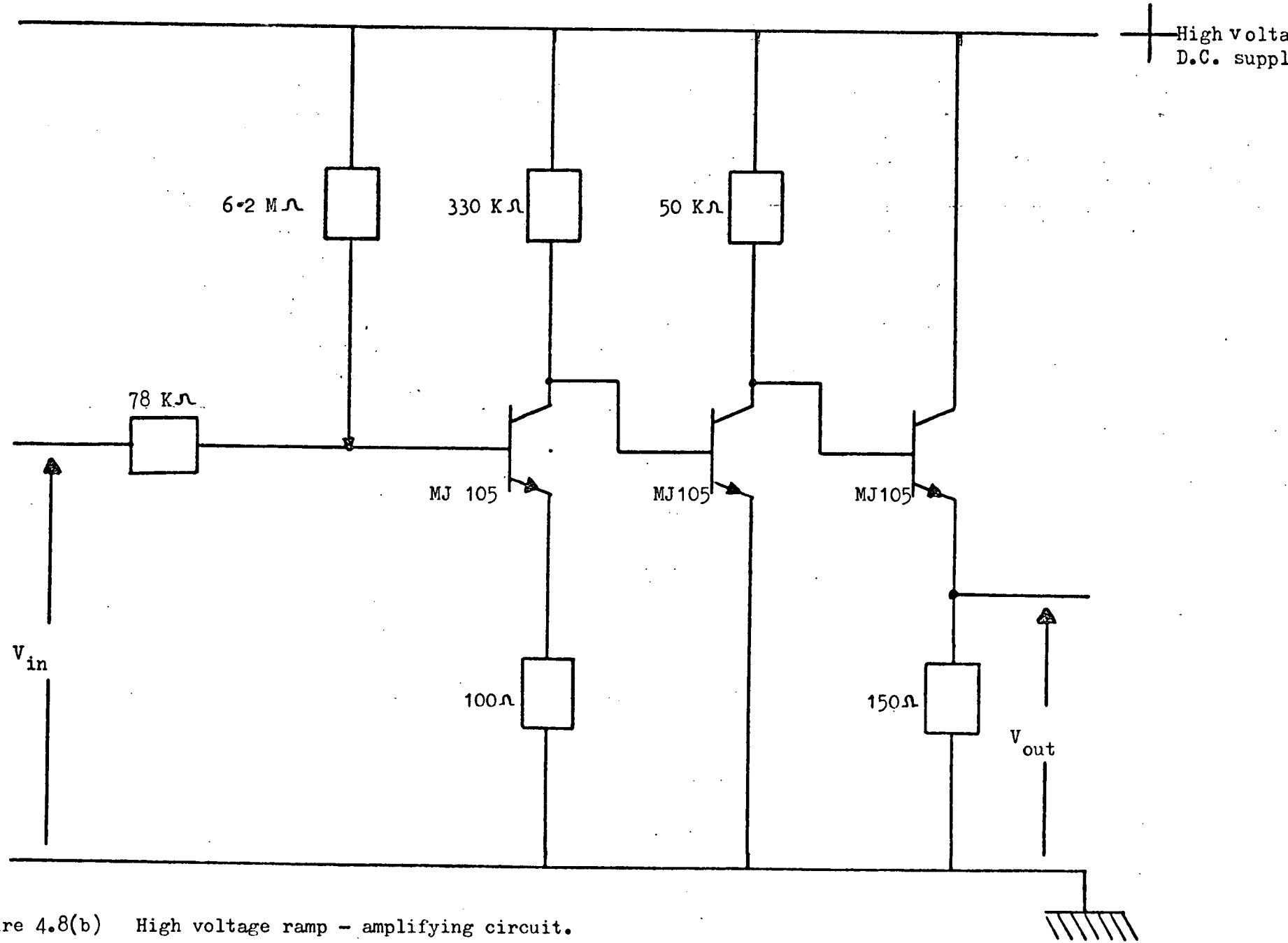

Figure 4.8(b) High voltage ramp - amplifying circuit.

(R_{in} =10^{14}Ohm.) Keighley 610C electrometer, connected across a 100:1 voltage dividing circuit designed to block out further stray capacitance, and of sufficiently high impedance that the current through the sample was much greater than the current through the parallel circuit. A proportional output from the electrometer was fed to the x-axis of a Hewlett-Packard 2000 x-y plotter. The capacitance of the sample was measured by a Tektronix 130 L-C meter, operating at a fixed frequency of 140KHz, and a proportional output fed directly to the y-axis of the HP 2000. The capacitance meter had a D.C. blocking input capacitance of 0.1 uF., and could not operate on devices of load impedance $< 30K\Omega$, hence the majority of the experimental data was obtained below room temperature. The product of the measurement frequency and the device thermal time constant was very large, $\omega\tau \gg 1$, see section (4.4) , so that the device temperature stayed at an approximately constant level: i.e. no thermal cycling. The D.C. current was measured by an electrometer operating in the fast mode, and an alternate output could be taken from this to the y-axis of the x-y plotter. Unfortunately only one pen was available on the particular model used, thus C-V and I-V plots were obtained sequentially rather than simultaneously.

4.3.4 Capacitance-Frequency Measurements

A modified version of the Lynch bridge[6], illustrated in Figure (4.9), was used to measure simultaneously the variation of capacitance and A.C.

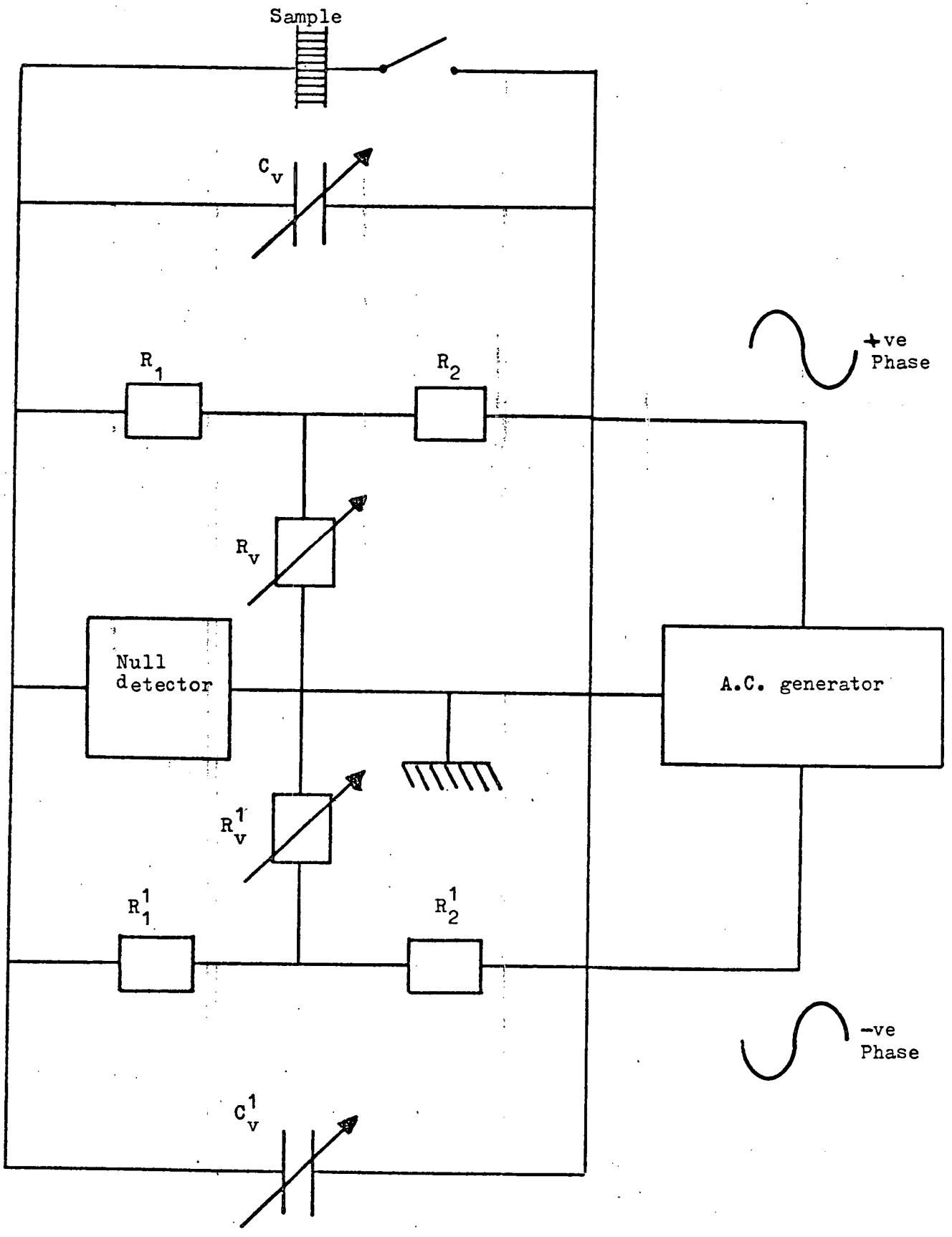

Figure 4.9 Modified Lynch bridge for capacitance-frequency measurements.

conductance with frequency. The main feature of the bridge is a T-network of resistors, having fixed arm resistors R_1 and R_2 and a third variable resistor R_V, connected in parallel with a variable air capacitor, C_V. Initially the sample was included in the circuit, and balanced with the opposite T-network by variation of C_V^1 and R_V^1, producing a null in the detector reading. The sample was then disconnected, and C_V and R_V were adjusted from their reference values to re-establish a null reading, thus substituting the sample impedance directly. Consequently, the sample capacitance was given by,

$$C = \Delta C_V$$

and the A.C. conductance was given by,

$$G = \frac{\Delta R_V}{R_1 R_2}$$

where ΔR_V and ΔC_V were the required adjustments.

The signal source; a Hewlett-Packard 3300A signal generator providing 180^o phase-separated sinusoidal waveforms of equal magnitude, variable from 20Hz to 100KHz, and the null detector, a General Radio model 1232A, were connected to a common earth point within the circuit. At frequencies below 100Hz the sensitivity of the bridge was greatly reduced, and an accuracy of $\pm$ 10% could not be improved upon, even when a tuned amplifier and oscilloscope arrangement was substituted for the 1232A detector.

4.3.5 Apparatus for Field-Effect-Modulated Conductance Measurements

The apparatus for the measurement of the field effect modulated conductance in GAT and STAG chalcogenide thin

films is illustrated in Figure (4.10). The steady-state drain-to-source current was measured at successive increments of the gate voltage, V_g, but the transient response was not recorded. The drain-to-source voltage was fixed at 20V, such that the coplanar conductance of the device at zero V_g was equivalent to the low-field value, and the polarity of the coplanar voltage was reversed during the experiments to check for symmetry. The normal field was provided by a Fluke 412B stabilised power supply, monitored by a standard digital voltmeter, while the coplanar current was measured by a Keighley 610C electrometer, operating in the fast mode. Prior to any experiment the gate-to-source and gate-to-drain leakage currents were checked at $V_g = \pm$ 500V. If either exceeded 1% of the zero V_g drain-to-source current the sample was rejected.

4.3.6 Apparatus for Transmission Spectra

Transmission spectra for thin films of the chalcogenide alloys, GAT and STAG, were obtained using a Carl-Zeiss spectrophotometer MQ-11, illustrated schematically in Figure (4.11). A dual light-source was used; a 6V-30W incadescent bulb for wavelenghts between 325nm. and 2500nm., and a type HS30 DS hydrogen lamp for the shorter wavelength region, 185nm. to 325nm. The required small waveband was selected from the light source in use by the monochromator. For room temperature measurements, the sample was contained in a specially designed dark metal box, mounted in a movable rack on a sliding rail so that the film could be placed in or out of

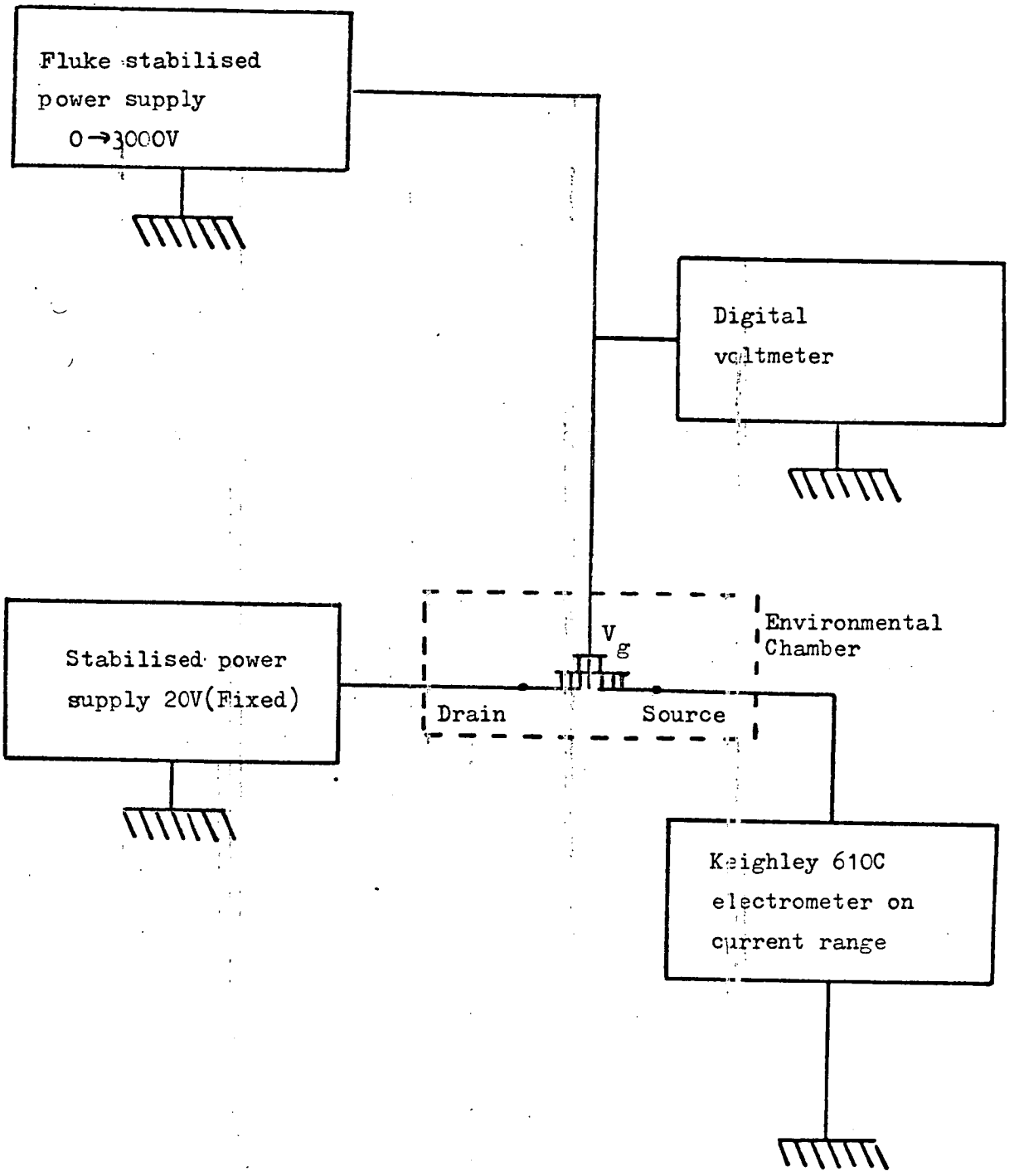

Figure 4.10 Circuit configuration for field-effect measurements.

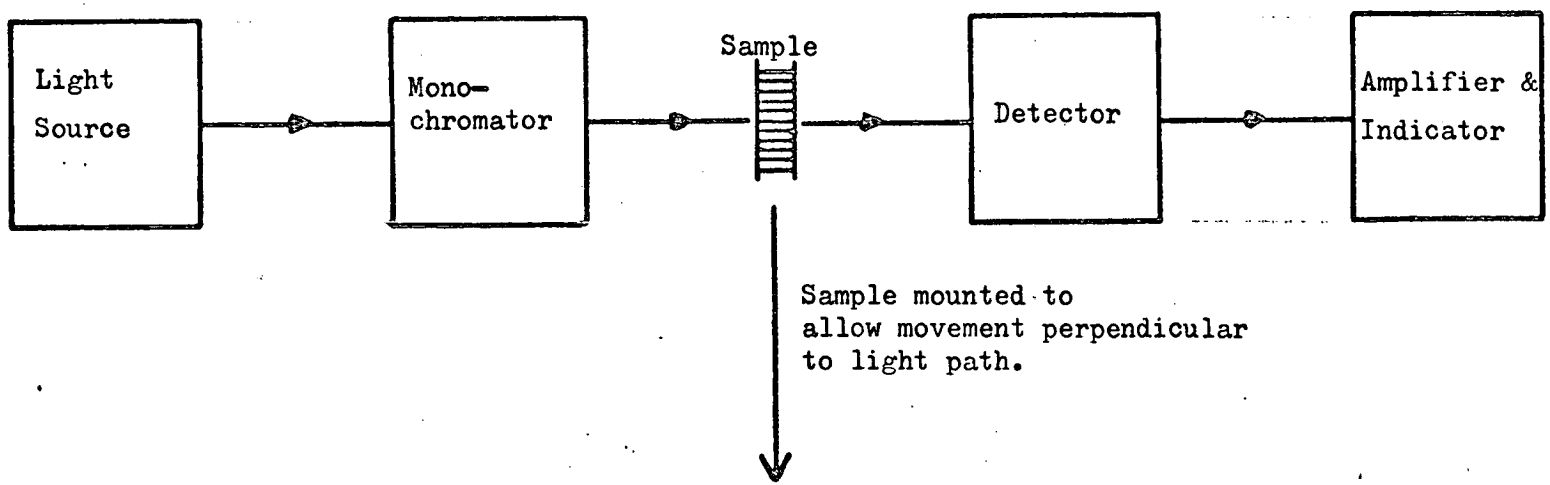

Figure 4.11 Apparatus for transmission measurements.

the path of the beam. For measurements below room temperature the optically modified coldfinger chamber was used, placed between two rails on a wooden platform, constructed to allow free movement of the whole chamber so that the sample could again be placed in or out of the light beam. Two detectors were used, a photomultiplier for measurements in the 185 - 600nm range, and a PbS photoconductive cell for the 600 - 2500nm range, the transmission of the sample relative to the free path transmission being measured automatically and displayed by means of a light spot on the translucent scale of the indicator, to an accuracy of at worst 2% of the actual reading at the high absorption end of the spectrum, but generally considerably better than this. Interconnections between the various units were designed to eliminate false readings due to entry of outside light, the risk being further reduced by carrying out the measurements in a darkened room.

4.3.7 Apparatus for Photo-voltaic Measurements

For measurements of the photo-electric response of thin film sandwich devices, the apparatus illustrated in Figure (4.12) was used. A narrow waveband light beam was provided by a tungsten lamp variable in intensity by means of a potentiometer circuit, and filtered through a standard Hilger-Schwarz monochromator. The spectral variation of the light intensity at maximum output, obtained from a preliminary experiment, is shown, in arbitrary units, in Figure (4.13). The light beam was focused on to either the sample or the detector equidistant

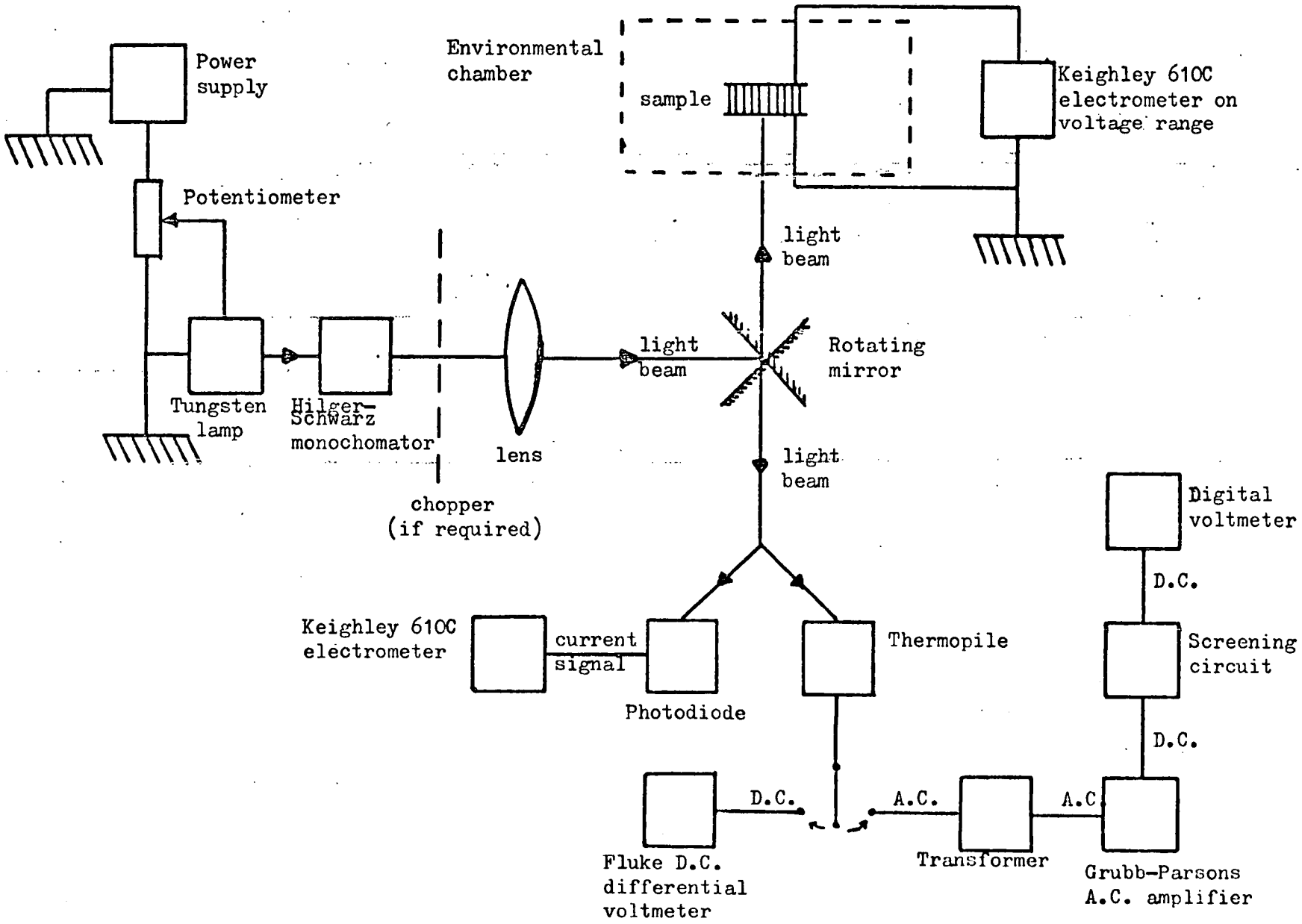
Power supply
Potentiometer
Tungsten lamp
Hilger-Schwarz monochomator
chopper (if required)
lens
Environmental chamber
sample
Keighley 610C electrometer on voltage range
light beam
light beam
Rotating mirror
light beam
Keighley 610C electrometer
current signal
Photodiode
Thermopile
Digital voltmeter
D.C.
Screening circuit
D.C.
D.C.
A.C.
A.C.
Fluke D.C. differential voltmeter
Transformer
Grubb-Parsons A.C. amplifier

Figure 4.13 Spectral variation of the maximum output light intensity in photovoltaic measurements.

from the light source by a lens and a rotating mirror. It was possible to illuminate the sample through either electrode, by rotating the complete coldfinger chamber through 180^{o}.

The photovoltaic response of the device was measured by a Keighley 610C electrometer on the high impedance voltage range. The absolute intensity of the beam was determined from the amplified A.C. response of a Hilger-Schwarz thermopile (D.C. sensitivity: 18 $uV.mW^{-1}$) to a chopped light signal, after prior calibration of the amplifier using a Fluke D.C. differential voltmeter. This detection system allowed accurate determination of the beam intensity down to an incident photon flux of 10^{15} photons $m^{-2}.s^{-1}$. The range could be extended to 10^{13} photons $m^{-2}.s^{-1}$ where necessary, by substituting a pre-calibrated planar diffused silicon photo-diode. The entire apparatus, except for the amplifying and indicating instruments, was enclosed in a darkened environment, so that all exterior light was excluded. The photovoltaic response of sandwich devices (and heterojunction samples) could thus be measured as a function of wavelength (photon energy), temperature, and light intensity.

4.4. Measurement of the Device Thermal Time Constant

The conductivity of sandwich type devices can be expressed in the form,[7]

$$\sigma(E,T) = \sigma_a . \exp(\frac{\Delta T}{T_1}) . f(F) \qquad (4.4.1)$$

where ΔT is the temperature deviation from the ambient, σ_a is the conductivity when $\Delta T=0$, and f(F) expresses the field

dependence of the conductivity. The steady-state energy balance can be expressed by the usual Newtonian expression,

$$VI = \Delta T . \Gamma \qquad (4.4.2)$$

where Γ is the thermal conductance of the film, which is related to the thermal time constant of the device by the relationship,

$$\tau = \frac{C.A.d}{\Gamma} \qquad (4.4.3)$$

C is the heat capacity of the glass, and A and d are the device area and thickness respectively.

When a voltage pulse is applied to a sample, the current rises from an initial value I_o to a final value which is ΔI greater, characterised by the thermal time constant τ, as illustrated schematically in Figure (4.14(a)). Assuming an approximate exponential rise in the excess current, the time constant can be estimated directly by measuring the time taken for this current to reach 0.63 of (i.e. $1_{/e}$ less than) its final value. Figure (4.14(b)) illustrates the current pulse obtained on application of a square voltage pulse to a sandwich device, and this was amplified, displayed and photographed as illustrated in Figure (4.14(c)). The value of τ was estimated as 200 us.

---

* T_1 is a constant with the dimensions of temperature, typically 20 K for chalcogenides of this type.

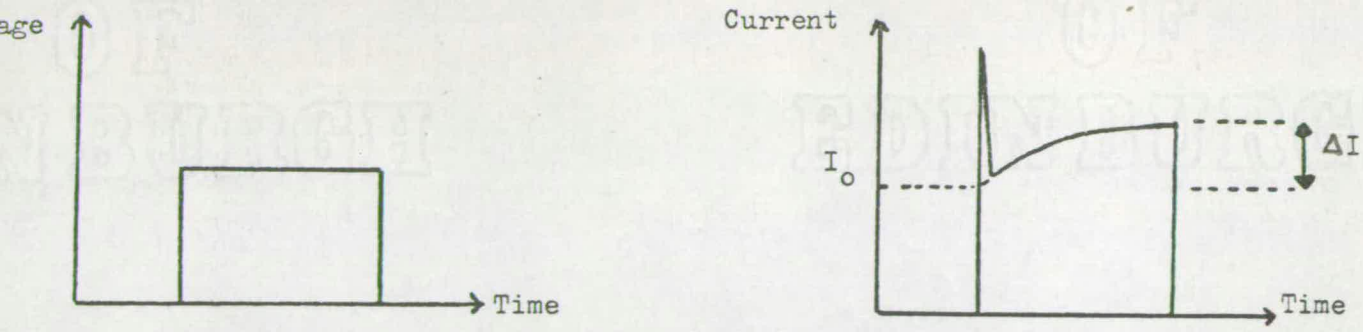

gure 4.14(a) Schematic diagrams of applied voltage pulse and current pulse obtained for measurement of thermal time constant.

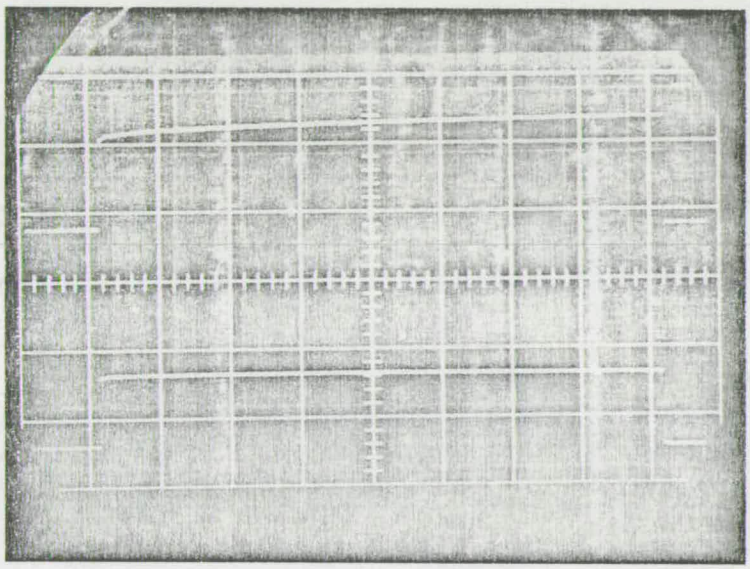

gure 4.14(b) Sandwich sample Au–$Ge_{10}As_{40}Te_{50}$–Au glass thickness–4um.

Top trace: Vertical–500uA.cm^{-1}. Horizontal–100us.cm^{-1}.

Bottom trace: Vertical– 10V.cm^{-1}. Horizontal–100us.cm^{-1}.

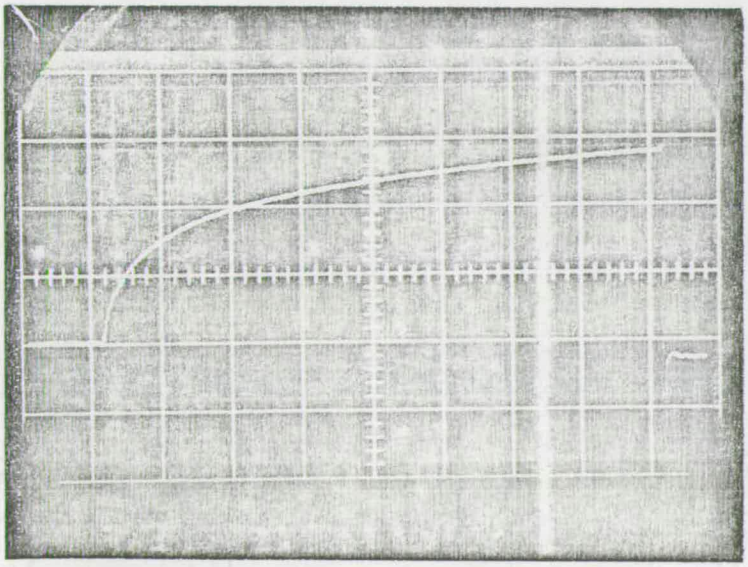

CHAPTER 5 STEADY STATE CURRENT-VOLTAGE CHARACTERISTICS OF A CHALCOGENIDE GLASS, $Ge_{10}As_{40}Te_{50}$

5.1 Introduction

Before commencing a study of the problems of contacts and surface layers on chalcogenide glasses, it was necessary to obtain basic data on thin films of the glass, $Ge_{10}As_{40}Te_{50}$. Therefore a study of the variation of D.C. conductivity with temperature and applied field was initiated. Throughout this experimental work, either gold or gold-backed molybdenum contacts were used, as these have previously been used successfully in making non-blocking contacts.[1]

5.2 The Variation of D.C. Conductivity with Temperature

The temperature dependence of the low-field D.C. conductivity, σ, of three sandwich-type thin film devices of various thicknesses is illustrated in Figure (5.1). The plot of ln. σ against $(10^3/T)$ is linear over a wide range of temperature, but a slight change of gradient is evident below 175K. This temperature dependence has been observed in a wide variety of chacogenides.[2-7] Above 175K the temperature dependence of the conductivity follows the usual Arrhenius-type law,

$$\sigma = \sigma_o \exp\left(\frac{-\Delta E}{kT}\right) \qquad (5.2.1)$$

where σ_o is a constant and ΔE is the activation energy. Thus within this temperature range, the electrical conduction is a thermally activated process, and a calculation of the pre-exponential constant σ_o from the data of Figure (5.1) yields a value of $4.65.10^4 \Omega^{-1}m^{-1}$, which suggests that the conduction is due to carriers excited beyond the mobility

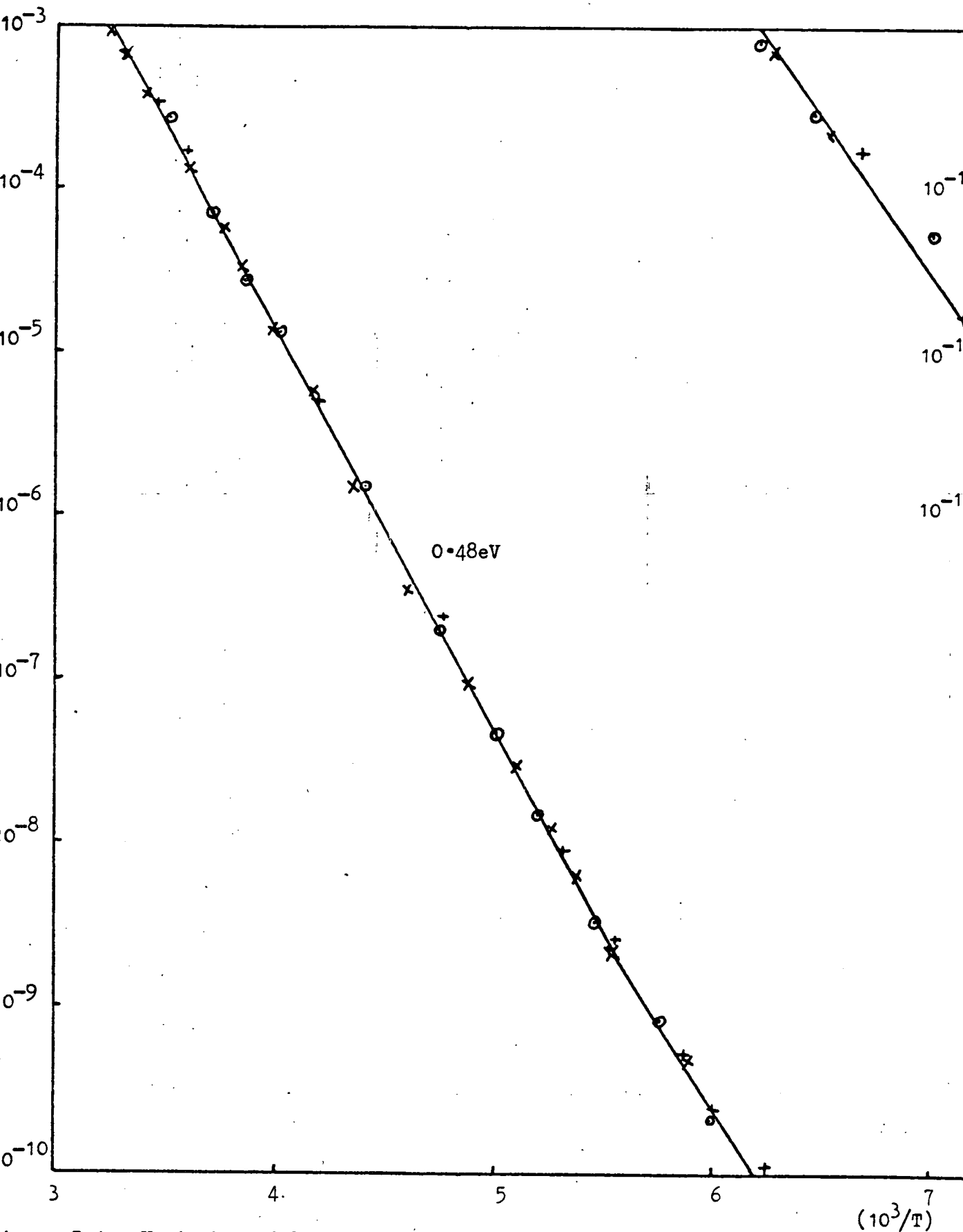

Figure 5.1 Variation of low-field conductivity with temperature of three typical $Ge_{10}As_{40}Te_{50}$ sandwich devices: (x) 0•9um.,(⊙) 2•25um., (+) 4•7um.

edges into non-localised or extended states.[8] From the data of Figure (5.1), the value of ΔE is calculated as 0.47-0.48eV, which is in reasonable agreement with the value quoted by Tanaka,[9] ΔE = 0.498eV.

A comparison of the temperature-dependent D.C. conductivity data presented here with the data for the absorption coefficient and optical gap of $Ge_{10}As_{40}Te_{50}$ as a function of temperature presented in Chapter 8 shows that the Fermi energy remains situated roughly at the gap centre over a wide temperature range. Accepting that the Fermi level is effectively fixed near the centre of the gap, it is possible to expand expression (5.2.1),

$$\sigma = \sigma_1 . \exp\left[\frac{-(E_c - E_F)}{kT}\right] + \sigma_2 . \exp\left[\frac{-(E_F - E_V)}{kT}\right] \qquad (5.2.2)$$

where E_c is the energy of the bottom edge of the conduction band, E_V is the energy of the top edge of the valence band, and E_F is the Fermi energy. Thus the two terms on the right hand side of the equation represent the contributions from mobile electrons and holes respectively, one or other of which may dominate the conduction. However, Fritzche[10] argues that ΔE is not equivalent to $(E_c - E_F)$ or $(E_F - E_V)$ because of the temperature dependence of the electron energy states, this temperature dependence arising from the thermal expansion of the material and the phonon contributions of electrons and holes. Thus at room temperature the dependence is quasi-linear,

$$(E_c - E_F) \text{ or } (E_F - E_V) \simeq \Delta E - \gamma T \qquad (5.2.3)$$

but at low temperatures it becomes temperature independent, as illustrated in Figure (5.2) taken from reference (10). Thus the ΔE of equation (5.2.1) is not a <u>direct</u> measure of

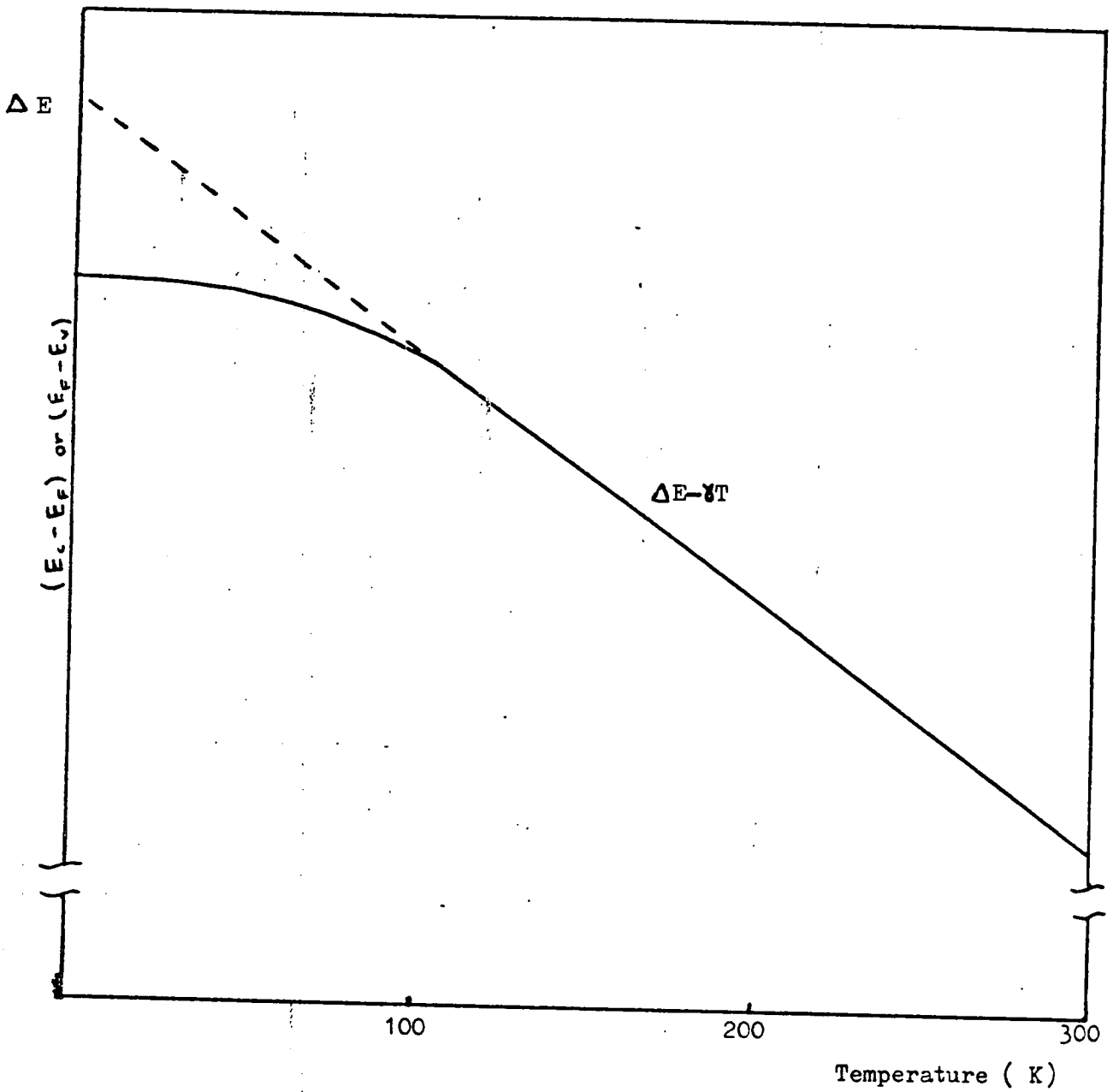

Figure 5.2 Schematic diagram of temperature dependence of (E_c-E_F) or (E_F-E_v) (From Fritzsche[10]). ΔE is the slope of the In. δ vs. $1/kT$ curve in the range $200 < T < 400$ K.

the energy difference between the mobility edge and the Fermi level, but is rather the T = O extrapolation of Figure (5.2). An estimate of the temperature coefficient of (E_F-E_V) or (E_c-E_F), $\gamma = 3.1.10^{-4}$eV/K, is obtained from the data on the variation of the optical gap with temperature presented in Chapter 8, assuming $\gamma \simeq \frac{1}{2}\beta$ where β is the temperature variation of the optical gap.[8]

The conclusion that the Fermi level is near the gap centre over a wide range of temperature can be explained in various ways:

(i) Highly symmetrical band tails are present

(ii) Donor and acceptor type defects are present in near-perfect compensation.

(iii) A high density of states exists in the middle of the mobility gap, effectively pinning the Fermi level.

The absence of polarity-dependent effects and contact resistance in $Ge_{10}As_{40}Te_{50}$ thin film devices with a variety of contacts discussed in Chapter 6 make the first two explanations unlikely, while an analysis of the field-effect data on $Ge_{10}As_{40}Te_{50}$ presented in Chapter 7 indicates that a high density of states ($\simeq 10^{25}m^{-3}.eV^{-1}$.) does exist at the Fermi level. Furthermore, recent reviews of the localised states in amorphous semiconductors[11-12] also suggest that a high density of states exists at the Fermi level in a number of chalcogenide alloys.

5.3 The Variation of D.C. Conductivity with Applied Field

The variation of the D.C. conductivity of a typical thin-film sandwich device with applied electric field, over

a wide temperature range, is illustrated in Figure (5.3). The lower geometric resistance of the device, as compared to the coplanar configuration, allowed current-voltage data to be obtained at much lower temperatures than would otherwise have been possible. The σ-F characteristics have an exponential field dependence down to low fields ($< 10^6 V.m^{-1}$), while at fields greater than about $1.75.10^7$ $V.m^{-1}$ the weakly temperature-dependent low-field exponential characteristic is superceded by a second non-linear regime, whose slope is more strongly temperature dependent. At high power levels, at temperatures above 210K, internal Joule heating effects are evident as a supra-exponential increase in the conductivity with respect to applied field.

Conductivity data of the form illustrated in Figure (5.3) has been observed in a wide variety of amorphous materials.[3-5,13] The low field characteristic can be expressed simply as,

$$\sigma(F) = \sigma_o . \exp(\frac{F}{F_o}) \qquad (5.3.1)$$

where F is the applied field, F_o a field constant, and σ_o the zero-field conductivity. Marshall and Miller[4] have modified this expression to include the temperature dependence of the low field slope by the introduction of a temperature dependent parameter with the dimensions of length, a(T), so that,

$$\sigma(F) = \sigma_o . \exp\left[\frac{a(T).q.F}{kT}\right] \qquad (5.3.2)$$

Values for a (T) deduced from the present data are plotted against temperature in Figure (5.4), which also includes

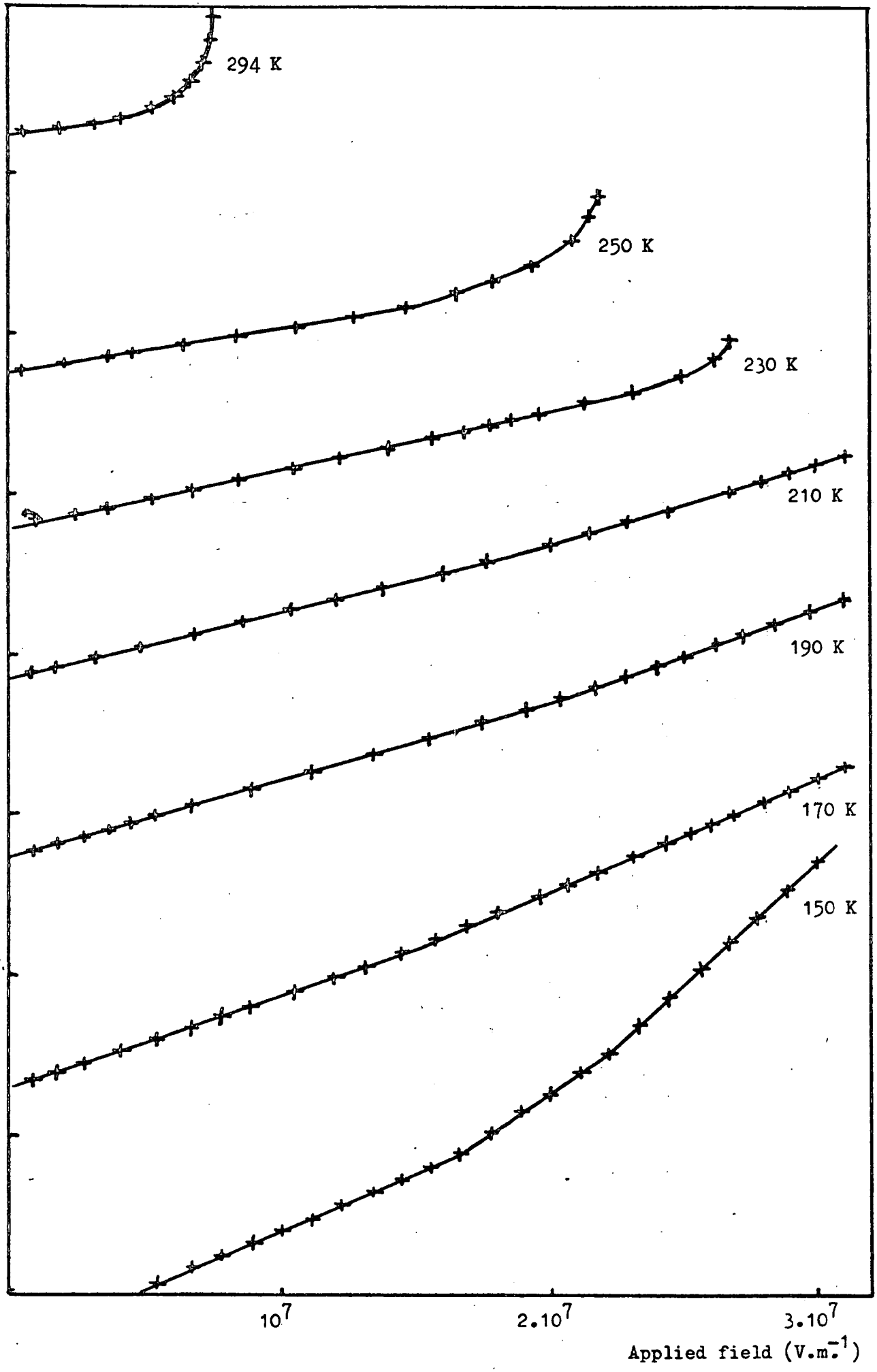

Figure 5.3 Variation of conductivity with applied field of a $Ge_{10}As_{40}Te_{50}$ sandwich device, thickness 2·25um.

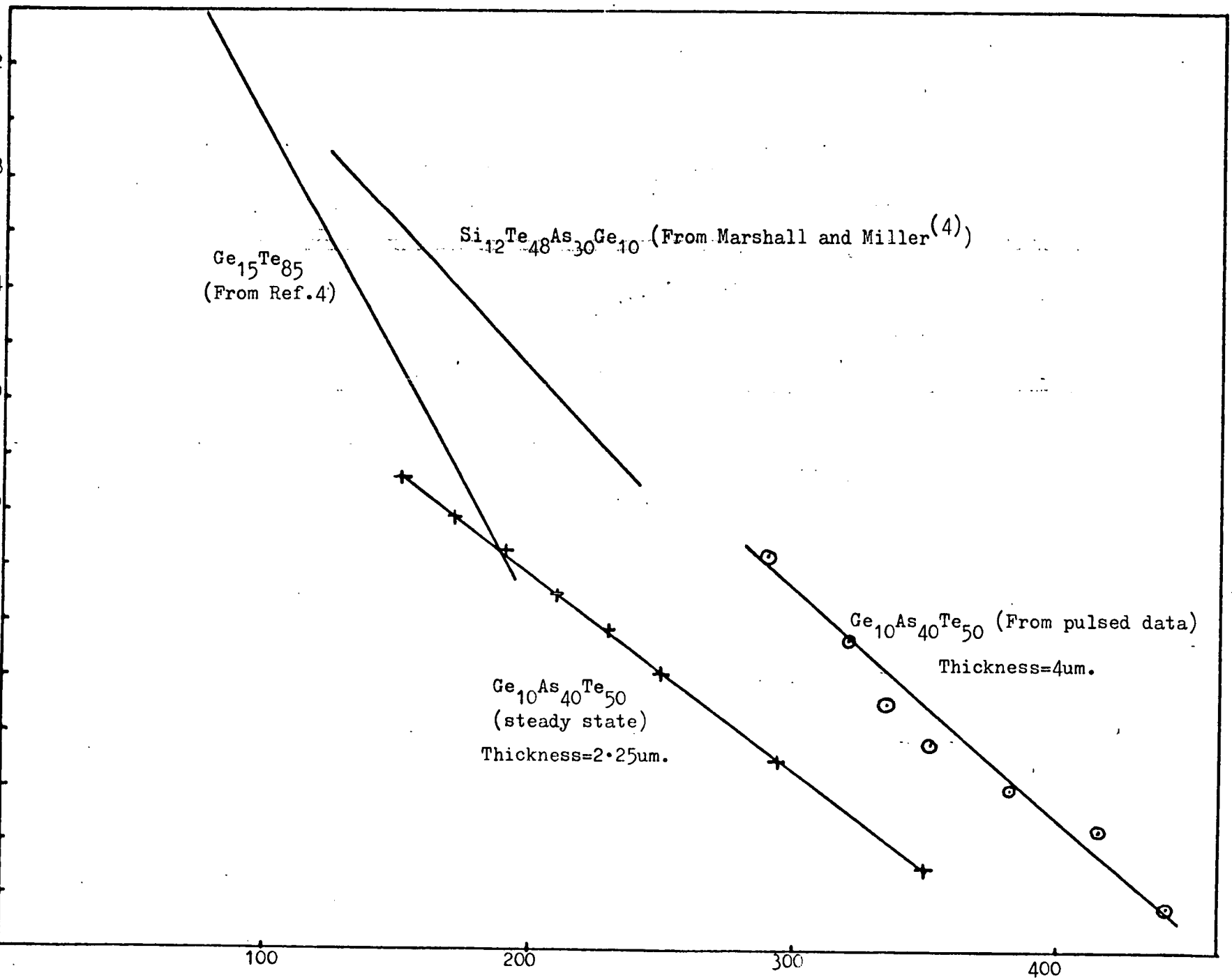

Figure 5.4 Variation of activation length, a(T), with temperature of chalcogenide thin film sandwich devices.

results from the high temperature pulsed measurements described in section (5.7), and data from other chalcogenides.[4] Discrepancies in the two sets of data for the $Ge_{10}As_{40}Te_{50}$ devices may be partly due to the use of two different samples, and partly to the inaccuracies inherent in the pulsed measurements. The physical significance of this parameter, the activation length, is as yet not fully understood.

Non-ohmic conduction in amorphous materials can be considered under three headings;

(i) Bulk electronic effects, independent of electrode characteristics.

(ii) Electrode effects; e.g. space charge limited current.

(iii) Internal Joule heating effects.

Mechanism (ii) is considered in detail in Chapter 6, but it is convenient to discuss here possible models for supra-ohmic conduction in the bulk.

5.4 The Poole-Frenkel Effect

One possible mechanism for the observed field dependence is the well-known Poole-Frenkel effect[14] which has been discussed and developed by various authors[5,15-17] with a view to particular experimental data. The simplest case of a single coulombic centre is illustrated in Figure (5.5), which for convenience is represented as a donor state. The application of a field, F, lowers the barrier in the downfield direction by an amount

$$\delta E = \beta . F^{\frac{1}{2}} \qquad (5.4.1)$$

where β is the Poole-Frenkel constant,

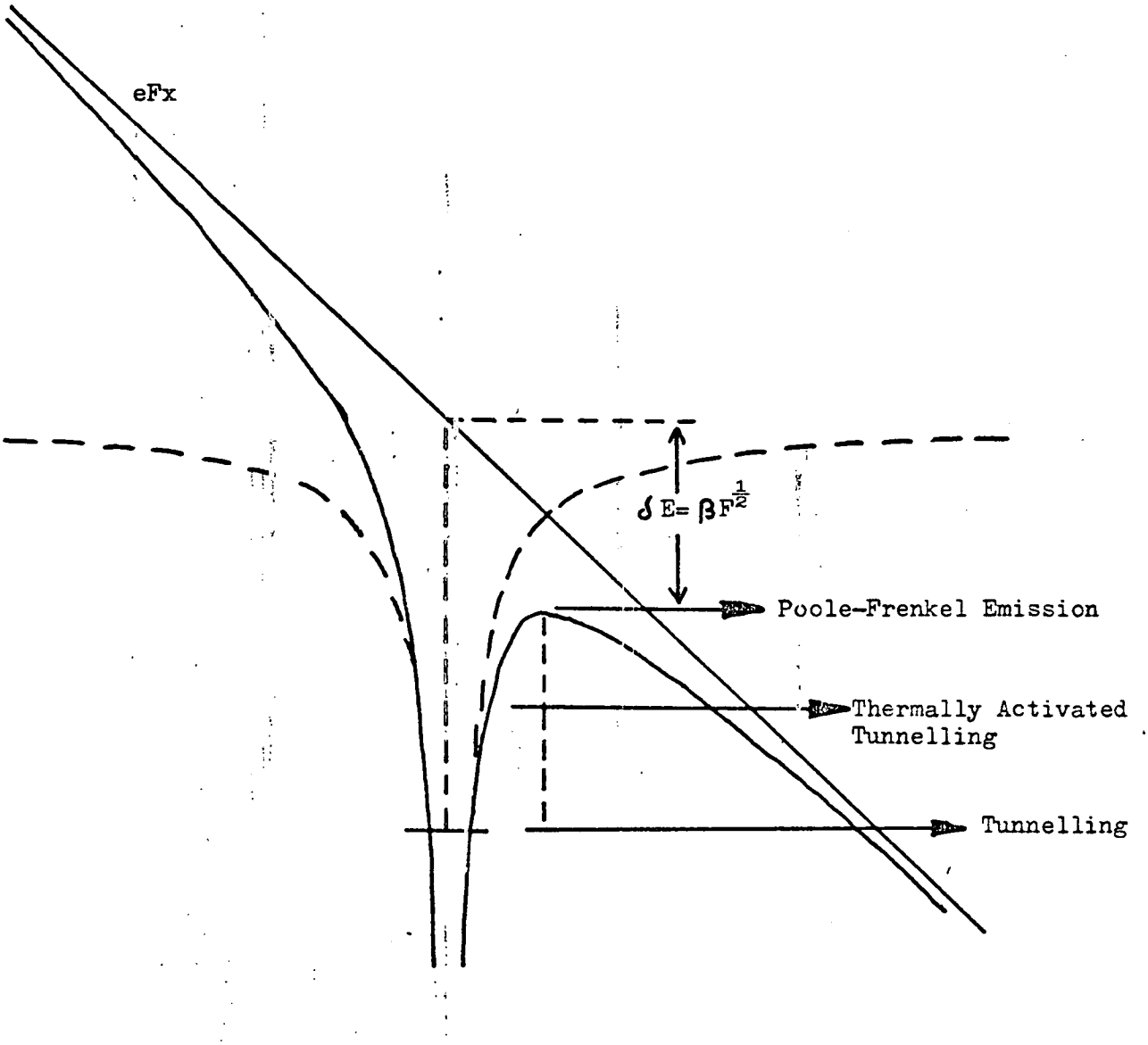

Figure 5.5 Illustration of the Poole-Frenkel effect for single coulombic centre.

$$\beta = \left(\frac{2q}{\epsilon^{\frac{1}{2}}}\right)^{3/2} \qquad (5.4.2)$$

and ϵ is the material dielectric constant. The electron can escape from the donor preferentially in the x-direction by one of three mechanisms.

(i) Thermal emission over the top of the barrier.

(ii) Direct tunnelling through the barrier.

(iii) Thermally assisted tunnelling through the barrier.

At low fields and finite temperatures, thermal emission over the barrier is likely to be the dominant mechanism.

The simple model has been extended to allow for carrier escape in all directions.[18-19] Hill[18] has assumed that the barrier height in the reverse direction is increased by the same factor that it is lowered in the forward direction, an assumption that implies zero current at zero field, which seems reasonable. Considering preferential emission along the field direction, he obtains,

$$\sigma \propto \exp\left(\frac{-E_i}{kT}\right).\sinh \alpha_1 \qquad (5.4.3)$$

where

$$\alpha_1 = \frac{\beta.F^{\frac{1}{2}}}{k.T} \qquad (5.4.4)$$

for a trap of depth, E_i. For amorphous materials, it is probably more applicable to consider emission into the complete sphere surrounding the site, in which case Hill obtains,

$$\sigma \propto \exp\left(\frac{-E_i}{kT}\right).\alpha_1^{-3}.(\alpha_1.\cosh \alpha_1 - \sinh \alpha_1) \qquad (5.4.5)$$

When a broad localised-state distribution is present, E_i can be considered as the energy gap between the conduction band and the upper limit of filled states.

Hill has also considered the case of multiple coulombic centres where the perturbations in potentials overlap, as illustrated in Figure (5.6). In this case, the potential lowering of the barrier is directly proportional to the applied field, rather than $F^{\frac{1}{2}}$, and the peak in barrier potential occurs at a point halfway between adjacent centres. For a pair of coulombic centres, separation s, the barrier lowering is expressed,

$$\delta E = \tfrac{1}{2}\, q.F.s \qquad (5.4.6)$$

Under the assumption that these multiple centres are limited in extent, occurring locally to give groups of sites, it is possible to deduce an expression for the conductivity in the field direction,

$$\sigma \propto \exp\left(\frac{-E_a}{kT}\right).\alpha_2^{-1}.\sinh\alpha_2^{-1} \qquad (5.4.7)$$

where,

$$\alpha_2 = \frac{q.F.s}{2k.T} \qquad (5.4.8)$$

and E_a is the experimentally observed ionisation potential. For emission into the complete sphere this becomes,

$$\sigma \propto \exp\left(\frac{-E_a}{kT}\right).\alpha_2^{-3}.(\alpha_2.\cosh\alpha_2-\sinh\alpha_2) \qquad (5.4.9)$$

The hyperbolic function $\alpha_2^{-3}.(\alpha_2.\cosh\alpha_2-\sinh\alpha_2)$ is plotted in Figure (5.7). This shows a quasi-linear regime on a log scale above $\alpha_2 = 5$. As α_2 is directly proportional to the applied field as given by Equation (5.4.8), this implies the correct functional behaviour of the conductivity at fields in excess of a value corresponding to $\alpha_2 = 5$, below which a transition to ohmic behaviour would be expected. At a temperature of 250K, say, and a state separation of 46.5Å (corresponding

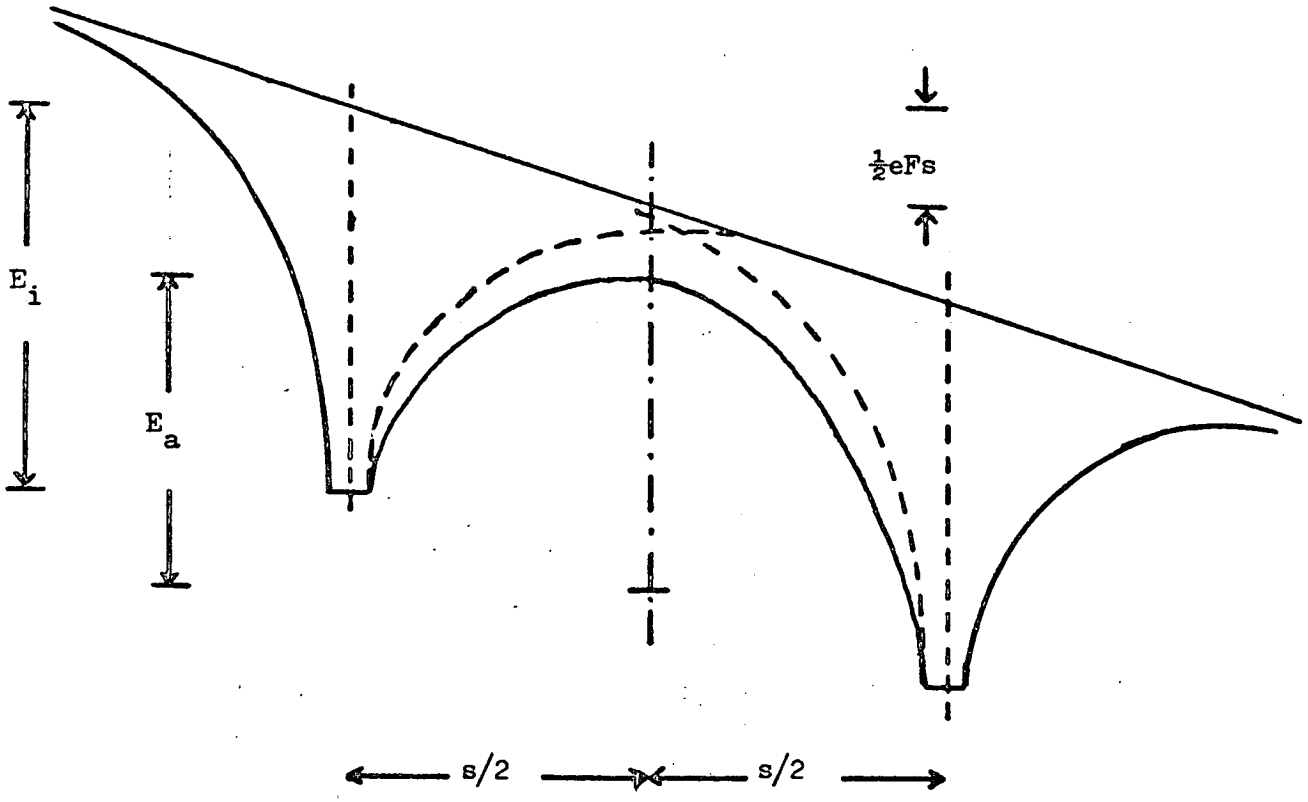

Figure 5.6 Illustration of the Poole–Frenkel effect for multiple coulombic centres.

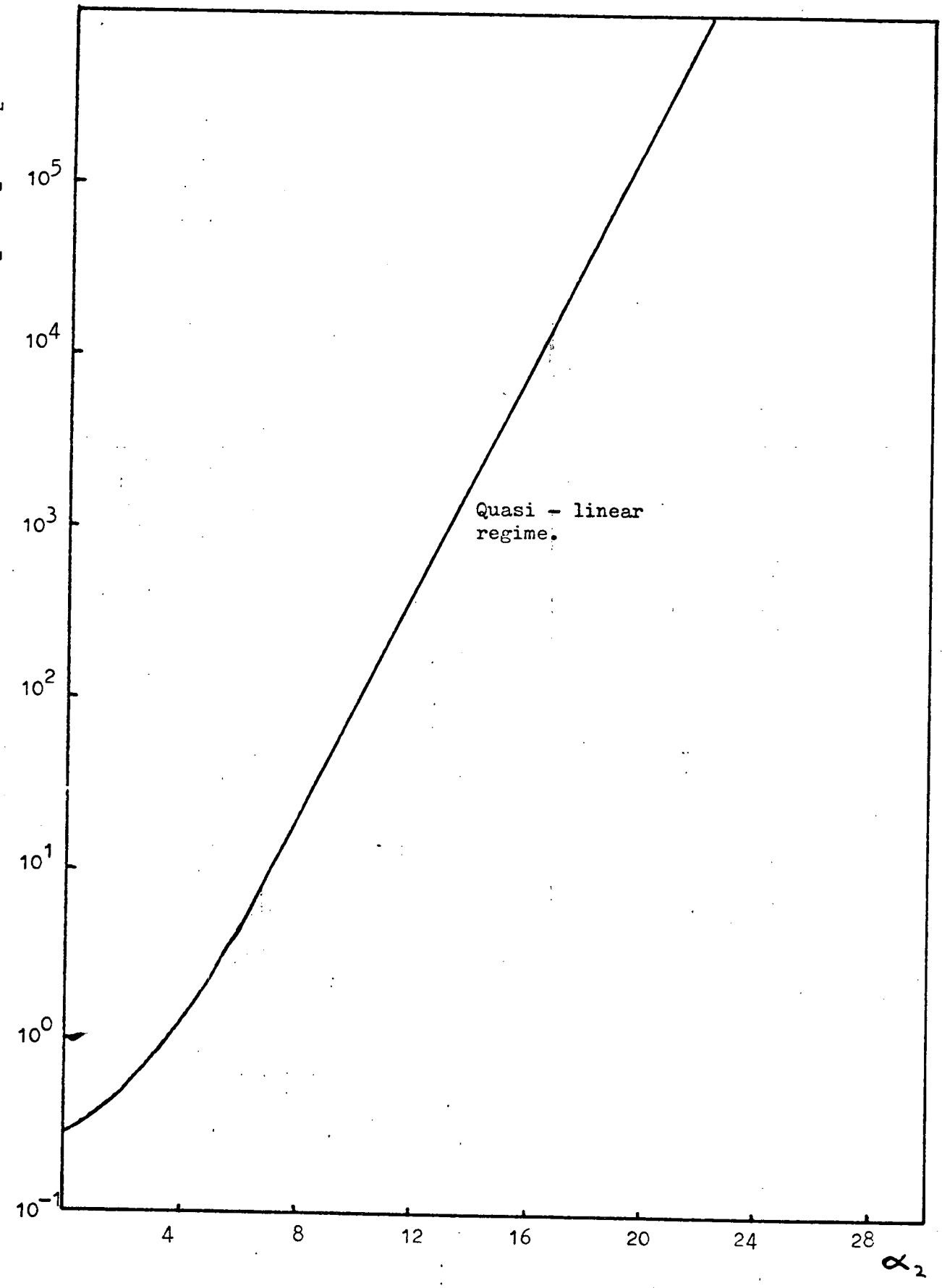

Figure 5.7 Plot of the hyperbolic function $\alpha_2^{-3}(\alpha_2\cosh\alpha_2-\sinh\alpha_2)$ vs. α_2.

to a density of states $\simeq 10^{25} m^{-3} eV^{-1}$, which seems reasonable as discussed in section (5.2), the predicted transition field is,

$$F = 4 \rightarrow 5.10^{7} V.m^{-1}$$

Thus the observed field dependence down to fields of $10^{6} V.m^{-1}$ and lower appears to contradict a model of this nature.

Moreover, it does not appear possible to explain the observed field dependence of the high field region ($F > 2.10^{7} V.m^{-1}$) in terms of this type of Poole-Frenkel mechanism. The gradient of the ln.δ vs. F data in the quasi-linear regime can be approximated by $q.s/2k.T$ according to equation (5.4.9) for $\alpha_2 > 5$. The observed temperature dependence of the second exponential regime at high fields is much greater than predicted by this expression. An attempt to fit the data to a Poole-Frenkel model results in state densities $< 10^{18} m^{-3} eV^{-1}$ which is much lower than expected.

5.5 Ionisation of Band Tail States

Another mechanism, suggested by Mott[20], is illustrated in Figure (5.8). According to this, the application of an electric field has a marked effect on the mobility by ionising the localised states in the immediate vicinity of the mobility edges, modifying the potential distribution so that direct tunnelling into the band states is greatly enhanced. This effectively pulls the state across the mobility edge into a region where the mobility is 1000 times higher. The effect would occur for

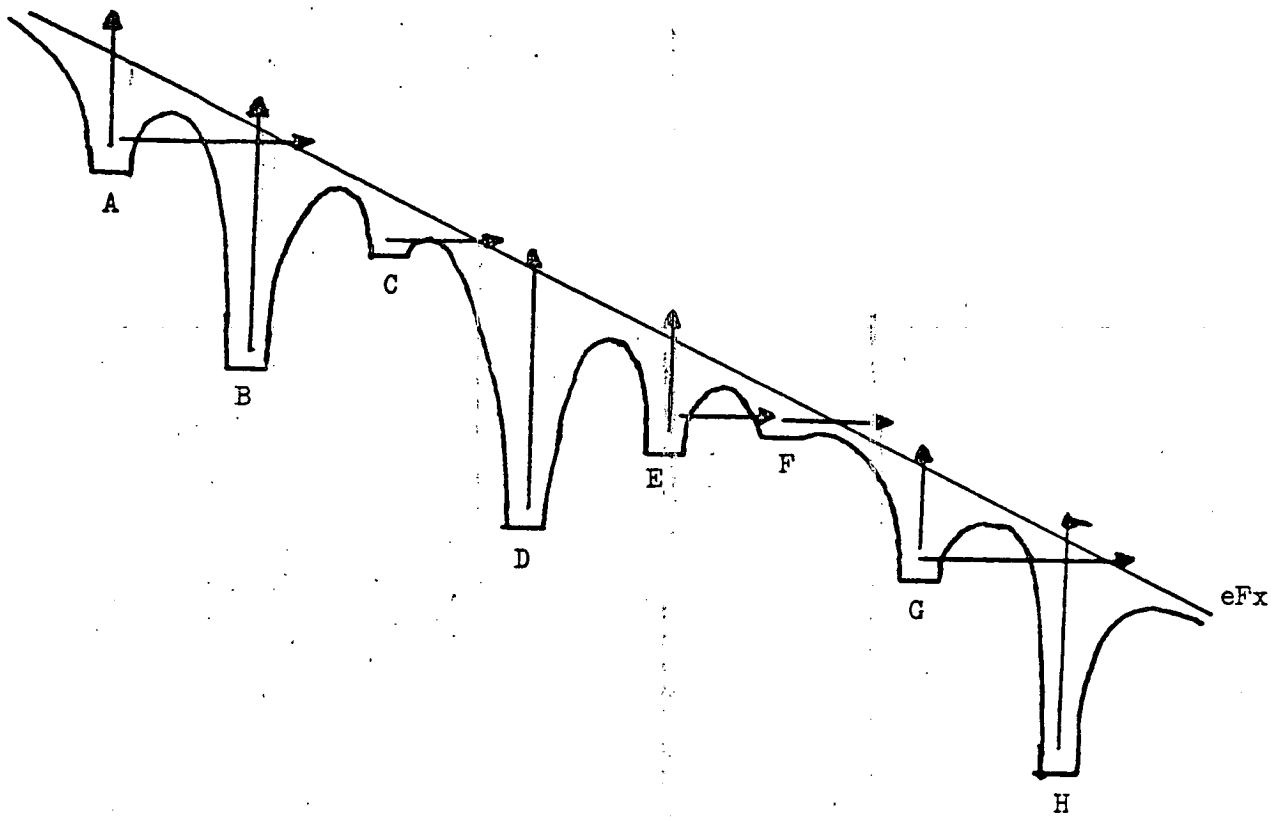

Figure 5.8 Schematic illustration of Band Tail Field Emission.
Diagram shows traps at C,F Effectively delocalised.
A,E,G Shallow traps: may become delocalised on small increase in applied field.
B,D,H Comparatively deep traps.

Arrows indicate principal mode of carrier emission.

both charged and neutral traps.

There are two main attractions of this "field stripping" model. Firstly, the exponential relationship between conductivity and field has been observed in a wide variety of amorphous semiconductors, and the existance of a mobility edge with a concomitant band tail of localised states is a prerequisite of most amorphous semiconductor band models. Secondly, this mechanism could, qualitatively at least, account for the observed exponential dependence down to very low fields, there always being states sufficiently weakly localised that they could be ionised on application of a finite field, and for a continuous state distribution, more states would be ionised at each increase in field strength.

5.6 Joule Heating Effects

The supra-exponential dependence of the conductivity on applied field due to internal Joule heating observed at high power levels, has been widely observed in chalcogenide alloys.[5,21-24] Chalcogenide glasses have a negative temperature coefficient of resistance so that any self-heating of a device leads to an increase in conductivity. Recently, many authors[25-30] have discussed the internal Joule heating in terms of thermal and electrothermal models. The simplest case requires the analysis of the heat conduction equation in a thin film with one-dimensional heat flow towards the electrodes and parallel to the conduction path,

$$K.\frac{\partial^2 T}{\partial z^2} + \sigma . F^2 = C.\frac{\partial T}{\partial t} \qquad (5.6.1)$$

where K is the thermal conductivity, F is the applied electric field in the z direction, σ is the electrical conductivity, C is the specific heat of the film, and $\frac{\partial T}{\partial t}$ is a measure of the rate of change of the film temperature with respect to time. Main[30] and others introduce a conductivity of the form,

$$\sigma = \sigma_o . \exp(\frac{-\Delta E}{kT}) . \exp(F/F_o) \qquad (5.6.2)$$

which they substitute into equation (5.6.1) in order to obtain a good fit to observed experimental data. Assuming the flow of heat out of the chalcogenide is a linear function of the temperature difference across the boundary, an S-shaped current-voltage characteristic of the type illustrated schematically in Figure (5.9) is predicted.

5.7 High Temperature Pulsed Measurements

The use of the pulsed technique described in Section (4.3.2) allows extension of the range of data on $Ge_{10}As_{40}Te_{50}$ to temperatures above room temperature, by substantially eliminating the Joule heating effects described above. This makes it possible to follow the linear exponential regime to fields in excess of $10^7 V.m^{-1}$, as illustrated by the conductivity-field data of another thin film sandwich device, illustrated in Figure (5.10). This data retains the main features of the lower temperature characteristics, namely an exponential dependence of conductivity on field down to low fields, and a continuation of the temperature dependence of the low field slope. Figure (5.11) illustrates the results of separate measurements of the low field conductivity as a function of temperature. The value

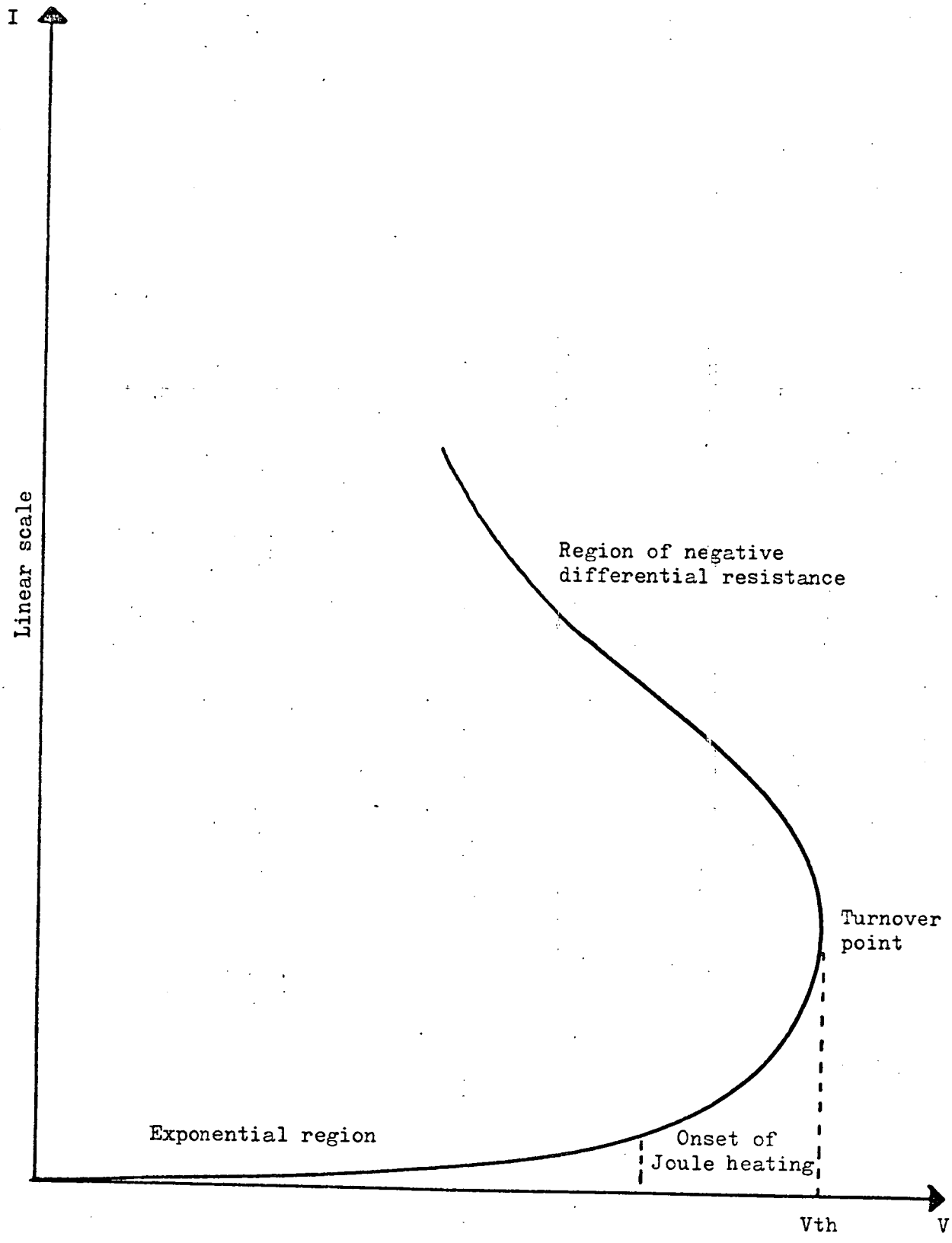

Figure 5.9 Schematic current-voltage characteristic for chalcogenide thin film sandwich devices.

Vth - Threshold voltage.

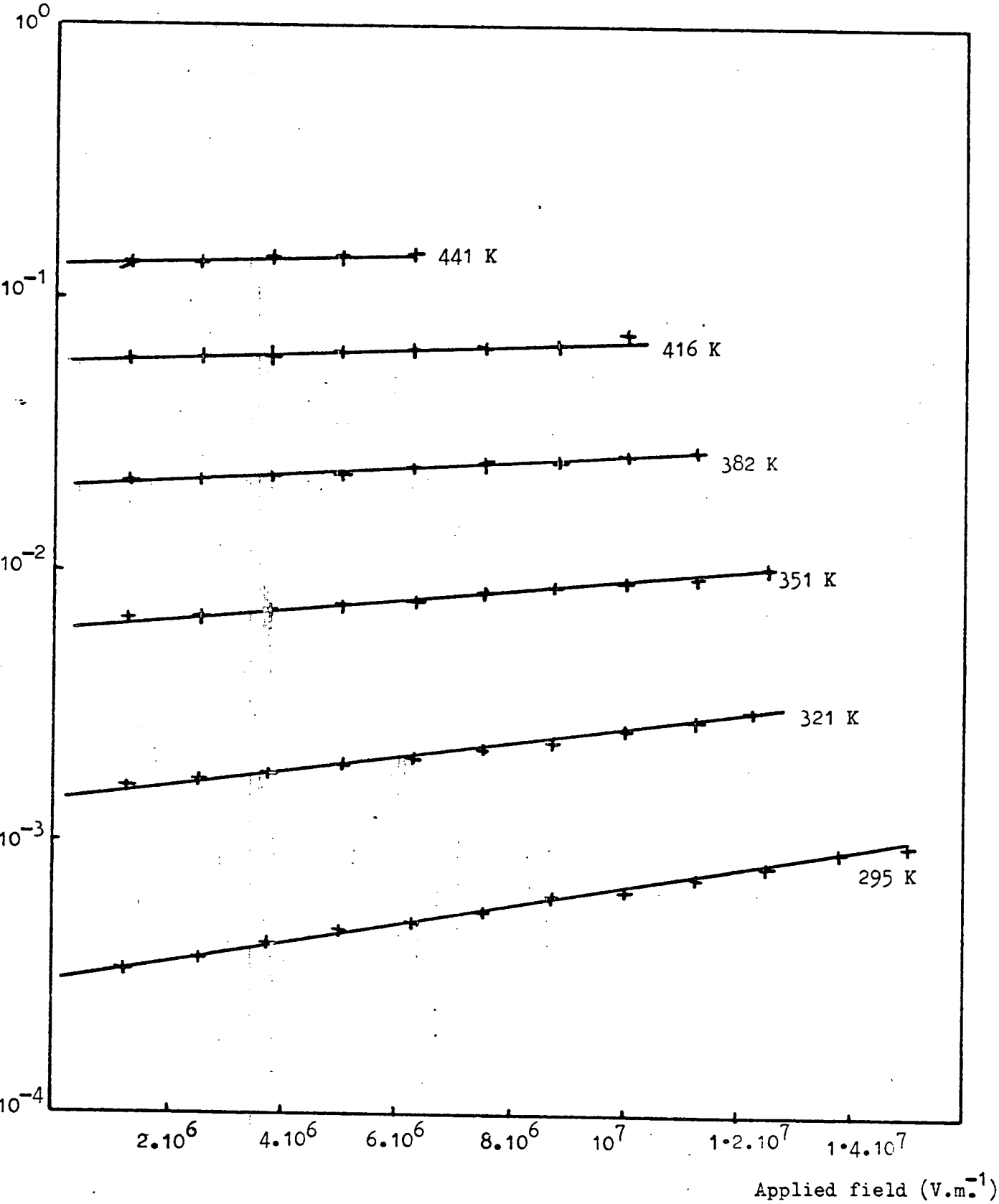

Figure 5.10 Variation of conductivity with applied field of a $Ge_{10}As_{40}Te_{50}$ sandwich device, thickness 4·7um, calculated from pulsed data.

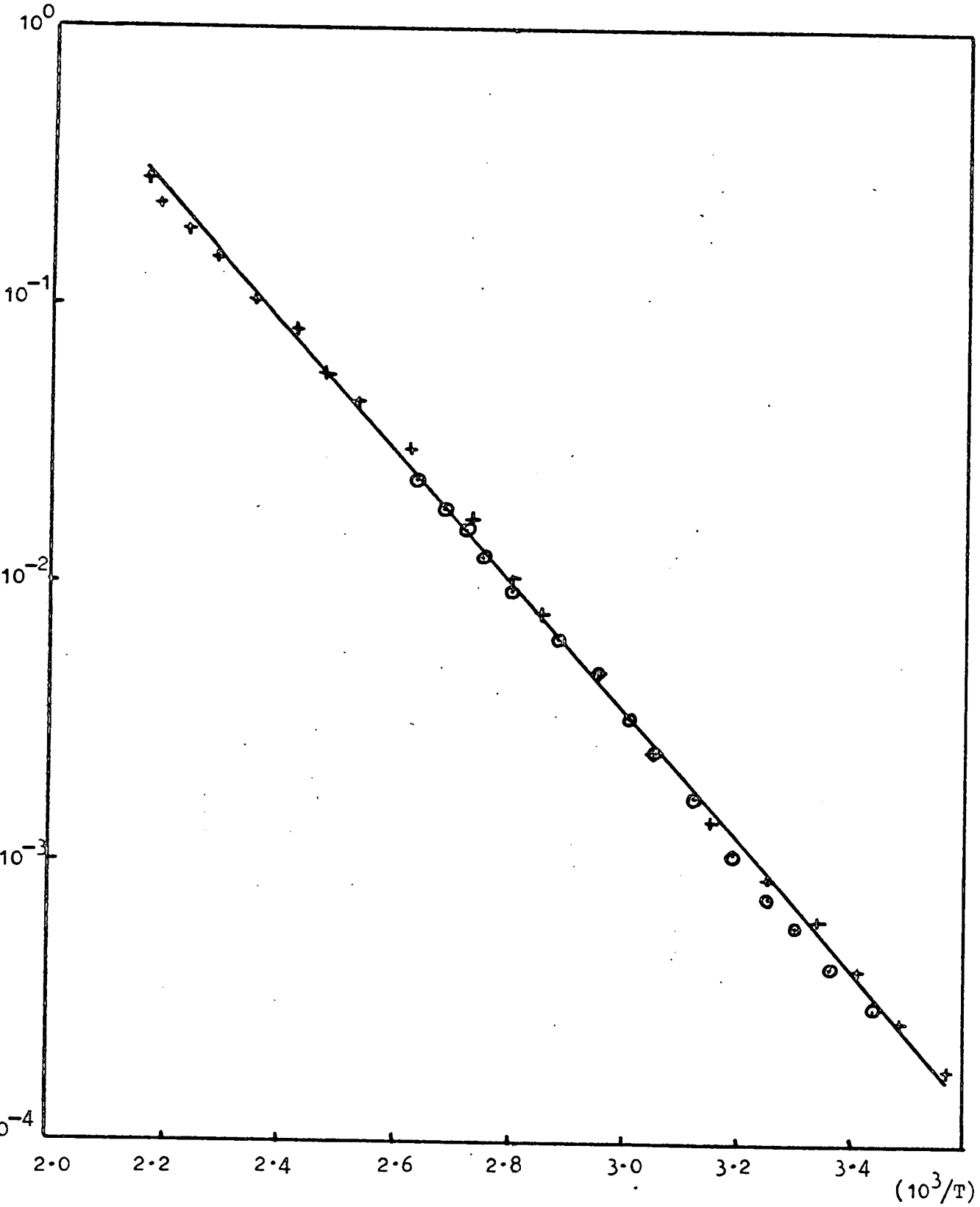

Figure 5.11 Variation of low field conductivity with temperature of a $Ge_{10}As_{40}Te_{50}$ sandwich device, thickness 4·7um., calculated from pulsed data. Different symbols refer to separate measurements.

for the activation energy ΔE = 0.46 - 0.47 eV is in reasonable agreement with that obtained from the lower temperature measurements.

5.8 Discussion

A study of the conductivity of the chalcogenide glass $Ge_{10}As_{40}Te_{50}$ as a function of applied field and temperature has shown several features in common with other chalcogenide glasses. The conduction process is thermally activated over the range of temperatures investigated; above 175K (approximately) conduction appears to be due to carriers excited into non-localised states, but the change of gradient in the graph of ln σ against $(10^3/T)$ below this temperature appears to reflect a transition to thermally activated hopping conduction due to carriers excited to localised states at the band edges, as discussed in Chapter 2. The exponential dependence of the conductivity on applied field may be explained in terms of a "field-stripping" model, but the emergence of a second high field exponential regime observable at low temperatures is not fully understood. However, the basic data presented here is invaluable in pursuing a study of the possible effects of electrical contacts and the surface region on chalcogenide thin film devices discussed in subsequent chapters.

CHAPTER 6 THE METAL-AMORPHOUS SEMICONDUCTOR CONTACT

6.1 Introduction

In this section, experimental data is presented on the metal-chalcogenide-metal sandwich structure with a variety of glass thicknesses and electrode materials. The metal-amorphous semiconductor contact is compared to its crystalline counterpart, discussed in Chapter 3, and a theoretical discussion of the transport processes within the barrier is included. Electron transport (as opposed to hole transport) is considered as the dominant conduction mechanism, and space charge regions adjacent to the electrodes are assumed to be parabolic in form, with the space charge layer thickness proportional to the square root of the surface potential, as this makes it easier to adapt existing theories to the amorphous case. In fact, the transport process in these materials is predominantly hole conduction, and the shape of the depletion layer is more probably exponential rather than parabolic, as will be discussed in Chapter 7. However, the arguments presented here apply to hole as well as electron conduction, and the discrepancy in form between the parabolic and exponential depletion region potentials should not alter substantially the calculations presented in the following sections.

6.2 Metal-Amorphous Semiconductor Contacts

Space charge regions at contacts or surfaces should be present in amorphous semiconductors, just as they are in crystalline semiconductors, although perhaps different in

form and magnitude. In the absence of interface states, the relative electron affinities of the amorphous semiconductor and the metal determine the polarity of the contact dipole layer. Where an appreciable density of interface states is present, the amorphous semiconductor and the metal come into equilibrium with the interface layer essentially independently. Figure (6.1) illustrates the metal-amorphous semiconductor interface compared with a typical rectifying contact between a metal and an n-type crystalline semiconductor. In an amorphous semiconductor the Fermi level is normally pinned near the centre of the gap, unlike an extrinsic crystalline semiconductor where it is much closer to the band edge. A large density of localised states exists within the interface layer of the amorphous material , distributed throughout the forbidden gap. Calculations for the screening length, λ , in materials which contain a high density of localised states at the Fermi level, have been performed by a number of authors.[1-5] Using the standard expression,

$$\lambda = \left[\frac{\varepsilon_r \varepsilon_o}{q^2 . N_F}\right]^{\frac{1}{2}} \qquad (6.2.1)$$

where N_F is the density of localised states at the Fermi level, ε_r is the dielectric constant, ε_o is the permittivity of free space and q is the electronic charge, values of less than 100Å can be deduced for reported values of N_F in chalcogenide alloys.[6] The screening length λ in amorphous semiconductors is thus much shorter than that usually associated with crystalline semiconductors.

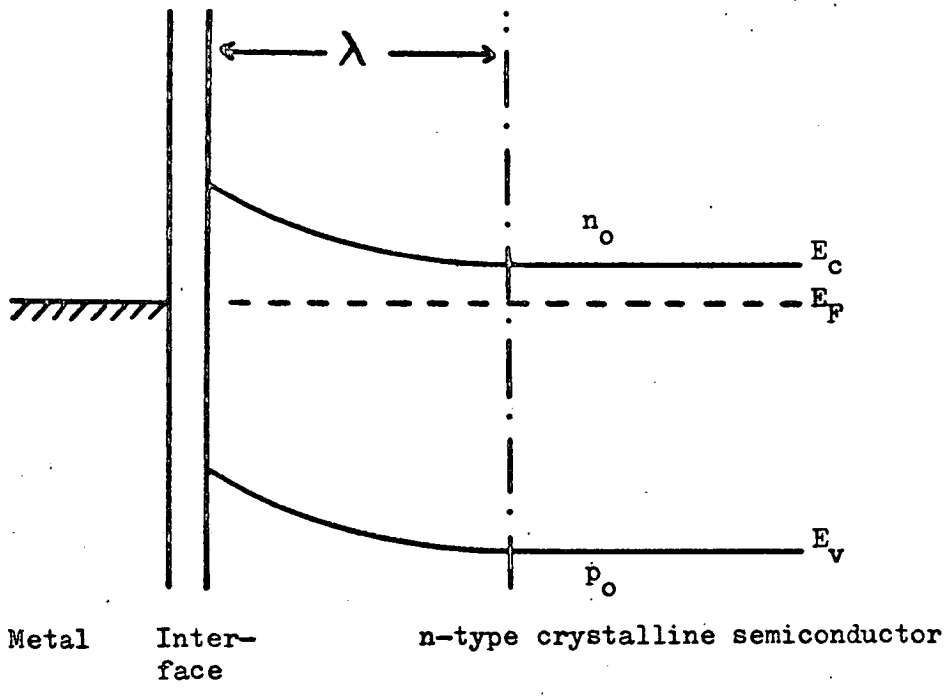

(a)

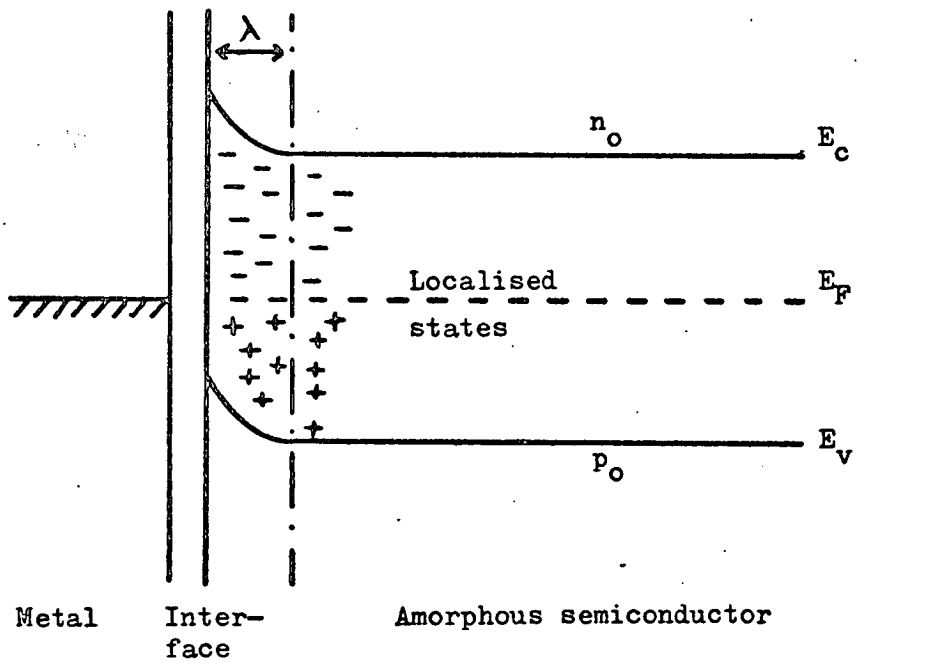

(b)

Figure 6.1 Potential distribution near metal-semiconductor contacts for (a) n-type crystalline semiconductor
(b) amorphous semiconductor.

6.3 Variable Thickness Measurements

A standard technique for the detection of blocking layers associated with barrier regions involves the measurement of the resistance of sandwich samples of various thicknesses. Any series resistance associated with the contact should be evident as an offset of the extrapolation of the graph of the device resistance against thickness on the resistance axis, R_o. The expression for the device resistance is,

$$R = R_o + \rho_B . t/A \qquad (6.3.1)$$

where R_o is the contact resistance, ρ_B is the bulk resistivity, t the device thickness and A the device area. Experimental data on a series of samples of $Ge_{10}As_{40}Te_{50}$ is shown in Figure (6.2). Molybdenum electrodes backed with gold to reduce the series electrode resistance were used in all cases. The sandwich devices were fabricated on one-inch square glass substrates, with 10 devices on each substrate, and the error bars in Figure (6.2) indicate the range of resistances found on each substrate with the relevant chalcogenide thickness. The resistance values quoted are in all cases measured at low fields such that the exponential term in Equation (5.3.1) tends to unity. Within the limitations imposed by variables in the batch preparation, Figure (6.2) indicates the absence of any large contact resistance.

Similar experiments were also performed on coplanar devices. For these measurements etched gold electrodes were used, and in this case,

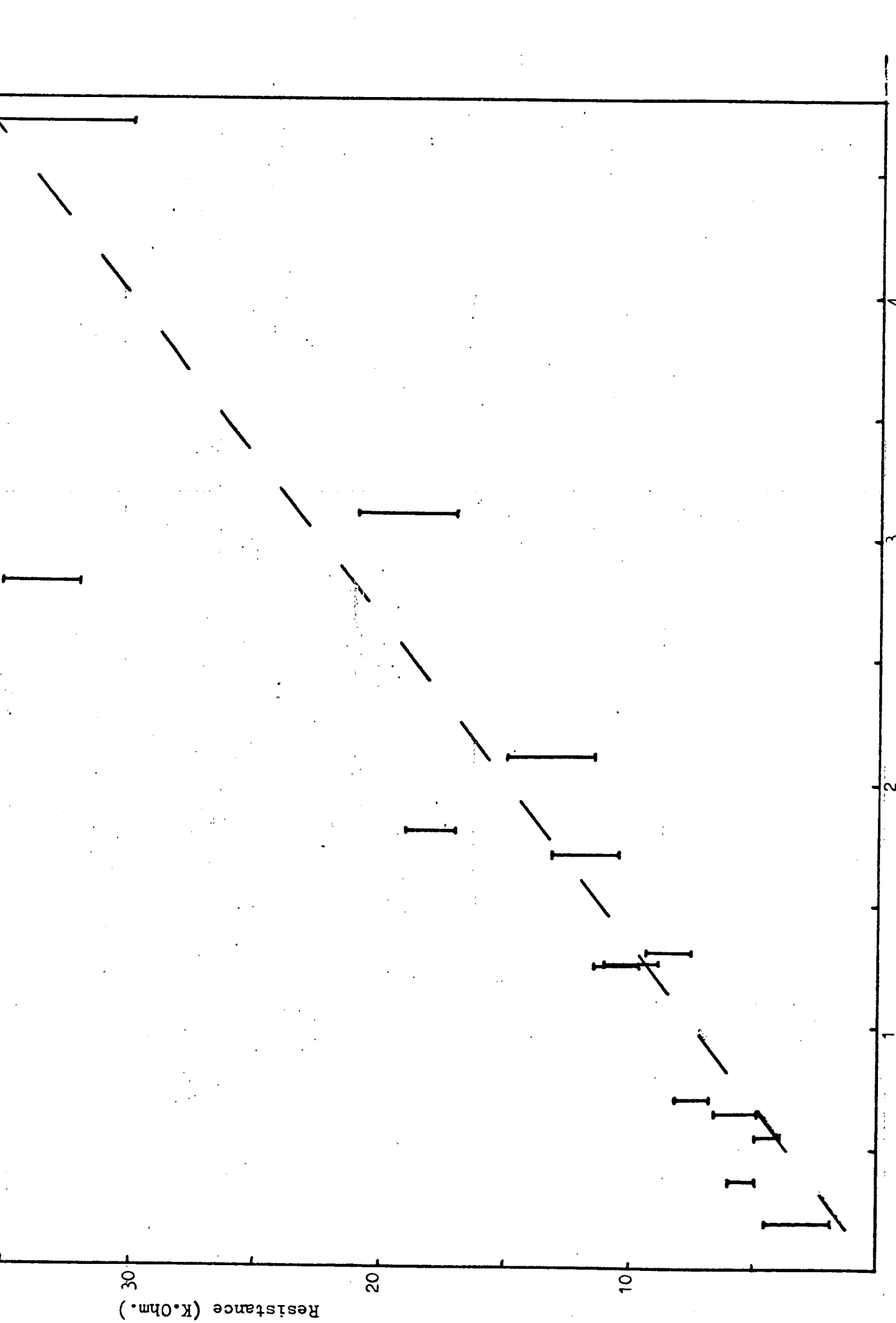

gure 6.2 Variation of resistance of $Ge_{10}As_{40}Te_{50}$ devices with device thickness
(i) Sandwich (T=294 K)

$$\frac{1}{R} = \frac{1}{R_s} + \frac{1}{\rho_B \cdot \frac{w}{t.b}} \qquad (6.3.2)$$

where R_s is the resistance of the surface layer, w is the width of the gap, t is the chalcogenide thickness and b the breadth of the electrodes. The graph of device resistance against reciprocal thickness plotted in Figure (6.3) again passes through or close to the origin, indicating the absence of a surface layer of significantly higher resistivity than the bulk. The points marked refer to individual samples, and errors due to different batch preparations must again be taken into account.

6.4 Various Contacts on $Ge_{10}As_{40}Te_{50}$ Devices

Sandwich devices were fabricated using metal electrodes with widely varying electrical and physical characteristics; viz, gold, aluminium, antimony, silver, tin, lead, indium, nickel, iron, platinum and molybdenum. In order to eliminate spurious results due to vagaries of batch preparation, each series of sputtered chalcogenide glass samples was produced having four electrode combinations, gold-gold, gold-metal, metal-gold and metal-metal, where the former is the bottom electrode, the latter the top electrode, and the metal is one from the above list.

Typical examples of the room-temperature ($\simeq$294K), current-voltage characteristics are illustrated in Figure (6.4), plotted on a log-log scale. The characteristics are completely symmetrical at low fields ($< 10^6 V.m.^{-1}$). At higher fields the characteristics remain essentially

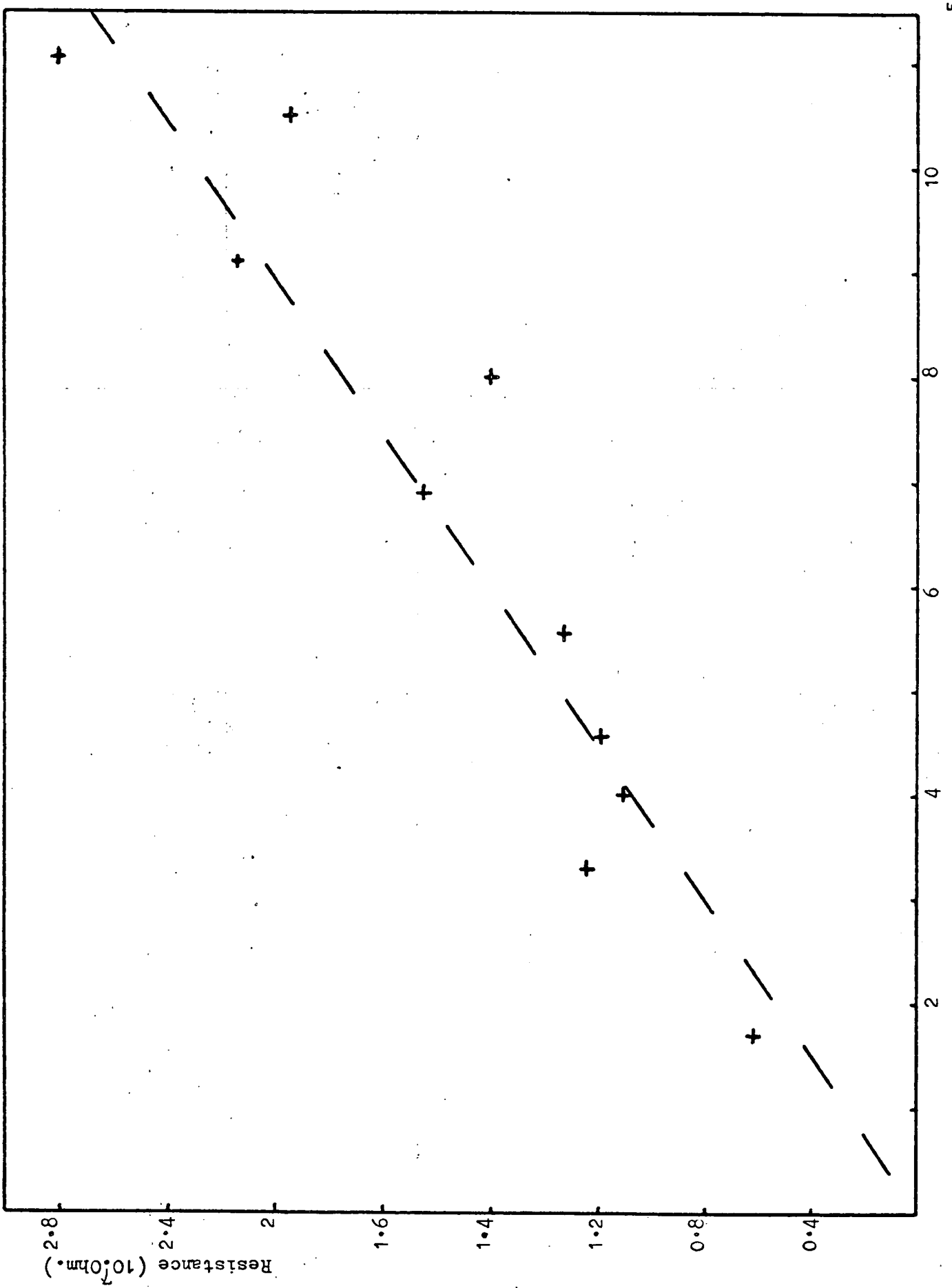

Figure 6.3 Variation of resistance of $Ge_{10}As_{40}Te_{50}$ devices with device thickness (ii) Coplanar (T=294 K).

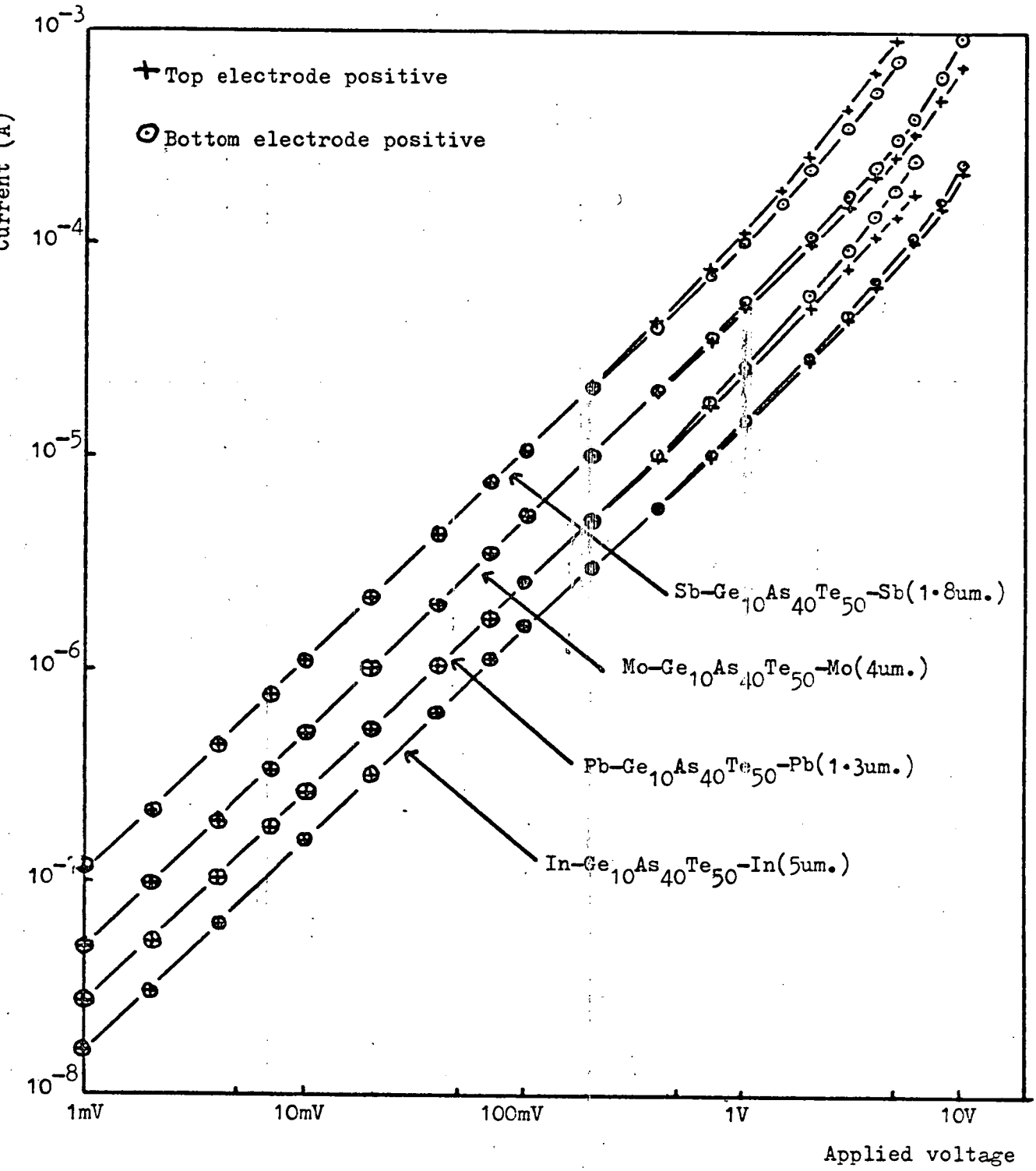

Figure 6.4 Current voltage characteristics of metal-$Ge_{10}As_{40}Te_{50}$-metal sandwich devices with various electrodes. (T=294 K)

symmetrical, though slight rectification was evident. The degree of rectification was observed to be a function of the particular batch rather than the electrode permutation, varying from batch to batch in both magnitude and sense. Similarily, computed values of the glass resistivity varied according to the particular batch rather than the electrode combination, and were generally within a factor of two of the measured bulk resistivity, as presented in Chapter 5. Thus the behaviour of the metal-chalcogenide glass film-metal device appears independent of the electronic and physical characteristics of the metal electrodes.

The essential symmetry of the characteristic, and the small asymmetry at high fields was maintained throughout the experimental temperature range, as illustrated in Figures (6.5(a)-(d)) which show typical characteristics for a Au-$Ge_{10}As_{40}Te_{50}$-Au device at progressively decreasing temperatures, plotted on a log-log scale. This data is also illustrated in Figure (6.6), plotted on a log-linear scale, which gives a clearer indication of the relative invariance in magnitude and sense of the high field asymmetry as a function of temperature.

At the present time there is no experimental evidence for blocking contacts to amorphous chalcogenide alloys of this nature, except where a junction is formed with an oxidising metal such as aluminium, or with a crystalline semiconductor. These situations are discussed in Section (6.5) and Chapter 9 respectively. Experimental evidence on the effects of various metal electrode contacts is rare. Vezzoli and Pratt[7] do not observe any rectification in

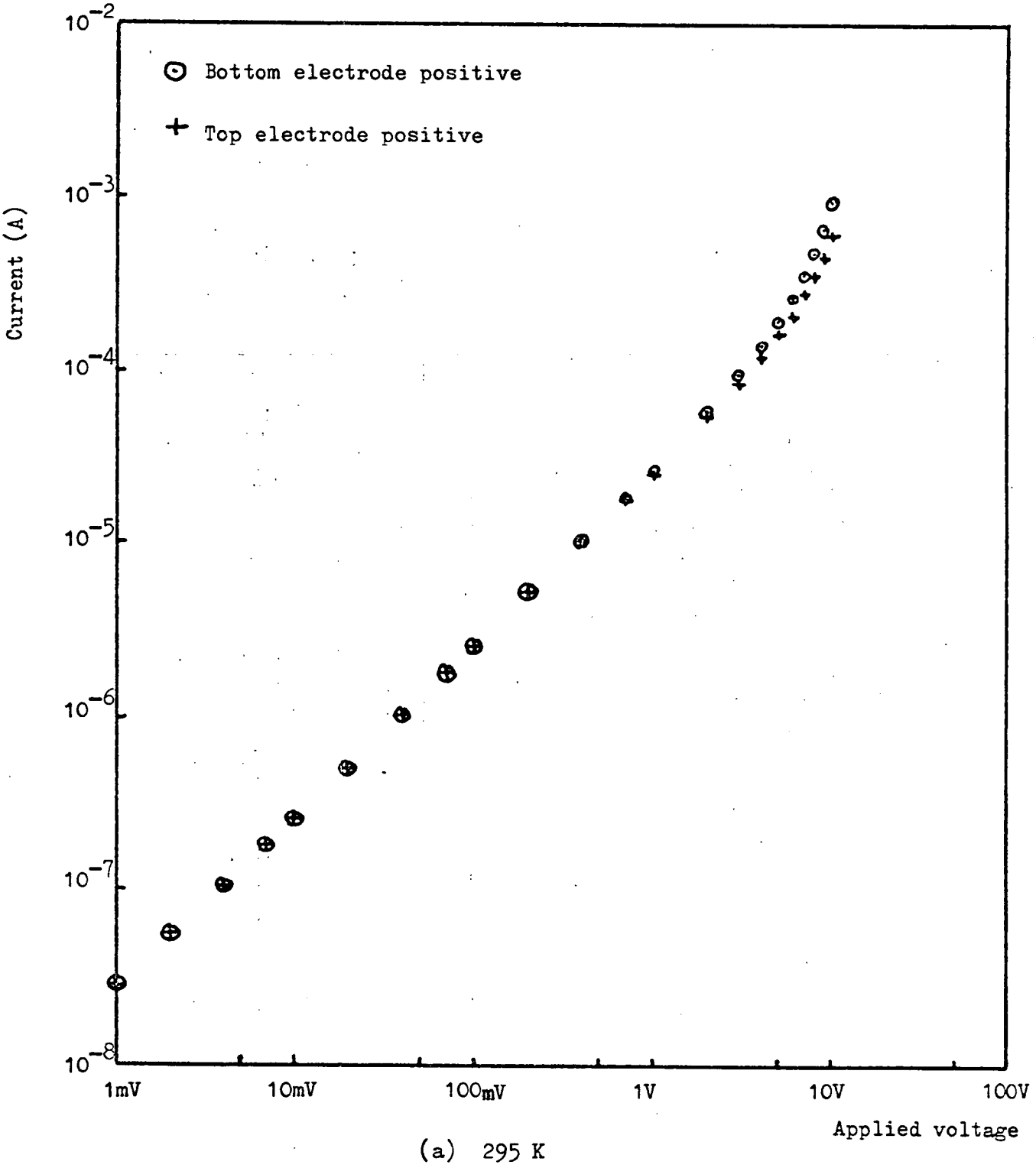

Figure 6.5 Current-voltage characteristics of an Au-$Ge_{10}As_{40}Te_{50}$-Au sandwich device (0·9um.) as a function of temperature.

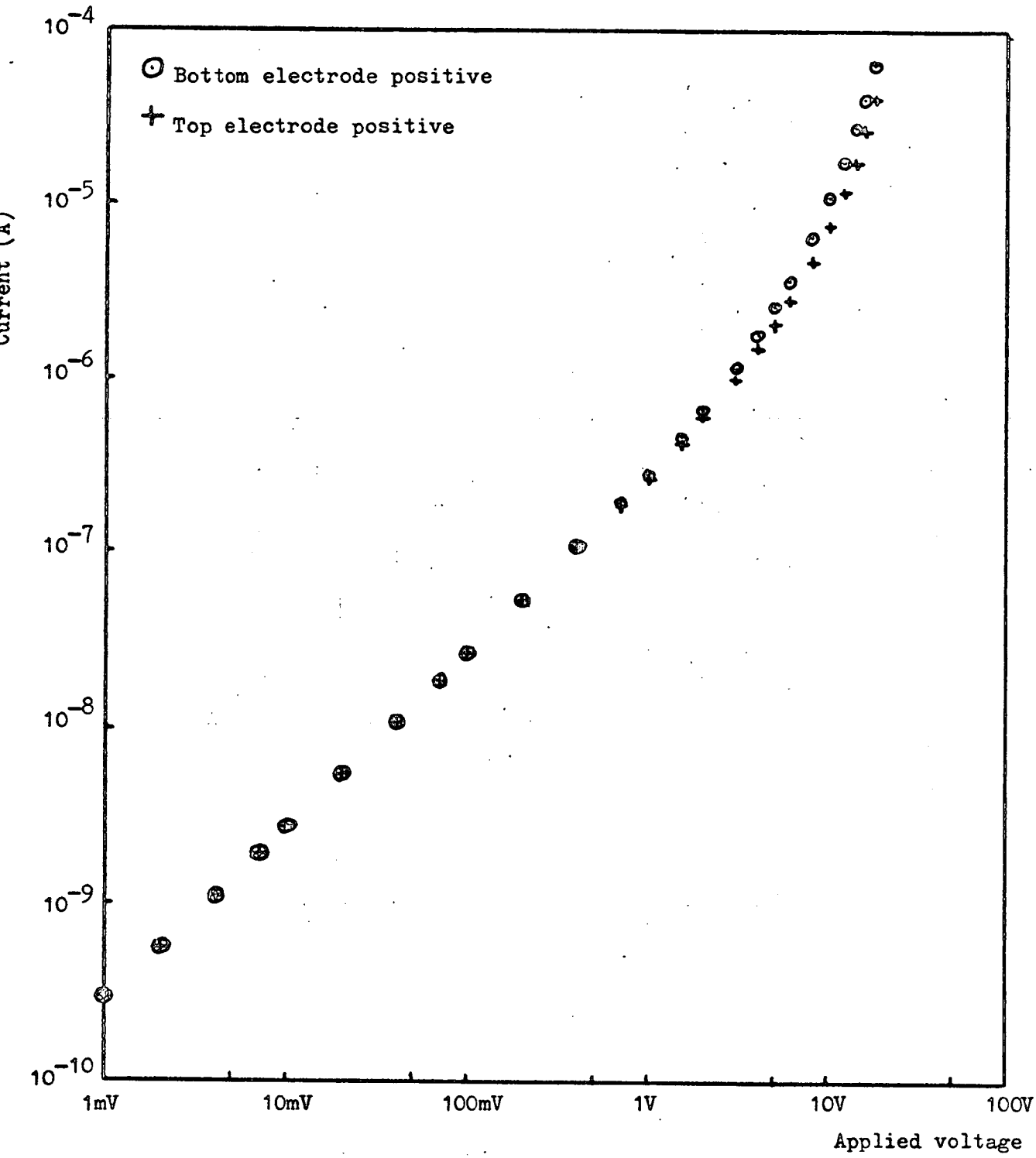
Bottom electrode positive
Top electrode positive
Current (A)
10^{-4}
10^{-5}
10^{-6}
10^{-7}
10^{-8}
10^{-9}
10^{-10}
1mV
10mV
100mV
1V
10V
100V
Applied voltage

(b) 240 K

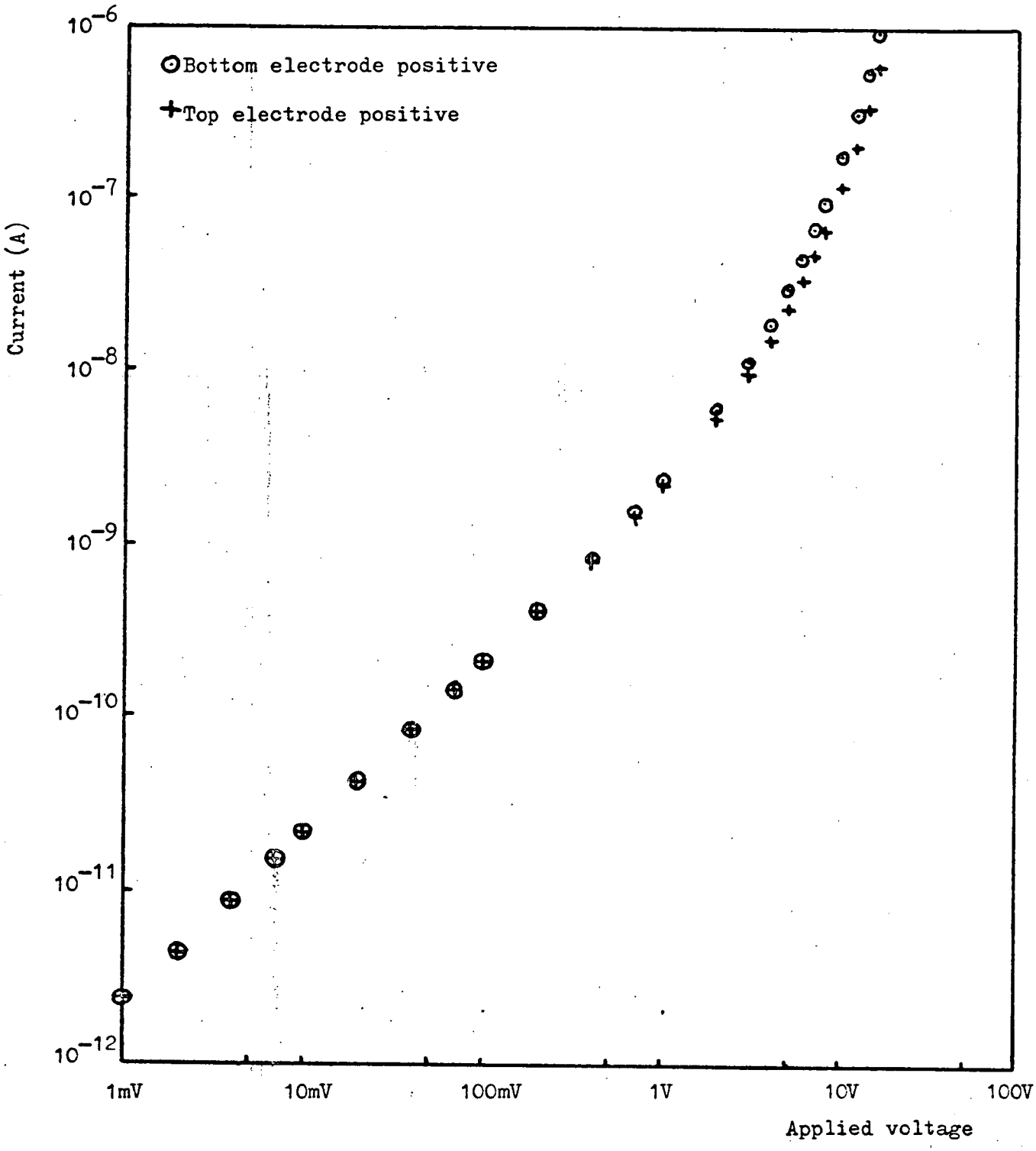
⊙Bottom electrode positive
+Top electrode positive
Current (A)
10⁻⁶
10⁻⁷
10⁻⁸
10⁻⁹
10⁻¹⁰
10⁻¹¹
10⁻¹²
1mV
10mV
100mV
1V
10V
100V
Applied voltage

(c) 200 K

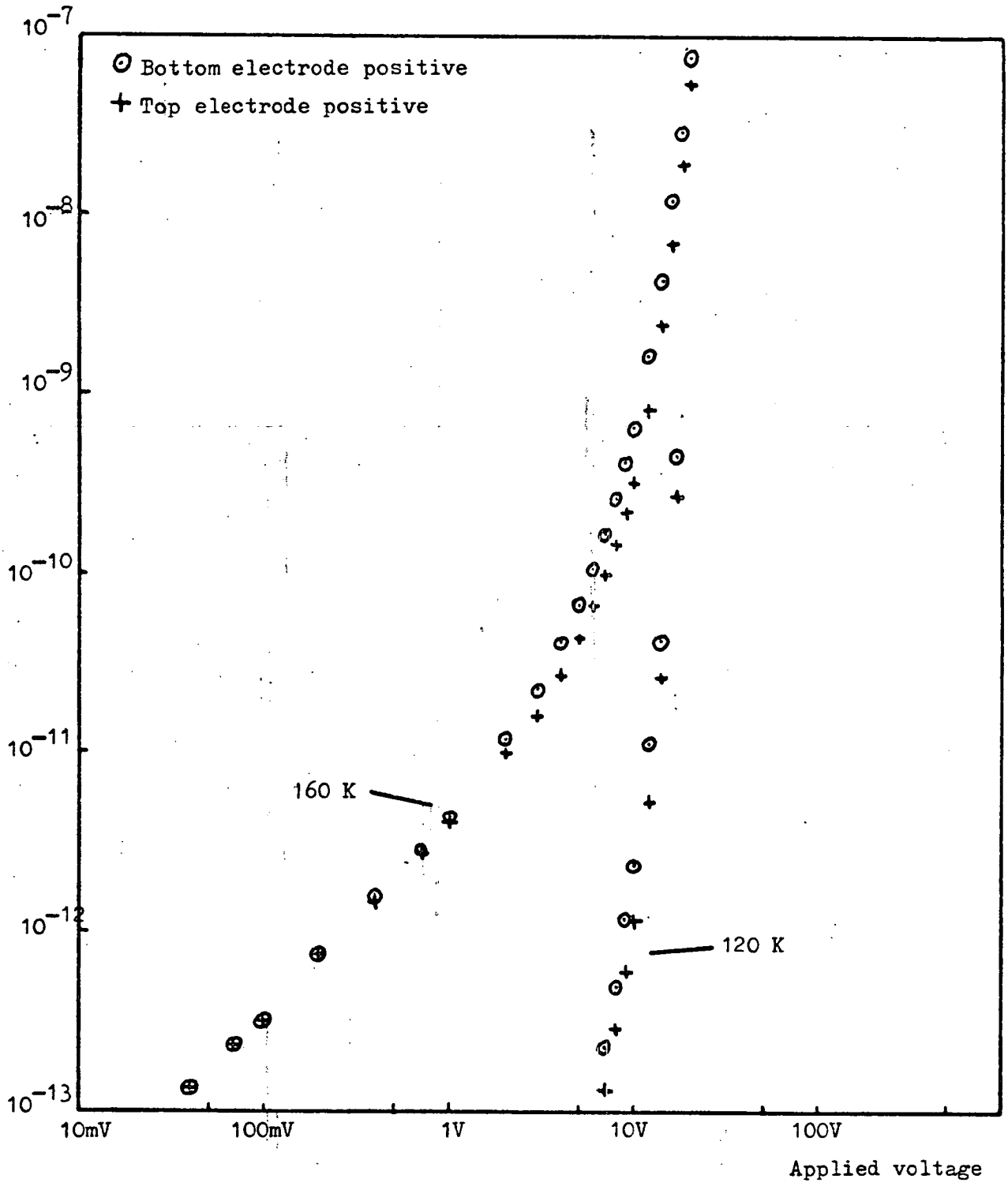

(d) 160 K and 120 K

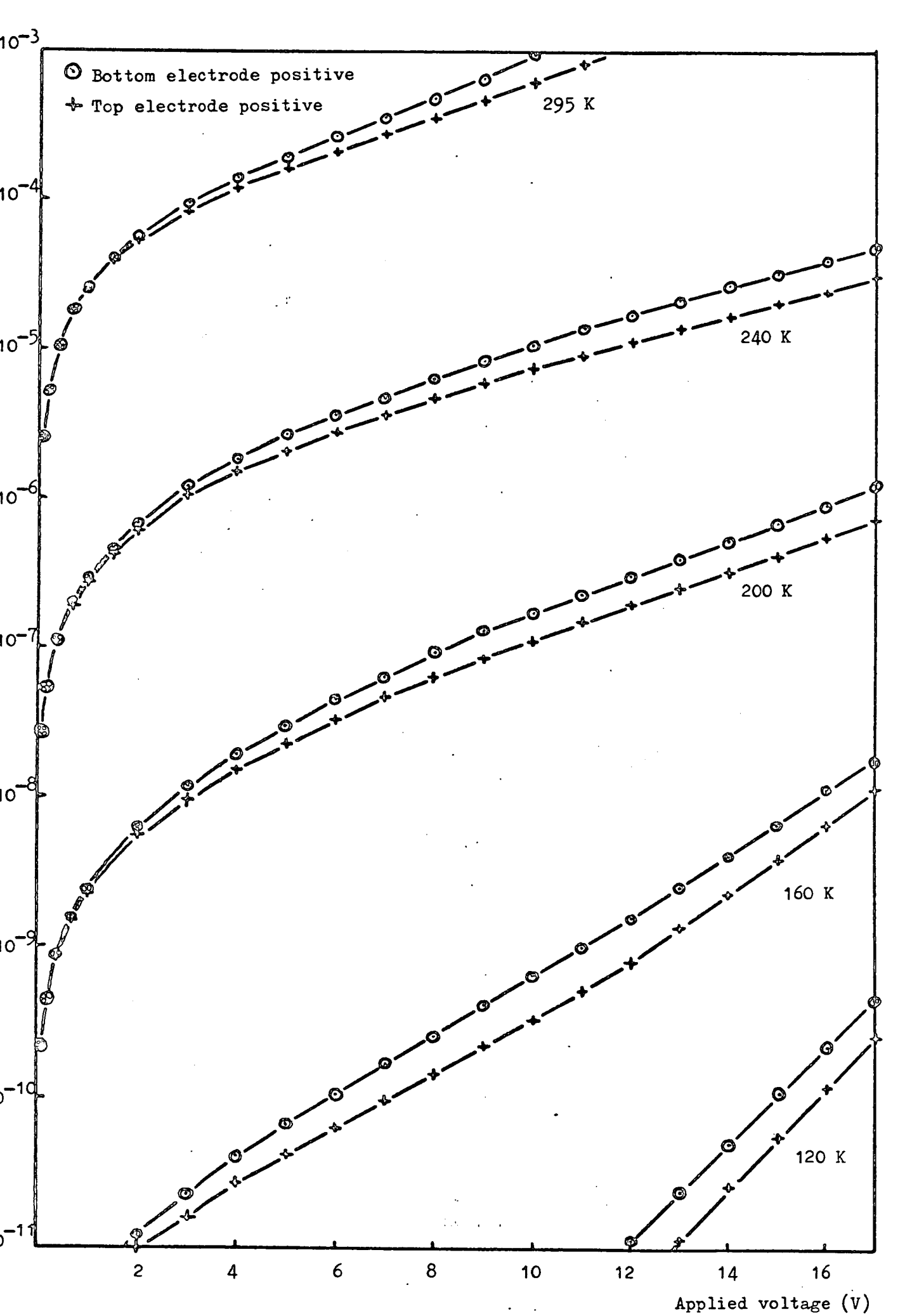

gure 6.6 Current-voltage characteristics of the Au-$Ge_{10}As_{40}Te_{50}$-Au device described in Figure (6.5) replotted on log-linear scale to illustrate more clearly the high-field asymmetry

the pre-switching characteristics of $Si_{12}Te_{48}As_{30}Ge_{10}$ devices using Al and Mo electrodes, while Altunyan and Stafeev[8] report non-blocking, symmetrical characteristics on a Si-Te-As-Ge glass using a wider range of electrodes. However, data by Petrillo and Kao[9] suggests that the switching mechanism in $Si_{12}Te_{48}As_{30}Ge_{10}$ can be strongly effected by the choice of electrode material, but they present no evidence of rectification in the pre-switching characteristic, and the effect of electrode materials on switching must be considered in a totally different context. Measurements made by the author on $Si_{12}Te_{48}As_{30}Te_{10}$ and As_2Te_3 sandwich structures using gold and molybdenum electrodes exhibit similar characteristics to those illustrated in Figures (6.4)-(6.6) for $Ge_{10}As_{40}Te_{50}$ devices, and it is probable that this behaviour is typical of a wide range of chalcogenide glasses.

The slight rectification observed in Figures (6.4)-(6.6) at fields in excess of about $10^6 V.m.^{-1}$ has not, to the author's knowledge, been reported on the more conducting chalcogenide glasses, but it has been observed on As_2Se_3[3] and As_2S_3[10], both glasses of much higher resistivity. Farooq and Hirsch[10] concluded that the small high field rectification was the result of some basic built-in asymmetry of the evaporated chalcogenide thin films, noting that the asymmetry was absent in self-supporting samples (bubbles blown from the bulk glass.). Electron micrographs of the As_2S_3[10] films indicated that the structure of the films was not symmetrical, the "roughness" of the exposed surface being more pronounced

with increasing film thickness. Thus the top and bottom contacts in chalcogenide glass films may be quite different. On the one hand the chalcogenide glass is sputtered onto a pre-evaporated metal, on the other the metal is evaporated onto a pre-sputtered chalcogenide glass. If the top surface of the sputtered glass films used here exhibited a similar increased 'roughness' with respect to the bottom surface to that observed in the evaporated As_2S_3 samples of Farooq and Hirsch[10] this might further emphasise the difference between the two formed contacts. However, the data of Farooq and Hirsch might also be interpreted as a variation in structure throughout the bulk of the film, adding a further asymmetry to the device configuration. If such inhomogeneities do exist throughout the bulk of the film they are thought to be structural rather than compositional. For example, Table (6.1) illustrates the results of an X-ray fluorescence analysis of successive 0.2 um.(approx.) layers of a sputtered $Si_{12}Te_{48}As_{30}Ge_{10}$ film. The results are for thin film samples taken in the time intervals (a) t = 0 to t = 15 minutes, (b) t = 15 to t = 30 minutes, and (c) t = 30 to t = 45 minutes, where t = 0 indicates the commencement of sputtering. The data does not indicate significant compositional variation throughout the film as might be caused by initial preferential discharge of one particular element, for example.

Thus, it is the author's conclusion that the observed small high-field rectification is due to some built-in structural asymmetry of the formed devices, rather than to the formation of rectifying contacts between the glass films

Table 6.1

	Sample no.	Te	As	Ge	(%)
t = 0-15 minutes	1	48	38.8	10.7	
	2	48	39.2	11.0	
	3	48	38.9	10.3	
t = 15-30 minutes	1	48	39.9	11.5	
	2	48	43.1	12.9	
	3	48	39.3	11.5	
t = 30-45 minutes	1	48	38.5	11.1	
	2	48	43.0	12.0	
	3	48	37.0	10.3	

This table shows the relative compositional variation of the elements As and Ge compared to a Te standard as a function of the time since the commencement of sputtering. The target used was powdered $Si_{12}Te_{48}As_{30}Te_{10}$, and the analysis was carried out by X-ray fluorescence techniques.

and the metal electrodes. Firstly, estimates of the current density through the interface region, detailed in the latter part of this chapter, indicate that the conduction process is bulk-limited rather than electrode limited. Secondly, the magnitude and sense of the rectification appears approximately constant throughout a wide range of temperature, as illustrated in Figure (6.6). This is reasonable if the device possesses a built-in structural asymmetry, but is inconsistent with contact rectification theories.

Finally, the possibility of chemical compound formation at the interface must also be considered. Nielsen[11] reports the formation of selenide layers at the interface between Cu and Ag electrodes and amorphous selenium, while Freeman et al[12] report compound formation between Cu and Ag electrodes and amorphous As_2Se_3, although Au, Al and Pt electrodes are inert. There is no evidence in the present work of compound formation at the interface, although a full electron microscope study would be desirable. Selected devices, tested immediately after fabrication and after a three-month period showed identical current-voltage characteristics.

6.5 Sandwich Devices using Aluminium Electrodes

When the bottom electrode of a sandwich device is an oxidising metal, a thin insulating layer is formed between the metal and the chalcogenide glass film. This was most manifest in the case of aluminium electrodes, the breaking of the vacuum previous to deposition of the glass

resulting in a thin Al_2O_3 layer at the bottom interface. When Al was used as a top electrode no oxide layer was formed. Batches were prepared in the usual Au-Au, Au-Al, Al-Au and Al-Al permutation, such that the conductance of the chalcogenide layer could be monitored from the Au-Au, or indeed Au-Al, devices.

The current-voltage characteristics of a typical Al-Al_2O_3 - $Ge_{10}As_{40}Te_{50}$ - Al device are plotted in Figure (6.7), with temperature as a parameter. The characteristics are symmetrical about zero bias, the principal feature being a very sharp rise in current through the device at bias voltages in excess of 500mV. (approximately). At low bias, $<$ 500mV (approx.) the applied voltage is principally across the insulating oxide layer, while at high bias, $>$ 4V (approx.), the limiting factor is the series resistance of the chalcogenide film. This is evident from a comparison of the characteristics of a complete batch at one particular temperature, as illustrated by Figure (6.8) for T = 294K. Figure (6.9) illustrates the calculated differential conductance of the device whose characteristics are plotted in Figure (6.7), plotted against device voltage. The low-field conductance of the corresponding Au - $Ge_{10}As_{40}Te_{50}$ - Au devices is also tabulated. In theory, it should be possible to plot the tunnelling conductance against the voltage drop across the oxide by comparison of the two sets of data, but in practise a small discrepancy between the conductances in the two chalcogenide films (i.e. that of the Au-Au device and that of the Al-Al device) can cause a large error in the

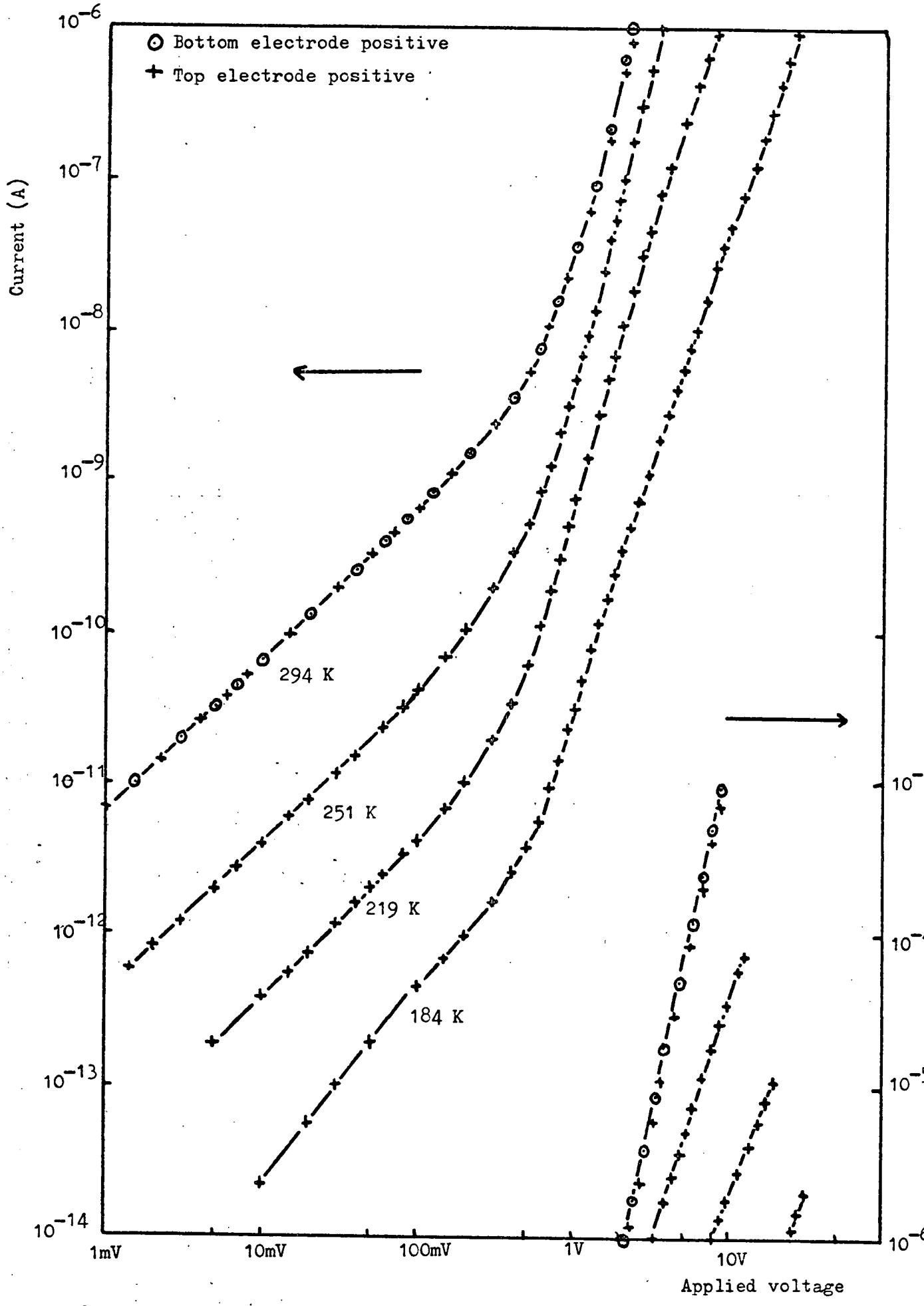

Figure 6.7 Current-voltage characteristics of an Al-Al_2O_3-$Ge_{10}As_{40}Te_{50}$-Al device - chalcogenide thickness, 1·3um.

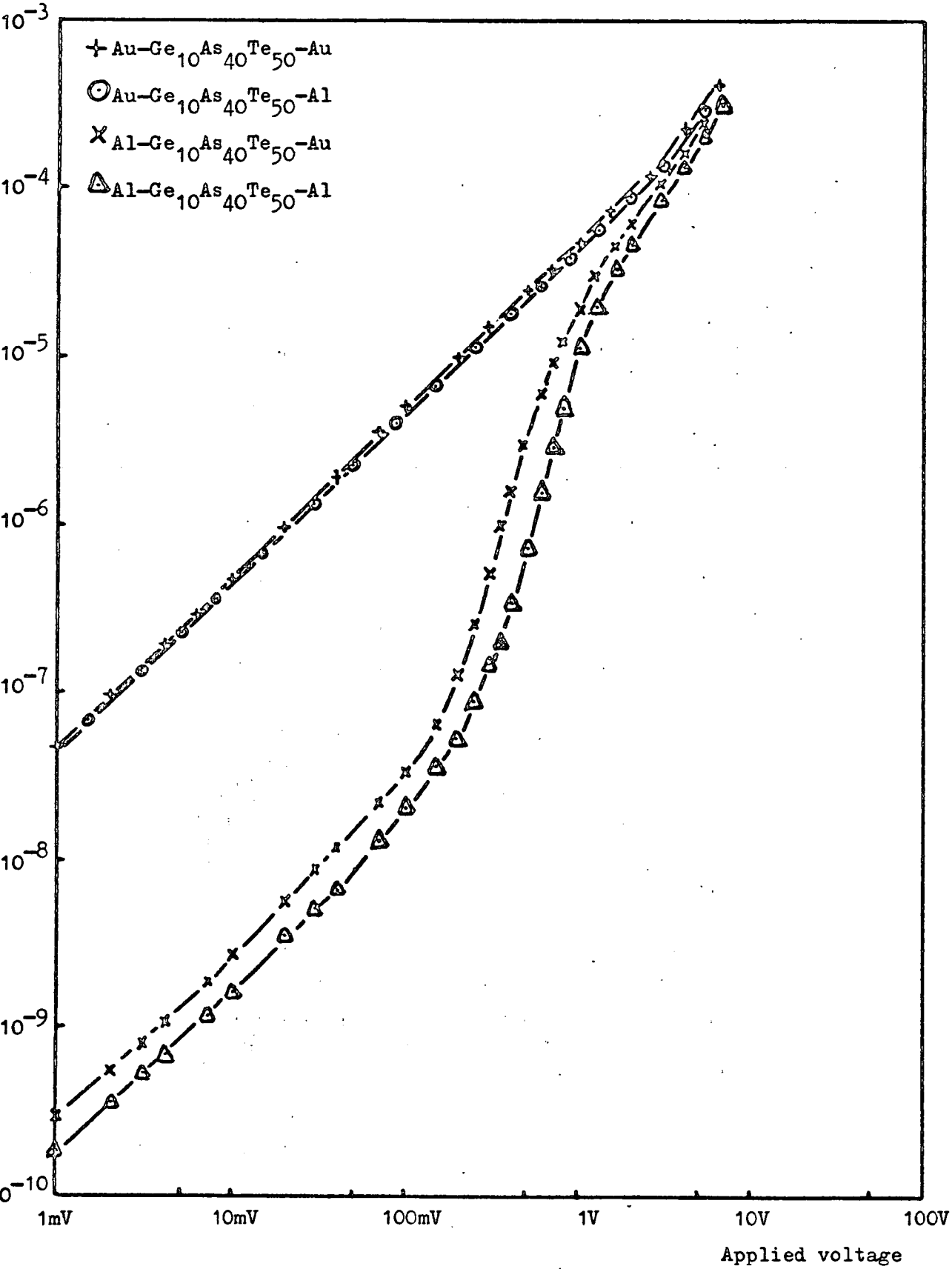

gure 6.8 Current voltage characteristics of a batch of $Ge_{10}As_{40}Te_{50}$ devices, thickness 1·8um., using Au/Al electrodes.
(T=294 K)

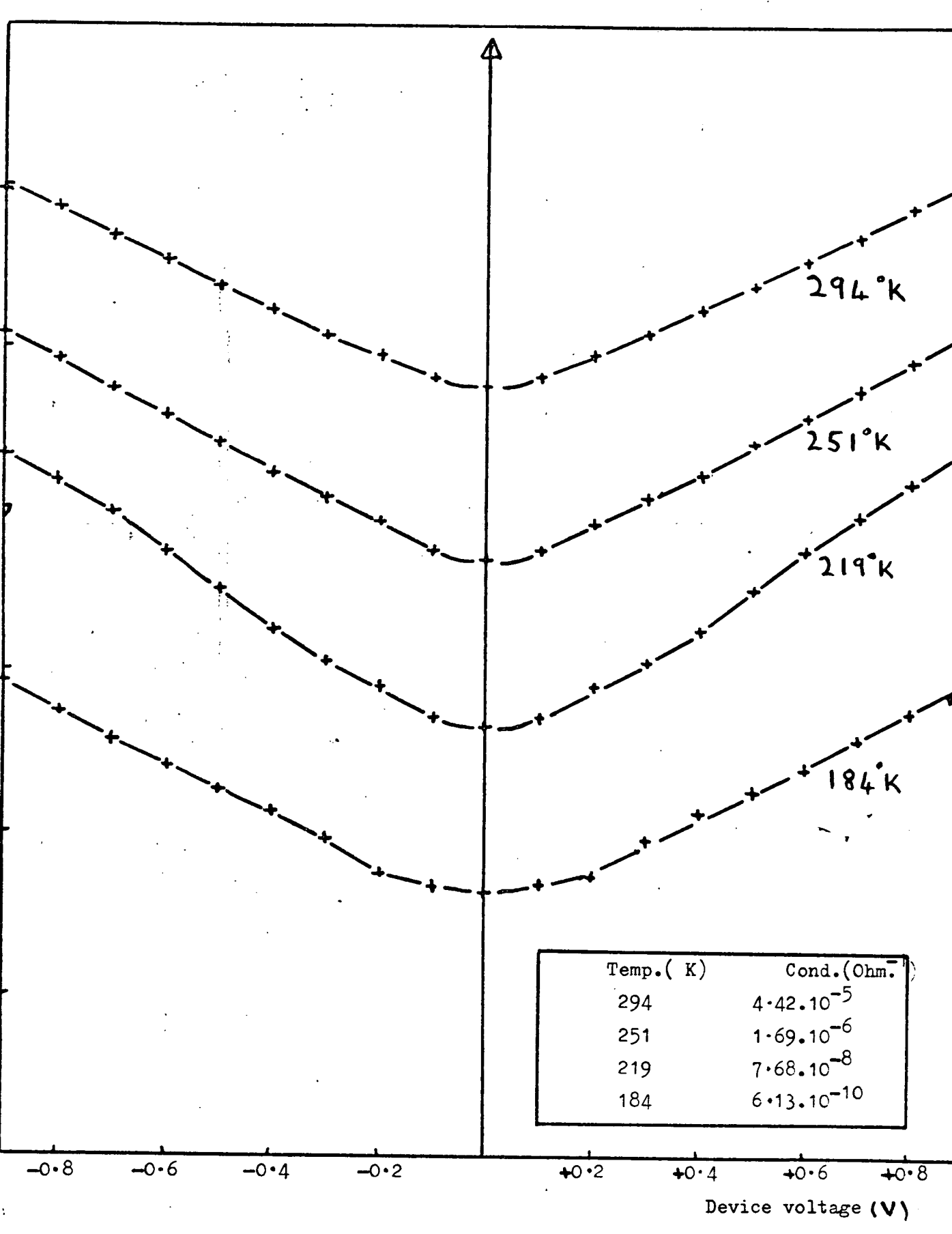

re 6.9 Differential conductance of an Al-Al_2O_3-$Ge_{10}As_{40}Te_{50}$-Al device as a function of applied device bias, calculated from data of Figure (6.7). Inset tabulates the low-field conductance of the corresponding Au-$Ge_{10}As_{40}Te_{50}$-Au device.

computed characteristic. As illustrated by Figure (6.1) such discrepancies do occur, even between devices on the same substrate. However, at relatively low voltages and high temperatures, the device voltage can be considered as equivalent to the voltage drop across the oxide.

The two main features of the tunnelling conductance data reported here, that is the symmetrical monotonic increase of tunnelling conductance with applied bias, and the variation of the low-field tunnelling conductance with temperature, have been observed by a number of authors on various amorphous materials. These include amorphous Ge[13-16], amorphous Si[15,17], and amorphous InSb and GaSb.[18] Asymmetric tunnelling into amorphous $Tl_2SeAs_2Te_3$ has been reported by Osmun;[19] and into amorphous GeTe by Yamashita et al[20], but these two sets of data do still retain the generally featureless rise in tunnelling conductance with applied bias. However, conflicting data is reported on amorphous Ge by Nwachuku and Kuhn[21]. They observe a 'conductance well', of width related to the energy gap, beyond which the conductance rises sharply, which they consider as a transition from tunnelling into localised states to tunnelling into extended states. In addition, the zero-bias conductance of the devices appears independent of temperature. However, Smith and Clark[15] suggest that the conflicting data of Nwachuku and Kuhn may be the result of the use of electronic, rather than hand, differentiation. They point out that in the constant current mode of electronic differentiation, the source must have an output impedance considerably higher than the

oxide resistance over the entire bias range, and that they obtained curves quite similar to Nwachuku and Kuhn by attempting to use electronic differentiation when they knew that this condition was not satisfied. It is the intention here to concentrate on the more generally observed type of behaviour, as illustrated in Figures (6.7)-(6.9).

The dependence of the differential conductance of $Al-Al_2O_3$ - $Ge_{10}As_{40}Te_{50}$ - Al devices on bias and temperature may be interpreted in terms of a tunnelling mechanism through the oxide layer into localised states in the surface region of the amorphous chalcogenide film. Although, hopping conduction at or near the Fermi level is not thought to contribute significantly to the transport process within this experimental temperature range, as discussed in Chapter 5, these states are in equilibrium with the conduction bands via recombination/generation kinetics. Thus one might expect to find strong structure in the localised state distribution reflected in the conductance data, and in particular a sharp rise in the tunnelling conductance might occur at a bias level where the Fermi level in the metal coincides in energy with the mobility edges. The lack of these features may be interpreted in various ways.

(i) A quasi-continuous distribution of states may exist within the energy gap of the semiconductor, with a minimum at the Fermi level. As it is probable that the tunnelling measurements only probe a thin surface layer of the semiconductor, from which conduction then proceeds according to the dominant transport mechanism in the bulk chalcogenide

film, it is not possible to say that such a featureless distribution of localised states is typical of the bulk chalcogenide film. Thus the bulk chalcogenide glass might have pronounced structural features, but these could be obscured by the monotonic distribution of states at or near the oxide-glass film interface.

(ii) It may not be valid to consider the interface region in two dimensions only, such that the metal Fermi level is at a unique energy separation from the semiconductor mobility edges at a fixed applied bias, but rather that at different points across the plane of the contact the metal Fermi level is at different energy separations from the band edges. Thus at a particular bias value, the transport process could be considered as a parallel combination of tunnelling into localised states and tunnelling into extended states. As the applied bias is increased, the proportion of conduction due to the latter mechanism increases, and hence the tunnelling conductance increases. In addition, the temperature dependence of the conductance should decrease at higher bias values, as tunnelling into extended states should be insensitive to temperature.[17,22,23] This is not clear from the data of Figure (6.9) as this has not been corrected for voltage drop across the semiconductor, though it is observed by Sauvage et al.[17] for tunnelling into amorphous Si, and in a review article by Hauser[24] for various amorphous materials.

Sauvage et al[17] have further considered tunnelling through the oxide layer into a random distribution of states within the semiconductor as a variable range tunnelling

process. This is analogous to Mott's[25] derivation of the $T^{-\frac{1}{4}}$ law for hopping conduction within localised states at the Fermi level, the main differences being the consideration of the attenuation of the current by the tunnel barrier, and a geometric factor considering tunnelling into a hemispherical region of the semiconductor. Considering an electron tunnelling from the metal into the semiconductor at energy E, it can either tunnel some distance into the semiconductor to a localised state of identical energy E, or it can tunnel a shorter distance (on average) to a state of some slightly different energy, $E + \delta E$, provided the temperature is high enough for phonons to be absorbed and energy conserved. Maximising the tunnelling probability with respect to distance, they obtain,[17]

$$P_{max} \propto \exp(-2\alpha_o d_o) \cdot \exp\left[\frac{-36\alpha_s^3}{N(E).kT}\right]^{\frac{1}{4}} \qquad (6.5.1)$$

where α_o and α_s are the wave function decay constants of the oxide and the semiconductor respectively, d_o is the oxide thickness, and N(E) is the density of states in the semiconductor at energy E. However, although such a model may be applicable to amorphous Si and Ge, in which the conductivity obeys a $T^{-\frac{1}{4}}$ low over a wide range of temperature, it is doubtful whether this is directly applicable to the tunnelling measurements on $Ge_{10}As_{40}Te_{50}$, where the conductivity is more accurately represented by a T^{-1} law over the experimental range, as discussed in Chapter 5.

6.6 The Schottky Barrier Model for the Metal-Amorphous Semiconductor Contact

In the following sections, the quantitative theories developed by various authors for transport through metal-crystalline semiconductor barriers are adapted and applied to the metal-amorphous semiconductor case by introducing into the equations the appropriate quantities. The differences between the metal-amorphous and metal-crystalline semiconductor barrier regions outlined in section (6.2) can seriously effect the dominant transport mechanisms. These are illustrated in Figure (6.10) and can be divided into 3 main groups.

(i) Electron transport across the barrier.

(ii) Hole transport across the barrier coupled with a recombination/generation process within the semiconductor.

(iii) Tunnelling to and from localised states at the Fermi level, again coupled with a recombination/generation mechanism.

Electron transport across the barrier may take place by a combination of three mechanisms, field emission, thermionic field emission and thermionic emission, the relative magnitude of each component being dependent on the temperature and the barrier height and thickness. In practice, electron transport can be considered as thermionic field emission within certain limits. For relatively high temperatures and wide barriers the first limiting case is pure thermionic emission over the top of the potential barrier. For relatively low temperatures and narrow barriers the second limiting case is pure field emission through the base of the potential barrier.

An appreciable recombination/generation current may

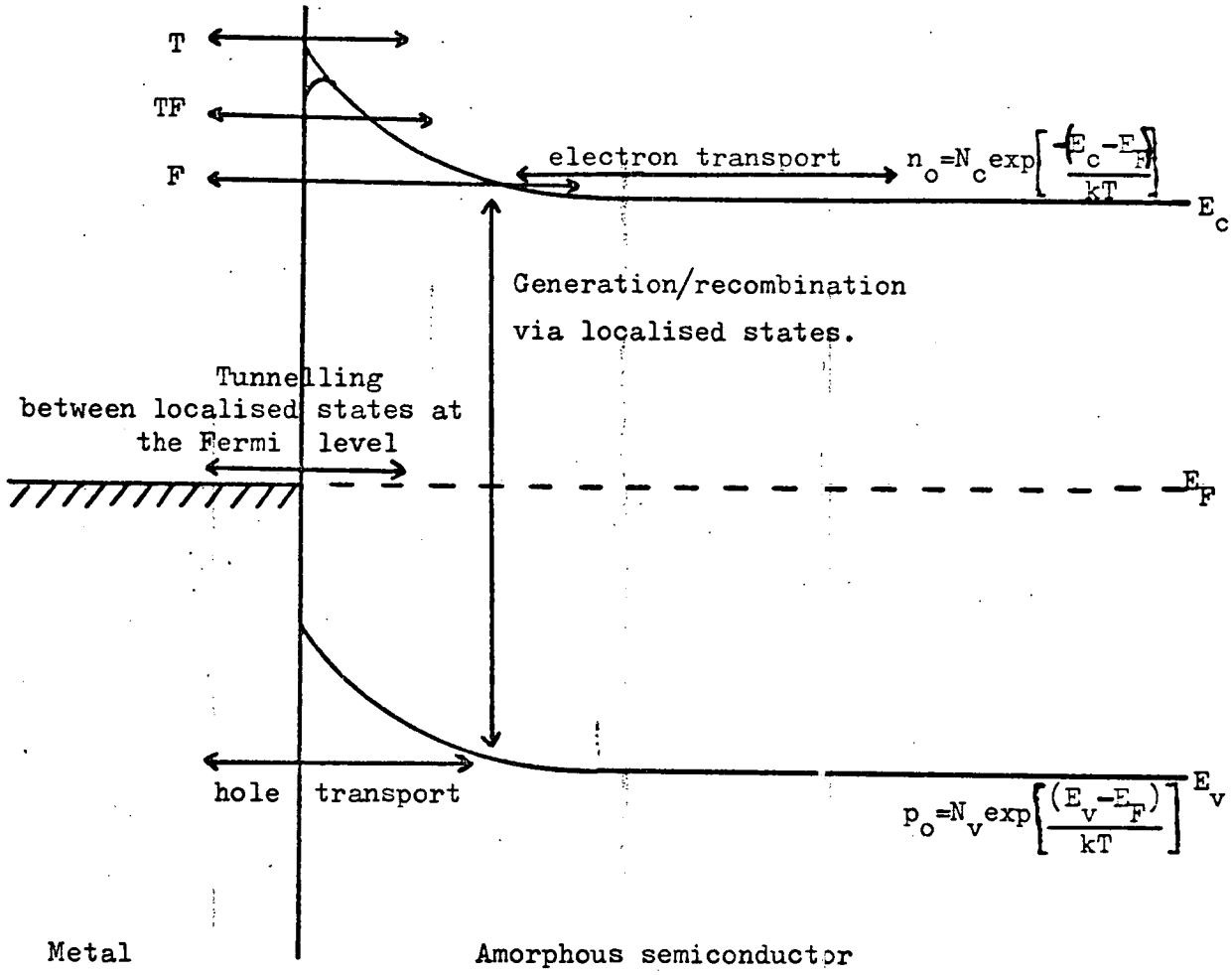

Figure 6.10 Transport processes in the metal-amorphous semiconductor contact.

T - Thermionic emission.

TF - Thermionic field emission.

F - Field emission.

flow for several reasons. Firstly, there is a large density of localised states present within the energy gap, providing a high density of recombination/generation centres. Secondly, the Fermi level in an amorphous semiconductor is close to the gap centre. Consequently the density of free electrons, n_o, in an amorphous semiconductor is approximately decreased by a factor of $\exp.\left[\frac{-(E_c-E_V)}{2kT}\right]$ and the density of free holes, p_o is increased by the reciprocal of this factor relative to the respective values in an extrinsic n-type crystal, as illustrated in Figure (6.1). Thus, the electron conductance in the bulk is no different from the hole conductance in the barrier region except for the difference in electron and hole mobilities. As the barrier width is generally small compared to the electrode separation, an appreciable difference in mobilities could exist without being noticeable. In addition, the accumulation of holes within the barrier region of Figure (6.10), and the increase in hole mobility due to the barrier field, could further increase the hole conductance in the barrier region.

Recombination/generation statistics may also be modified by a tunnelling process between states at the metal Fermi level, and localised states within the energy gap of the semiconductor. This does not imply that an appreciable hopping current will occur at the Fermi level in the bulk of the semiconductor. Hill[26] has estimated that the ratio of the probability of emission into extended states to the probability of hopping transport can be written,

$$P_{e/P_h} = \exp\left[\frac{-(E_i - \Delta E)}{kT} - 2\alpha R\right] \qquad (6.6.1)$$

where E_i is the energy required to excite the carrier into an extended state, ΔE is the incremental energy between traps at distance R, and α is the reciprocal localisation distance for a trap. Assuming a density of traps at the Fermi level $\simeq 10^{25} m^{-3}.eV^{-1}$ and a value for E_i concomitant with the data of Chapter 5, one would only expect hopping transport to dominate at temperatures of 100K (approximately) and below.

The thermionic field emission electron current may be significantly affected by image force lowering of the potential barrier caused by the high field strength within the space charge region. This form of barrier lowering assumes greater importance at higher temperatures as thermionic emission becomes proportionally more important. Below the top of the barrier, the high field strength could delocalise states adjacent to the mobility edges, effectively reducing the width of the barrier to thermionic field emission.

Finally, one must consider that the two-dimensional model of the metal-amorphous semiconductor contact may not be valid, as the space charge region may be too narrow for conventional assumptions to hold true, that is uniform charge distribution and equipotential surfaces parallel to the interface. Discrete localised charges in the barrier may cause strong potential fluctuations across the plane of the contact, allowing charge carriers to pass preferentially at certain spots. With a state density of

10^{25} centres $.m^{-3}$ the average separation of sites is approximately 47Å, which is not too different from the barrier width. Hence the barrier may be essentially heterogeneous, capable of injecting carriers of either sign at different locations.

6.7 The Effect of Tunnelling

As stated previously in this chapter the presence of a high density of localised states within the energy gap of the amorphous semiconductor leads to very thin potential barriers (< 100Å), and hence the effect of tunnelling current through the barrier may become significant. In order to estimate this contribution, tunnelling current flow through the barrier is calculated over a suitable range of temperature, using a simple model of thermionic field emission[27].

To apply this model certain assumptions are made. A simple parabolic barrier shape is assumed. Calculations by Stratton[28] on tunnelling through insulating films indicate that the shape of the barrier is not critical, the height and width of the barrier being the main factors. The impurity concentration is assumed independent of temperature, and the contribution of free electrons to the space charge density is assumed small compared to that of charge trapped in localised states. The effect of the image force lowering is neglected; the inclusion of an image force would increase the transmission probability, but where the transmission occurs principally by a combination of field and thermionic field emission the

error is minimal, as discussed further later in this section. Finally, the tunnelling effective mass is assumed independent of energy.

The potential energy diagram for a forward biased Schottky diode between a metal and an amorphous semiconductor is illustrated in Figure (6.11). The expression for the electron potential energy in the depletion region relative to the bulk is

$$q.V(x) = \frac{q^2.N.x^2}{2\varepsilon_s} \qquad (6.7.1)$$

for $o \leqslant x \leqslant w$, where x is the distance measured from the onset of the depletion region, width w, and N is density of localised states in the depletion region. Using the WKB approximation, the classical transmission probability is given by,[29]

$$\tau(E) = \exp -\frac{4\pi}{h} \int_{x_1}^{w} \left(2m^*.(qV(x)-E)\right)^{\frac{1}{2}}.dx \qquad (6.7.2)$$

$$\underline{\text{or}} \quad \tau(E) = \exp\left(-Q(E)\right) \qquad \text{for } E < E_B$$

$$\text{and} \quad \tau(E) = 1 \qquad \text{for } E > E_B$$

where m* is the effective mass of carriers in the direction of flow and E is the energy of the carriers associated with momentum normal to the interface. In order to calculate the total net current density, J, it is necessary to obtain the integral over the entire energy range of the flux of carriers flowing towards and away from the depletion region, J_F and J_R respectively, such that,

$$J = J_F - J_R = \frac{A^{**}T}{k} \int_o^{\infty} f_s(E).\tau(E).dE - \frac{A^{**}T}{k} \int_o^{\infty} f_m(E).\tau(E).d(E) \qquad (6.7.3)$$

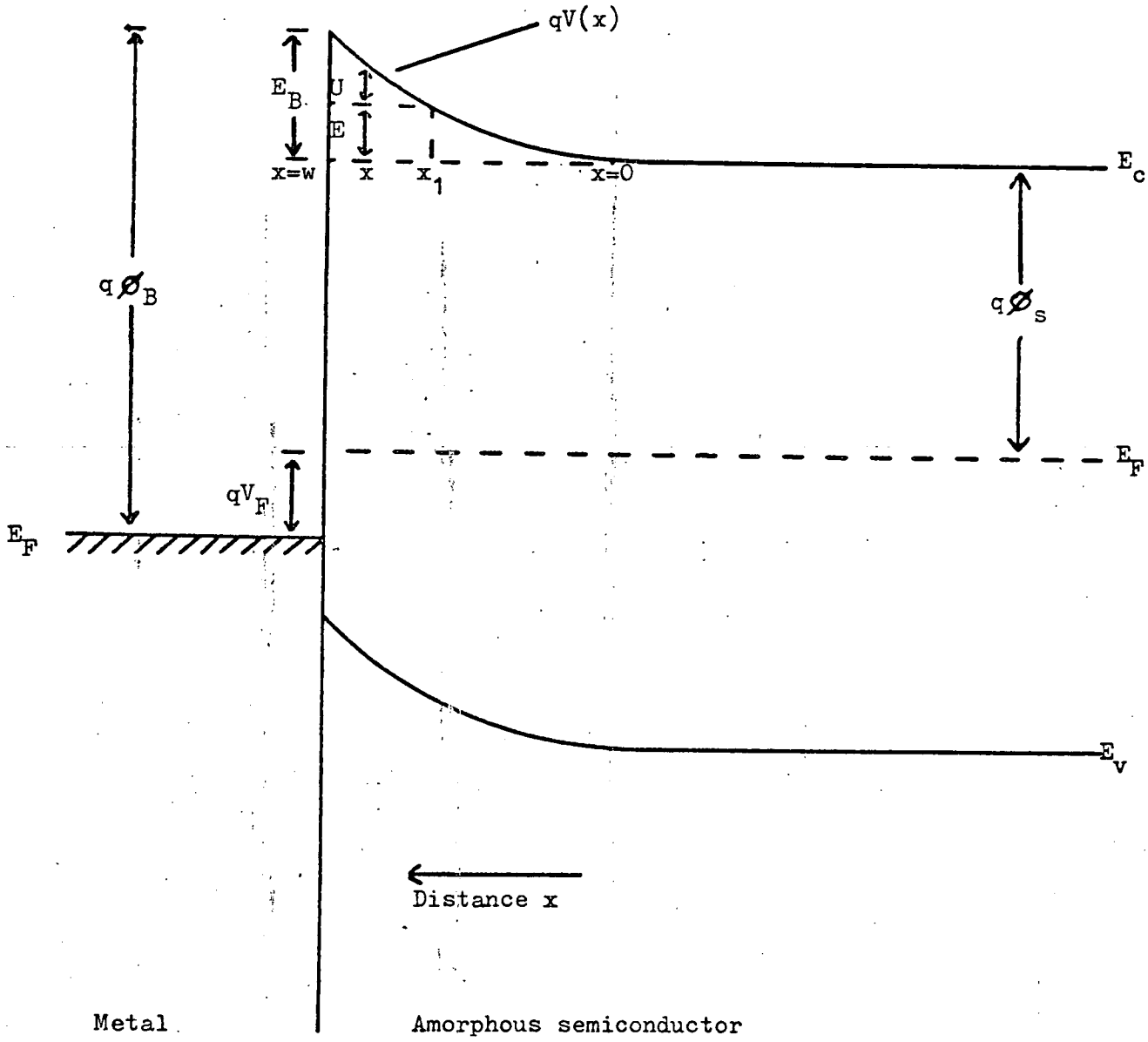

Figure 6.11 Potential energy diagram for forward-biased Schottky diode between metal and amorphous semiconductor:- Model for calculation of thermionic emission current.

where $f_s(E) = \exp\left[\frac{-(q\phi_s+E)}{kT}\right]$ and is the occupation probability for states of zero transverse energy in the semiconductor, and $f_m(E) = \exp\left[\frac{-(q\phi_s+E+V_F)}{kT}\right]$ and is the occupation probability for states of zero transverse energy in the metal, and A** is the effective Richardson constant. In order to normalise this expression, Crowell and Rideout[27] have introduced three parameters;

$$\text{(i)}\quad J_m = A^{**}T^2 \exp\left[\frac{-q\phi_s}{kT}\right] \qquad (6.7.4)$$

J_m is the flat band current density incident on the depletion layer associated with the Maxwell distribution of carriers.

$$\text{(ii)}\quad E_{oo} = 2q\left[\frac{N}{2\xi_s}\right]^{\frac{1}{2}}/\alpha \qquad (6.7.5)$$

where $\alpha = 2(2m^*)^{\frac{1}{2}}/\hbar$

E_{oo} is a material constant associated with the transmission of the barrier for carriers of energy E = O, and was first introduced by Padovani and Stratton.[30] This can be simplified to[27]

$$E_{oo} = 18.5.10^{-12} \cdot \frac{N}{m_r \xi_r} \cdot \text{eV} \qquad (6.7.6)$$

where m_r is the tunnelling effective mass measured in units of the free electron mass, ξ_r is the relative dielectric constant, and N is measured in $cm.^{-3}$

$$\text{(iii)}\quad E_B = q\,(\phi_B - \phi_s - V_F) \qquad (6.7.7)$$

where E_B is the amount of band bending at the interface, and V_F is the forward bias voltage. This is evident from Figure (6.11).

The mathematical formulation of the expression for the current-voltage characteristic is complex; the full process

is detailed in Reference (27). In the relatively high carrier concentration, low temperature range ($E_{oo} \gg kT$), carrier transport occurs via a combination of field and thermionic field emission,

$$J/J_m = \frac{J_{ma}}{J_m} \cdot \exp\left[\frac{-q(\phi_B-\phi_s)}{E_o}\right]\exp\left[\frac{qV_F}{E_o}\right].\left[1 - \exp\left[\frac{-qV_F}{kT}\right]\right] \quad (6.7.8)$$

where $E_o = E_{oo} \coth\left[\frac{E_{oo}}{kT}\right]$ (30)

and J_{ma} is the apparent normalised flat band current density. Computerised solutions for $\frac{J_{ma}}{J_m}$, a constant between 1 and 10, have been performed by Crowell and Rideout[27]. In the relatively low carrier concentration, high temperature range ($E_{oo} \leqslant kT$), carrier transport occurs via a combination of thermionic field and thermionic emission,

$$J/J_m = \frac{J_{ma}}{Jm}. \exp\left[\frac{-q(\phi_B-\phi_s)}{nkT}\right] .\exp\left[\frac{qV_F}{nkT}\right].\left[1 - \exp\left[\frac{-qV_F}{kT}\right]\right] \quad (6.7.9)$$

Computerised solutions of (J_{ma}/J_m) and n are again available[27]. Figure (6.12) illustrates the energy distribution of the transmitted carriers as a function of (kT/E_{oo}) and the barrier height, E_B[27].

In order to evaluate E_{oo} for $Ge_{10}As_{40}Te_{50}$, certain assumptions are made. The density of localised states in the depletion region is taken as $10^{25} m^{-3} eV^{-1}$ from the evidence of the field effect data in Chapter 7. The low frequency dielectric constant appropriate to materials of this type is approximately $\varepsilon_r = 10$[31-33]. The relative effective mass is taken to be $m_r = 0.2$, taken from calculations by Stratton[28] for triangular and parabolic

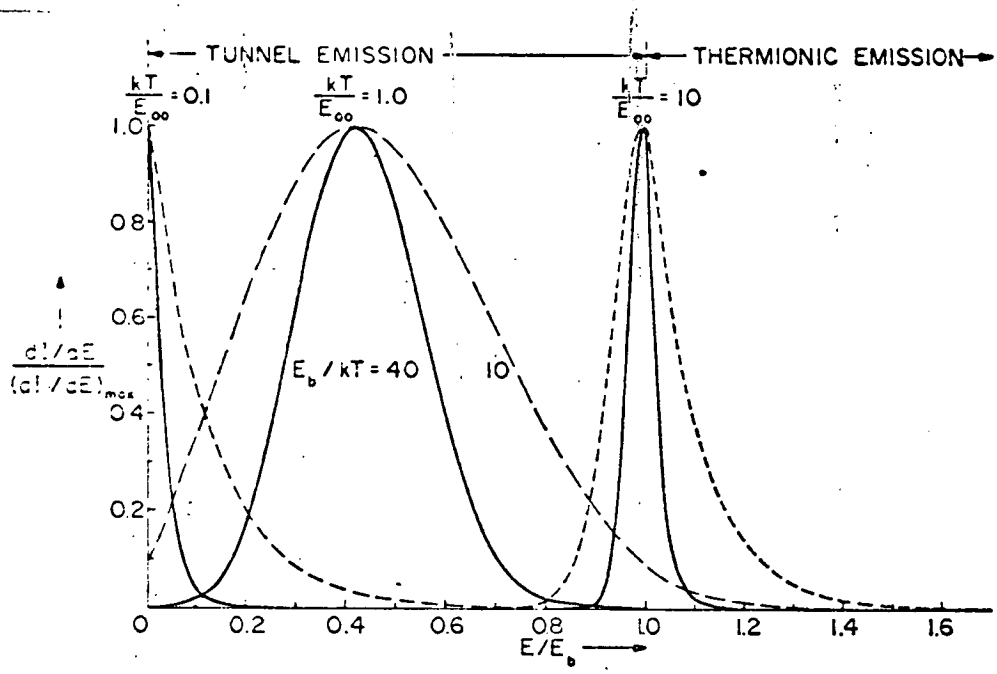

Figure 6.12 Normalised energy spectra of transmitted carriers as a function of kT/E_{oo} and E_B. (From Crowell and Rideout[27]).

barriers. Using these values, E_{oo} is calculated from Equation (6.7.6) to give,

$$E_{oo} \simeq 41.5 \text{ m eV}$$

This implies that $E_{oo} = kT$ at $T = 482K$, a temperature above the glass transition temperature for this particular chalcogenide alloy. Thus transport can be considered as a combination of thermionic field and field emission, and Equation (6.7.8) applies over the entire range of experimental data.

The zero field barrier height is $E_B = q(\phi_B - \phi_s)$ from an examination of Equation (6.7.7). This is equivalent to,

$$q\ V(w) = \frac{q^2 N . w^2}{2\varepsilon_s} \qquad (6.7.10)$$

from Equation (6.7.1), where w is the barrier width. Assuming $w = 74\text{Å}$ calculated from Equation (6.2.1), $q(\phi_B - \phi_s) = 0.495\text{eV}$.

To satisfy the thermionic field emission case, certain criteria must be considered. First of all, the maximum of the transmitted current, as illustrated in Figure (6.12), must occur below the top of the barrier (or more than $\Delta\phi$ below the top of the barrier where an image force is considered), otherwise a thermionic emission approach is more appropriate. This criterion is well satisfied for the metal-amorphous semiconductor contact at low bias values in the relevant temperature range. However, when the forward bias, V_f, exceeds the initial band bending this can no longer be the case, so that a maximum forward voltage limit, $V_{f\ max}$, is set

$$q\ V_{f\ max} = q\ (\phi_B - \phi_s) \qquad (6.7.11)$$

beyond which the barrier is essentially transparent.

Under reverse bias conditions, the maximum in the energy spectrum of the transmitted current must occur at an energy greater than the Fermi level in the metal by at least kT. The critical reverse bias for this condition is calculated to be[27]

$$V_{r\ max} = \phi_s + \phi_B . \sinh^{-2}(E_{oo}/kT) - (kT/q) . \coth^2(E_{oo}/kT) \quad (6.7.12)$$

For a reverse bias in excess of $V_{r\ max}$, transmission through the barrier is essentially pure field emission from the metal Fermi level into the conduction band of the semiconductor, and the treatment of Padovani and Stratton[30] becomes more applicable. However, as ϕ_s in amorphous semiconductors of this nature is far larger than the equivalent ϕ_s in an extrinsic n-type crystalline semiconductor, the treatment used here is applicable over a wide bias range.

Certain deficiences of this theory have been pointed out by Padovani[34]. He states that it is incorrect to use the WKB approximation to obtain the transmission coefficient expressed in Equation (6.7.2), which neglects image force lowering and the quantum mechanical reflection of carriers near the top of the barrier. When the potential energy peak of the barrier is quasi-parabolic, as happens under image force lowering, it is more appropriate to use the transmission coefficient of Kemble,[35]

$$\tau_k(E) = \left[1 + Q(E)\right]^{-1} \quad \text{for } E < E_B - \Delta\phi$$

$$\tau_k^1(E) = \left[1 + \exp(-Q(E))\right] = 1 - \tau_k(E) \quad \text{for } E \geq E_B - \Delta\phi$$

This fact was subsequently recognised by Rideout and Crowell[36] and included in a more complex theory. The effect of the inclusion of image force lowering and quantum mechanical reflection is to substantially increase the current when the maximum in the energy spectrum of transmitted current occurs near the top of the barrier; i.e. when the thermionic and thermionic field emission case applies. For the thermionic field and field emission case, where the maximum in the energy spectrum of transmitted current occurs at energies far below the barrier peak, the error is comparatively small. Chang and Sze[37] have computed an exact transmission coefficient considering both tunnelling and quantum mechanical reflection by solving the Schroedinger equation for the barrier potential profile, and note that for dopings in excess of $10^{22} m.^{-3}$ the WKB approximation including image force lowering is in good agreement with the simpler form, but that for lower doping levels an exact solution must be used. The use of Equation (6.7.2) in the amorphous semiconductor case may thus result in a slight underestimate of the magnitude of the transmitted current, but in view of the arguments presented above, this is negligible. The advantage of the use of the simpler theory is that solutions can be obtained by hand, rather than by complex computer solutions.

Padovani[34] has also objected to the failure of Crowell and Rideout[27] to use degenerate statistics, since in most practical crystalline semiconductors, field emission only occurs if the doping is high enough for the semiconductor to be degenerate at the temperature

considered. However, in the case of amorphous materials, the presence of a high density of localised states within the energy gap of the semiconductor leads to the formation of thin space charge layers, while the Fermi level remains approximately at the gap centre. Consequently non-degenerate statistics are probably applicable, within the limits set by Equations (6.7.11) and (6.7.12).

The computed thermal field emission characteristics for the metal-chalcogenide glass interface are illustrated in Figure (6.13)*. Figure (6.13(a)) illustrates the current-voltage characteristics at five different temperatures under forward bias conditions, while Figure (6.13(b)) illustrates the corresponding reverse bias characteristics. A comparison with the current-voltage characteristics of sandwich type devices, as illustrated in Figure (6.6) indicates that this mechanism in itself cannot be responsible for the negligible contact resistance of metal-chalcogenide glass-metal sandwich structures at low bias, although at contact potentials in excess of approximately 0.5V (for the stated parameters) the barrier becomes essentially transparent to tunnelling current of this nature. This is further discussed in Section (6.9). Theoretical calculations by Stöttzel and Kottwitz[38,39] confirm this conclusion. Using the simplest form of the WKB approximation, and treating the amorphous alloy-electrode interface as a Schottky barrier, they present calculations for the thermal field emission current as a function of barrier height and width, diffusion potential, Debye length, and temperature. Their

* from Eq. (6.7.8)

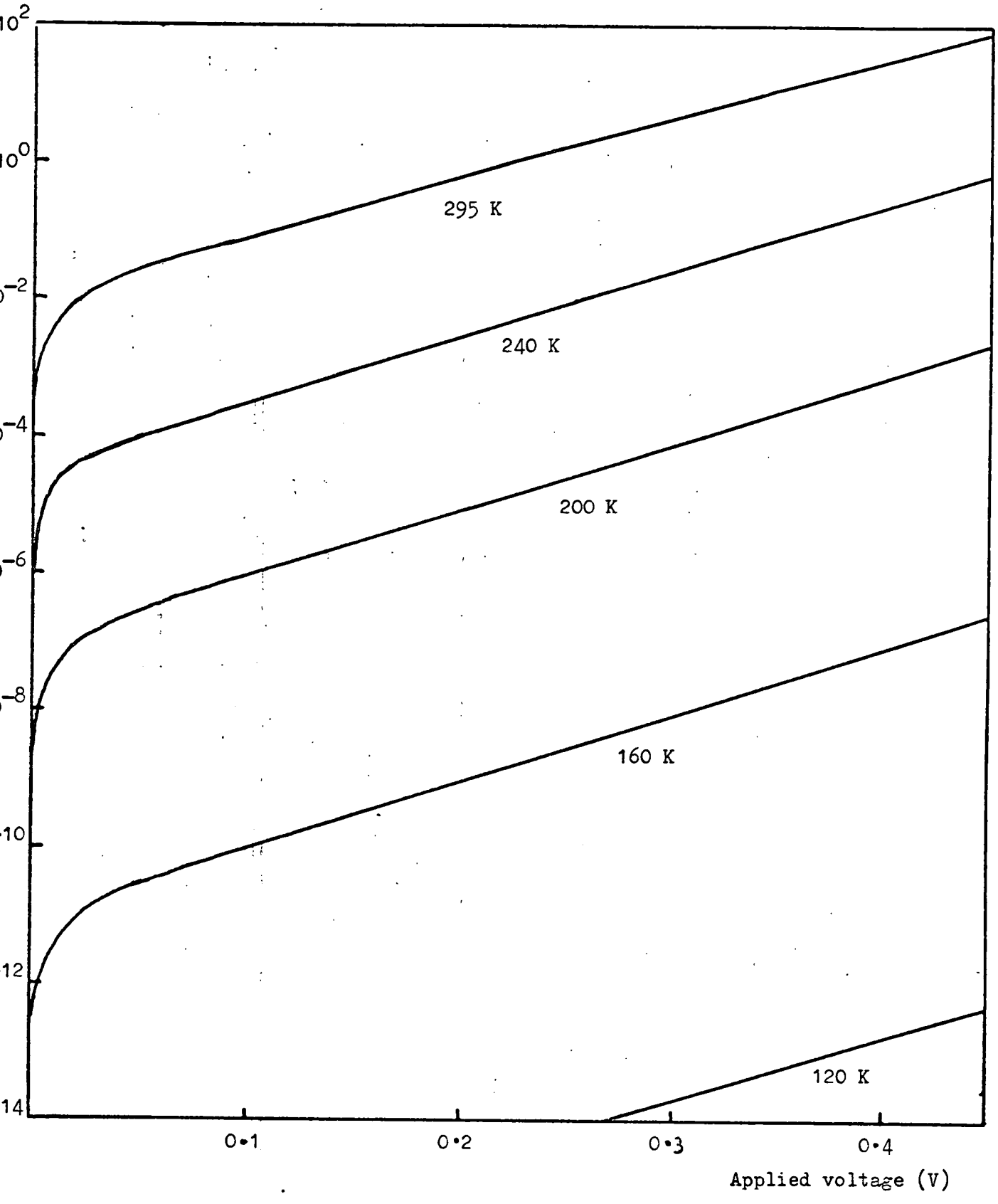

igure 6.13(a) Forward bias TF emission characteristics for the metal-$Ge_{10}As_{40}Te_{50}$ contact as a function of temperature.

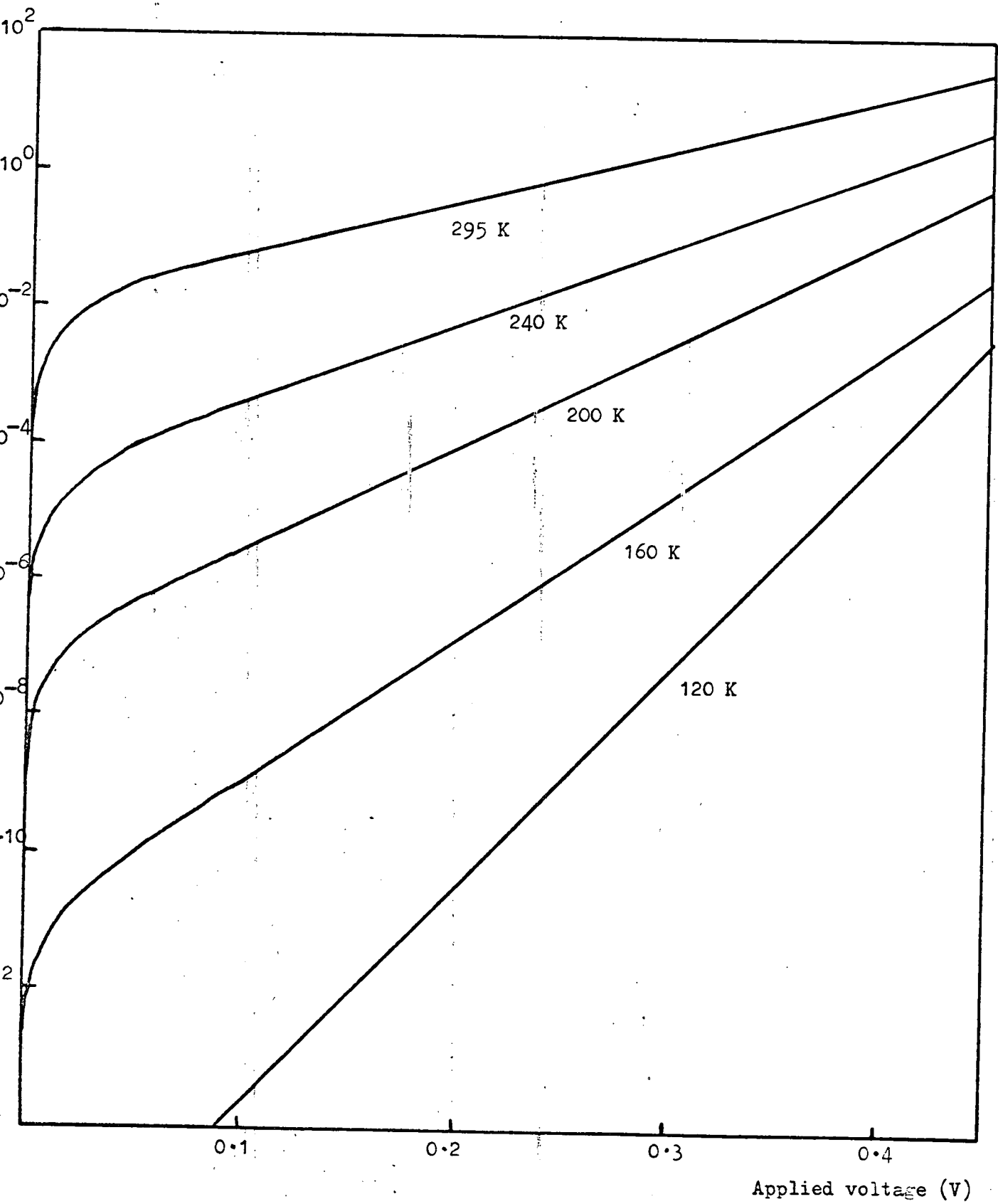

gure 6.13(b) Reverse bias TF emission characteristics for the metal–$Ge_{10}As_{40}Te_{50}$ contact as a function of temperature.

model predicts a rectifying characteristic and a high contact resistance at low field, at variance with the experimental data presented here.

6.8 Generation/Recombination Current

Whenever the thermal equilibrium condition of a physical system is disturbed, that is $pn \neq n_i^2$, where p and n are the densities of free holes and free electrons respectively and n_i is the intrinsic carrier concentration, the system can return to equilibrium by means of recombination/generation processes. Recombination and generation centres in semiconductor depletion regions can have a significant effect on the current-voltage characteristic. In general, these centres are most effective when located near the centre of the band gap, when communication between the conduction and valence bands through these centres tends to be greatest. The various recombination processes are depicted by the Sah-Noyce-Shockley [40] model, illustrated in Figure (6.14). Figure (6.14(a)) illustrates the direct band-to-band recombination case, where the transition of one electron from the conduction band to the valence band is made possible by the emission of a photon (radiative process) or by transfer of energy to another free electron or hole (Auger process). Figures (4.12(b)) and (4.12(c)) illustrate the single level and multiple level recombination cases respectively, where one or more trapping levels is present in the energy gap of the semiconductor. Single level recombination consists of four steps, viz; electron

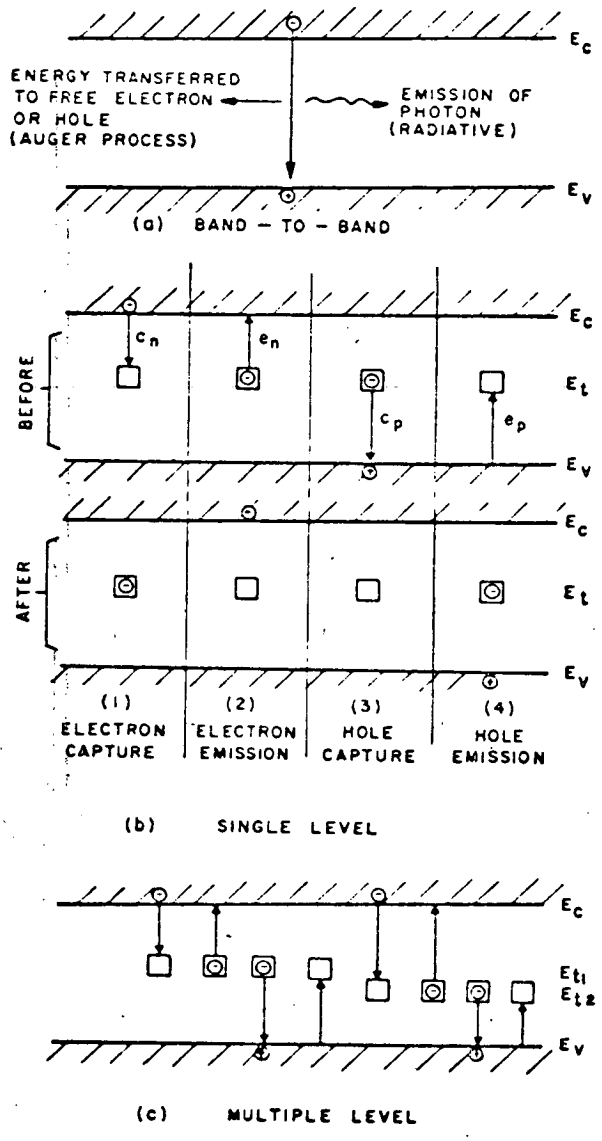

Figure 6.14 Recombination processes (From Sah et al[40], Sze[29]).

capture, electron emission, hole capture, hole emission. The recombination rate, U, for a single trapping level at energy, E_t, is given by;[40]

$$U = \frac{\sigma_p \cdot \sigma_n \cdot \upsilon_{th} \cdot (pn - n_i^2) \cdot N_t}{\sigma_n \left[n + n_i \exp\left[\frac{E_t - E_i}{kT}\right]\right] + \sigma_p \cdot \left[p + n_i \exp\left[\frac{-(E_t - E_i)}{kT}\right]\right]} \qquad (6.8.1)$$

where σ_p, σ_n are the hole and electron capture cross sections respectively, $\upsilon_{th} = \frac{3kT}{m^*}$ is the carrier thermal velocity, N_t is the trap density, E_i is the intrinsic Fermi level and the intrinsic carrier density $n_i = N_{c,v} \cdot \exp\left[\frac{-E_g}{2kT}\right]$, where E_g is the energy band gap.

In order to estimate the magnitude of the generation/recombination current at the metal-amorphous semiconductor contact, certain assumptions are made. Firstly, the metal-semiconductor junction is treated essentially like a p-n junction;[41] that is to say quasi-equilibrium exists across the depletion region with the metal Fermi level corresponding to the quasi-Fermi level for holes in the semiconductor. This situation is illustrated in Figure (6.15) for forward and reverse bias conditions. Secondly it is assumed that a single level of traps exists at the intrinsic Fermi level, with density $N_t = 10^{25} m^{-3} eV^{-1}$. This is artificial, in that one would expect to find a distribution of traps throughout the energy gap of the semiconductor, according to one of the models discussed in Chapter 2. The latter assumption may therefore produce a quantitative underestimate, but this should not effect the main qualitative argument proposed in Section (6.9). In

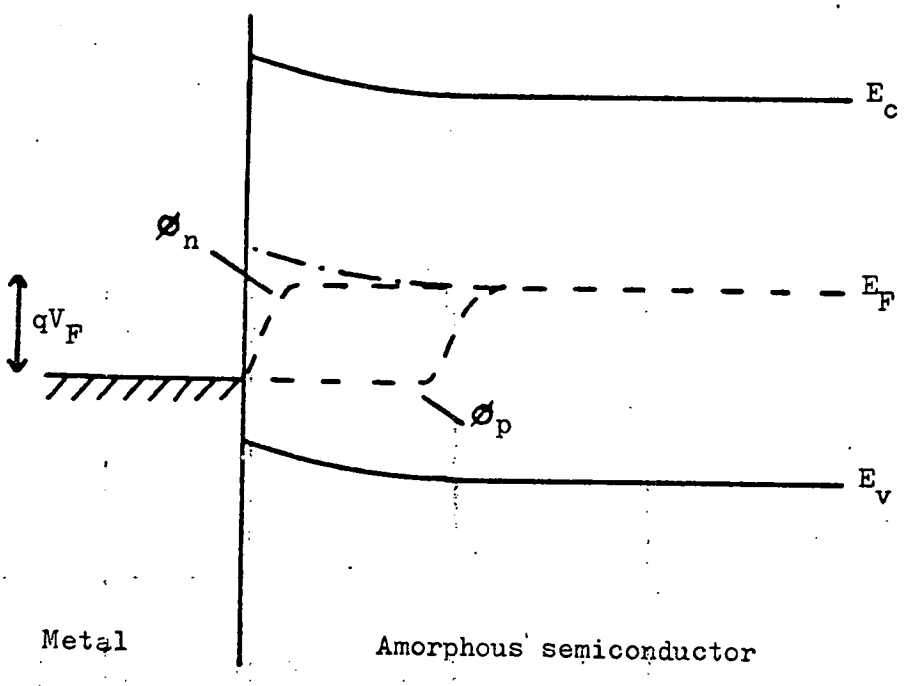

Forward bias.

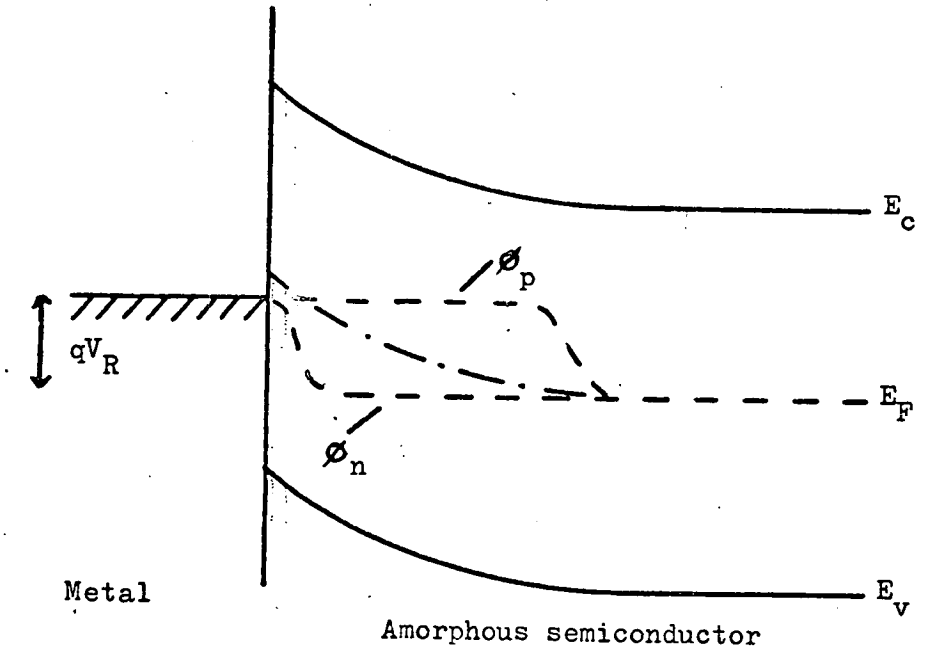

Reverse bias.

Figure 6.15 Potential energy diagram at metal-amorphous semiconductor contact:- Model for calculation of generation/recombination current.

addition, it is evident from Equation (6.8.1) that the generation/recombination centres are most effective when $E_t = E_i$.

From Figure (6.15) an expression for the pn product in Equation (6.8.1) can be written,

$$pn = n_i^2 . \exp\left[\frac{q(\phi_p-\phi_n)}{kT}\right] \qquad (6.8.2)$$

where ϕ_p and ϕ_n are the quasi-Fermi levels for holes and electrons respectively. Under reverse bias $q(\phi_p-\phi_n)$ is negative, hence $pn < n_i^2$, while under forward bias $q(\phi_p-\phi_n)$ is positive, hence $pn > n_i^2$. In fact, this can be written,

$$pn = n_i^2 . \exp(\frac{qV}{kT}) \qquad (6.8.3)$$

where $V = (\phi_p-\phi_n)$ is the junction potential difference. Under the assumptions, $\delta_p = \delta_n = \delta$, and $E_t \triangleq E_i$, Equation (6.8.1) reduces to

$$U = \frac{\delta . \upsilon_{th} . N_t . (pn-n_i^2)}{n+p+2n_i} \qquad (6.8.4)$$

Under high reverse bias, $V > \frac{3kT}{q}$ and $n_i^2 > pn$, the generation rate can be expressed,[40]

$$U = -\frac{n_i}{\tau_e} \qquad (6.8.5)$$

where the effective lifetime τ_e is given by,

$$\tau_e = \frac{2}{\delta . \upsilon_{th} . N_t} \qquad (6.8.6)$$

Under high forward bias, $p = n = n_i \exp\left[\frac{q(\phi_p-\phi_n)}{2kT}\right]$ from Equation (6.8.2), and $pn > n_i^2$. Hence Equation (6.8.3) reduces to an expression for the recombination rate,

$$U = \frac{n_i}{\tau_e} . \exp\left[\frac{qV}{2kT}\right] \qquad (6.8.7)$$

The total generation current density in the depletion region is found by integrating Equation (6.8.5) over the total width, w, such that,

$$J = \int_o^w q./U/.dx = \frac{qn_i w}{\tau_e} \qquad (6.8.8)$$

Similarily, the total recombination current density is found by integrating Equation (6.8.7),

$$J = \int_o^w q./U/.dx = \frac{qn_i w}{\tau_e} \exp\left[\frac{qV}{2kT}\right] \qquad (6.8.9)$$

To obtain solutions for Equations (6.8.8) and (6.8.9) it is necessary to know the value of the effective lifetime, τ_e. Unfortunately, as far as the author is aware, no such data exists for $Ge_{10}As_{40}Te_{50}$, but Main[42] has measured the photoconductive decay time, τ_{PD}, as a function of temperature for As_2Te_3 (Figure (16.3) in Ref.(42)). At low excitation levels, when the density of excess carriers is less that the density of thermally activated free carriers (i.e. $T > 200K$[42]), monomolecular kinetics apply characterised by a free recombination lifetime, τ_r, so that[42]

$$\tau_{PD} = \tau_r \times \frac{\text{trapped carriers}}{\text{free carriers}} = \tau_r \cdot \left[\frac{N_t . f_t}{n_i}\right] \qquad (6.8.10)$$

where f_t is the occupation probability for the traps. Below 200K, at relatively high excitation levels, bimolecular kinetics apply, and the behaviour of τ_{PD} has not been fully analysed. If it is assumed that the photodecay pattern in $Ge_{10}As_{40}Te_{50}$ follows a similar pattern to that in As_2Te_3, which is reasonable in view of

the many other similarities between the two materials, it is possible to deduce values for τ_e in Equations (6.8.8) and (6.8.9), as this is equivalent to τ_r in the notation of Main.[42]

The calculated characteristics for recombination and generation current density as a function of applied bias and temperature are illustrated in Figures (6.16) and (6.17) respectively. The barrier is again assumed parabolic in form, and of similar height and width to the model used in the previous section. Thus the generation current increases with applied reverse bias, as w increases with applied reverse bias, according to,

$$w = \left[\frac{2\varepsilon_s(E_B - V - kT/q)}{qN_t}\right]^{\frac{1}{2}} \qquad (6.8.11)$$

In the forward direction, the reduction in barrier width is dominated by the exponential term in Equation (6.8.9).

As will be demonstrated in the next section, this is a more likely mechanism to explain the absence of any appreciable contact resistance at low fields, the calculated current densities being greater than those calculated for the thermionic field emission process.

6.9 The Theoretical Current-Voltage Characteristics for Sandwich Devices

The complete current path through a metal-$Ge_{10}As_{40}Te_{50}$-metal sandwich device can be considered as a series combination of transport in the bulk and the depletion regions, transport in the depletion region being a parallel combination of the various mechanisms illustrated

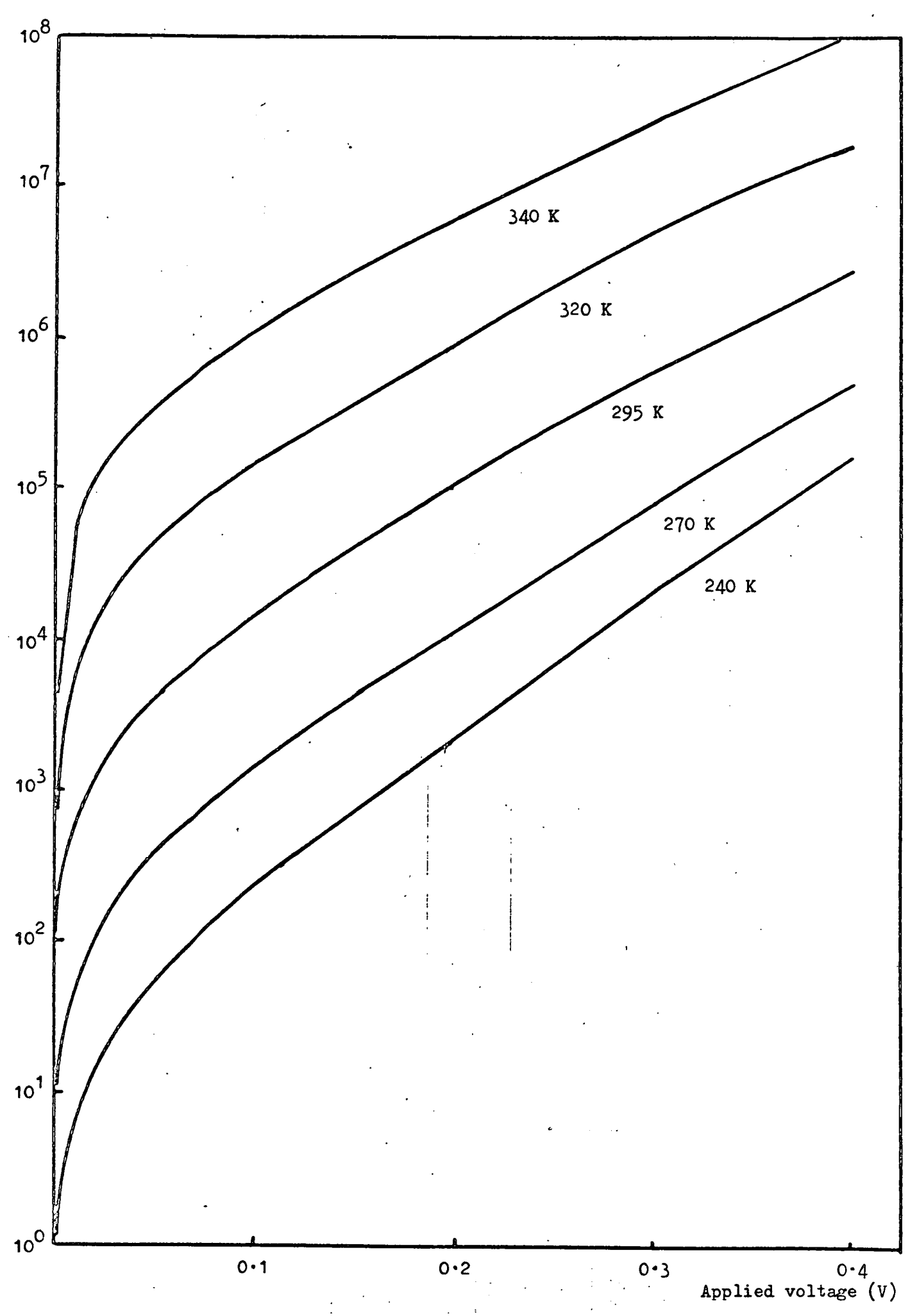

Figure 6.16 Forward bias recombination characteristics for the metal-$Ge_{10}As_{40}Te_{50}$ contact as a function of temperature.

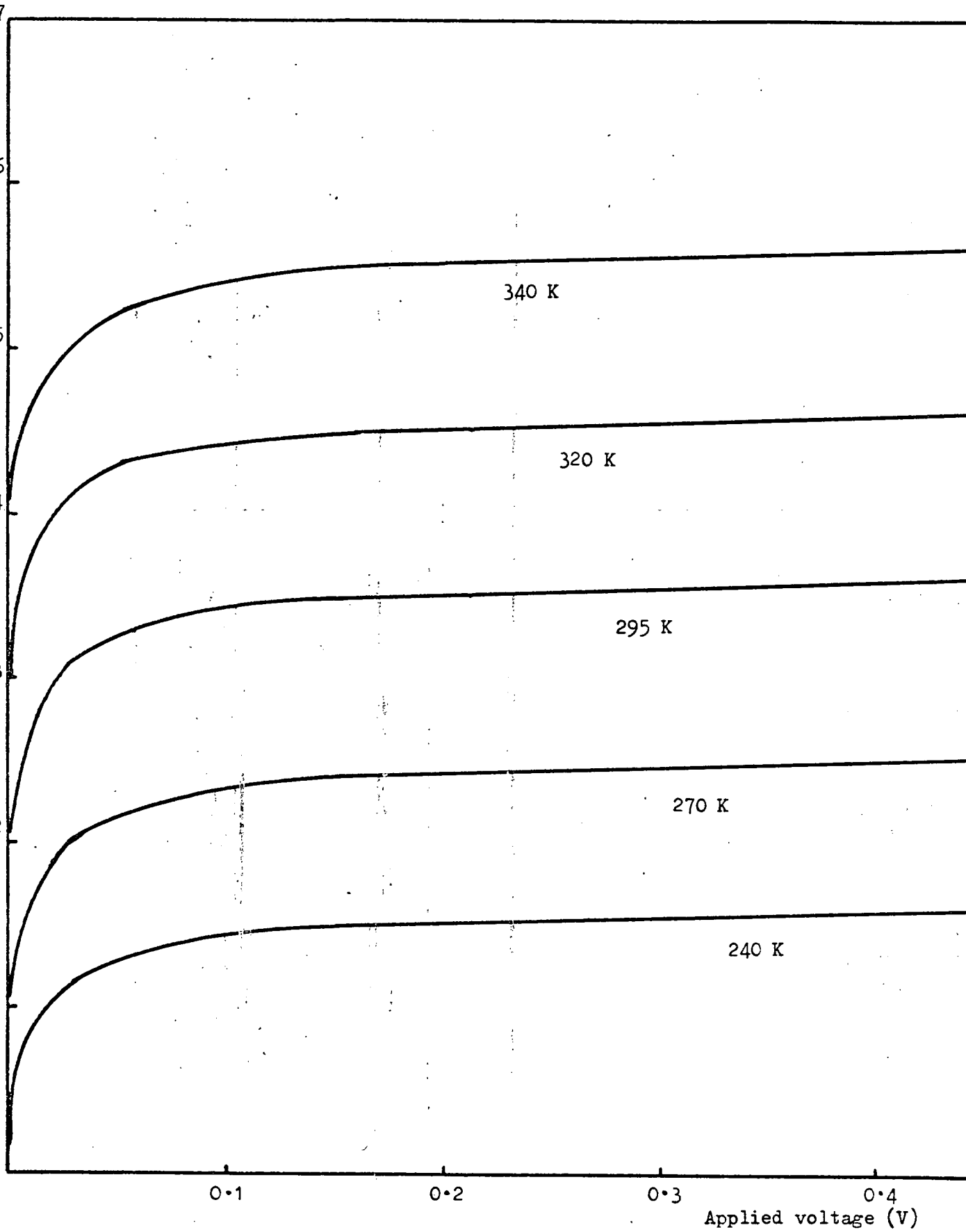

re 6.17 Reverse bias generation characteristics for the metal-$Ge_{10}As_{40}Te_{50}$ contact as a function of temperature.

in Figure (6.10). As an example, Figures (6.18) and (6.19) illustrate the relative magnitudes of the various current density components at 295K under forward and reverse bias respectively. The bulk characteristic is calculated assuming a 1 um. film with a conductivity, $\sigma = 3.10^{-4} Ohm^{-1}.m.^{-1}$, taken from the data of Chapter 5. The estimates of Figures (6.18) and (6.19) indicate that the dominant component of current transport through the depletion region is liable to be recombination/generation current rather than a thermionic field emission process, but no quantitative estimate is made of the effect of tunnelling to and from states at the metal Fermi level, and the effect such a process has on the recombination/generation statistics. However, it is evident from these calculations that one would not expect to observe a high contact resistance or rectification in the current-voltage characteristics of metal-$Ge_{10}As_{40}Te_{50}$-metal devices, a fact borne out by the experimental data, as the limiting factor in these characteristics is the bulk resistance of the glass film.

6.10 Capacitance-Voltage Measurements

A common method of obtaining information about barrier layers in conventional crystalline semiconductors is to measure the variation of capacitance with applied voltage, as discussed in Chapter 3. Experiments of this nature have been made on the same samples which were used for the current-voltage data described in Section (6.4), using the apparatus detailed in Section (4.3.3). Data for a typical sandwich device is illustrated in Figure (6.20).

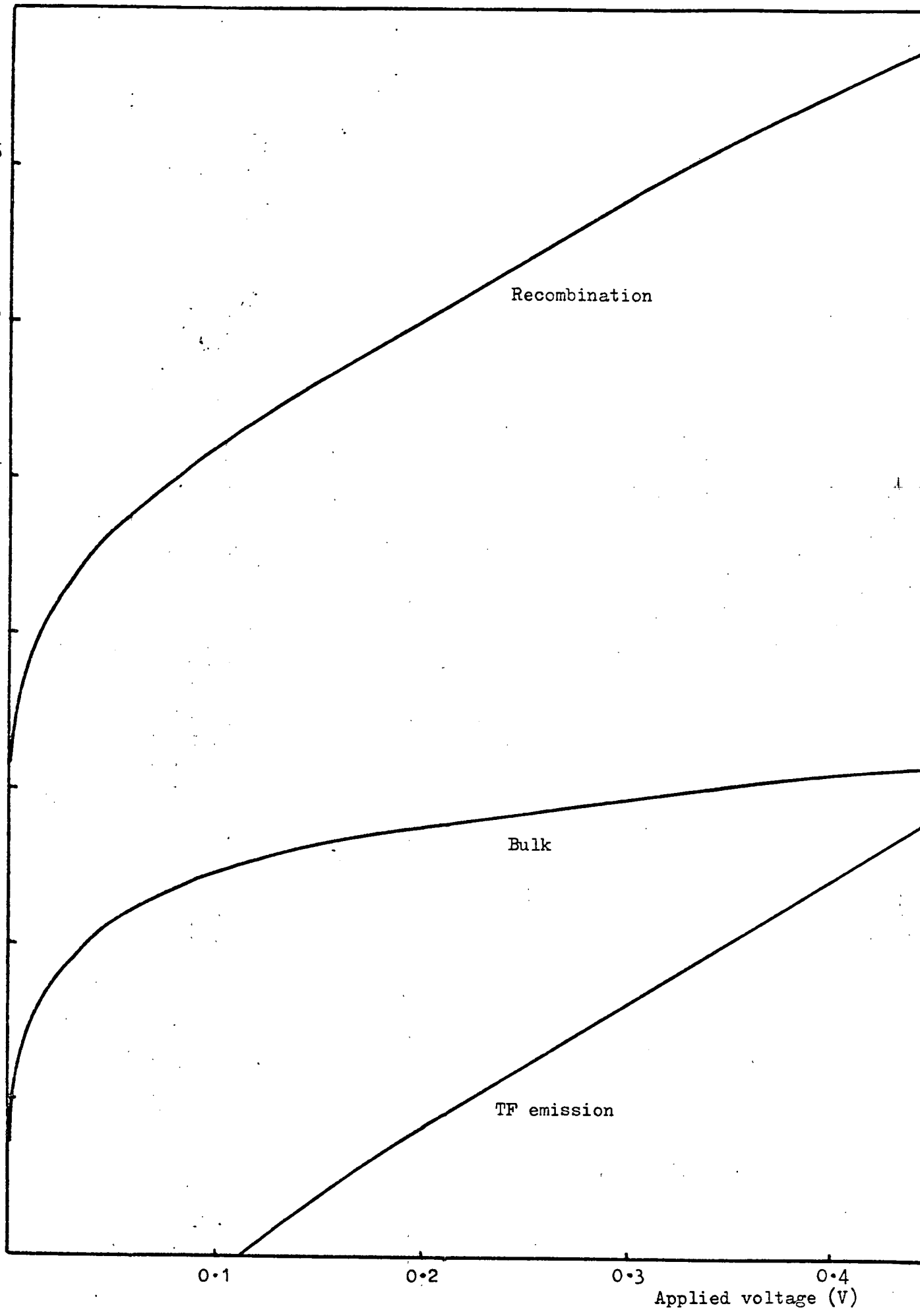

e 6.18 Comparison of the magnitudes of the various current density components through the metal-$Ge_{10}As_{40}Te_{50}$-metal sandwich device at 295 K.

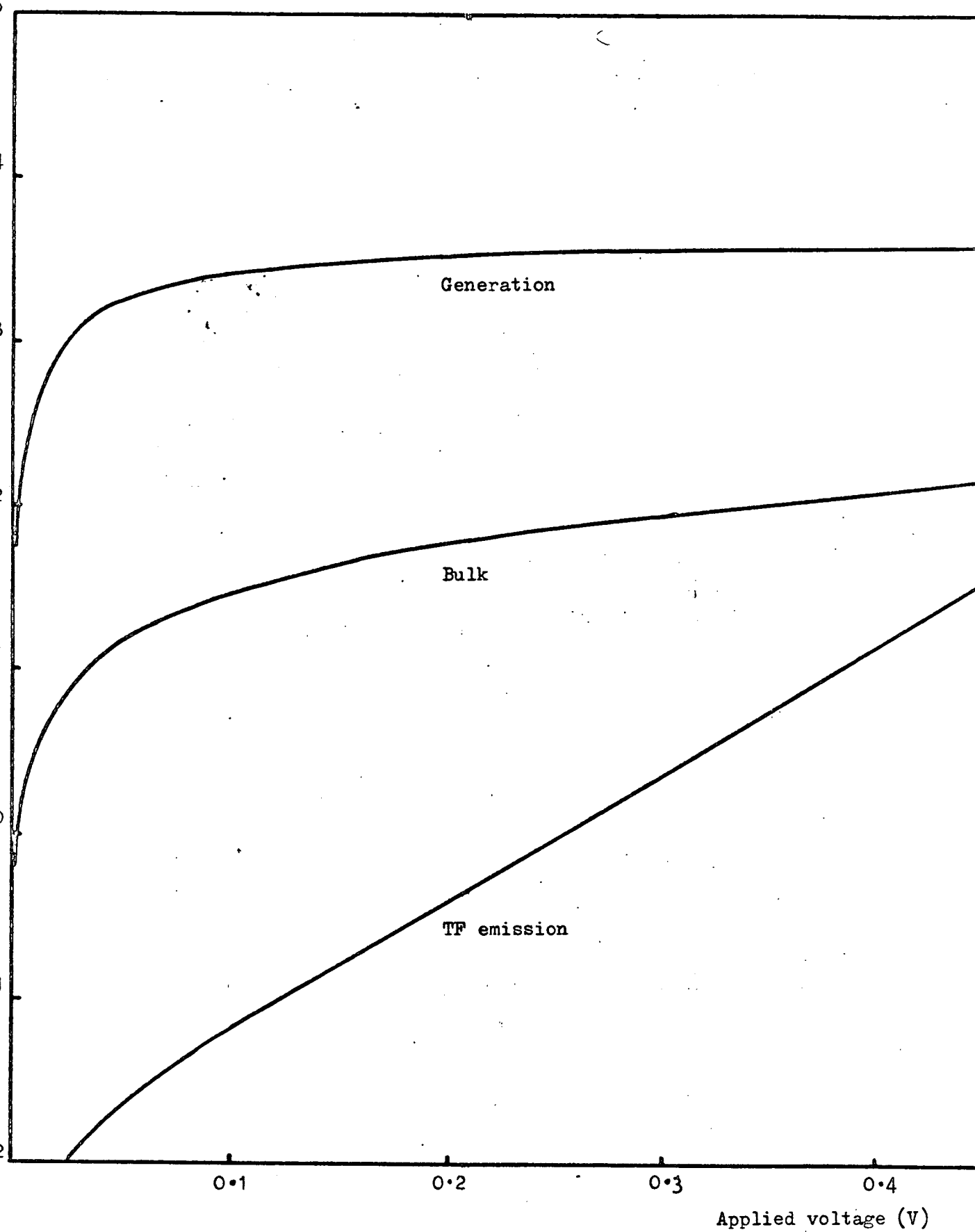

re 6.19 Comparison of the magnitudes of the various current density components through the metal-$Ge_{10}As_{40}Te_{50}$-metal sandwich device at 295 K.

(ii) Reverse bias.

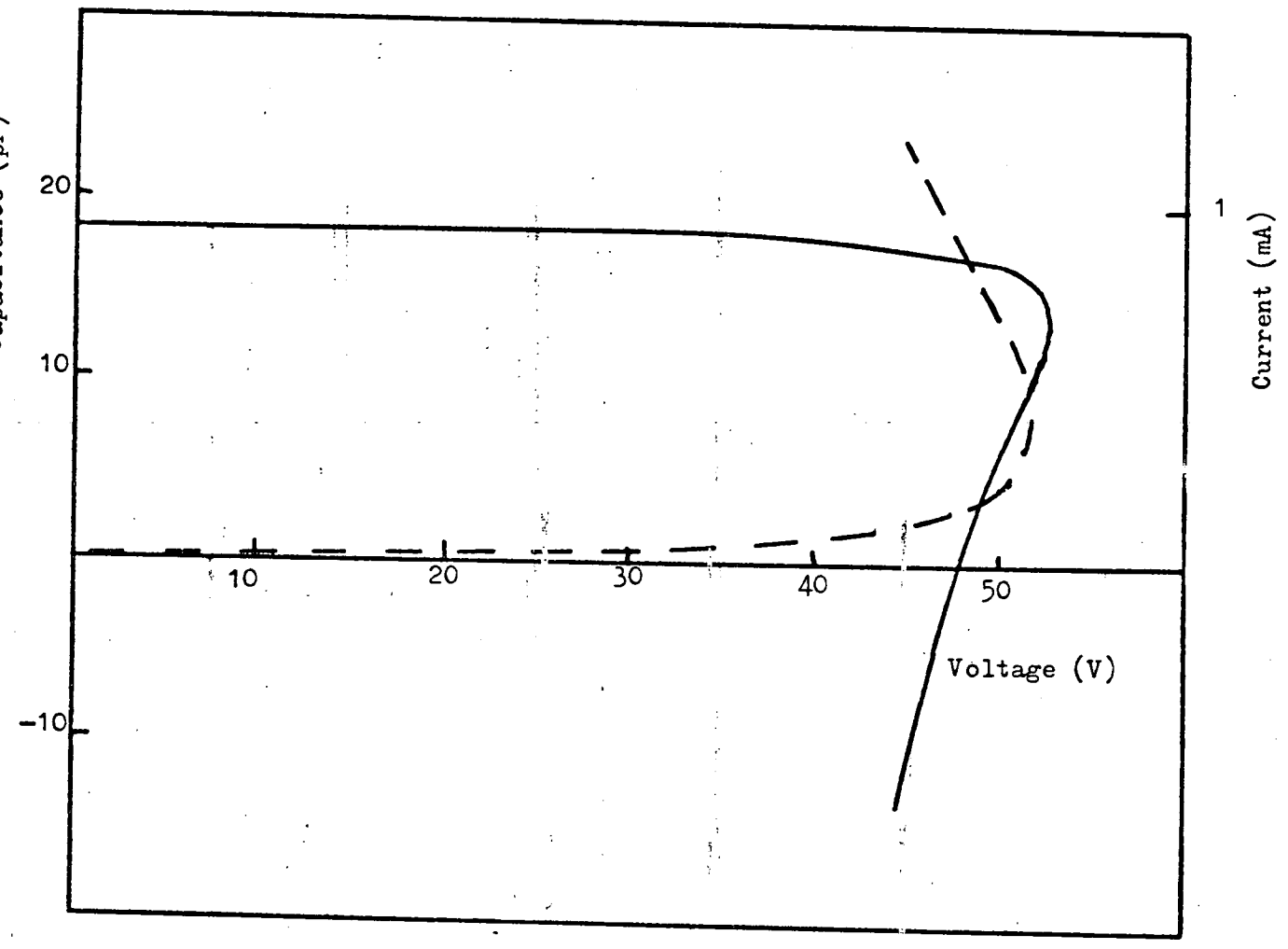

Figure 6.20 Capacitance-voltage and current-voltage characteristics of a thin-film $Ge_{10}As_{40}Te_{50}$ sandwich device at a temperature of 235 K, test frequency 140KHz. Full curve: capacitance. Broken curve: current.

The main characteristics are as follows;

(i) The current-voltage characteristic is of the form discussed in Chapter 5, the negative differential resistance region discussed in Section (5.6) being a noticeable feature.

(ii) The capacitance remains essentially constant over a wide range of applied bias. Just below the turnover point, the capacitance starts to fall slightly. At and after the turnover point the capacitance drops rapidly, becoming negative in some cases.

The absence of any capacitance variation with applied bias over a wide range is contrary to the type of behaviour illustrated in Figure (3.3(b)), and confirms the absence of highly resistive barrier layers adjacent to contacts. Rather, the measured capacitance is thought to be equivalent to the geometric bulk capacitance of the sample, a conclusion which is dealt with at greater length in the latter half of Chapter 7 when the full capacitance equivalent circuit of these devices is considered. The high field pre-switching "dip" has been observed elsewhere in chalcogenide alloy films[43,44] and can probably be explained by means of a thermal model, based on small-signal analysis of the heat conduction equation[45,46]. However, existing treatments assume that the electrodes are maintained at the ambient temperature, which precludes the existence of a region of negative differential resistance[47]. If a more realistic heat transfer condition is employed; i.e. the flow of heat out of the glass is a linear function of the temperature difference

across the boundary, a closer fit to the data of Figure (6.20) may possibly be obtained.

6.11 Discussion

Experimental evidence indicates the absence of blocking contacts on sandwich devices of a typical chalcogenide glass, $Ge_{10}As_{40}Te_{50}$, where metallic, non-oxidising electrodes are used. Where oxidising electrodes such as Al are used, a thin barrier layer of Al_2O_3 may be formed on the bottom electrode previous to deposition of the glass film, resulting in a device resistance (at low bias) considerably higher than those devices where non-oxidising electrodes are used. Limited data on coplanar devices with Au and Mo electrodes shows no evidence of a device resistance higher than the theoretical bulk resistance, nor the existence of a surface layer of higher resistivity than that of the bulk. In addition, measurements by the author on sandwich-type As_2Te_3 and $Si_{12}Te_{48}As_{30}Ge_{10}$ devices, and experimental evidence elsewhere in the literature indicate that this behaviour is fairly typical of a wide range of chalcogenide alloys.

Theoretical calculations of the approximate magnitude of the current transport processes in the barrier region agree that the current density through the device is limited by the bulk rather than the contact resistance. At low contact potentials ($<0.5V$) the dominant transport mechanism may be generation/recombination current in the depletion region, possibly coupled with tunnelling to and from states at the Fermi level, but at high contact

potentials (>0.5V) the barrier is essentially transparent to thermal emission (forward bias) or field emission current (reverse bias). In addition, potential fluctuations across the plane of the contact may cause carriers to flow preferentially at certain spots.

It is difficult to demonstrate the effect of contact resistance in chalcogenide devices, because of the relatively high bulk series resistance. In order to reduce the bulk resistance, one might use a fairly conducting glass, such as As_2Te_3, and attempt to produce films only a few hundred $\mathring{A}$ thick. However it was found difficult to produce continuous glass films of thickness less that 0.1 um. using the techniques described here, and even if this could be achieved it is unlikely that a contact resistance would be observed, as the magnitude of the theoretical current density through the depletion regions has most likely been underestimated.

7.1 Introduction

Measurements of the field-effect modulated conductance in a variety of chalcogenide glasses[1-6], and in other amorphous materials, notably Si[7-10] and Ge[11], have been performed in the hope of obtaining a better understanding of the density and distribution of localised states within the band gap of the semiconductor concerned. In the first half of this chapter experimental data is presented on the field-effect modulated conductance of thin films of $Ge_{10}As_{40}Te_{50}$ and $Si_{12}Te_{48}As_{30}Ge_{10}$ as a function of applied gate voltage and temperature, and a possible interpretation , based on the analysis of Barbe[12], is considered, which takes into account the effects of surface states and bulk states within the space charge region. It has also been proposed[13] that measurement of the change in surface capacitance with applied field would prove a useful tool in the investigation of the energy spectrum of localised states in amorphous materials. In the latter half of this chapter, an expression for the variation of state density with energy in terms of the variation of the measured capacitance of metal-insulator-semiconductor-metal (MISM) devices is derived, but it is shown that this is only applicable when the surface conductivity is significantly lower than the bulk conductivity. Measurements of the variation in capacitance of MISM and metal-semiconductor-metal (MSM) devices with frequency considered with the data of Chapter

6 suggest that this is not the case with these materials.

7.2 Measurements of the Field-Effect Conductance

Using the sample configuration and experimental techniques outlined in Chapter 4, the change in steady-state current between the coplanar electrodes was monitored at successive increments of applied gate voltage. Figures (7.1) and (7.2) show typical data for $Ge_{10}As_{40}Te_{50}$ and $Si_{12}Te_{48}As_{30}Ge_{10}$ devices respectively. Certain factors are immediately apparent:-

(i) The increase in the measured current observed on application of a negative gate voltage is relatively small compared with that of crystalline semiconductors (see for example Many et al.[14]). This suggests that modulation of the surface potential is slight, and that a high density of localised states is present within the gap.

(ii) Under negative bias conditions, the monotonic rise in the drain-source conductance may be concomitant with an absence of any strong feature in the localised state distribution over the sampled energy range. However, this does not imply that no such features exist, as the modulation of the surface potential is very small, and the conditions at the surface may not be representative of the bulk.

(iii) Under positive bias conditions, there is a slight decrease in drain-to-source conductance, but this tends to saturate at gate voltages in excess of about 100V, there being no evidence for the development of an inversion layer. The data of Figures (7.1) and (7.2) indicate that

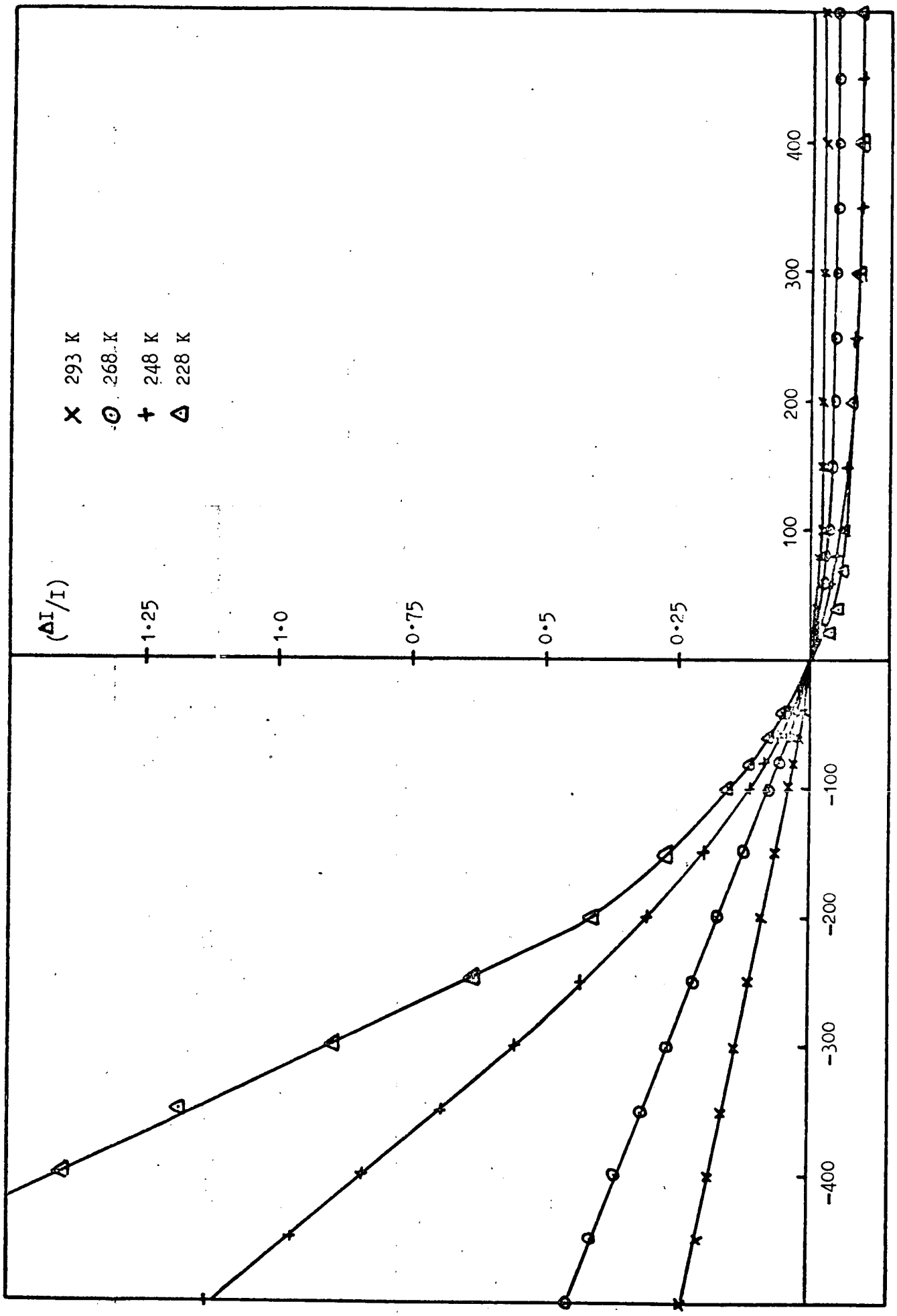

Figure 7.1 Field effect conductance data for a $Ge_{10}As_{40}Te_{50}$ device.
$Ge_{10}As_{40}Te_{50}$-0·48um; As_2S_3-4um.

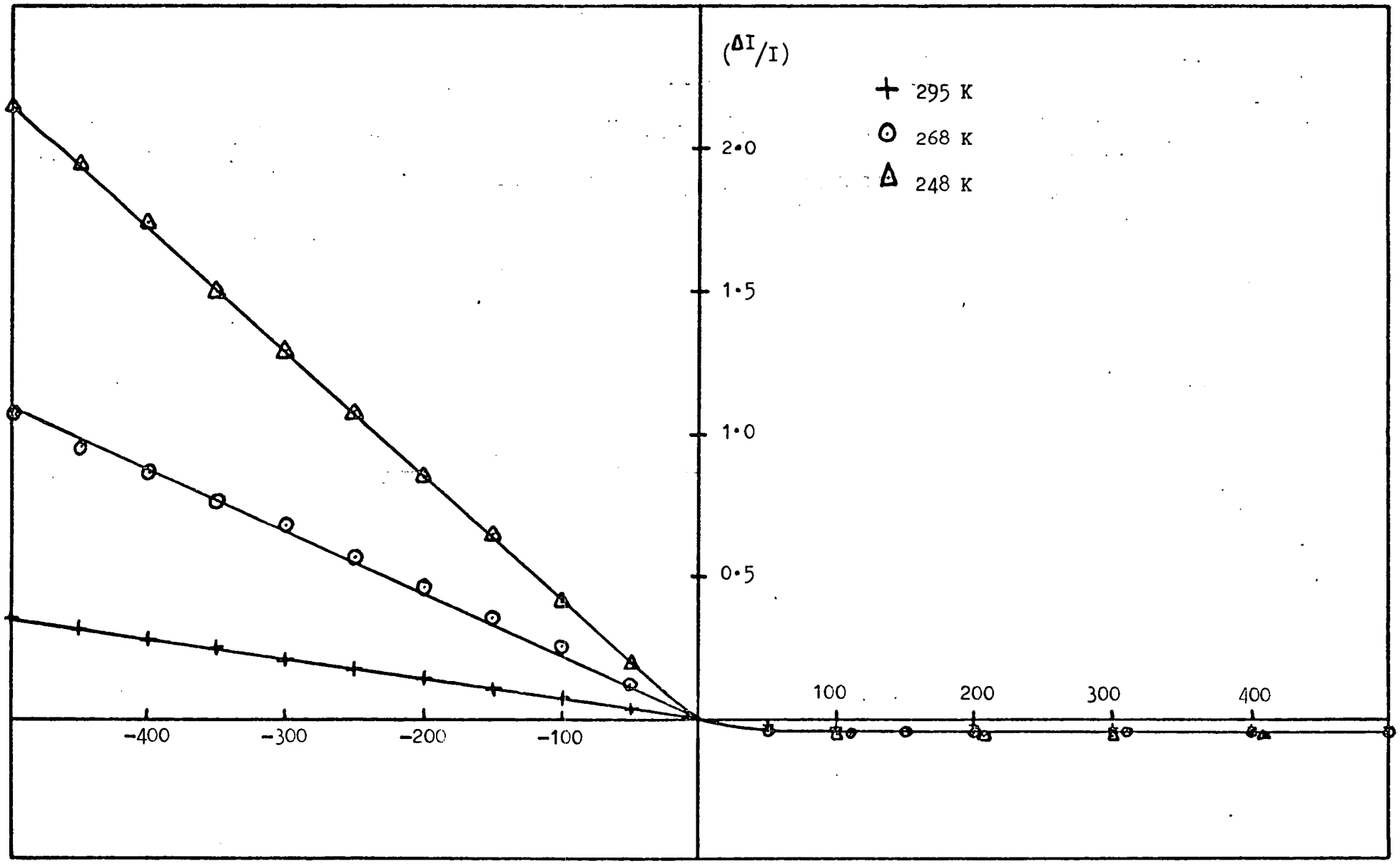

Figure 7.2 Field effect conductance data for a $Si_{12}Te_{48}As_{30}Ge_{10}$ device. $Si_{12}Te_{48}As_{30}Ge_{10}$ -0·85um; As_2S_3 -3·8um.

the conduction in the surface channel of these materials is primarily by hole transport, at least in this temperature range.

(iv) The data on the two alloys is very similar, and also resembles closely the reported data on other chalcogenide alloys.[1-6] Therefore it is reasonable to suppose that all these materials have certain common features.

7.3 Theory of the Field-Effect in Chalcogenide Alloys

At this time, two principal models exist for the analysis of the field-effect in amorphous materials, that due to Spear and Le Comber[7] and that due to Barbe.[12] The former analysis was developed to interpret the experimental data obtained from amorphous silicon specimens, and includes several assumptions necessary to provide a mathematically workable model:-

(i) The energy distribution of localised states in the surface region is assumed to be substantially the same as the bulk localised state distribution.

(ii) All the induced charge in the surface layer falls into localised states, thus neglecting the space charge of the free carriers.

(iii) Zero-temperature trap occupation statistics are used.

(iv) The accumulation/depletion region has a square potential distribution.

(v) The density of localised states is assumed constant over successive incremental energy 'steps', corresponding to successive step increases in the applied gate voltage.

Briefly, the width of the accumulation/depletion region is obtained from a solution of Poisson's equation,

and the displacement of the Fermi level at the surface from the flat-band position is calculated at successive voltage increments. Under the assumption that the Fermi level is several kT from the band edges in a non-degenerate semiconductor, Maxwell-Boltzmann statistics are used to calculate the density of mobile carriers in the surface layer, such that the measured increase in conductance depends exponentially on the shift in the Fermi level. An iterative procedure is used to calculate the density of localised states at various energy levels within the gap.

Spear and Le Comber[7] estimated that space charge regions of the order of 1000 Å were being probed in their experiments on amorphous silicon, but in chalcogenide thin film devices of the type employed here, the width of the space charge region is less than 100 Å, as discussed in Chapter 6. Therefore, it becomes less likely that a representative distribution of bulk localised states is being sampled, and it is increasingly important to consider the effects of interface states. The theoretical treatment of Barbe[12] also assumes zero-temperature trap occupation statistics, and the induced charge is likewise assumed to fall entirely into localised states. Maxwell-Boltzmann statistics are again used, predicting an exponential increase in the measured surface conductance with the shift in surface potential. In this case, however, Barbe assumes that the density of localised bulk states and the density of surface states are approximately constant at the Fermi level, and Poisson's equation is solved to depict an exponential potential distribution, with an associated

screening length, λ. In the following pages, the essentials of Barbe's theory are presented, refined slightly to allow calculations of the variation in localised state density with displacement from the equilibrium Fermi level.

Figure (7.3(a)) illustrates the potential energy distribution at the surface of an amorphous semiconductor in the flat-band condition. On application of a positive gate voltage, V_g, say, a number of localised states will cross the Fermi level and change their occupancy from empty to full, bending the bands at the surface downward by an amount y_s, in units of kT. This situation is illustrated in Figure (7.3(b)). The space charge density as a function of distance into the semiconductor, $\rho(x)$, can be expressed in arbitrary units of energy, E,

$$\rho(x) = -kTq \int_o^{y(x)} N(E).dE \qquad (7.3.1)$$

where y(x) is the amount of band bending at a distance x into the semiconductor, also in units of kT, and N(E) is the density of bulk localised states at energy E within the space charge region. Using the assumption of a slowly varying density of states function over the energy range, this reduces to,

$$\rho(x) = -kTq.N(E).y(x) \qquad (7.3.2)$$

This simplication facilitates a solution of Poisson's equation to obtain the exponential form,

$$y(x) = y_s.\exp(-x/\lambda) \qquad (7.3.3)$$

where,

$$\lambda = \left[\frac{\varepsilon_r \varepsilon_o}{q^2 N(E)}\right]^{\frac{1}{2}} \qquad (7.3.4)$$

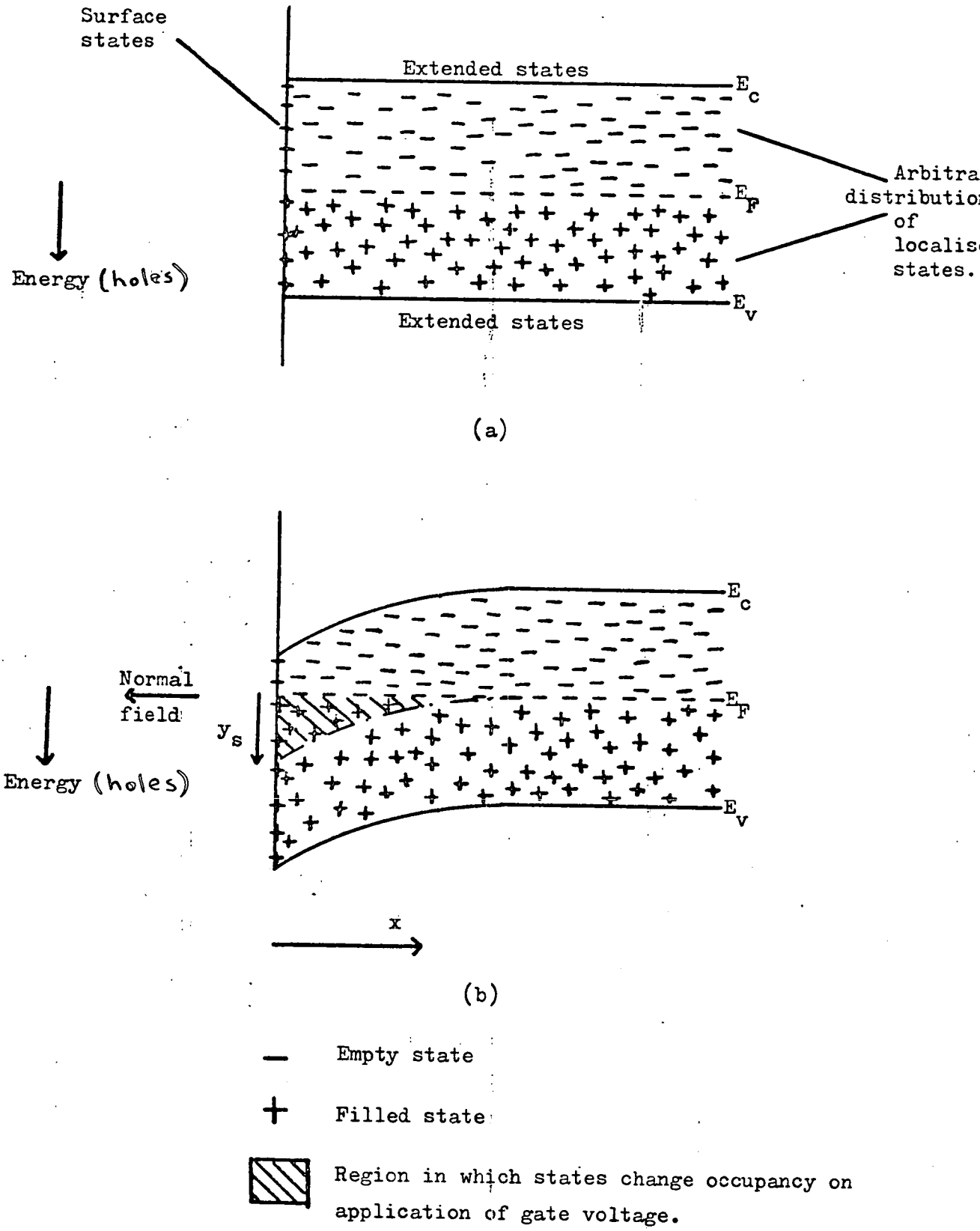

Figure 7.3 Potential energy distribution at the surface of an amorphous semiconductor.

(i) Flat band condition.

(ii) Applied gate voltage.

and ε_r is the dielectric constant of the amorphous material and ε_o is the permittivity of free space. This expression is identical to Equation (6.2.1).

In order to express the relationship between y_s and V_g, an examination of the characteristics of the space charge region is required. The induced charge is considered as falling partly into surface states and partly into localised states within the surface region. The space charge per unit area in the semiconductor, Q_{sc}, is given by Gauss's law,

$$Q_{sc} = - \frac{\varepsilon_r \varepsilon_o kT}{q \lambda} \cdot y_s \qquad (7.3.5)$$

and the space charge per unit area in surface states, Q_{ss}, is given by,

$$Q_{ss} = -kTq.N_{ss}(E).y_s \qquad (7.3.6)$$

where N_{ss} is the surface state density. The total charge induced into the semiconductor by action of the gate is,

$$Q_{induced} = Q_{sc}+Q_{ss} = -C_g.V_g. \qquad (7.3.7)$$

assuming the insulator capacitance C_g is equal to the equivalent capacitance of the device. This is readily seen to be a valid assumption for the insulators of thickness $\triangleq$ 5 um used here, if typical magnitudes are inserted for the capacitance due to Q_{sc} and Q_{ss}. This is discussed further in Section (7.5). Combining Equations (7.3.5), (7.3.6) and (7.3.7), y_s is expressed,

$$y_s = C_g.V_g \Big/ \left[\frac{\varepsilon_r \varepsilon_o kT}{q} \left[\frac{1}{\lambda} + \frac{q^2 N_{ss}}{\varepsilon_r \varepsilon_o} \right] \right] \qquad (7.3.8)$$

Finally, Barbe relates the measured change in conductance to the surface band bending, y_s, and hence the applied gate voltage, V_g. The change in the conductance of the film, ΔG, from the flat band conductance, G(o), to the bent band conductance $G(y_s)$, is given by

$$\Delta G = G(y_s)-G(o) = q.(\mu_n.\Delta n + \mu_p.\Delta p) \qquad (7.3.9)$$

where μ_n and μ_p are the electron and hole mobilities respectively, and Δn and Δp are the corresponding excess carrier concentrations. Using the Maxwell-Boltzmann approximation, these can be expressed,

$$\Delta n = \int_o^\infty n_b(e^{y(x)}-1).dx \qquad (7.3.10)$$

$$\Delta p = \int_o^\infty n_b(e^{-y(x)}-1).dx \qquad (7.3.11)$$

where n_b is the intrinsic bulk density of mobile electrons. As the Fermi level is situated approximately at the gap centre, this is considered equal to the intrinsic bulk density of holes. Equations(7.3.10) and (7.3.11) can be expressed as an integral with respect to y, rather than x, in which case

$$\Delta n = -\int_o^{y_s} n_b.(e^{y(x)}-1).\frac{dx}{dy}.dy = \lambda\int_o^{y_s} \frac{n_b(e^{y(x)}-1).dy}{y} \qquad (7.3.12)$$

since $\frac{dy}{dx} = \frac{-y}{\lambda}$ from the differential form of Equation (7.3.3). Similarily

$$\Delta p = \lambda\int_o^{y_s} \frac{n_b(e^{-y(x)}-1).\ dy}{y} \qquad (7.3.13)$$

Substituting these last two equations into Equation (7.3.9), Barbe[12] obtains an expression for the measured change in

conductance,

$$\Delta G/_{G(o)} = \frac{\lambda}{t} \sum_{n=1}^{\infty} \frac{y_s^{2n}}{(2n)(2n)!} = \frac{\lambda}{t} \cdot S \qquad (7.3.14)$$

where t is the thickness of the chalcogenide film. Calculations of the series S are obviously complex, but it has been summed with the help of a digital computer[12].

It is now possible to obtain an estimate of the average density of localised states over an energy range between $y_s = o$ and $y_s = f(V_g)$ from a comparison of Equations (7.3.14) and (7.3.8). It is probable that both bulk states and surface states are concerned, but as it is impossible to ascertain the relative importance of these factors, separate calculations have been performed, firstly neglecting surface states, and secondly, assuming all the induced charge falls into surface states. This at least allows an estimate of the relevant magnitudes involved. In order to obtain the variation of state density with energy, calculations of $N(E)$ and $N_{ss}(E)$ are performed for successively larger values of V_g, and it is necessary to subtract from the calculated total average state density the sum of the previously calculated incremental state densities. This is expressed mathematically,

$$N_r . \Delta y_{sr} = N_{ave.} y_s(V_g) - \sum_{i=o}^{i=r-1} N_i . \Delta y_{si} \qquad (7.3.15)$$

where $N_{ave.}$ is the calculated average density of states between $y_s = o$ and $y_s = y_s(V_g)$, N_r and Δy_{sr} are the state density and the shift in surface energy over the r^{th} step, and N_i and Δy_{si} are the state densities and the shifts in surface energy for the preceding steps. However,

as the value of y_s increases, the assumptions that N(E) and $N_{ss}(E)$ are approximately constant become increasingly suspect. Therefore, calculations at high values of y_s must be spurious.

In calculating values of N(E) and $N_{ss}(E)$ it is necessary to assume a particular value of V_g where the bands are flat. Spear and Le Comber[7] suggest that this might occur at a marked transition in the conductance data. Such a transition probably occurs at $V_g \simeq$ 100V in Figures (7.1) and (7.2), and this has been taken as an origin in the computed results. Separate calculations taking the origin at V_g = O do not show a markedly different value for the density of states at the Fermi level, nor in the apparent increasing values of N(E) and $N_{ss}(E)$ with increasing displacement from the equilibrium situation.

Figures (7.4) and (7.5) show the densities of bulk localised states in the surface region, computed from the data of Figures (7.1) and (7.2), as a function of energy displacement towards the valence band for $Ge_{10}As_{40}Te_{50}$ and $Si_{12}Te_{48}As_{30}Ge_{10}$ respectively, neglecting the effect of surface states. The predominance of hole conduction in these materials does not allow an investigation of the variation of N(E) towards the conduction band. The corresponding calculated equivalent surface state densities (i.e. assuming all the induced charge falls into surface states) are shown in Figures (7.6) and Figure (7.7). The values of N(E) and $N_{ss}(E)$ are calculated from the data at all the experimental temperatures, and appear reasonably

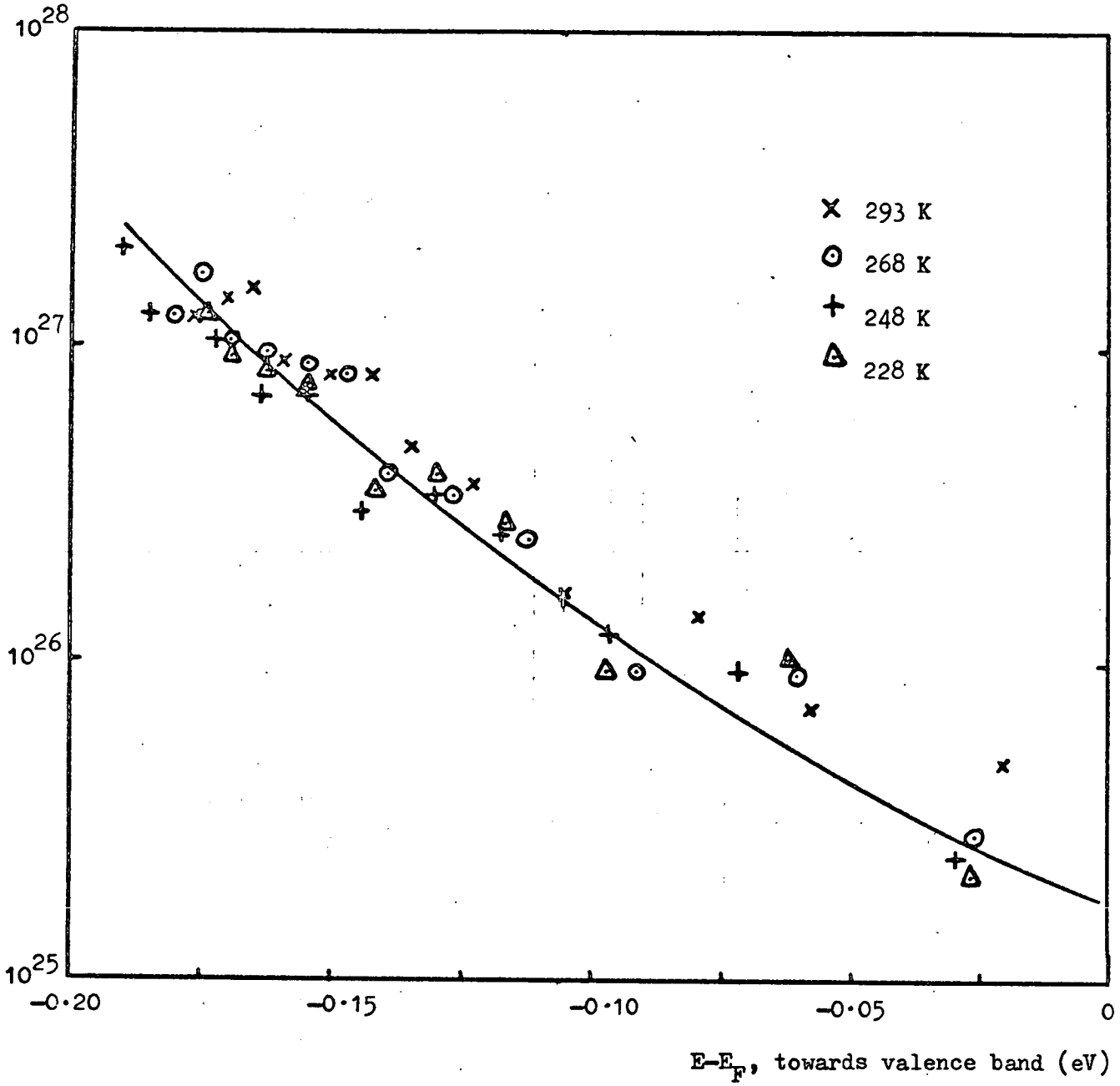

Figure 7.4 Computed variation of localised bulk state density as a function of energy separation from the Fermi level for $Ge_{10}As_{40}Te_{50}$.
The values are calulated at all experimental temperatures.

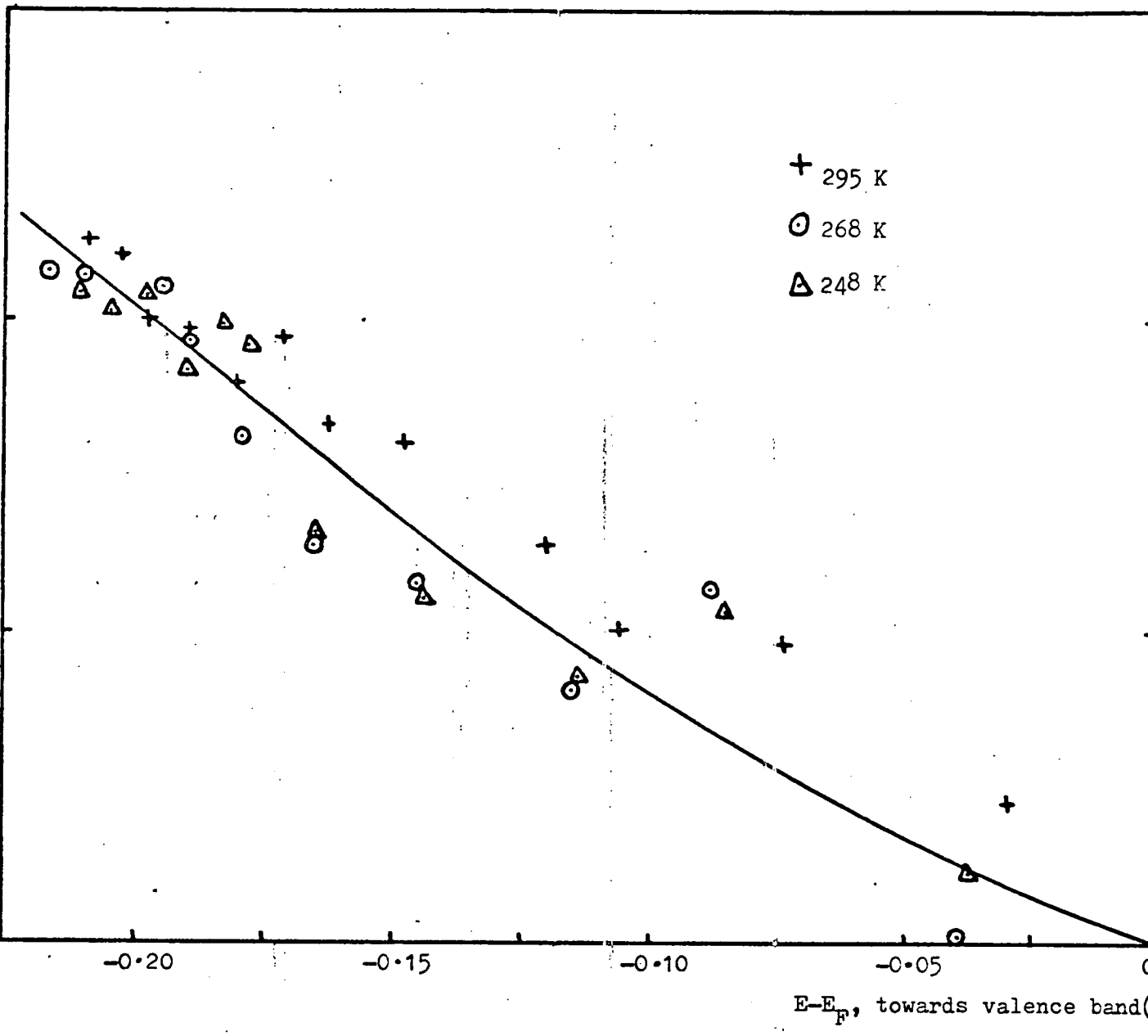

ure 7.5 Computed variation of localised bulk state density as a function of energy separation from the Fermi level for $Si_{12}Te_{48}As_{30}Ge_{10}$. The values are calculated at all experimental temperatures.

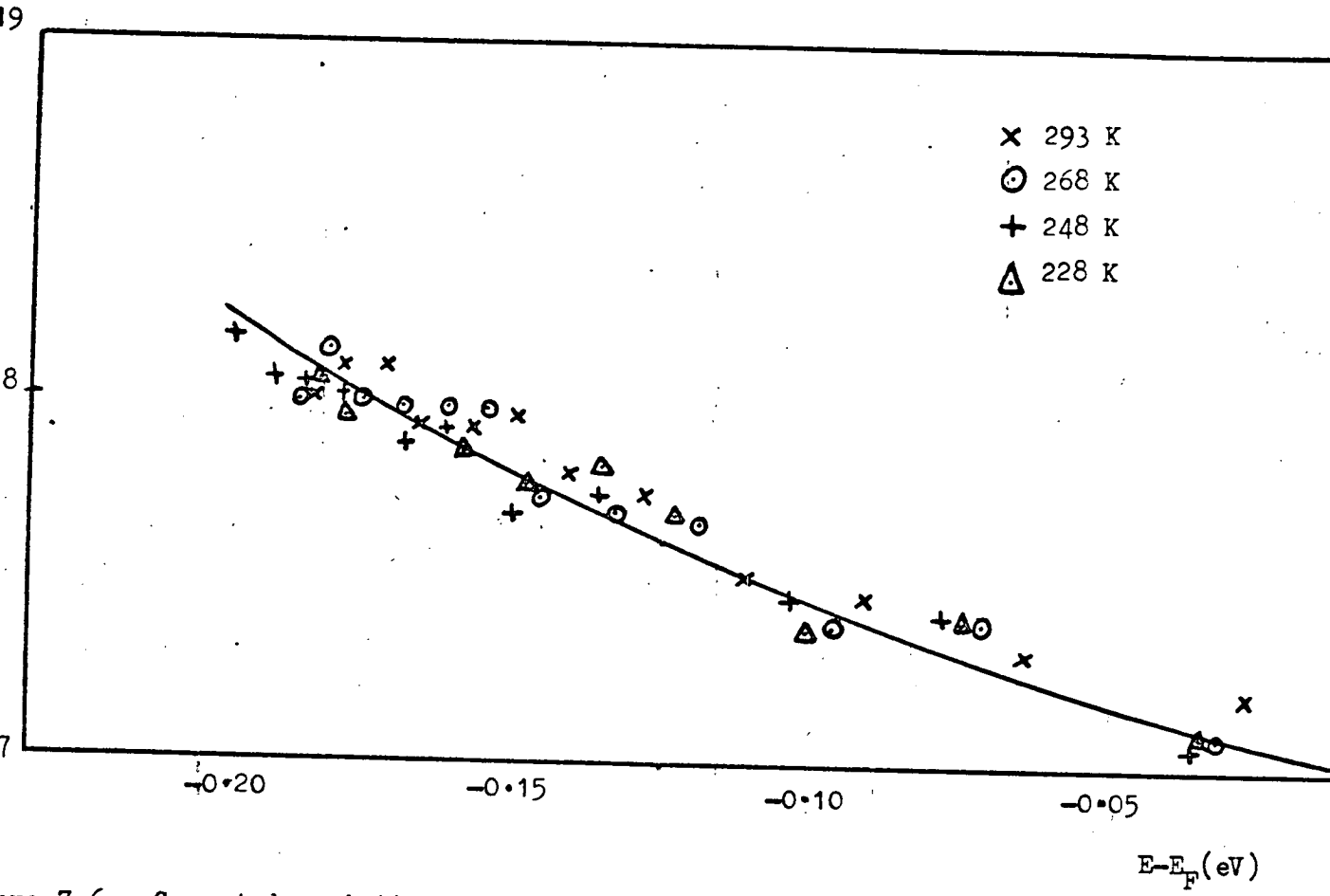

ure 7.6 Computed variation of surface state density as a function of energy separation from the Fermi level for $Ge_{10}As_{40}Te_{50}$.

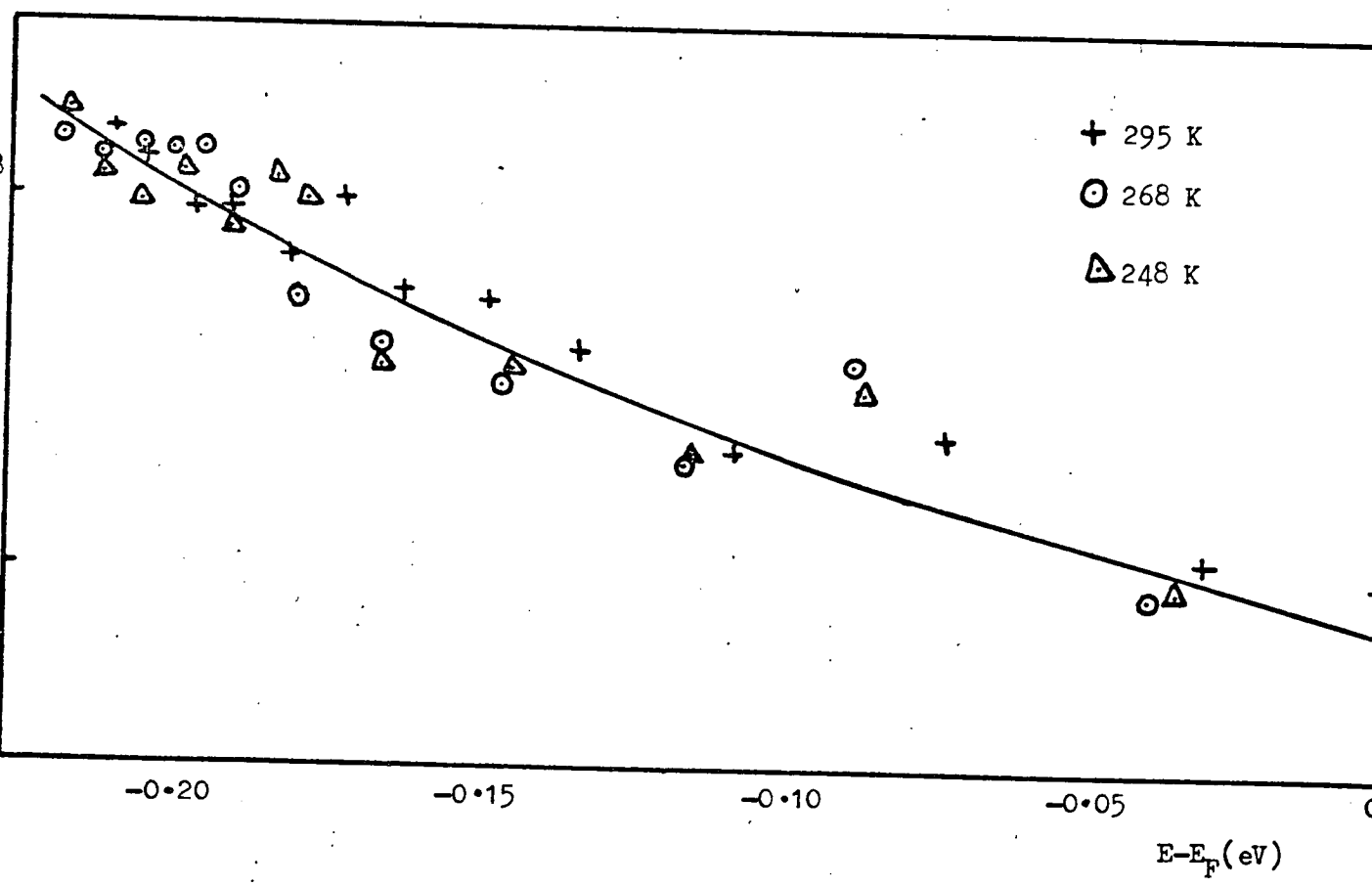

ure 7.7 Computed variation of surface state density as a function of energy separation from the Fermi level for $Si_{12}Te_{48}As_{30}Ge_{10}$.

consistent.

7.4 Discussion of the Field-Effect Data

The relatively small magnitude of the conductance change observed in these experiments and those of other workers[1-5], coupled with a general uniformity of interpretation, has not unnaturally led to closely corresponding calculations for the density of states at the Fermi level in chalcogenide glasses. Thus Egerton[1] reports a value for $N(E_F)$ between $10^{25} m^{-3} eV^{-1}$ and $10^{26} m^{-3} eV^{-1}$ for amorphous $Te_x(Si_{24}Ge_{20}As_{56})_{1-x}$, Marshall[3] reports $N(E_F) \simeq 10^{24} m^{-3} eV^{-1}$ in $Si_{12}Te_{48}As_{30}Ge_{10}$, and Bube, Arnoldussen et al[2,4] report $N(E_F)$ between $3.10^{25} m^{-3} eV^{-1}$ and $4.10^{26} m^{-3} eV^{-1}$ in a wide variety of compositions formed from the elements, As,Se,Ge,Te and Sb. In some cases[2,4] the calculations for $N(E_F)$ have been supported by photoconductive decay measurements. From the data presented here, it is reasonable to conclude that a high density of localised states exists at the Fermi level at or near the surface of chalcogenide glasses. The relative proportion of surface states and bulk localised states is uncertain, but neglecting surface states, a value for $N(E_F) \simeq 10^{25} m^{-3} eV^{-1}$ is calculated. Whether this high value is representative of the localised state density throughout the entire film thickness must also be a matter of conjecture, as there may be an increase in localised state density at the surface associated with an increase in structural and/or compositional disorder. However, the presence of a high density of localised states close to

the surface explains the ease of formation of non-blocking contacts to chalcogenide thin films, by virtue of the arguments presented in Chapter 6.

The variation of localised state density with energy remains problematic. It is unlikely that the smooth monotonic rise of the calculated state densities represented in Figures (7.4) - (7.7) represents the true picture. In the first place, as $(E-E_F)$ increases so the assumption of a slowly varying state density over the relevant energy range becomes increasingly suspect. Secondly, the possibility of localised heterogeneities across the plane of the contact must also be considered. Thus at high values of V_g, a situation may exist where the semiconductor surface is degenerate at specific points, but at other points the Fermi level remains several kT above the valence band. Therefore, no firm conclusions are drawn from the interpretation of the field effect data at high values of V_g.

Recently, Marshall[6] has suggested that the data of Figures (7.1) and (7.2) could be analysed in terms of a hypothetical model such as that of Figure (7.8), where 'donor' and 'acceptor' type defects are present in near perfect compensation, 0.2eV either side of the Fermi level. The absence of a high density of states at the Fermi level would significantly alter the theories presented in Chapter 6 for the absence of blocking contacts in chalcogenide devices, and it is not certain whether an interpretation of this phenomenon in terms of recombination/ generation processes using the model of Figure (7.8) would

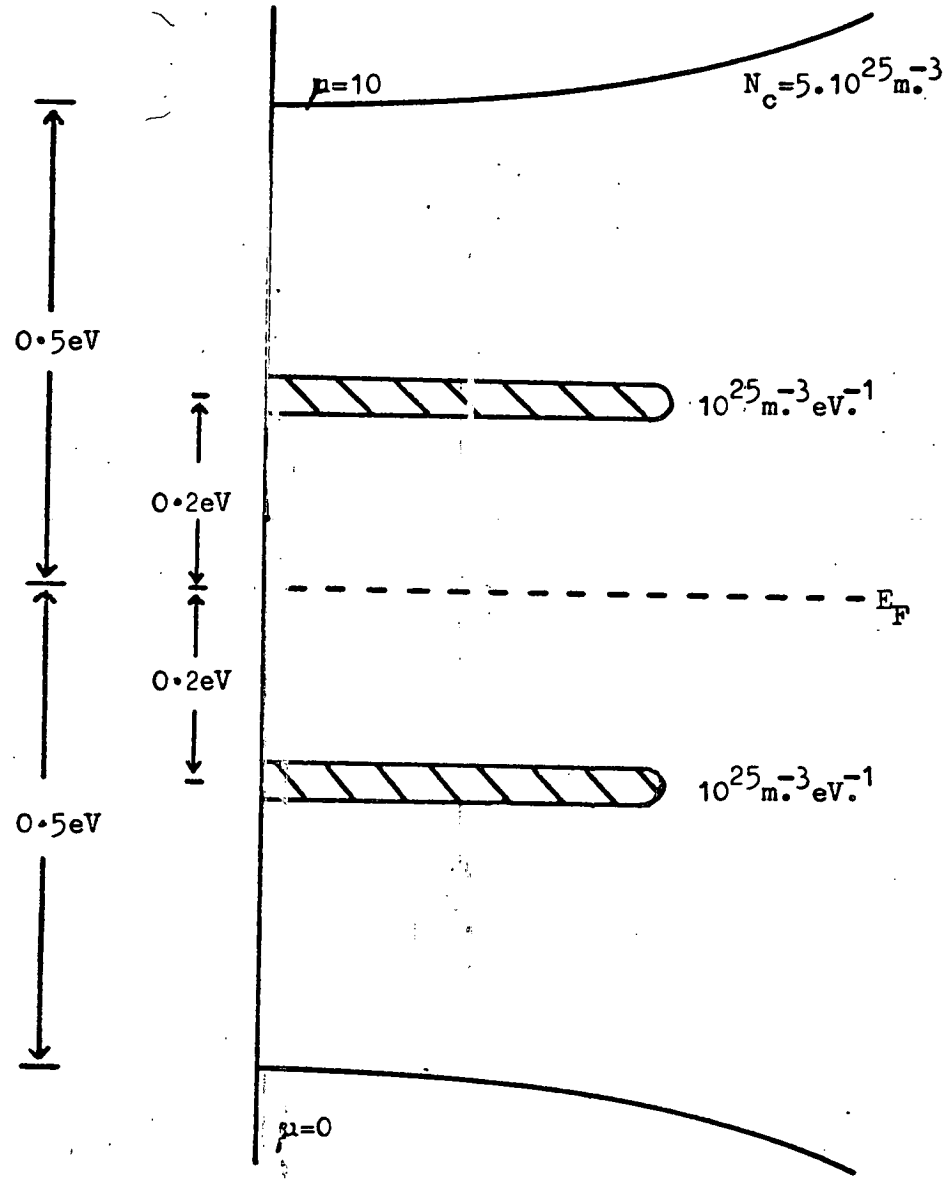

Figure 7.8 Hypothetical model of Marshall[6] for interpretation of field effect data.

provide an adequate explanation. However, if the assumption of a high density of states at the Fermi level made by Barbe[12] is correct, then the surface conductivity at the 'flat band' surface condition should have an activation energy equal to the bulk activation energy (data contained in Chapter 5), and as the bands are bent by a progressively larger amount towards the valence band through the accumulation regime, the surface conductivity should exhibit a progressively decreasing activation energy. Re-arranging Equation (7.3.8), neglecting surface states, we obtain

$$kTy_s = C_g.V_g.\frac{q.\lambda}{\epsilon_r \epsilon_o} \qquad (7.4.1)$$

Thus, as a consequence of the use of zero-temperature trap occupation statistics, the amount of band bending in units of electron volts is directly proportional to the applied gate voltage. The surface conductivity σ_s is calculated from,

$$\sigma_s = \frac{\Delta I \ . \ l}{V \ . \lambda \ . \ b} \qquad (7.4.2)$$

where ΔI is the measured increase in current, V is the source-drain voltage, l is the gap length, b is the width of the coplanar electrodes, and λ is the width of the space charge layer, calculated from Equation (7.3.4), and thus constant at all temperatures for a specific value of V_g. The use of equation (7.4.2) can only give a first approximation to the true situation, as it implicitly assumes a square shape for the space charge region. However, as $\lambda \ll t$, the film thickness, the use of ΔI for

the actual current flowing in the accumulation region constitutes a comparatively small error. Figure (7.9) illustrates the conductivity of the surface layer of $Ge_{10}As_{40}Te_{50}$ plotted against $(10^3/_T)$ with the applied gate voltage, and hence the amount of band bending, as a parameter. Calculations of the surface activation energy ΔE_s from the formula

$$\sigma_s = \sigma_{os} \cdot \exp\left[\frac{-\Delta E_s}{kT}\right] \qquad (7.4.3)$$

where σ_{os} is a constant, do show a progressively decreasing value for ΔE_s, equivalent to the bulk activation energy at the flat-band condition, but decreasing to a substantially lower value, $\Delta E_s = 0.32eV$ at $V_g = -400V$, thus reinforcing the idea that the field-effect data is controlled by a high density of localised states at the Fermi level, $N(E_F) \simeq 10^{25} m.^{-3} eV.^{-1}$ The results of the corresponding calculations on $Si_{12}Te_{48}As_{30}Ge_{10}$ are illustrated in Figure (7.10), but these are less conclusive as only three points are available, although the same general trend is maintained.

7.5 Model for the Field-Effect Modulated Capacitance-Simplified Equivalent Circuit

It has been suggested by Barbe[12], Egerton[13] and others that the metal-insulator-amorphous semiconductor-metal (MISM) device illustrated in Figure (7.11(a)) can be represented by the simple equivalent circuit illustrated in Figure (7.11(b)), i.e. an insulator capacitance, C_g, in series with a parallel combination of the surface state capacitance, C_{ss}, and the space charge layer capacitance, C_{sc}. Using this model it is possible to obtain an

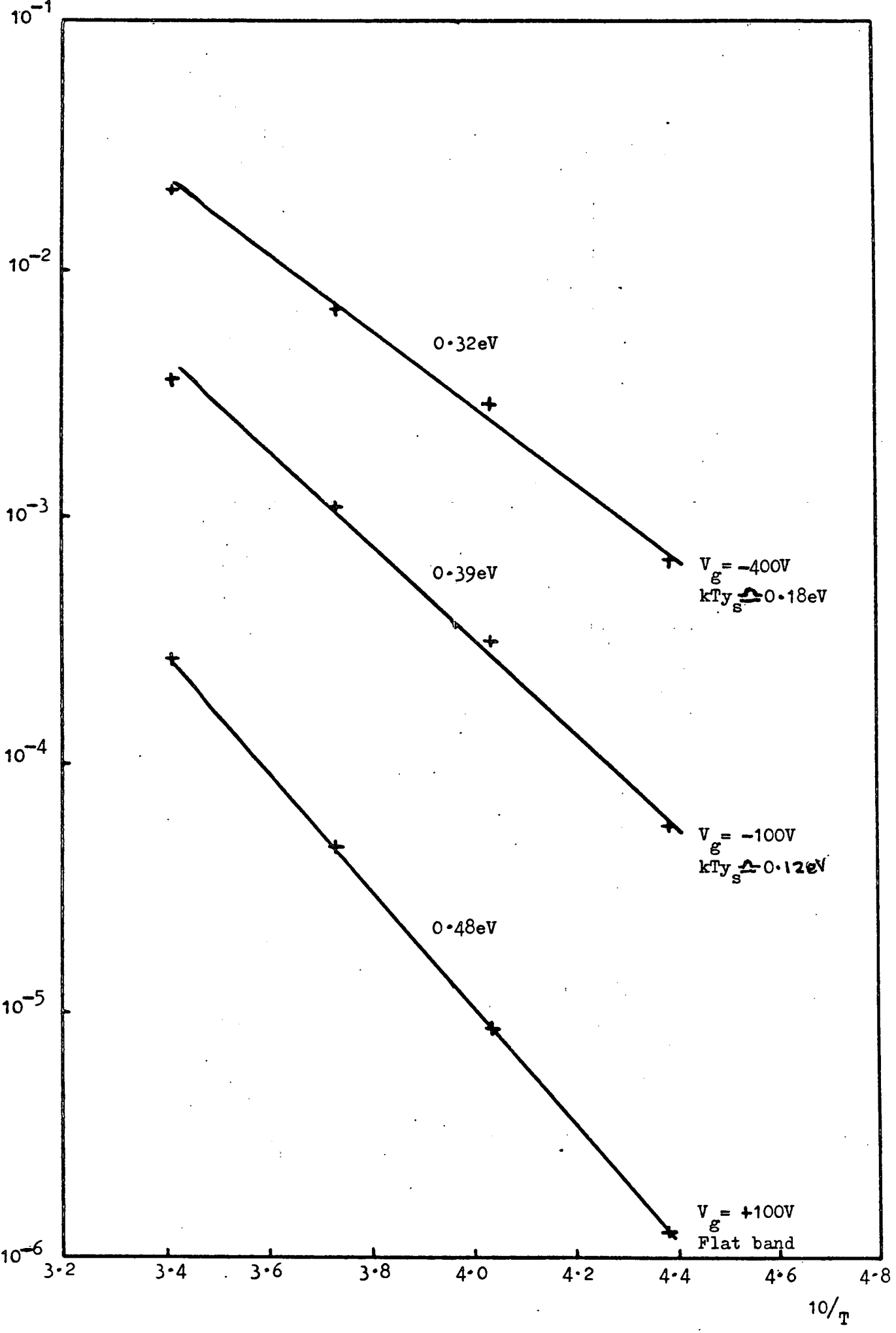

Figure 7.9 Conductivity of surface layer of $Ge_{10}As_{40}Te_{50}$ vs. $10^3/_T$ with V_{gate} as parameter.

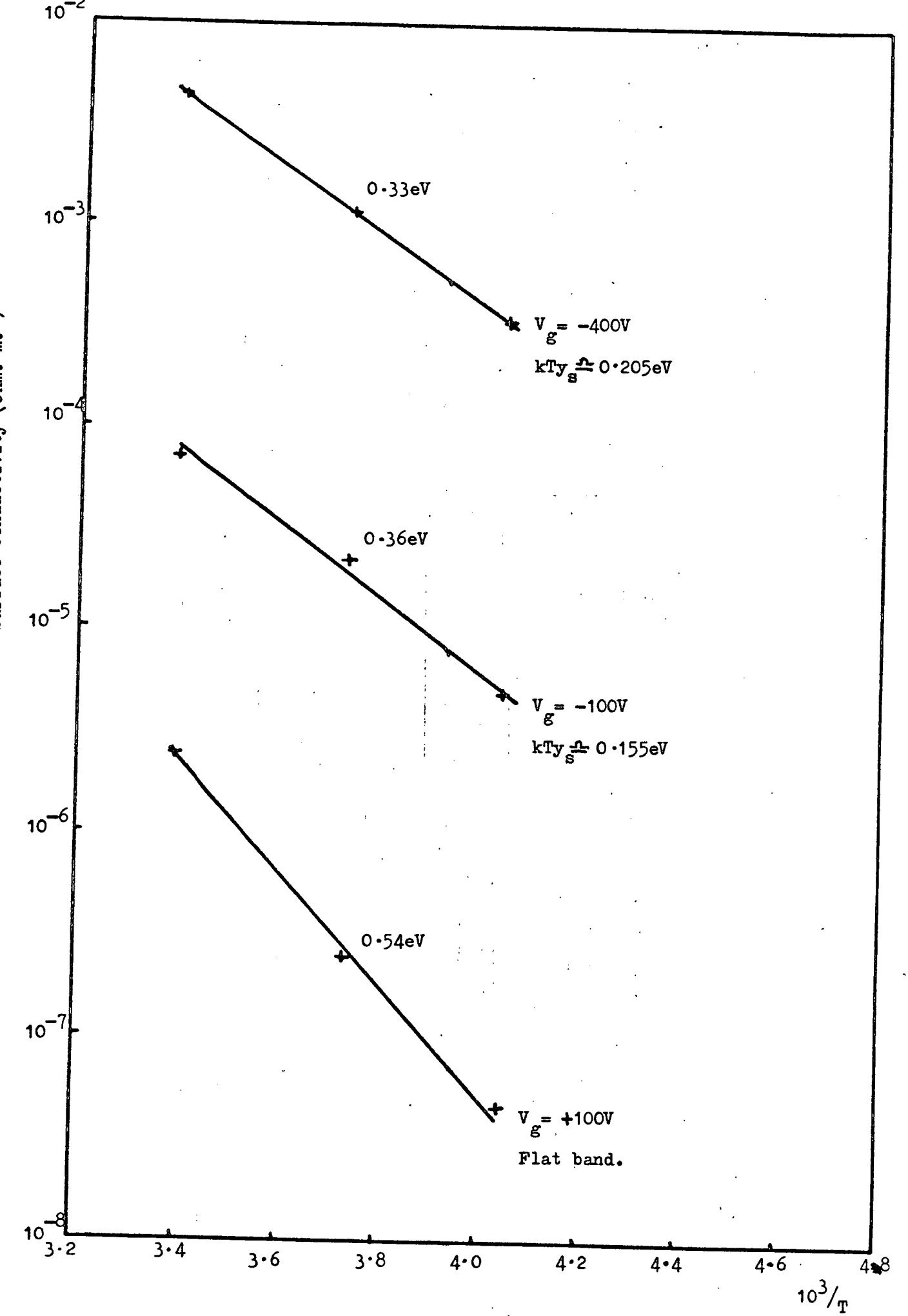

Figure 7.10 Conductivity of surface layer of $Si_{12}Te_{48}As_{30}Ge_{10}$ vs. $10^3/_T$ with V_{gate} as a parameter.

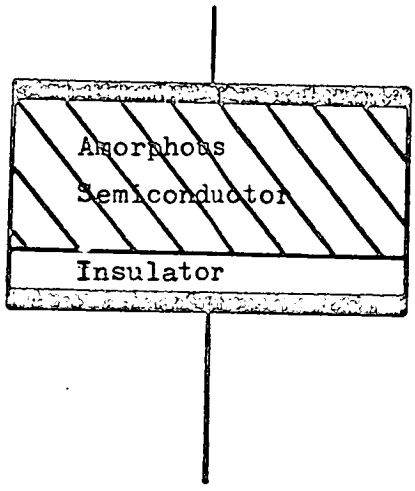

Figure 7.11(a) MISM device.

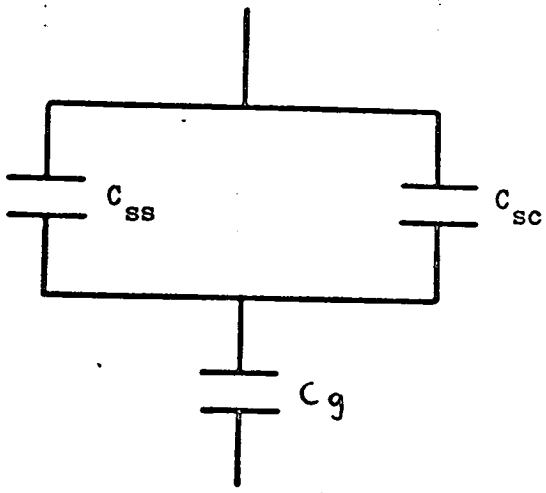

Figure 7.11(b) Simple equivalent circuit.

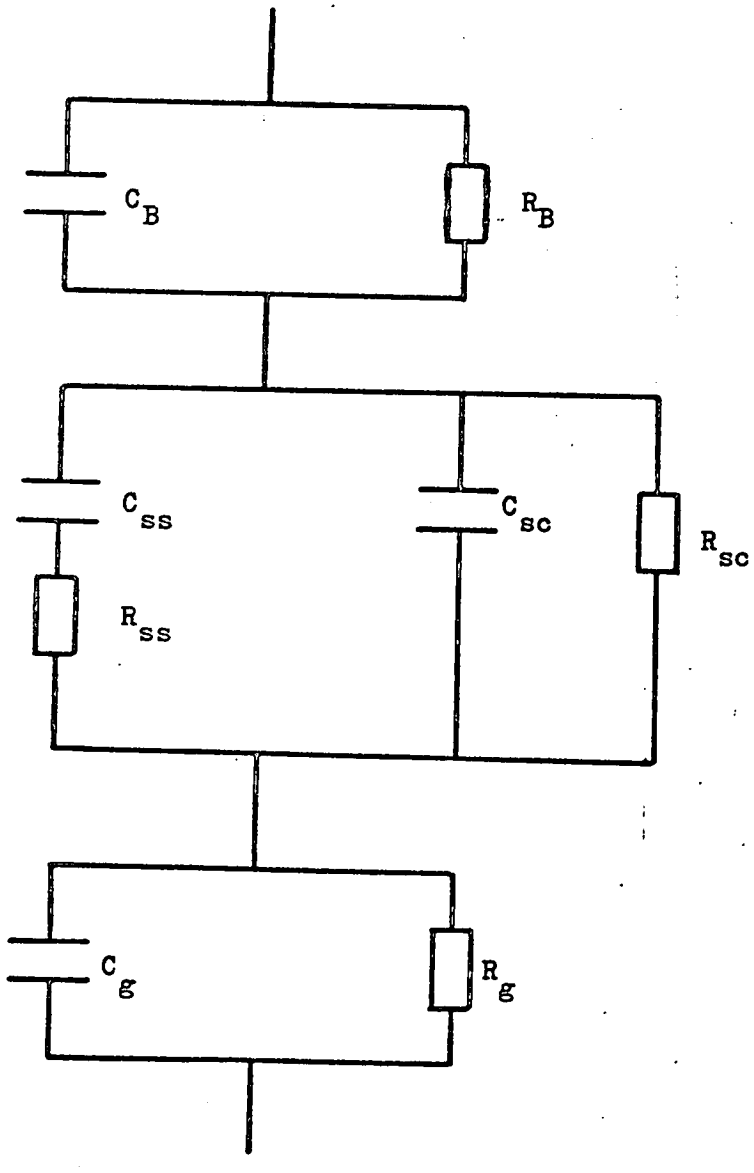

Figure 7.11(c) Full equivalent circuit.

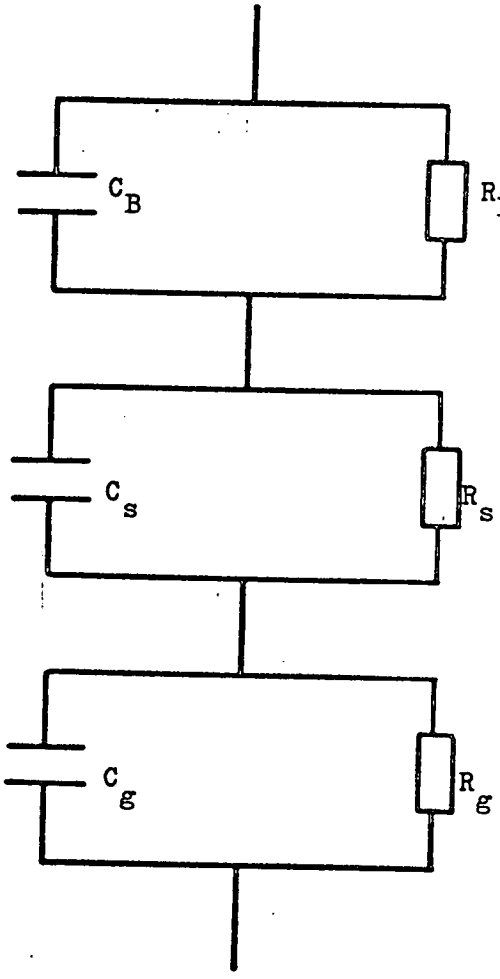

Figure 7.11(d) Modified full equivalent circuit.

expression for the variation of the measured differential capacitance as a function of applied voltage, from which the localised state density at the surface can be deduced as a function of energy displacement from the Fermi level. The total equivalent capacitance of the circuit in Figure (7.11(b)) is given by,

$$C_{eq} = \frac{C_g.(C_{sc} + C_{ss})}{C_g + C_{sc} + C_{ss}} \qquad (7.5.1)$$

where C_{eq}, C_g, C_{sc} and C_{ss} are all in units of $F.m^{-2}$. Thus

$$C_g = \frac{\varepsilon_g \varepsilon_o}{d} \qquad (7.5.2)$$

where ε_g is the insulator dielectric constant, ε_o the permittivity of free space and d the insulator thickness. The expressions for C_{sc} and C_{ss} are deduced from Equations (7.3.5) and (7.3.6) respectively,

$$C_{sc} = {}^{-q}/_{kT} \cdot \frac{dQ_{sc}}{dy_s} = \frac{\varepsilon_r \varepsilon_o}{\lambda} \qquad (7.5.3)$$

$$C_{ss} = {}^{-q}/_{kT} \cdot \frac{dQ_{ss}}{dy_s} = q^2 N_{ss} \qquad (7.5.4)$$

It should be noted that Equations(7.5.3) and (7.5.4) implicitly assume slowly varying density-of-states functions around the equilibrium Fermi level, so that the second terms in the differentials of Equations (7.3.5) and (7.3.6) can be neglected. This is a similar assumption to that made in the section on field-modulated conductance and has the same inherent disadvantages.

Inserting typical values for $N_{ss}(E_F)$ and λ (and hence $N(E_F)$)into Equations (7.5.3) and (7.5.4) gives $C_{sc} + C_{ss} \simeq$

$1.6.10^{-2}$ F.m.$^{-2}$ Thus, in order to obtain a significant modulation of the total equivalent capacitance, given by equation (7.5.1), it is necessary to make C_g have a comparable value, implying the use of very thin insulators. For example, with an insulating Al_2O_3 film, $\varepsilon_g = 8.8$[17], of thickness $\simeq 100\text{Å}$, the oxide capacitance $C_g = 8.10^{-3}$F.m.$^{-2}$ When thick insulators are used, $C_g \ll C_{sc} + C_{ss}$, and hence $C_{eq} \simeq C_g$.

If C_g is of the same order as $C_{sc} + C_{ss}$, the full expression for y_s becomes, (cf. Equation (7.3.8)

$$y_s = \frac{C_g\, C_s}{C_g + C_s} \cdot V_g \Big/ \left[\frac{\varepsilon_r \varepsilon_o kT}{q} \left[\frac{1}{\lambda} + \frac{q^2 N_{ss}}{\varepsilon_r \varepsilon_o} \right] \right] \qquad (7.5.5)$$

where $C_s = C_{sc} + C_{ss}$. Using Equations (7.5.3) and (7.5.4) this simplifies to

$$y_s = \frac{C_g}{C_g + C_s} \cdot {}^{q}/_{kT} \cdot V_g \qquad (7.5.6)$$

Differentiating, this becomes,

$$\frac{dy_s}{dV_g} = \frac{C_g}{C_g + C_s} \cdot {}^{q}/_{kT} \qquad (7.5.7)$$

Returning to Equation (7.5.1) and differentiating with respect to y_s,

$$\frac{dC_{eq}}{dy_s} = \left[\frac{C_g}{C_g + C_s} \right]^2 \cdot \frac{dC_s}{dy_s} \qquad (7.5.8)$$

Thus, using Equation (7.5.7), this gives

$$\frac{dC_{eq}}{dy_s} = \frac{dC_{eq}}{dV_g} \cdot \frac{dV_g}{dy_s} = \frac{kT}{q} \cdot \frac{C_g + C_s}{C_g} \cdot \frac{dC_{eq}}{dV_g} \qquad (7.5.9)$$

Equating the expressions (7.5.8) and (7.5.9) leads to,

$$\frac{dC_s}{dy_s} = \left[\frac{C_g + C_s}{C_g}\right]^3 \cdot \frac{kT}{q} \cdot \frac{dC_{eq}}{dV_g} \qquad (7.5.10)$$

Equation (7.5.10) makes it possible to deduce the variation of surface state capacitance as a function of displacement from the Fermi level from the measured variation of the total equivalent circuit capacitance with applied voltage. Using Equations (7.5.3) and (7.5.4) this can readily be translated into a variation of bulk localised state density with energy;

$$\frac{dN}{dy_s} = \frac{2\,N^{\frac{1}{2}}}{q(\varepsilon_r\,\varepsilon_o)^{\frac{1}{2}}} \cdot \left[\frac{C_g + q(\varepsilon_r\,\varepsilon_o)^{\frac{1}{2}}N^{\frac{1}{2}}}{C_g}\right]^3 \cdot \frac{kT}{q} \cdot \frac{dC_{eq}}{dV_g} \qquad (7.5.11)$$

or, using Equation (7.5.4), into a variation of the surface state density with energy;

$$\frac{dN_{ss}}{dy_s} = \frac{C_g + q^2 N_{ss}}{C_g} \cdot \frac{kT}{q} \cdot \frac{dC_{eq}}{dV_g} \qquad (7.5.12)$$

Analytical solutions of Equations (7.5.11) and (7.5.12) would be very complex, and probably unjustifiable in view of previous assumptions. Nevertheless, an average value of N or N_{ss} could be obtained from the field-effect conductance data and inserted into Equation (7.5.11) or (7.5.12) respectively, so that the general trend in the localised state distribution as a function of displacement from the Fermi level could be deduced from measurements of the differential capacitance as a function of applied voltage. Certainly, the use of field-effect modulated capacitance measurements could prove valuable in that no assumptions are necessary with regard to the mode of carrier transport.

7.6 The Variation of Capacitance with Frequency in MISM and MSM Devices - Consideration of Full Equivalent Circuit

In the equivalent circuit of Figure (7.11(b)), and hence in the analysis presented above, it was implicitly assumed that the insulator resistance, R_g, and the resistance of the surface space charge region, R_{sc}, were large in comparison to the bulk resistance R_B. However, from the arguments of Chapter 6, it is unlikely that this is a good assumption; it is more probable that $R_B \gg R_{sc}$. The full equivalent circuit can probably best be represented by Figure (7.11(c))[18,19], which can be simplified to the six-element network of Figure (7.11(d)) if C_s is considered as the surface capacitance and R_s is considered as the surface resistance. This network can be analysed in two stages; the four-element network, C_g, C_s, R_g, R_s, is expressed in terms of an equivalent parallel capacitance,

$$C_p = \frac{R_g^2 C_g + R_s^2 C_s + \omega^2 R_g R_s C_g C_s (C_g + C_s)}{(R_g + R_s)^2 + \omega^2 R_g^2 R_s^2 (C_g + C_s)^2} \qquad (7.6.1)$$

and an equivalent parallel A.C. conductance,

$$G_p = \frac{(R_g + R_s) + \omega^2 R_g R_s (C_g^2 R_g + C_s^2 R_s)}{(R_g + R_s)^2 + \omega^2 R_g^2 R_s^2 (C_g + C_s)^2} \qquad (7.6.2)$$

These in turn can be considered as part of a four-element network comprising, C_p, R_p ($=1/G_p$), C_B and R_B to obtain a total equivalent capacitance,

$$C_{eq} = \frac{R_p^2 C_p + R_B^2 C_B + \omega^2 R_p R_B C_p C_B (C_p + C_B)}{(R_p + R_B)^2 + \omega^2 R_p^2 R_B^2 (C_p + C_B)^2} \qquad (7.6.3)$$

and a total equivalent A.C. conductance,

$$G_{eq} = \frac{(R_p+R_B) + \omega^2 R_p R_B (C_p{}^2 R_p + C_B{}^2 R_B)}{(R_p+R_B)^2 + \omega^2 R_p{}^2 R_B{}^2 (C_p+C_B)^2} \qquad (7.6.4)$$

The complexity of Equations (7.6.1) - (7.6.4) can be reduced in the two limiting cases, $\omega \to 0$ and $\omega \to \infty$, making certain realistic assumptions,

(i) The geometric bulk capacitance of the thin film, C_B, may be assumed much less than either C_g or C_s. Considering the Al-Al_2O_3-$Ge_{10}As_{40}Te_{50}$-Al devices discussed in Chapter 6, with very thin insulators of the order of 100Å, this is a reasonable assumption, as discussed in Section (7.5).

(ii) The resistance of the insulating layer, R_g, is assumed to be more than two orders of magnitude greater than the bulk resistance, R_B. This was observed to be the case in the Al-Al_2O_3-$Ge_{10}As_{40}$-Te_{50}-Al devices, discussed in Chapter 6, by comparing the current-voltage data obtained from MISM and MSM devices.

(iii) The bulk resistance R_B is taken to be at least two orders of magnitude greater than the surface resistance, R_S, since $R_B \triangleq t/\lambda . R_S$ assuming comparable mobilities in the bulk and surface regions. This is also reasonable from the current-voltage data of the MSM devices presented in Chapter 6.

Using these assumptions, and under the condition $\omega \to 0$, Equations (7.6.1) and (7.6.2) simplify to,

$$C_p \triangleq C_g \qquad (7.6.5)$$

and,

$$G_p \simeq {}^{1}/R_g, \text{ i.e. } R_p \simeq R_g \qquad (7.6.6)$$

Inserting these values into Equations (7.3.3) and (7.3.4),

$$C_{eq} \simeq C_g \qquad (7.6.7)$$

and,

$$R_{eq} \simeq R_g \qquad (7.6.8)$$

Thus at low frequencies the total device capacitance and resistance should approximate to the oxide parameters. Under the assumption $\omega \to \infty$, Equations (7.3.1) and (7.3.2) become,

$$C_p \simeq \frac{C_g C_s}{C_g + C_s} \qquad (7.6.9)$$

and,

$$G_p \simeq \frac{C_g^2}{R_s(C_g+C_s)^2} \quad \text{i.e. } R_p \simeq \frac{R_s(C_g+C_s)^2}{C_g^2} \qquad (7.6.10)$$

Using these values in Equations (7.3.3) and (7.3.4) leads to,

$$C_{eq} \simeq C_B \qquad (7.6.11)$$

and,

$$R_{eq} \simeq R_B \qquad (7.6.12)$$

Thus at high frequencies the total device capacitance and resistance approximate to the bulk chalcogenide thin-film parameters.

The implications of this analysis with regard to the measurement of the field-effect modulated capacitance are evident. Since $R_s \ll R_g$, and $R_s \ll R_B$, any modulation of the surface capacitance by an applied field will not be

reflected in a variation of the measured device capacitance.

The variation of the capacitance and A.C. conductance of MSM and MOSM devices with frequency was measured using the Lynch Bridge apparatus described in Section (4.3.4). The data of Figure (7.12) on an Au-$Ge_{10}As_{40}Te_{50}$-Au sandwich device is typical of a number of sandwich devices tested, all of which had non-oxidising electrodes. The capacitance and A.C. conductance are essentially frequency independent, and appear to correspond to the bulk values C_B, R_B, thus confirming the conclusion of Chapter 6 that the resistivity of the space charge region is no greater than that of the bulk. Wey and Fritzche[15,16] suggest that if the dielectric relaxation time,

$$\tau_{rel} = \frac{\varepsilon_r \varepsilon_o}{\sigma} \qquad (7.6.13)$$

in the space charge region is longer than that in the bulk, that is if the conductivity in the space charge region is lower than that in the bulk (assuming ε_r is the same in both regions), the effect of the space charge region capacitance should be observed as an increase in measured capacitance at low frequencies. Data on Ni/Cr-$Ge_{16}As_{35}Te_{28}Si_{21}$-$SnO_2$ and Ni/Cr-$Ge_{16}As_{35}$-$Te_{28}Si_{21}$-Sb devices[15,16] show a rise in the measured capacitance at low frequencies, and this is interpreted as evidence of a space charge region of width $\simeq 160\text{Å}$ with a resistivity more than 100 time the bulk resistivity. If a similar situation existed here, the low-frequency increase in capacitance would occur well within the frequency range of the bridge, thus it is

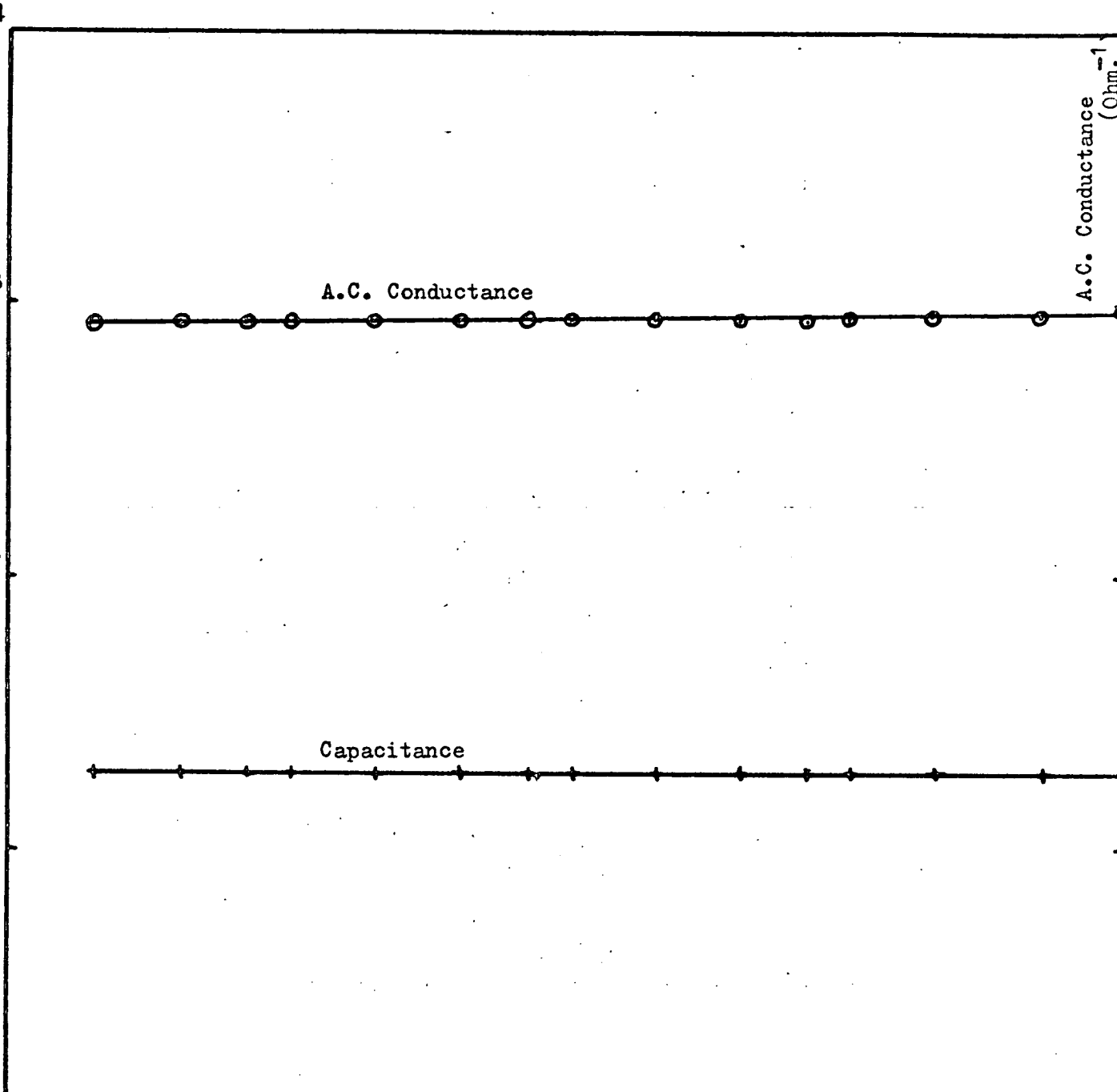

ure 7.12 Variation of capacitance and A.C. Conductance with frequency of an Au-$Ge_{10}As_{40}Te_{50}$-Au device, thickness 1·8um.

unlikely that a comparable situation exists. As Wey and Fritzsche[15,16] give no details of the method of preparation of their devices, it is possible that the low frequency rise in measured capacitance was caused by interfacial layers between the electrode and the chalcogenide film.

The data of Figure (7.13), obtained from an Al-Al_2O_3-$Ge_{10}As_{40}Te_{50}$-Al device prepared at the same time as the Au-$Ge_{10}As_{40}Te_{50}$-Au device in order to ensure that the chalcogenide layers were as nearly identical as possible, is likewise typical of a number of such devices. At high frequencies the device capacitance and A.C. conductance tend to the bulk values, as illustrated in Figure (7.12) and predicted by Equations (7.6.11) and (7.6.12). At low frequencies, the device capacitance rises by two orders of magnitude to a value corresponding to C_g, and the A.C. conductance drops sharply to a value corresponding to $^1/R_g$. Between the two extremes the characteristics are approximated by Equations (7.6.3) and (7.6.4). Assuming a dielectric constant for $Al_2O_3 \simeq 8.8$, the thickness of the insulating layer is estimated to be of the order of 100Å. The value of R_g is in good agreement with that calculated from the current-voltage data in Chapter 6.

7.7 Conclusions

The main conclusion of the field-effect data is that near the surface of the semiconductor, a large density of localised states exists at the Fermi level. The relative magnitudes of the surface state density and the bulk

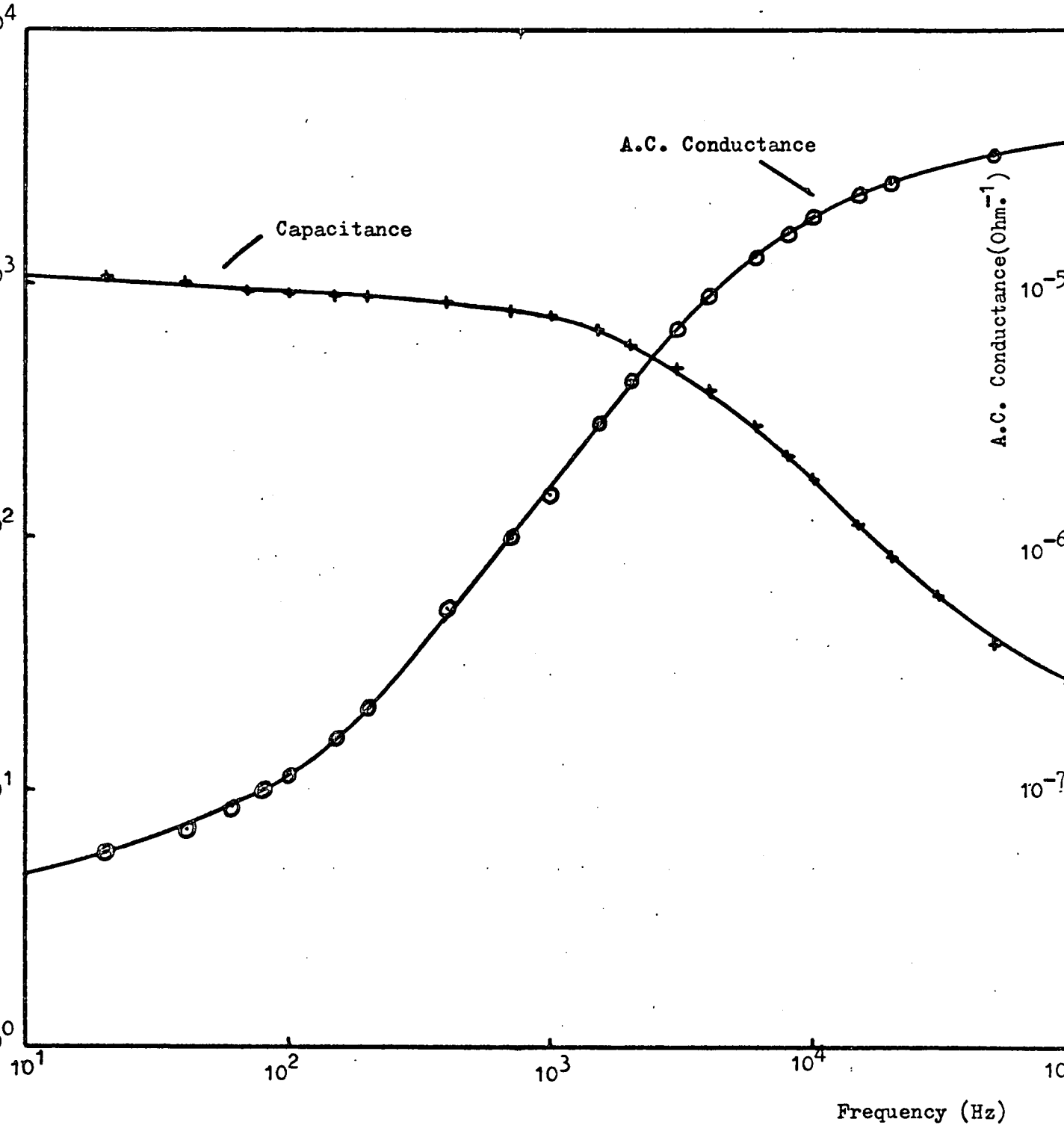

gure 7.13 Variation of capacitance and A.C. conductance with frequency of an Al–Al_2O_3–$Ge_{10}As_{40}Te_{50}$–Al device, thickness 1·8um.

localised state density are not certain, and it cannot be assumed that the magnitude and distribution of localised states at the surface is representative of the true situation throughout the bulk. However, the existence of these states has important consequences with regard to the formation of non-blocking contacts on chalcogenide thin film devices, as discussed in Chapter 6. Data on the variation of capacitance and A.C. conductance of MSM and MISM devices with frequency are in good agreement with the D.C. current-voltage data of Chapter 6, in that they also show the lack of highly resistive space charge regions adjacent to contacts in MSM devices, but do indicate the presence of an interfacial layer in devices where oxidising electrodes are used.

CHAPTER 8 OPTICAL MEASUREMENTS

8.1 Introduction

Although non-blocking contacts are generally formed between chalcogenide glass films and metal electrodes, as discussed in Chapter 6, it is probable that space charge regions do exist adjacent to the contacts, as is evidenced by photovoltaic data.[1-5] Before commencing a study of the photovoltaic effect in thin film sandwich devices of $Ge_{10}As_{40}Te_{50}$ and $Si_{12}Te_{48}As_{30}Ge_{10}$, a preliminary investigation of the optical transmission characteristics of these materials was required, in order to determine the dependence of the absorption coefficient, α, on the incident photon energy and temperature, and to obtain the optical gap, E_o.

8.2 Transmission Measurements

For transmission spectra of the chalcogenide glasses, $Ge_{10}As_{40}Te_{50}$ and $Si_{12}Te_{48}As_{30}Ge_{10}$, R.F. sputtered films on one inch square glass substrates were used, taking care to ensure clean surfaces and to avoid pinhole effects, which could result in a spuriously high transmission level at high photon energies. Typical transmission spectra are shown in Figures (8.1) and (8.2) for $Ge_{10}As_{40}Te_{50}$ and $Si_{12}Te_{48}As_{30}Ge_{10}$ respectively. The data is essentially similar; at high photon energies, in excess of 1.5eV, say, the transmission is almost negligible, but at an intermediate photon energy, approximately 1eV for $Ge_{10}As_{40}Te_{50}$ and 1.15eV for $Si_{12}Te_{48}As_{30}Ge_{10}$, there is a sharp rise in the tranmission characteristic. At low photon energies, less than 1eV, say,

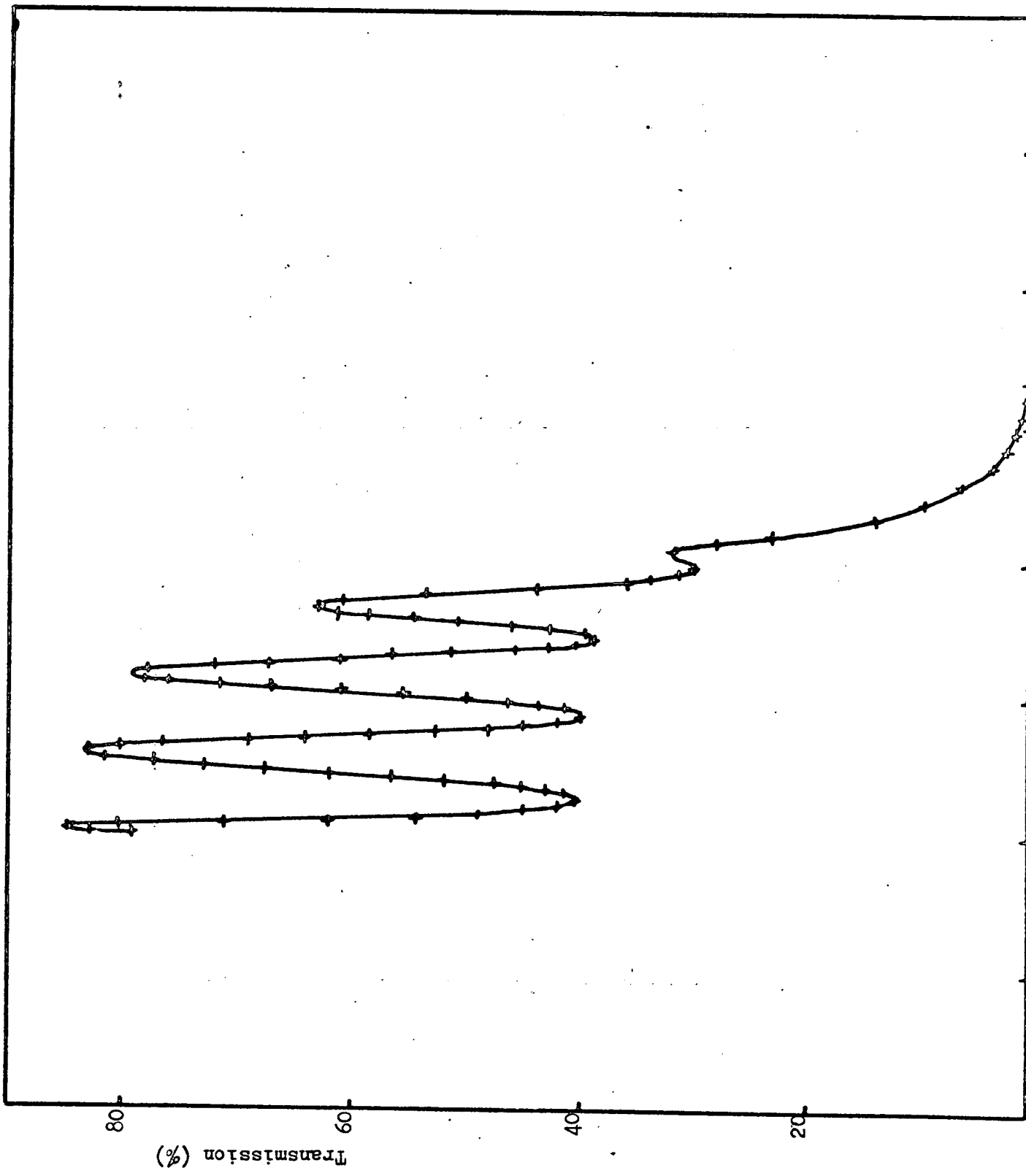

Figure 8.1 Transmission spectrum for $Ge_{10}As_{40}Te_{50}$ film - thickness 1um.

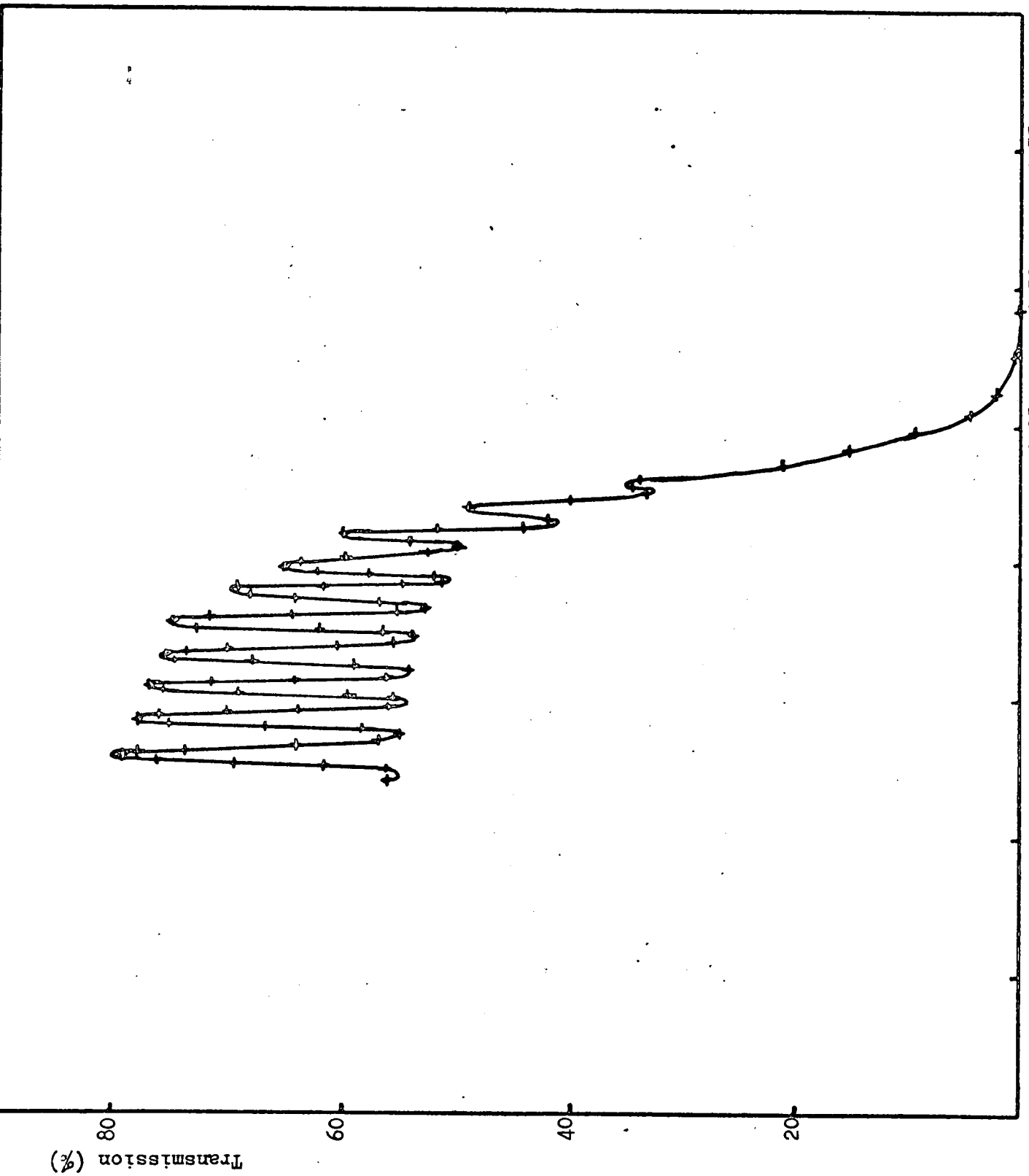

Figure 8.2 Transmission spectrum for $Si_{12}Te_{48}As_{30}Ge_{10}$ film - thickness 2•95um.

the data is characterised by interference fringes. The presence of these fringes enables the refractive index of the chalcogenide alloy films, n_s, to be calculated from basic optical theory.[6] The condition for maximum transmission is given by,

$$2.n_s.d = m.\lambda \qquad (8.2.1)$$

and for an adjacent minimum transmission, by,

$$2.n_s.d = (m + \tfrac{1}{2}).\lambda \qquad (8.2.2)$$

where d is the film thickness, m is an integer denoting the order of the fringe, and λ is the wavelength of the light. Eliminating m from the simultaneous Equations (8.2.1) and (8.2.2) and using the data of Figures (8.1) and (8.2) gives n_s approximately 3.5 for both chalcogenides.

8.3 The Absorption Coefficient and the Optical Gap in $Ge_{10}As_{40}Te_{50}$ and $Si_{12}Te_{48}As_{30}Ge_{10}$

When considering absorption processes in semiconductors, electrons in four types of state must be considered; i.e. valence band electrons, inner shell electrons, free carriers, and electrons bound in localised states.[6] The most important of these in the present context is the first; it involves the optical excitation of valence band electrons across the forbidden gap to the conduction band. Thus it is common in semiconductors to find a region of relatively high transmission at low photon energies (high wavelengths), bounded by a steep "absorption edge" where the photon energy $h\nu$ corresponds to the optical gap, E_o, beyond which, at high photon energies, there is a region of intense absorption. Thus an analysis of the transmission

spectra of Figures (8.1) and (8.2) yields information on the band-gap of the semiconducting alloys.

The absorption coefficient, α, is related to the measured transmission, T, by the expression,[6,7]

$$T = \frac{(1-R_1).(1-R_2).(1-R_3).e^{-\alpha d}}{(1-R_2R_3).(1-(R_1R_2+R_1R_3(1-R_2)^2).e^{-2\alpha d})} \qquad (8.3.1)$$

This equation is appropriate to the situation illustrated in Figure (8.3), where d is the chalcogenide thickness, and R_1, R_2 and R_3 are the reflectances at the air-film, film-substrate, and substrate-air boundaries respectively. The formula includes the effect of multiple reflections, but coherence and interference effects between reflections are ignored. The reflectance at the interface between medium A and medium B is calculated from the formula,[6]

$$R_{AB} = \frac{(n_B - n_A)^2}{(n_B + n_A)^2} \qquad (8.3.2)$$

where n_B and n_A are the relevant refractive indices. Equation (8.3.2) is valid providing the absorption index of the materials $\left[= \frac{\lambda.\alpha}{4.\pi}\right]$ is much less than unity. According to section (8.2) the refractive index of the chalcogenides is approximately 3.5, while the refractive indices of the substrate glass and air are 1.5 and 1 respectively. Thus, using Equation (8.3.2)

$$R_1 = 0.31,$$

$$R_2 = 0.16,$$

and $$R_3 = 0.04.$$

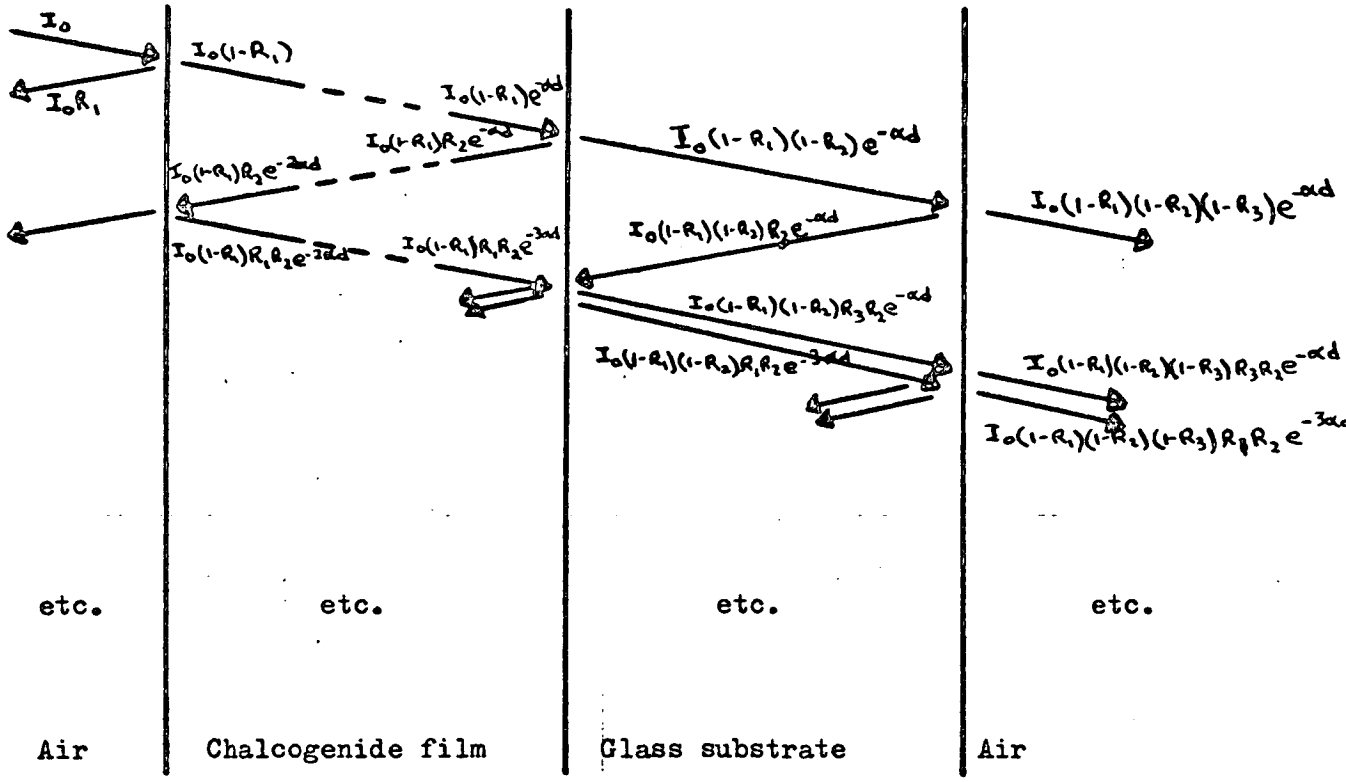

R_1 Reflectance at air–film interface.

R_2 " " film–glass interface.

R_3 " " glass–air interface.

α Absorption coefficient.

d Film thickness.

Figure 8.3 Multiple reflections in chalcogenide thin film devices.

Table (8.1)

```
E.R.C.C. FORTRAN COMPILER  RELEASE 5 VERSION 4  DATED 15/02/74


 1              READ,A,B,C,D
 2              WRITE (6,3)
 3      3       FORMAT('1',5X,'T      VS.      ALPHA')
 4              READ,J
 5              DO 1 I=1,J
 6              READ,T
 7              ALPHA=(ALOG((-8/T-SQRT((B/T)**2-4*A*C))/
                      (2*A))/D)
 8              WRITE(6,2)T,ALPHA
 9      2       FORMAT(1X,/5X,F6,4,5X,F14.4)
10      1       CONTINUE
11      99      STOP
12              END


CODE+GLA+LOADDATA+SYMTABS+ARRAYS = 520+ 360+ 88+ 112+ 0 =
 1080 BYTES

*COMPILATION SUCCESSFUL


PARAMETER FOR FILING:- SPACE=(3056.1)  JOB-STEP RETURN CODE = 0
```

A,B,C	Quadratic coefficients
D	Thickness of film
T	Transmission
ALPHA	Absorption coefficient

Hence Equation (8.3.1) can be written as a quadratic in ,

$$16.3 - \left[{}^{9.1}/_{T}\right].e^{-\alpha d} - e^{-2\alpha d} = 0 \qquad (8.3.3)$$

Computer solutions for α were obtained by means of the Fortran IV program detailed in Table (8.1).

Figure (8.4) shows the variation of the absorption coefficient of $Ge_{10}As_{40}Te_{50}$ with photon energy and temperature, while Figure (8.5) compares room temperature data of $Ge_{10}As_{40}Te_{50}$ and $Si_{12}Te_{48}As_{30}Ge_{10}$. At high photon energies, absorption presumably occurs by excitation of electrons across the mobility gap into band states. In amorphous materials the spectral dependence of α in this region has often been observed to obey an equation of the form,

$$\alpha h\nu = \text{Constant}.(h\nu - E_o)^n \qquad (8.3.4)$$

where n is an integer. The value of n is 2 in a wide variety of chalcogenides,[8] although Fagen has reported that n = 3 in three multi-component glasses,[9] and Davis has observed that n = 1 in amorphous selenium.[8] The data for the chalcogenide alloys under investigation here is best fitted by n = 2, as illustrated in Figures (8.6) and (8.7) where $(\alpha h\nu)^{\frac{1}{2}}$ is plotted against photon energy. By extrapolating the high absorption data on to the horizontal axis it is possible to obtain an estimate of E_o. Thus the optical gap, E_o, is approximately 0.94eV for $Ge_{10}As_{40}Te_{50}$ and 1.09eV for $Si_{12}Te_{48}As_{30}Ge_{10}$, at room temperature. As the temperature is decreased, so the optical gap increases; in the case of $Ge_{10}As_{40}Te_{50}$ to approximately 1.05eV at 120K.

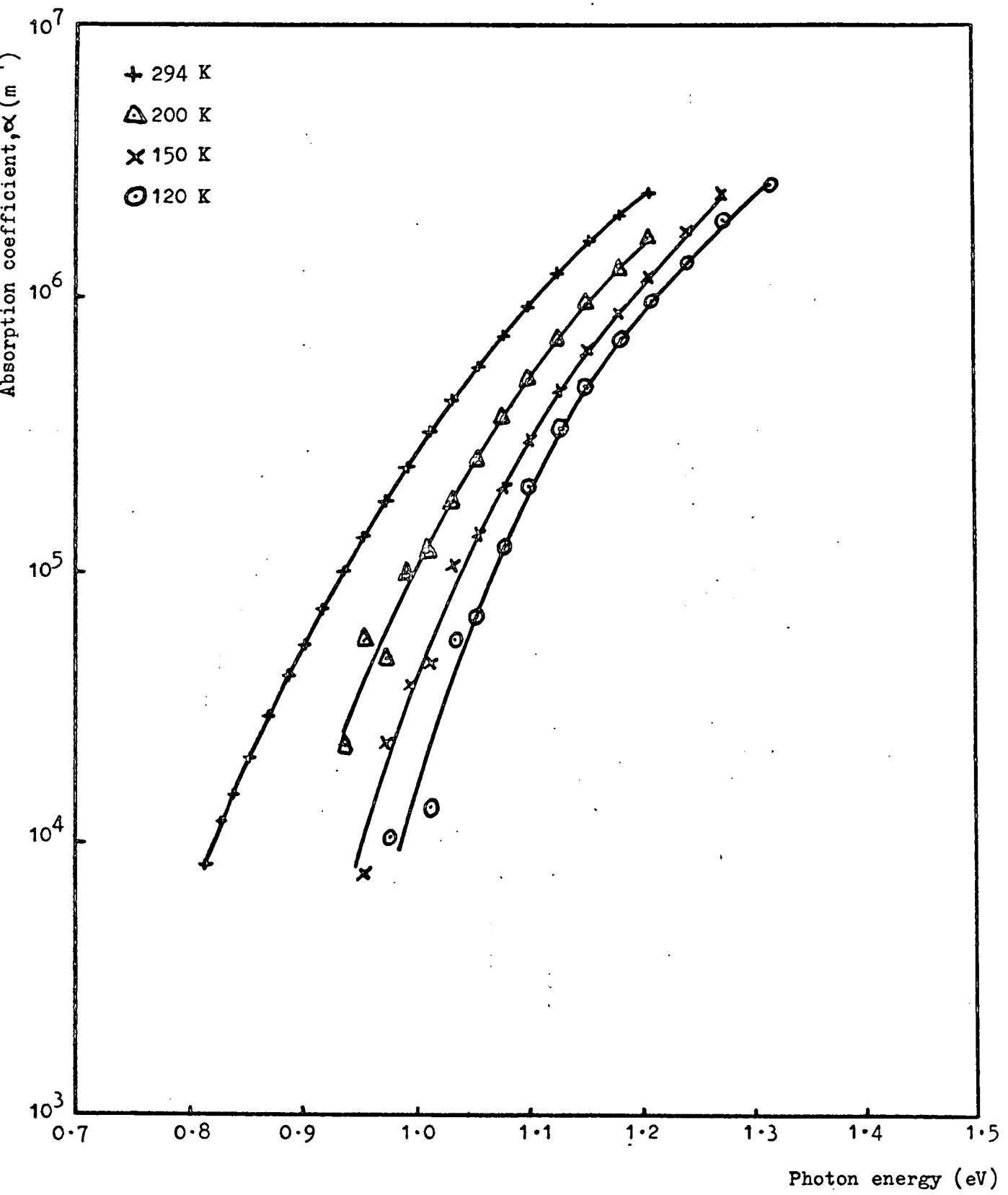

Figure 8.4 Absorption spectra of $Ge_{10}As_{40}Te_{50}$ film, thickness 3·8um, with temperature as a parameter.

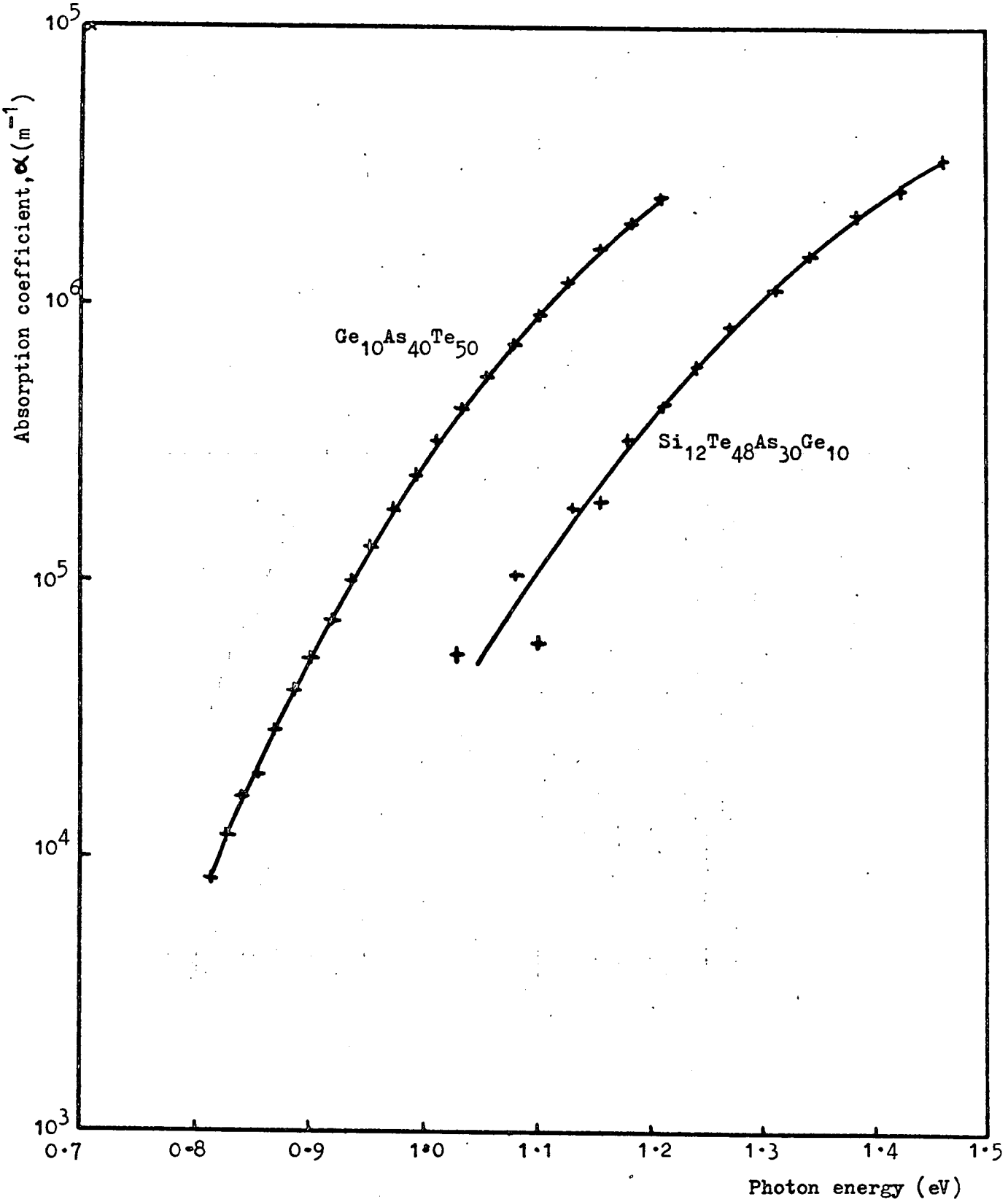

Figure 8.5 Absorption spectra of $Ge_{10}As_{40}Te_{50}$ film (3·8um) and $Si_{12}Te_{48}As_{30}Ge_{10}$ film (2·95um) at 294 K.

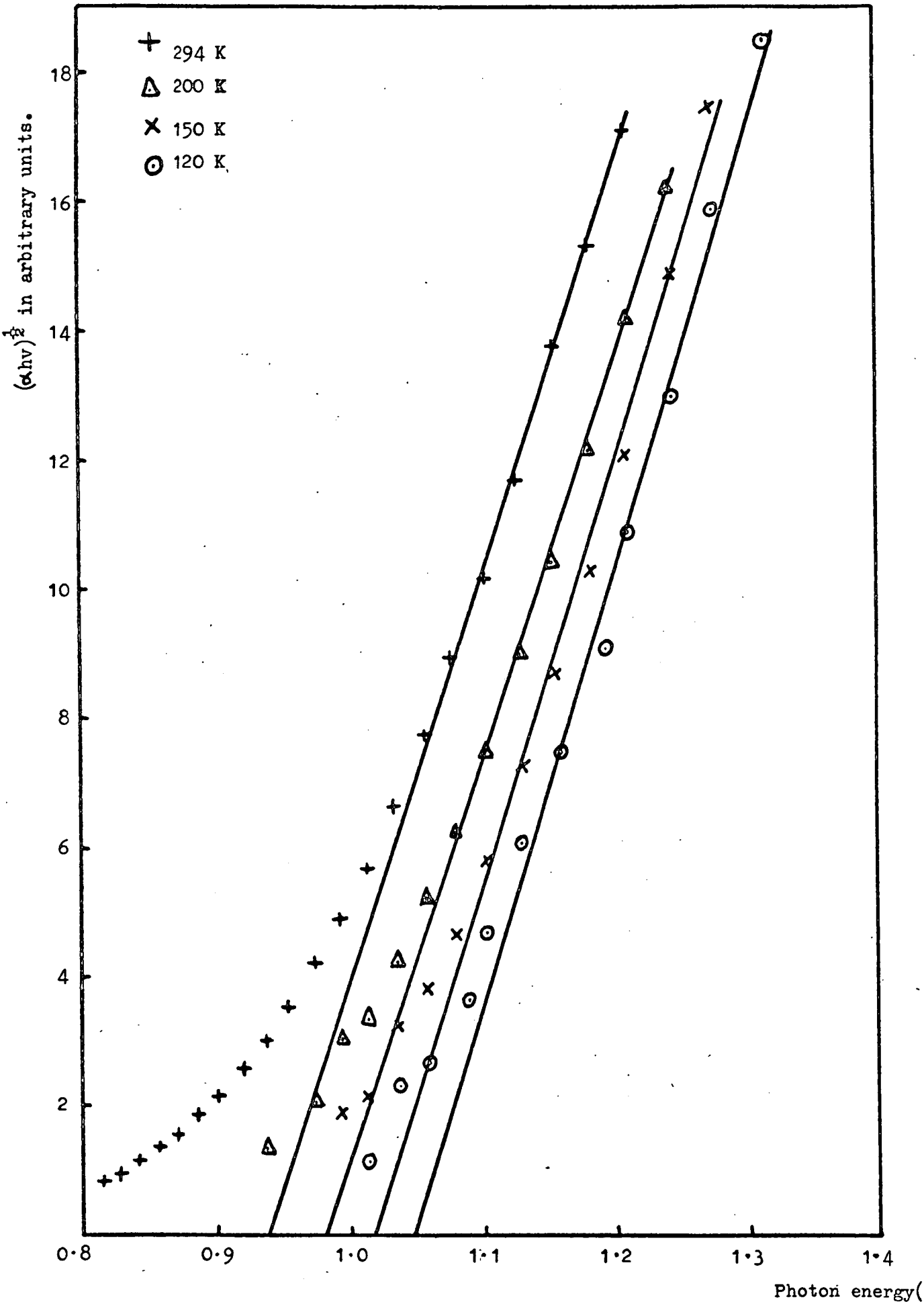

Figure 8.6 $(\alpha h\nu)^{\frac{1}{2}}$ v. photon energy for $Ge_{10}As_{40}Te_{50}$ film (3·8um) with temperature as a parameter.

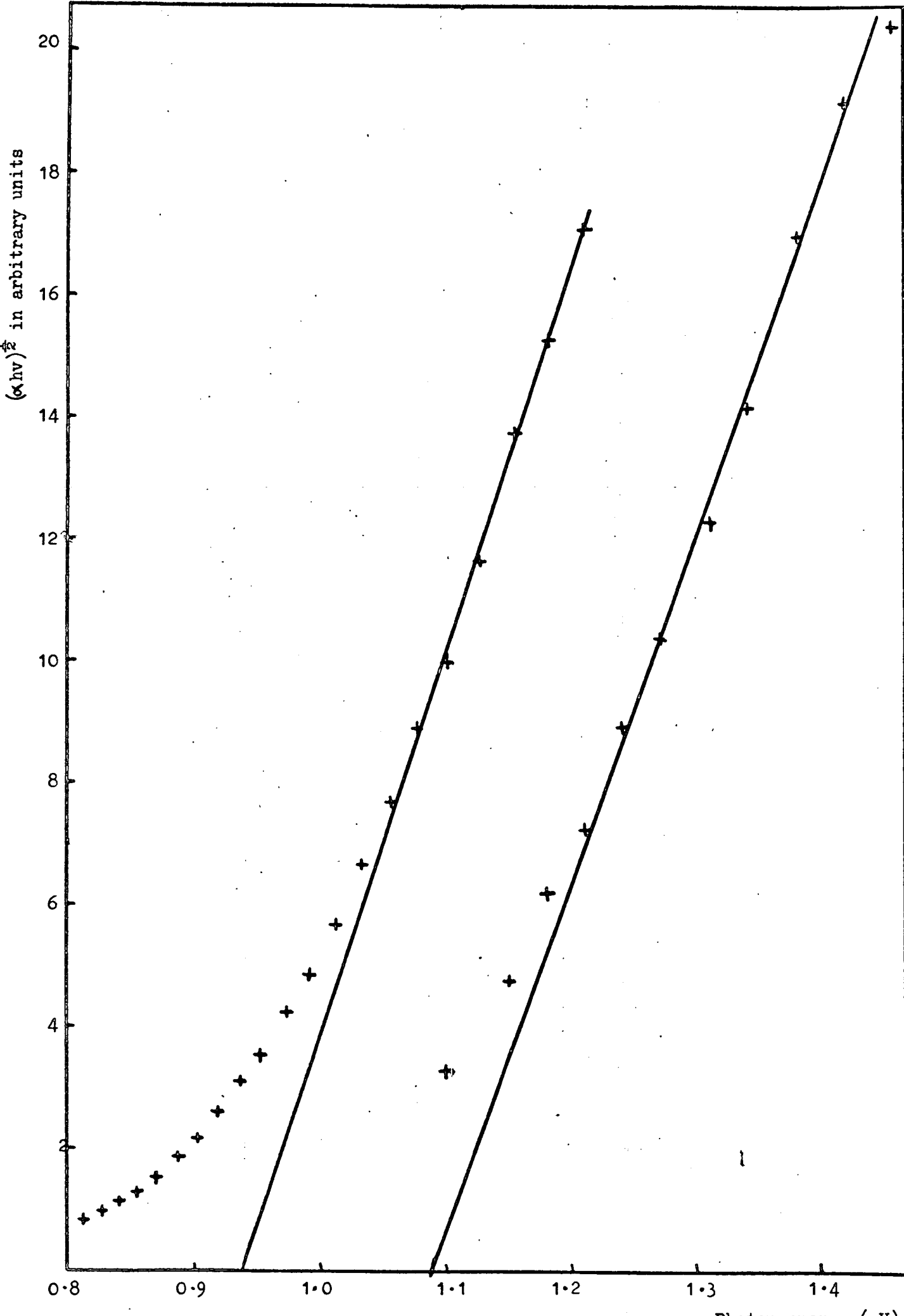

Figure 8.7 $(\alpha h\nu)^{\frac{1}{2}}$ v. photon energy for $Ge_{10}As_{40}Te_{50}$ film (3·8um) and $Si_{10}Te_{60}As_{20}Ge_{10}$ film (2·95um) at 294 K.

8.4 Photovoltaic Measurements

Employing the techniques described in Section (4.3.7), the steady-state photovoltaic response of a number of sandwich devices with semi-transparent electrodes was measured, as a function of photon energy, light intensity and, in some cases, temperature. In order to obtain a measurable response, the data was generally measured at 200K, though sometimes also at 175K and/or 150K. Figure (8.8) illustrates the typical dependence of the measured photovoltage on temperature for a fixed photon energy, $\hbar\omega$ = 1.55eV. As the temperature is decreased, so the photovoltaic response is increased, but this is accompanied by a larger and more prolonged transient response. Thus, for most measurements, an operating temperature of around 200K was desirable. Figures (8.9) and (8.10) illustrate the measured responses of typical $Ge_{10}As_{40}Te_{50}$ sandwich devices, with Au-Au and Mo-Mo electrodes respectively, while Figure (8.11) illustrates the response of a Au-$Si_{12}Te_{48}As_{30}Ge_{10}$-Au device. In each case the response to illumination through top and bottom electrodes was recorded, and the measured response is always taken at the "far" electrode (i.e. the electrode furthest from the light source) relative to earth potential at the "near" electrode (i.e. the electrode nearest the light source). The respective results are indicated appropriately in Figures (8.9) - (8.11).

Examining the data for $Ge_{10}As_{40}Te_{50}$, a broad positive response is evident, peaking around 1.35eV, on illumination through the top electrode. However, on illumination

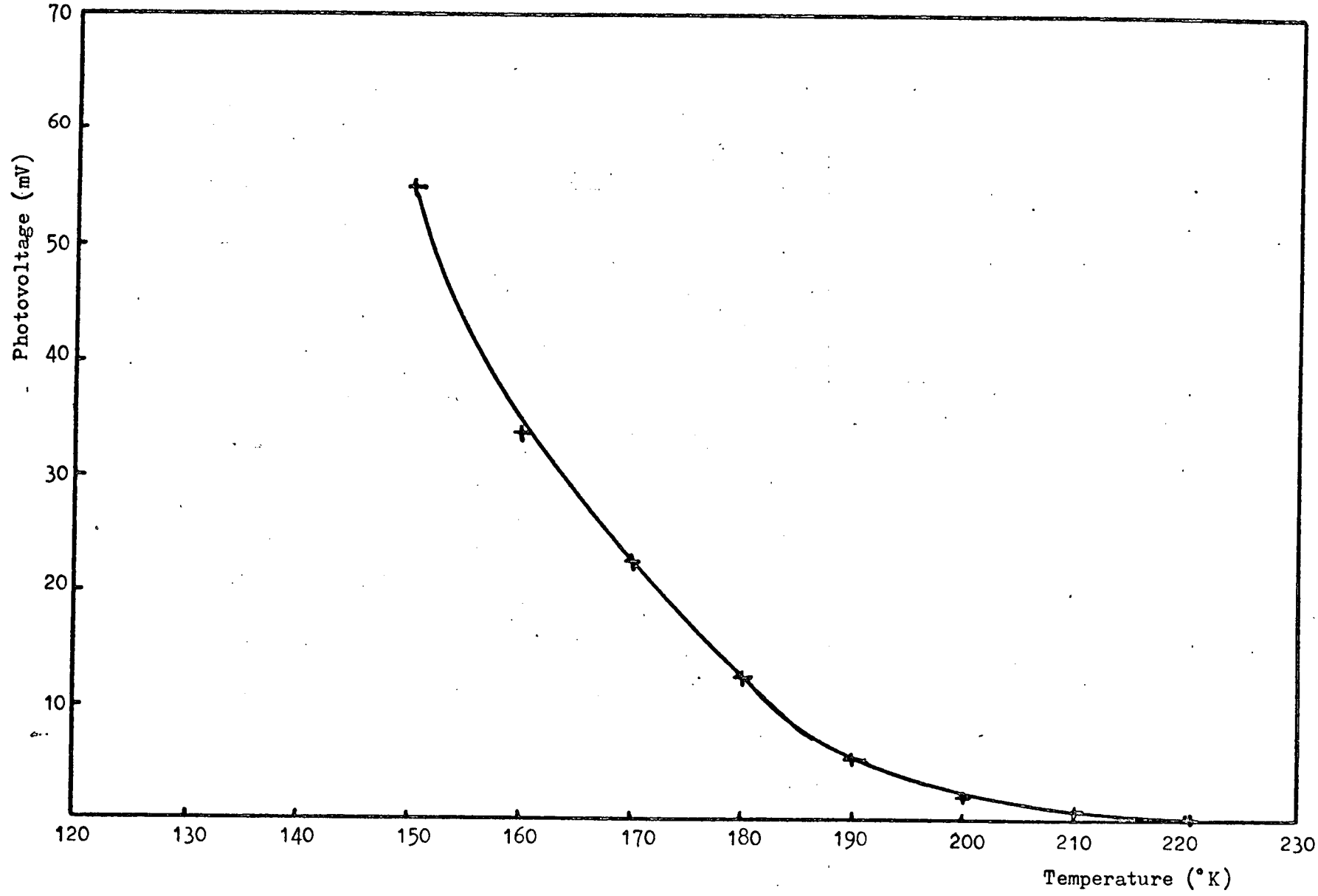

Figure 8.8 Variation of photovoltage with temperature; Au-$Ge_{10}As_{40}Te_{50}$-Au, thickness 3·7um. $h\nu$ = 1·55eV.

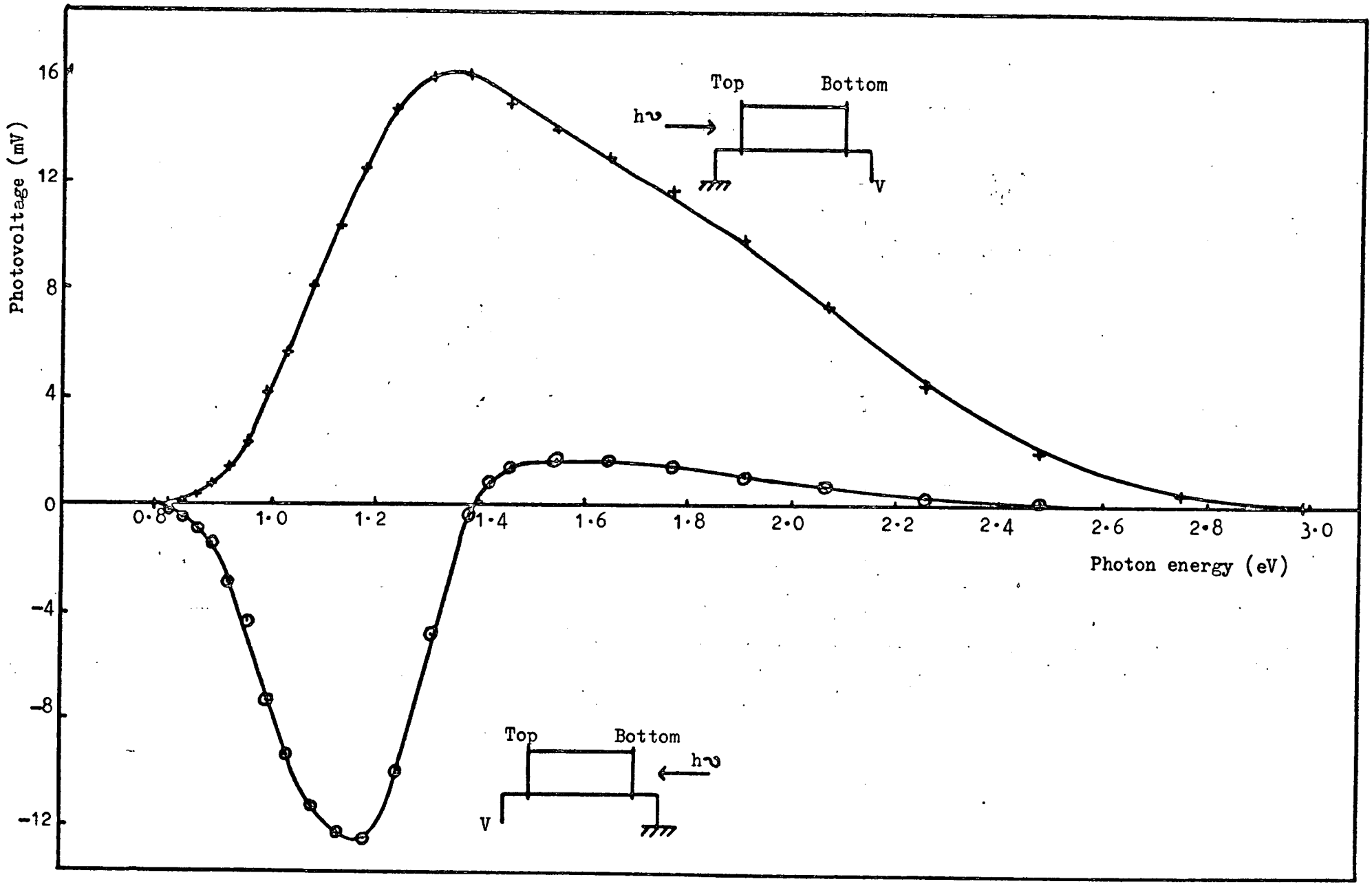

Figure 8.9 Photovoltaic spectrum of Au-$Ge_{10}As_{40}Te_{50}$-Au device, thickness 1·6μm. Temperature = 200 K

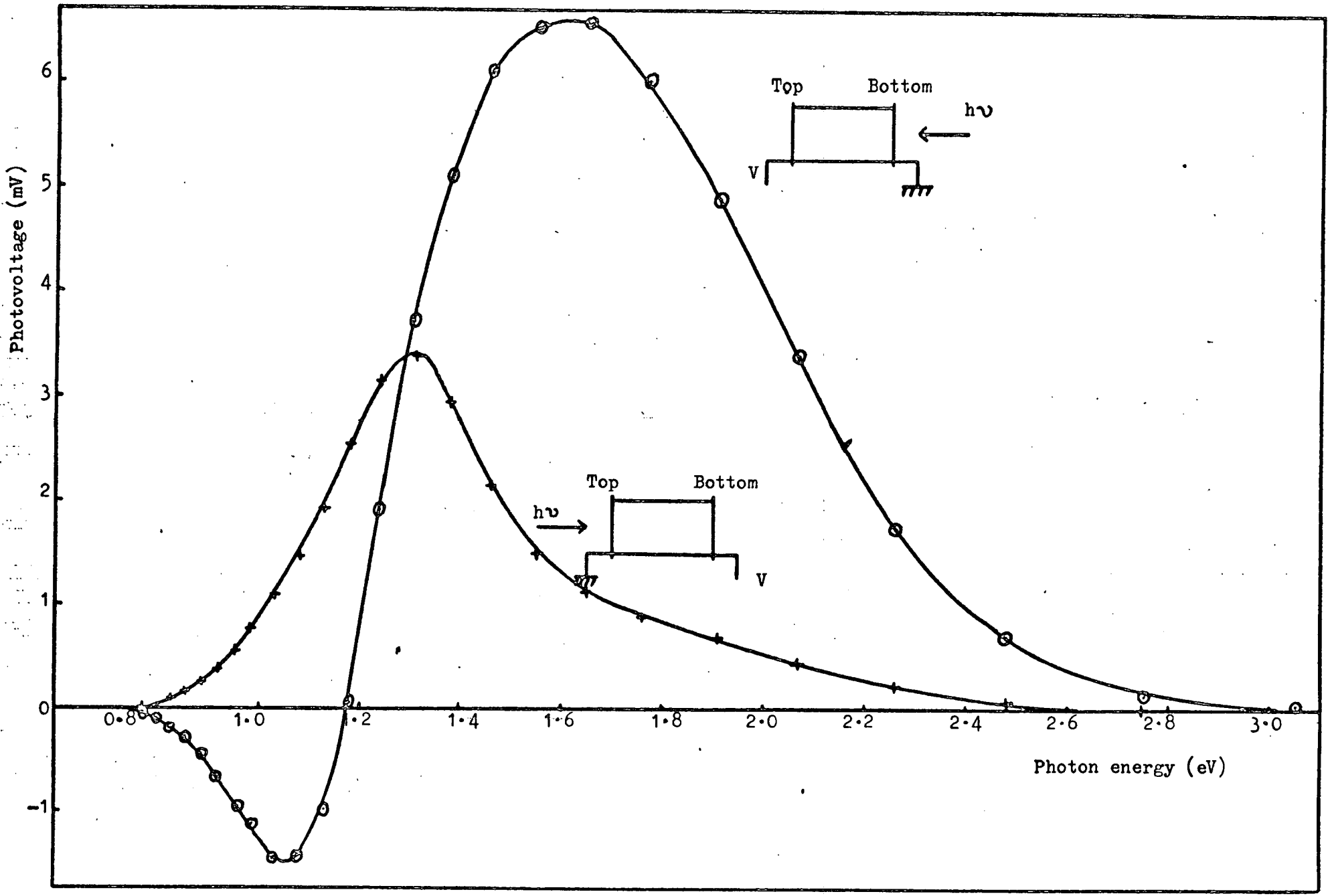
Photovoltage (mV)
6
5
4
3
2
1
0
-1
0·8
1·0
1·2
1·4
1·6
1·8
2·0
2·2
2·4
2·6
2·8
3·0
Photon energy (eV)
Top
Bottom
hυ
V
Top
Bottom
hυ
V

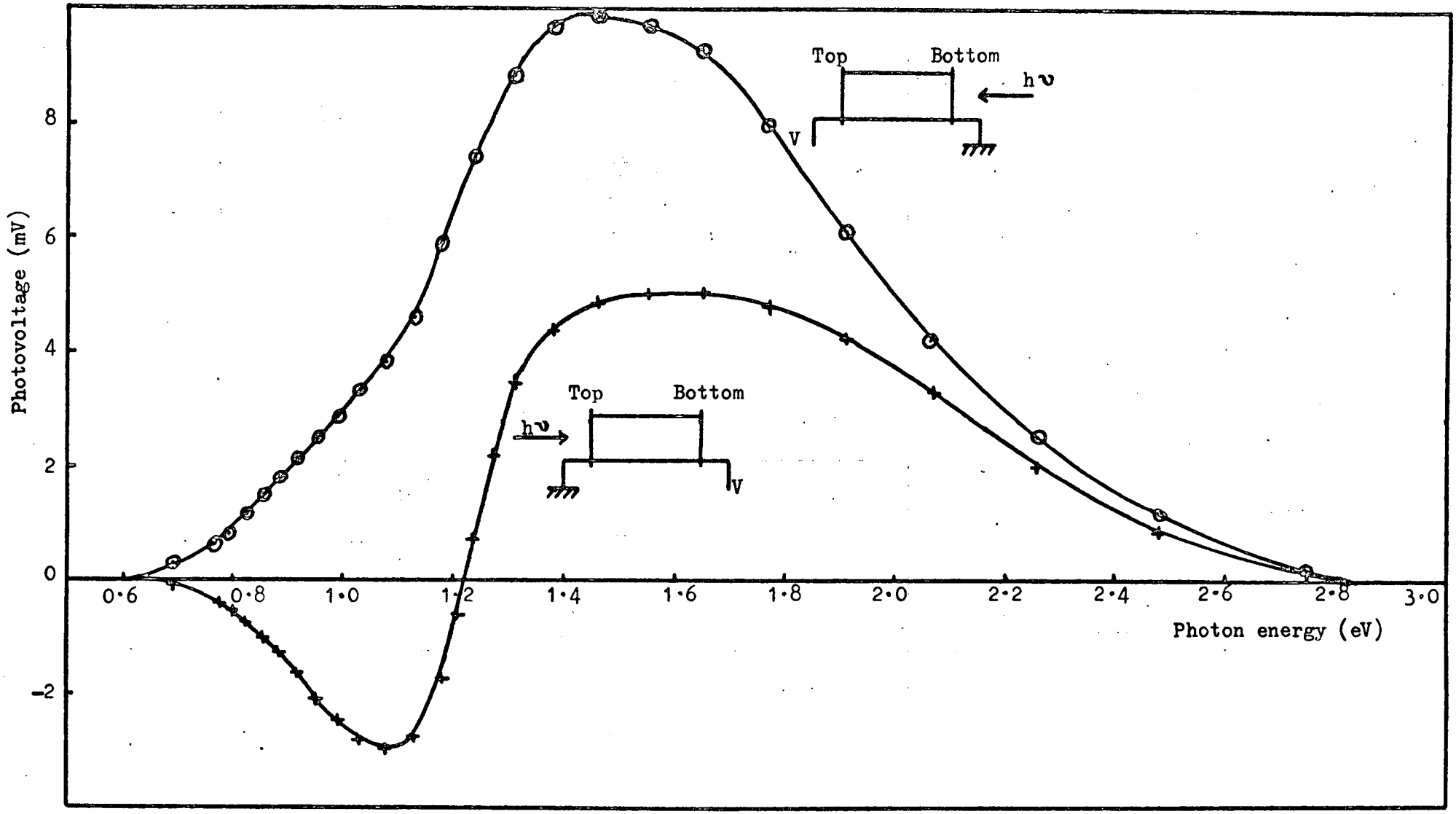

Figure 8.11 Photovoltaic spectrum of Au-$Si_{12}Te_{48}As_{30}Ge_{10}$-Au device, thickness 2·1um. Temperature = 200 K.

through the bottom electrode, there is a negative response at low photon energies, which rapidly changes polarity on approaching the high absorption region of the spectrum. On the other hand, the response of the $Si_{12}Te_{48}As_{30}Ge_{10}$ device is exactly opposite; a broad positive peak is observed on illumination through the bottom electrode and a low photon energy negative peak is observed on illumination through the top electrode. However, it must be emphasised that the spectra illustrated here apply to the majority of cases only (between 80 - 90% of the twenty $Ge_{10}As_{40}Te_{50}$ devices and the eight $Si_{12}Te_{48}As_{30}Ge_{10}$ devices tested), and it is not suggested that the results are definitive. Similarily, definite generalisations cannot be drawn with regard to the various electrode combinations from the polarity and relative magnitudes of the peaks, as the sample preparation procedure involves many imponderables, particularly in connection with the various interfaces. Nevertheless, it is possible to discuss the band structure in the sandwich devices appropriate to the data of Figures (8.9) - (8.11).

Qualitatively, the data presented here is similar in many respects to the results of Wey and Fritzsche[2] on $Ge_{16}As_{35}Te_{28}Si_{21}$ devices with a SnO_2 bottom electrode and a variety of top electrodes including Au, Sb, Al and Ni/Cr. The response to illumination through the bottom SnO_2 electrode was measured and differences in the spectra thus obtained were attributed to the different top electrode materials. Reinhard et al[3] observe that the spectral response of the zero bias photocurrent in Mo-$Te_{40}As_{35}Si_{15}Ge_7P_3$-

Mo sandwich devices has a negative peak at low photon energies but that this reverses and becomes positive at high photon energies. This is attributed to a higher barrier at the bottom contact, a quite feasible conclusion in view of the different preparation conditions of the two interfaces.

The measured photovoltage as a function of the incident photon flux, with photon energy as a parameter, is illustrated in Figure (8.12) for a Au-$Ge_{10}As_{40}Te_{50}$-Au device. This data resembles that obtained from similar experiments by Wey and Fritzsche[2] in two respects; firstly, in the general shape of the various characteristics, and secondly, while there is a considerable increase in the magnitude of the response between the $h\nu$ = 0.95eV curve and the $h\nu$ = 1.55eV curve, there is little variation between $h\nu$ = 1.55eV and $h\nu$ = 2.25eV, when $h\nu \gg E_o$ in both cases. Taking into consideration the functional dependence of the photovoltage on light intensity, the spectral output of the light source, and the electrode transmission characteristics relevant to the sample concerned, the spectrum of Figure (8.9) has been normalised to that of Figure (8.13), which shows more clearly the rapid rise in response at the absorption edge and the subsequent levelling out of the photovoltage at high photon energies, thus giving a truer representation of the relative magnitudes of the various peaks.

8.5 Theory of the Photovoltaic Response

The measured photo-response of the sandwich devices

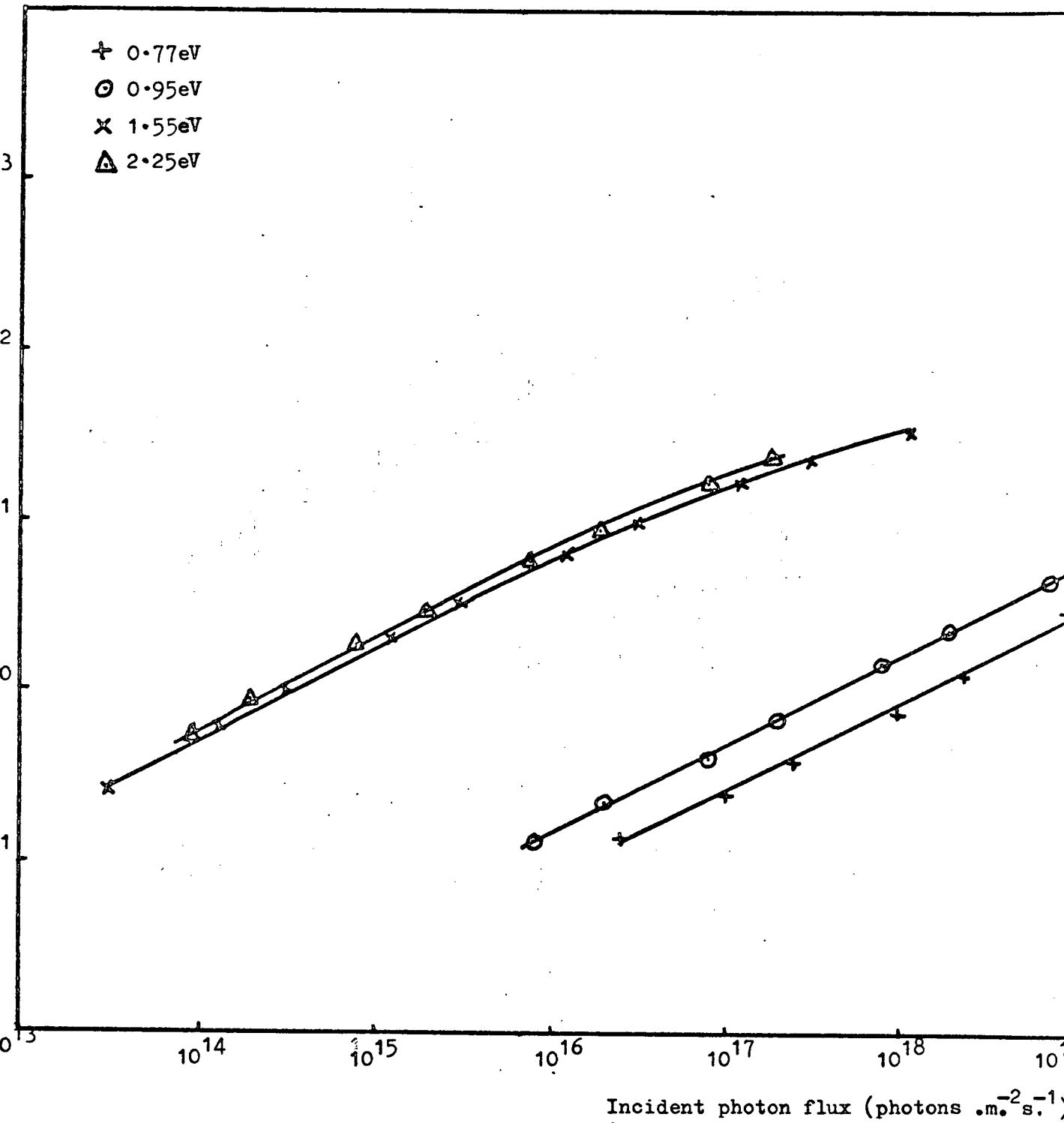

igure 8.12 Photovoltage v. incident photon flux for Au-$Ge_{10}As_{40}Te_{50}$-Au device, thickness 0·5um, with photon energy as a parameter. Temperature = 150 K.

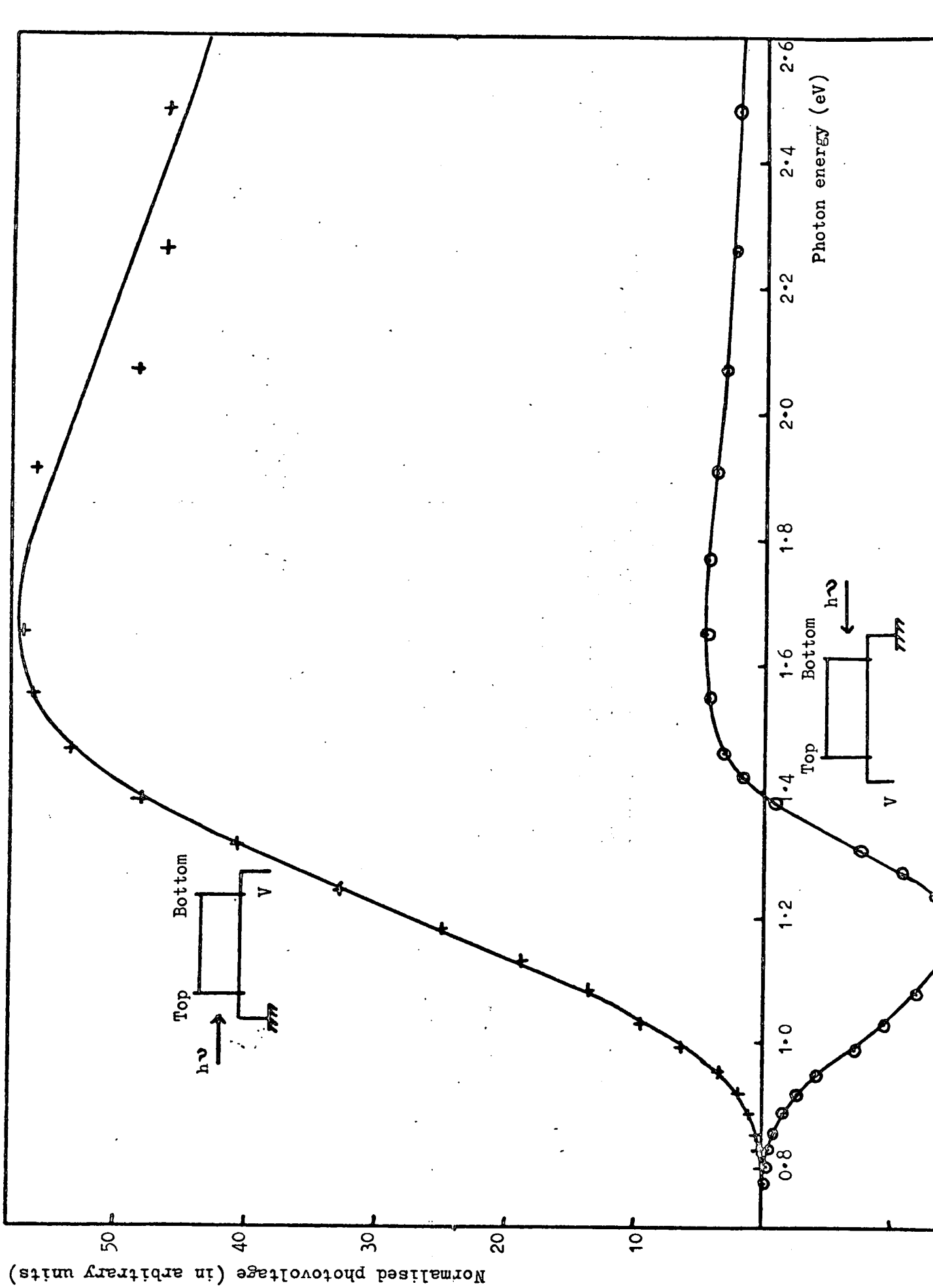

Figure 8.13 Normalised photovoltaic spectrum for Au- $Ge_{10}As_{40}Te_{50}$-Au device, thickness 1·6um. Temperature = 200 K.

is unlikely to be due to any single mechanism, rather it is a combination of three possible effects;

(i) Contact photovoltage[6] caused by band bending in the space charge regions.

(ii) Dember photovoltage[10-12] caused by the difference in mobility between electrons and holes.

(iii) Photovoltage of surface traps[13,14], due to the different capture rates of these traps for electrons and holes.

The contact photovoltage is caused by the action of the surface field on photo-excited carriers in the surface region, as illustrated in Figure (8.14). Firstly, carriers may be excited from the metal Fermi level over the potential barrier into the semiconductor. Where the barrier is very thin, as is the case in amorphous materials, this may be enhanced to some extent by an effective lowering of the barrier as carriers may quantum mechanically tunnel through the barrier below the peak. Secondly, interband transitions may occur within the semiconductor itself, either directly or via localised states, generating electron-hole pairs which drift under the influence of the barrier field. The polarity of the measured bipolar photovoltage indicates directly the nature of the band bending at the surface.

At low absorption levels, $h\upsilon \ll E_o$, the samples are illuminated uniformly throughout the bulk, but at high absorption levels, $h\upsilon \gg E_o$, the samples are opaque and an excess of electron-hole pairs is produced at the top surface, so that any difference in the diffusion rates of the carriers will result in a Dember photovoltage. As

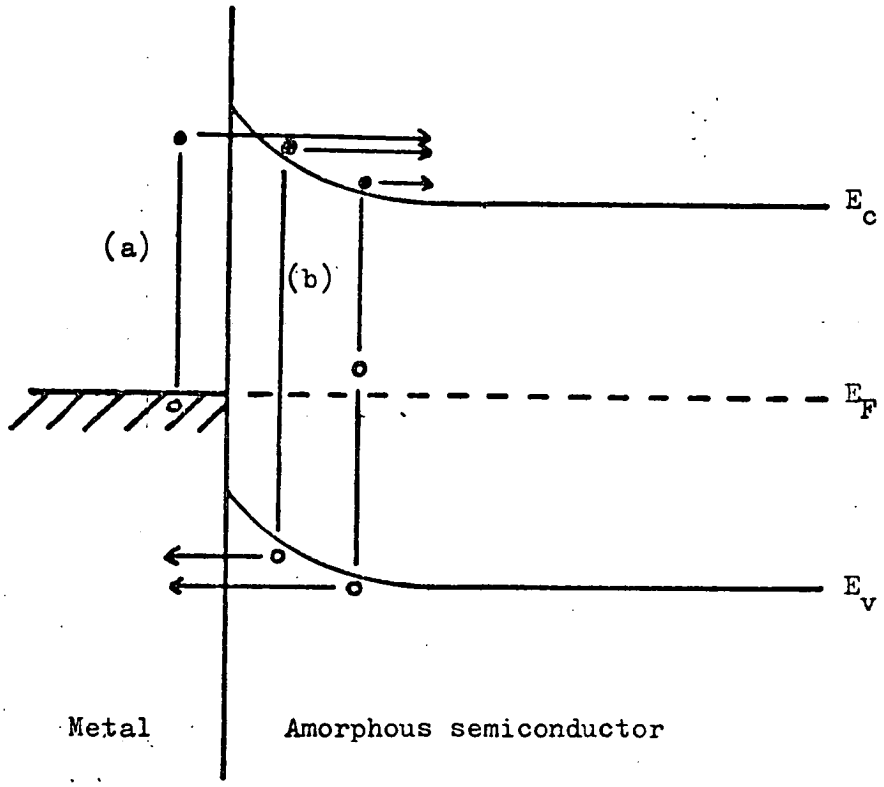

Figure 8.14 Photovoltaic processes at metal - amorphous semiconductor contact.

(a) Photoemission from the metal.
(b) Photoemission from interband transitions.

discussed in previous chapters, the dominant carriers in materials of this nature are holes. Thus any Dember contribution would be manifest as a positive photovoltaic response at high photon energies, added to the contact photovoltage at the near contact. In all the samples tested, a positive response at high photon energies was evident, which suggests strongly that the Dember contribution may be significant.

The magnitude of the Dember photovoltage is given by[11,12]

$$V_D = \frac{(\mu_n/\mu_p - 1)}{(\mu_n/\mu_p - 1)} \cdot (kT/q) \cdot \ln\left[\frac{n_{light}}{n_{dark}}\right] \qquad (8.5.1)$$

where μ_n and μ_p are the electron and hole trap limited drift mobilities and n_{light} and n_{dark} are the light and dark carrier densities respectively. The ratio of n_{light}/n_{dark} has been estimated for a particular photon energy $h\nu$ = 1.35eV by measuring the dark conductivity and the conductivity under illumination of a coplanar sample of $Ge_{10}As_{40}Te_{50}$, thickness 0.22 um., using the technique of Heilmeier and Zanoni[15]. At this particular wavelength, the product of the absorption coefficient and the sample thickness is unity, and hence the ratio of the light and dark carrier densities can be approximated by the ratio of the light and dark conductivities; i.e.

$$\frac{n_{light}}{n_{dark}} \simeq \frac{\sigma_{light}}{\sigma_{dark}} \simeq 11 \qquad (8.6.2)$$

Assuming a mobility ratio, $\frac{\mu_n}{\mu_p}$, as between 0.1 and 0.3, appropriate to materials of this nature,[16] the value

of the Dember photovoltage is then,

$$V_D = 22 - 26mV$$

Allowing for electrode transmission values between 10% and 20%, this is reduced to

$$V_D = 2 - 7mV$$

for the particular wavelength considered. Thus the effect of the Dember photovoltage must be considered at high photon energies, although there is insufficient information to allow an exact calculation.

The surface photovoltage is in some ways analogous to the Dember voltage, and is most significant at high photon energies, when a high non-equilibrium carrier density is created on the surface of the semiconductor. Preferential trapping of carriers of one sign in surface states, accompanied by diffusion of carriers of the opposite sign through the bulk, may result in a further photovoltaic contribution. The effect can be useful in obtaining information about the surface trapping statistics in crystalline semiconductors;[13] if the contact photovoltage can be eliminated by straightening the bands with an applied field; i.e. achieving the "flat-band" condition. In the case of the chalcogenide glasses investigated, however, it adds an additional ambiguity to the interpretation of the photovoltaic spectra.

In a discussion of the photovoltaic response, the data of Figure (8.13) is considered, although the same arguments apply to all the devices tested. At low photon energies, the light penetrates throughout the sample

illuminating it uniformly throughout the bulk, and the photovoltaic response can be considered as the resultant of the two contact photovoltages. As a negative peak is observed on illumination through the bottom contact (in this case), but a positive response is evident on illumination through the top contact, this implies either;

(i) a dominant region of negative space charge at the top contact.

(ii) a dominant region of positive space charge at the bottom contact.

(iii) a combination of factors (ii) and (i).

Between $h\nu = 1.1eV$ and $h\nu = 1.4eV$ approximately, there is a steep positive gradient in the measured characteristic, probably dominated by a substantially increasing Dember contribution as the absorption coefficient increases. At high photon energies, the response is considered to be the resultant of the near contact photovoltage, the Dember contribution, and the surface photovoltage. Under the assumptions that the Dember response is the same in both directions, and that the characteristic is not dominated by asymmetric trapping statistics, the considerably greater magnitude of the response to illumination through the top contact suggests that the characteristic is dominated by downward bending of the bands at the top contact.

8.6 Discussion

The photovoltaic effect in sandwich devices does appear to indicate that space charge regions exist at

metal-chalcogenide thin film interfaces, but the possibility of complicating additional photo-responses does not permit a totally unambiguous model of the device structure. For this reason, the author does not believe that any model presented here or elsewhere[4,17] for the metal-chalcogenide-metal device can be entirely definitive. However, in Figures (8.15) and (8.16), partial models of the metal-$Ge_{10}As_{40}Te_{50}$-metal and metal-$Si_{12}Te_{48}As_{30}Ge_{10}$-metal devices are illustrated, representative of the majority of devices tested. An asymmetric model of these devices is quite plausible, even where identical electrode materials are used, as the reverse sequence of deposition of metal and semiconductor film may have a significant effect on the interfacial characteristics. Although both models have pronounced negative space charge regions at one of the contacts, there is no reason to expect blocking contacts, as discussed in Chapter 6.

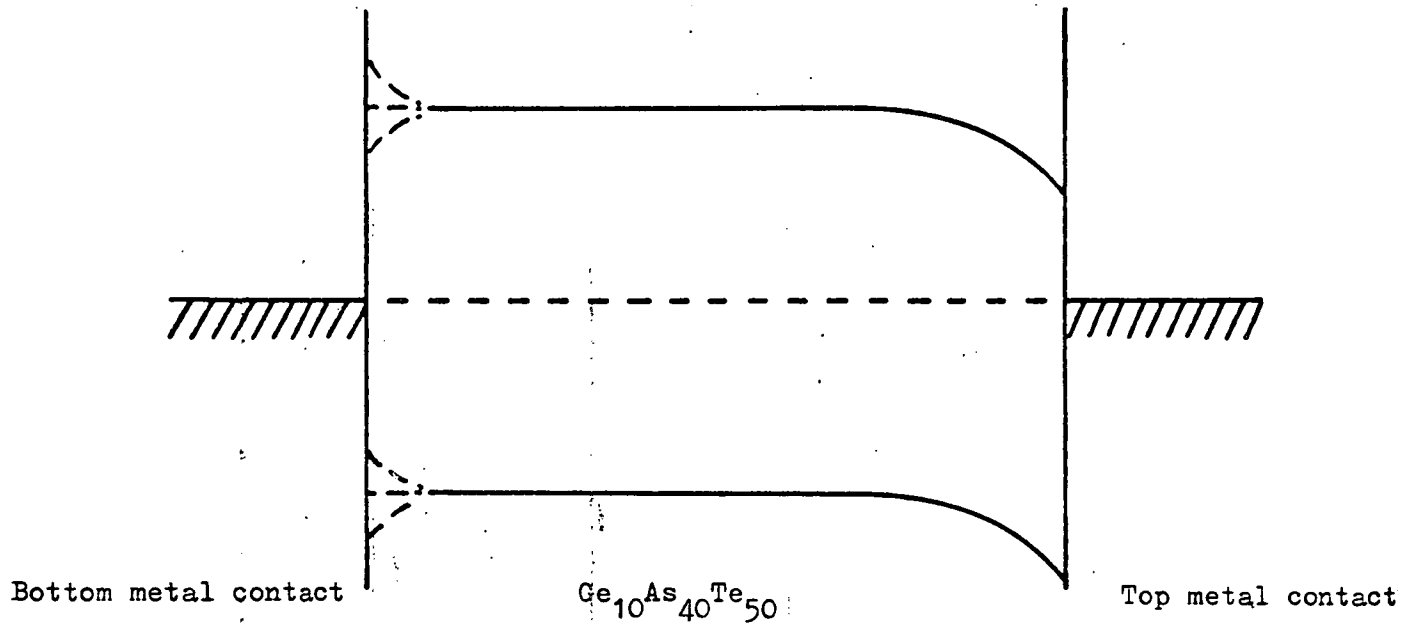

Figure 8.15 Band model for $Ge_{10}As_{40}Te_{50}$ sandwich device.

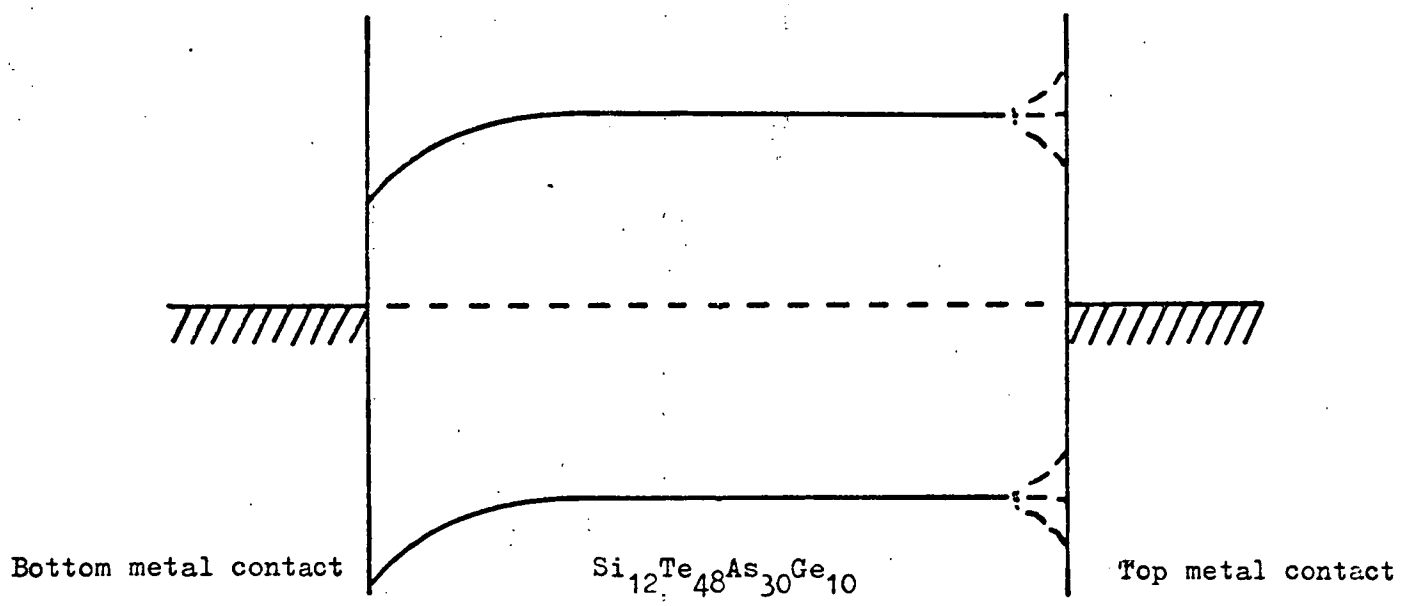

Figure 8.16 Band model for $Si_{12}Te_{48}As_{30}Ge_{10}$ sandwich device.

9.1 Introduction

In recent years, increasing interest has developed in the behaviour of heterojunctions formed between crystalline and amorphous semiconductors. The bulk of this work can be divided into two categories; firstly junctions formed between amorphous and crystalline silicon[1-5], and secondly junctions formed between amorphous chalcogenide glasses and a crystalline semiconductor, usually silicon,[6-12] although germanium[13,14] and cadmium-sulphide[15] have also been used. Whereas non-blocking contacts are generally observed at metal contacts to chalcogenide alloy films, the silicon-chalcogenide heterojunction is highly rectifying, and it is desirable to assess to what extent the observed characteristics depend on the respective band structures of the two materials in contact. The amorphous $Ge_{10}As_{40}Te_{50}$ - crystalline silicon heterojunction is particularly interesting as the optical band gaps are similar (for $Ge_{10}As_{40}Te_{50}$, approximately 0.94eV at room temperature and for silicon approximately 1.1eV at room temperature). Furthermore the fact that hole transport is the dominant conduction mechanism in the chalcogenide glass might result in different junction behaviour with n- and p-type silicon. To this end, amorphous $Ge_{10}As_{40}Te_{50}$ - crystalline n-type Si(NSC) and amorphous $Ge_{10}As_{40}Te_{50}$ - crystalline p-type Si (PSC) junctions were prepared, as detailed in Section (4.2.7), and the current-voltage characteristics, the photo-electric behaviour, and the

variation of capacitance with applied reverse bias have been investigated.

9.2 Experimental Results

The current-voltage characteristics of PSC heterojunction samples with progressively higher resistivity substrates (i.e. lower doping concentrations) are illustrated in Figures (9.1) to (9.3), while Figures (9.4) and (9.5) contain the corresponding data for NSC devices. The characteristics are strongly rectifying in all cases, a relatively high sample resistance being evident for positive bias on the chalcogenide in the case of p-type substrates, and for negative bias on the chalcogenide in the case of n-type substrates. The slope resistance of the forward characteristic (measured from larger scale diagrams than those in Figures (9.1) to (9.5)) corresponds closely to a theoretical value calculated from the known resistivity of $Ge_{10}As_{40}Te_{50}$ films obtained from the data of Chapter 5. For instance, the calculated resistance for a $Ge_{10}As_{40}Te_{50}$ film of thickness 1.2 um. and with an electrode area defined by a circle of radius 0.87 mm. (the appropriate dimensions in the case of the device of Figure (9.1)) is approximately 2K.Ohm.

The reverse characteristics of PSC and NSC devices are, however, noticeably different. Consider first of all the typical low field characteristics illustrated by the dark characteristics of Figures (9.6) and (9.7) respectively. The PSC devices reach a saturation current level almost immediately; i.e. a current of the order of 10^{-7}A at 1V for

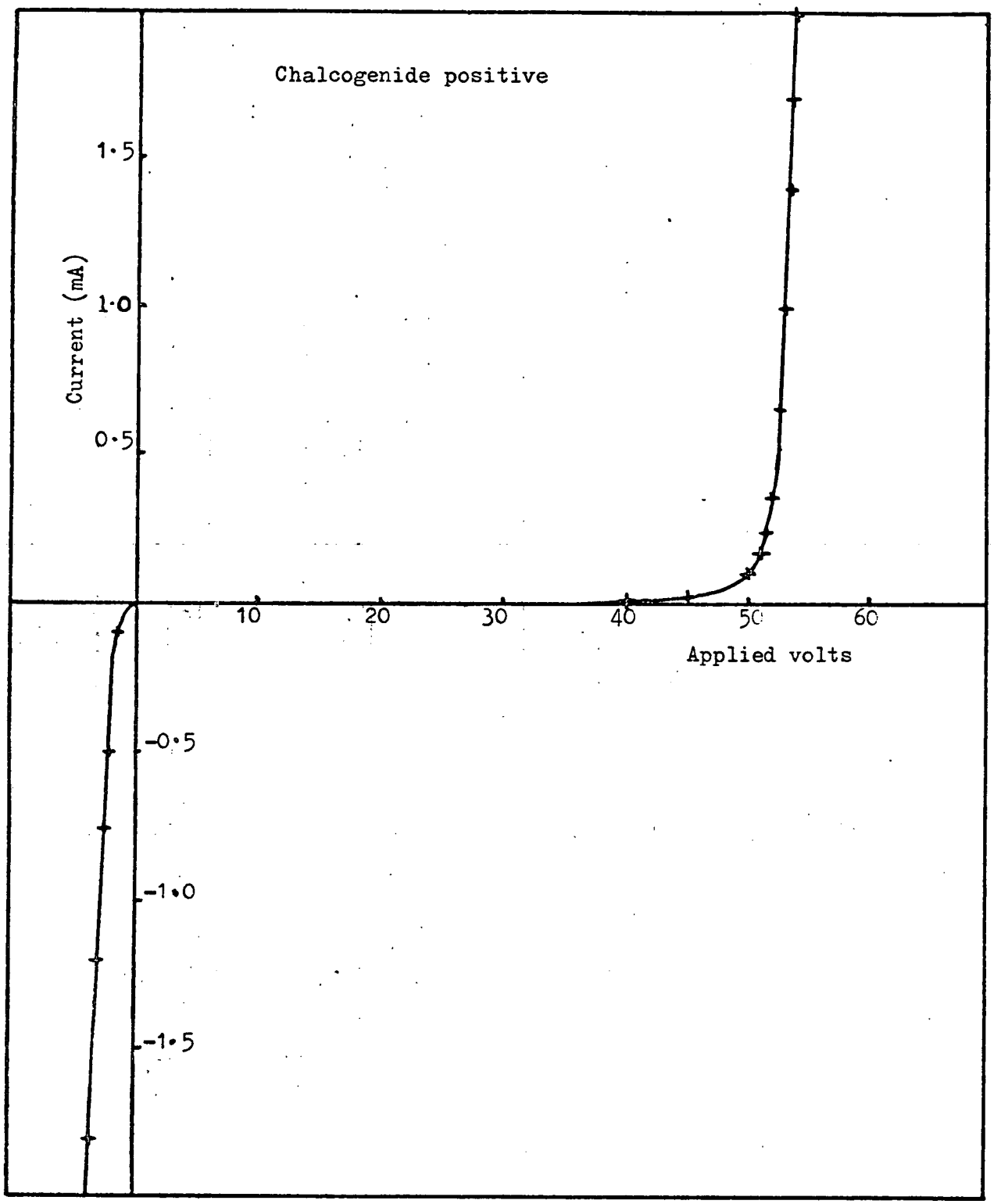

Figure 9.1 Current-voltage characteristic of PSC device.
Resistivity (Si) = 0·01250hm.m.
$Ge_{10}As_{40}Te_{50}$ thickness = 1·2um.
Spot diameter = 0·87mm.
Temperature = 293 K.

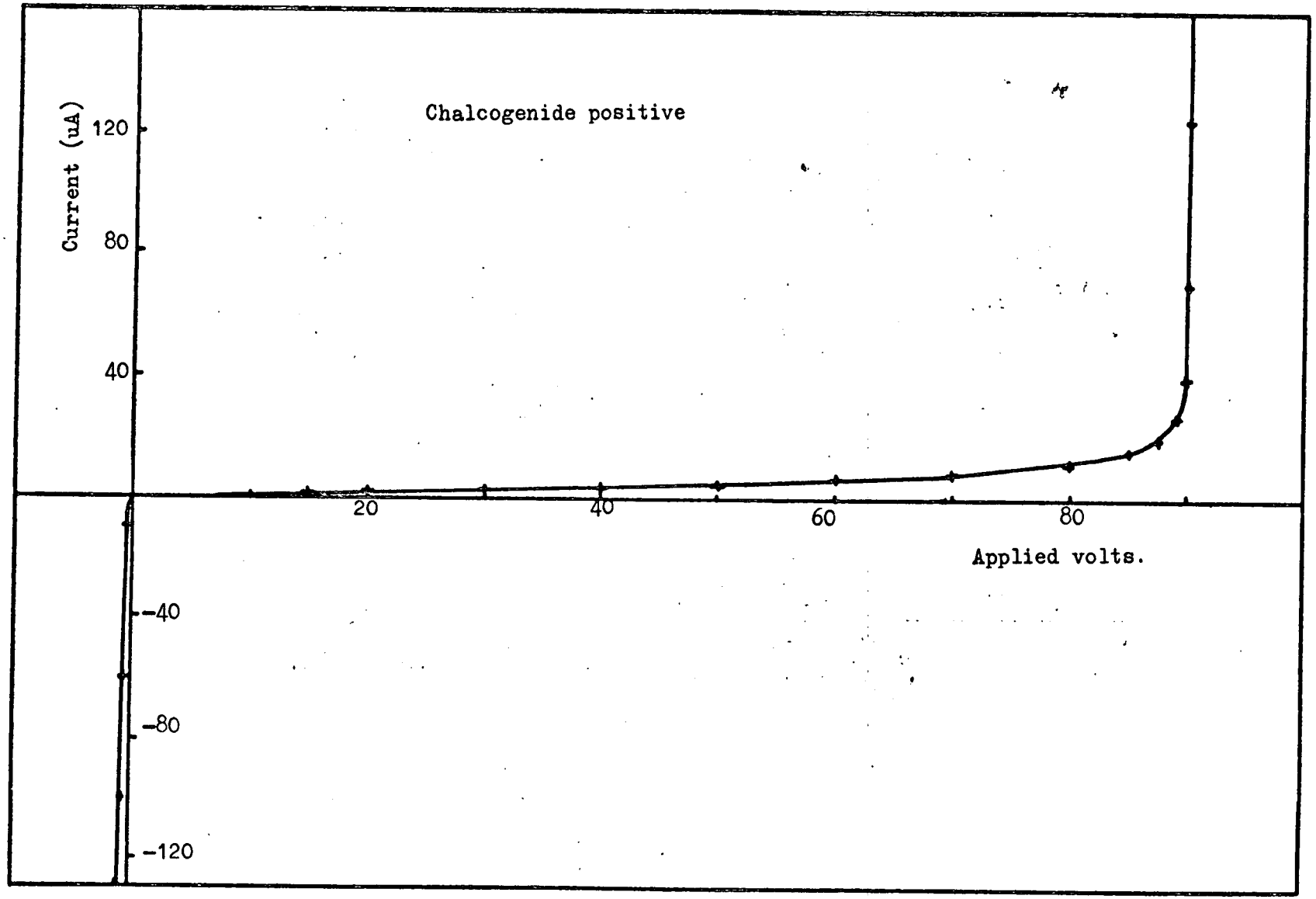

Figure 9.2 Current-voltage characteristic of PSC device. Resistivity(Si) = 0·025Ohm.m. $Ge_{10}As_{40}Te_{50}$ thickness = 2um. Spot diameter = 0·23cm. Temperature = 293 K.

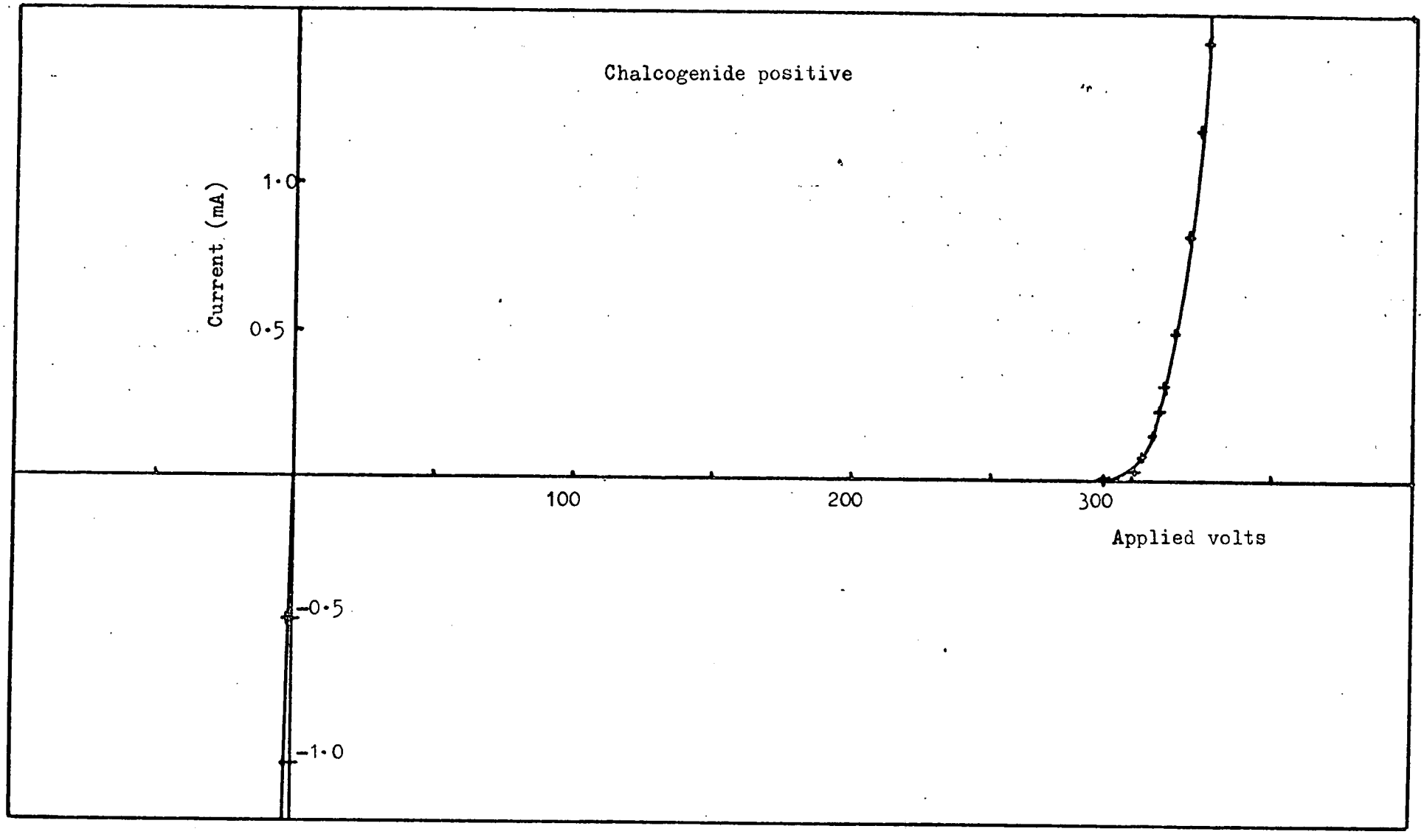

Figure 9.3 Current-voltage characteristic of PSC device. Resistivity (Si) = 0·15Ohm.m. $Ge_{10}As_{40}Te_{50}$ thickness = 1·3um. Spot diameter = 0·87mm. Temperature = 293 K.

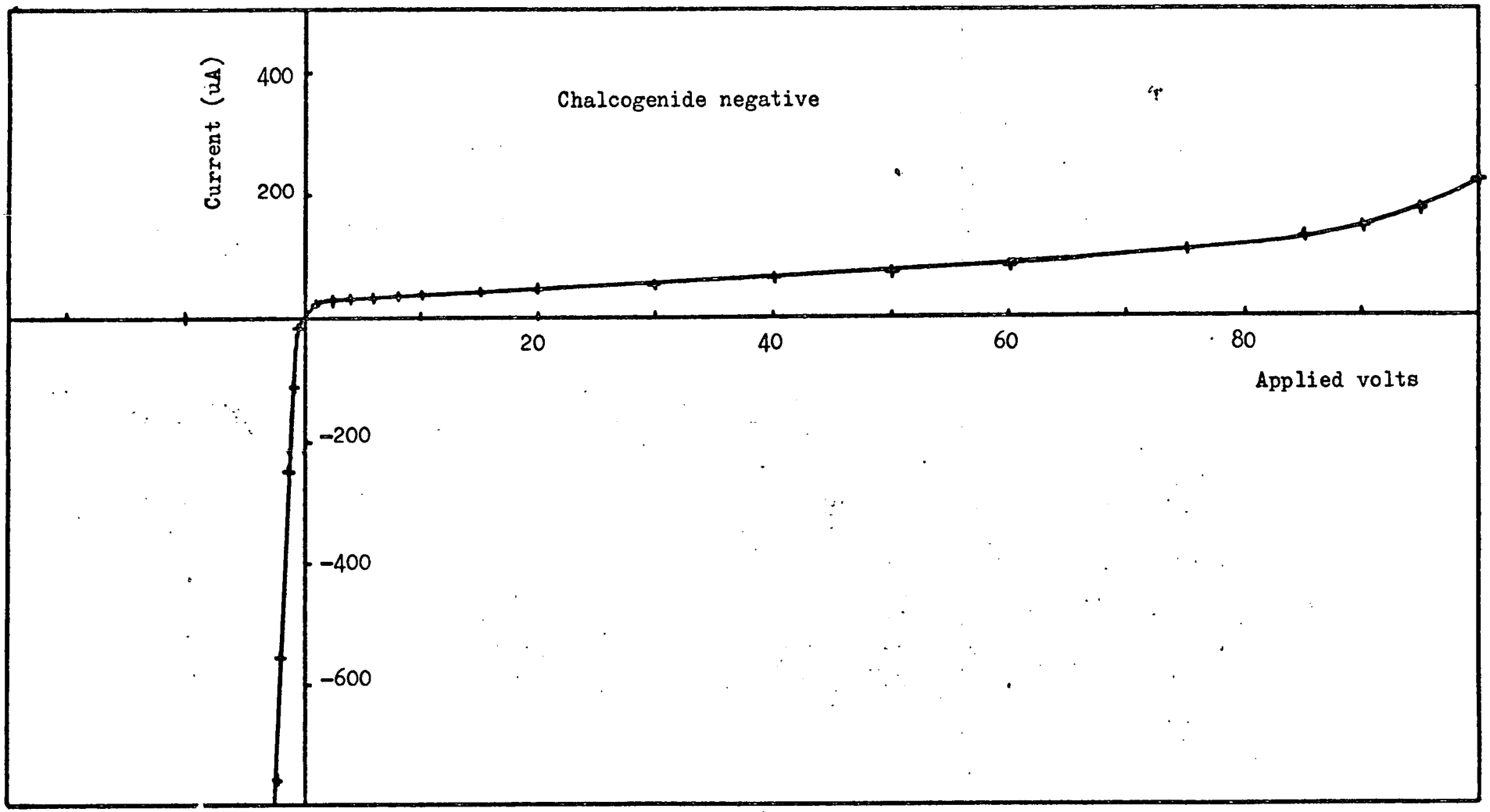

Figure 9.4 Current-voltage characteristic of NSC device. Resistivity (Si) = 0·025Ohm.m. $Ge_{10}As_{40}Te_{50}$ thickness = 0·7um. Spot diameter = 0·87mm. Temperature = 293 K.

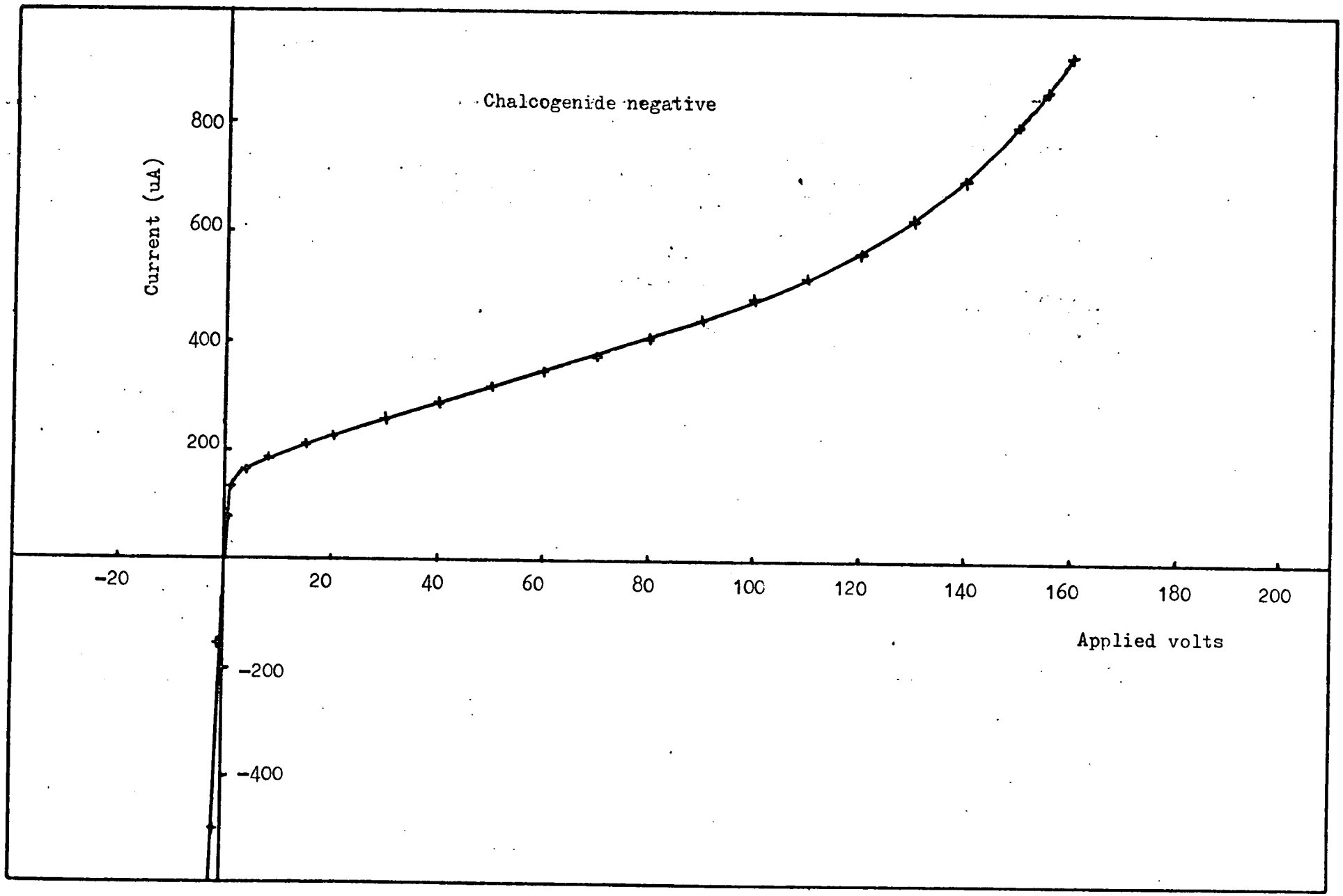

Figure 9.5 Current-voltage characteristic of NSC device. Resistivity (Si) = 0·08Ω.m. $Ge_{.28}As_{.12}Te_{.6}$ thickness = 0·7um.

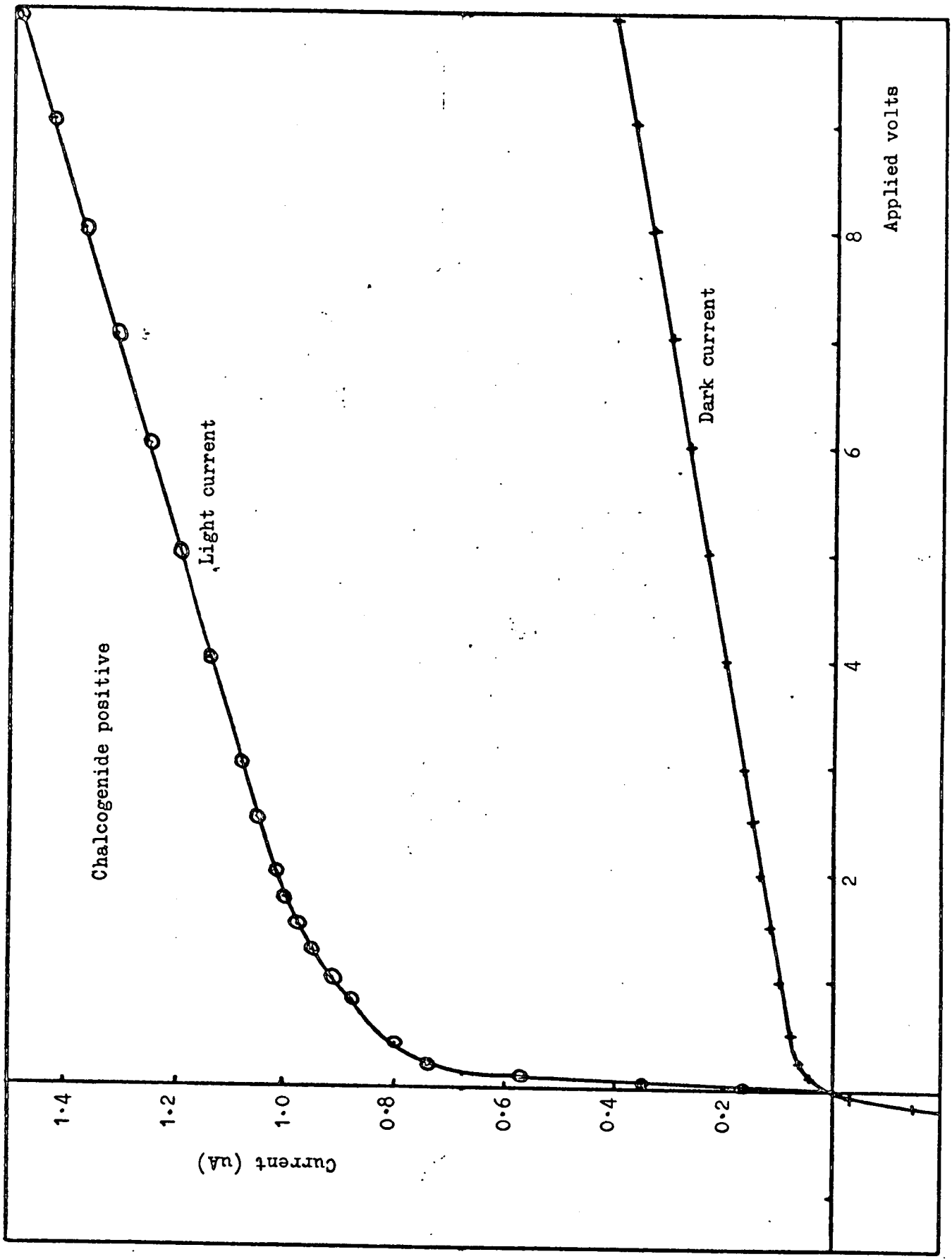

Figure 9.6 Expanded characteristics of PSC device. Resistivity (Si) = 0·01250hm.m
$Ge_{10}As_{40}Te_{50}$ thickness = 1·2um. Spot diameter = 0·23cm.
Temperature = 293 K.

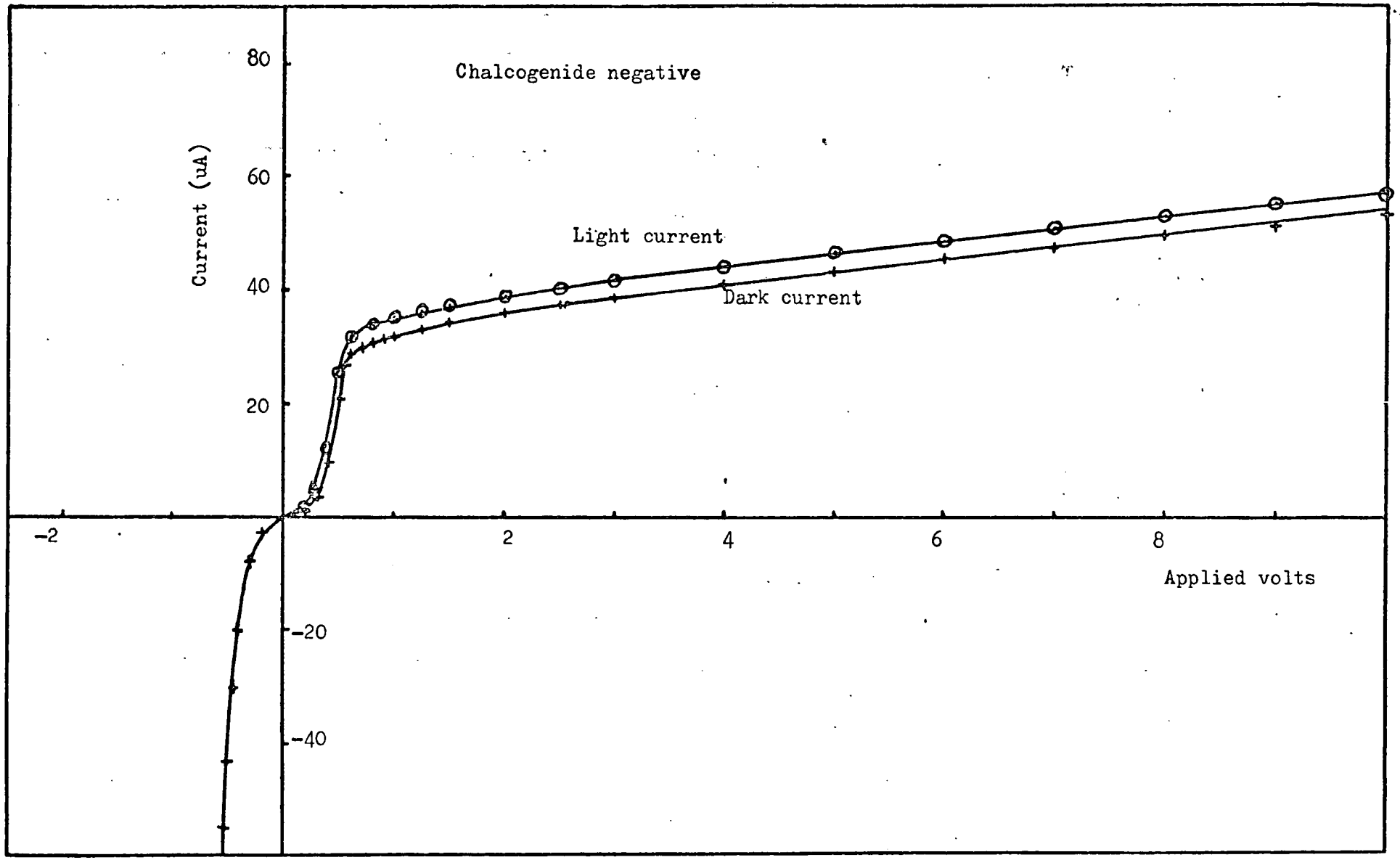

Figure 9.7 Expanded current-voltage characteristics of NSC device. Resistivity (Si) = 0·025Ohm.m $Ge_{10}As_{40}Te_{50}$ thickness,1

the particular device illustrated. On the other hand, the NSC device characteristics are almost symmetrical up to 0.5V, and attain a much higher reverse saturation current, of the order of 3.10^{-5}A at 1V for this device. In both cases the reverse saturation current increases with applied reverse bias, but returning to the data illustrated in Figures (9.1) to (9.5), it is evident that the reverse characteristic of the NSC devices is much "softer". While a clearly defined reverse breakdown point is evident in the PSC devices, the high current level through the chalcogenide film in the NSC samples generally led to switching of the device.

Using the techniques described in Section (4.3.3), the variation of device capacitance with applied reverse bias was measured at a frequency of 140KHz, and examples of the $^1/_{C2}$ vs. V characteristics are shown in Figures (9.8) and (9.9). A linear dependence is observed over the entire range and the extrapolated negative intercept on the horizontal axis is typically about 0V for NSC devices, and ranges between -1.0V and -4.2V for PSC devices. As a better illustration of this, Figure (9.10) contains expanded low-field characteristics of a number of PSC and NSC devices.

The spectral photoresponses of a PSC and an NSC device are illustrated in Figures (9.11) and (9.12) respectively. In each case, the light beam was incident on the thin molybdenum top electrode, adjacent to the $Ge_{10}As_{40}Te_{50}$ film. The two samples were prepared simultaneously, so that the chalcogenide layers and the semi-transparent electrodes are

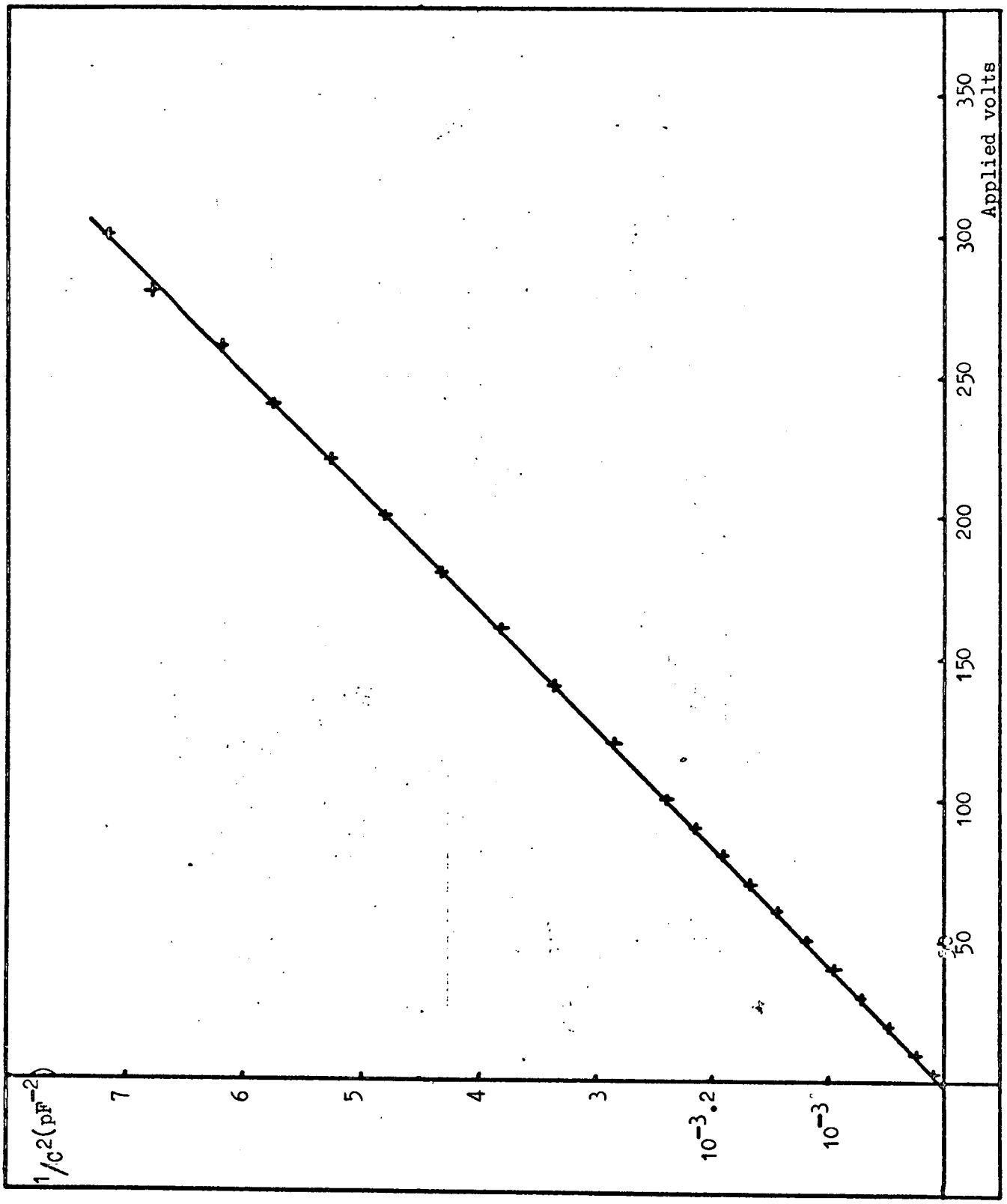

Figure 9.8 $1/C^2$ vs. V characteristic of PSC device. Resistivity (Si) = 0·15Ωm. $Ge_{10}As_{40}Te_{50}$ thickness = 1·3um. Spot diameter = 1·7mm. Temperature Temperature = 293 K.

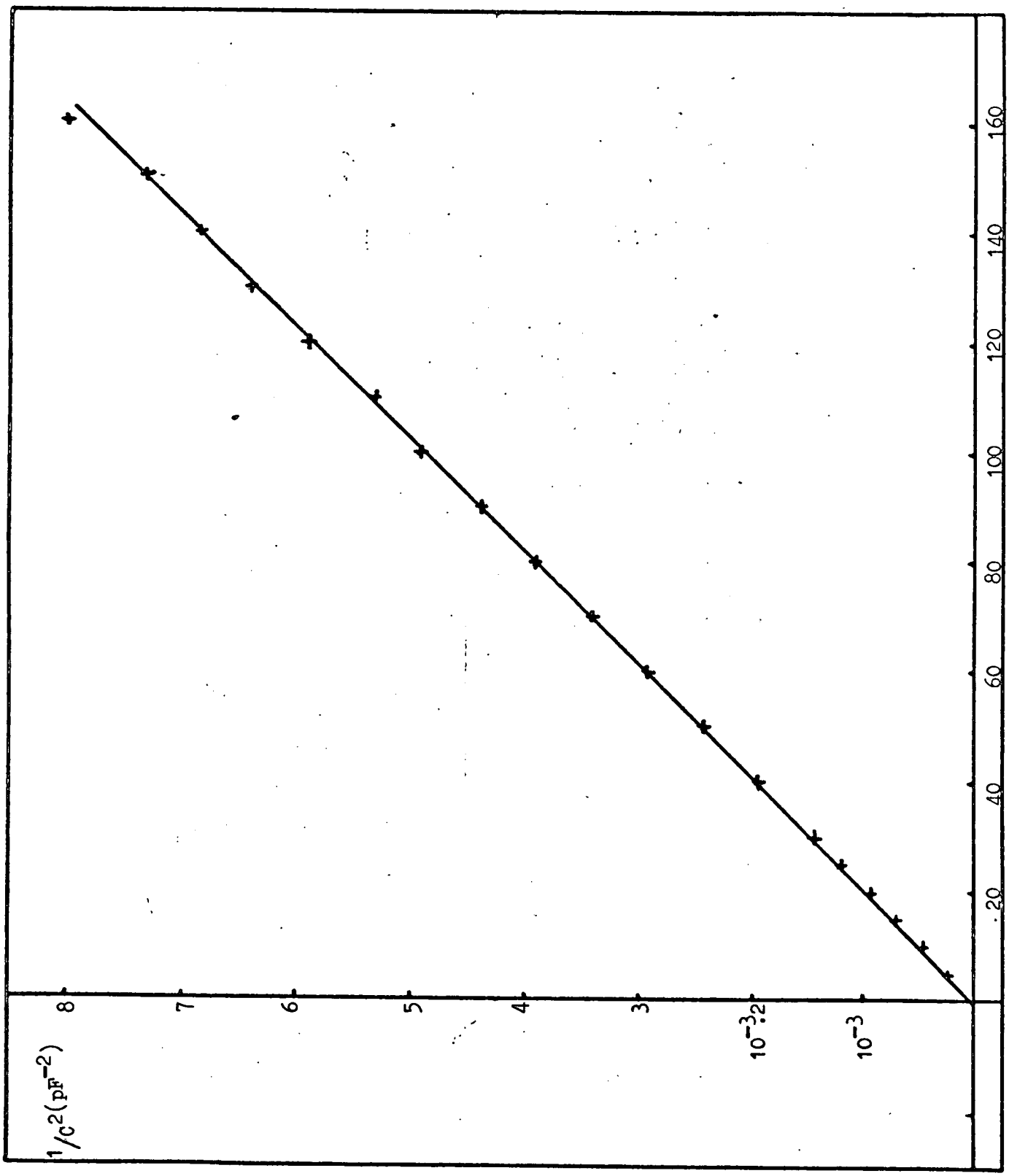

Figure 9.9 $1/C^2$ vs V characteristic of NSC device. Resistivity (Si) = 0·08Ohm.m. $Ge_{10}As_{40}Te_{50}$ thickness = 0·7um. Spot diameter = 1·7mm. Temperature = 293 K.

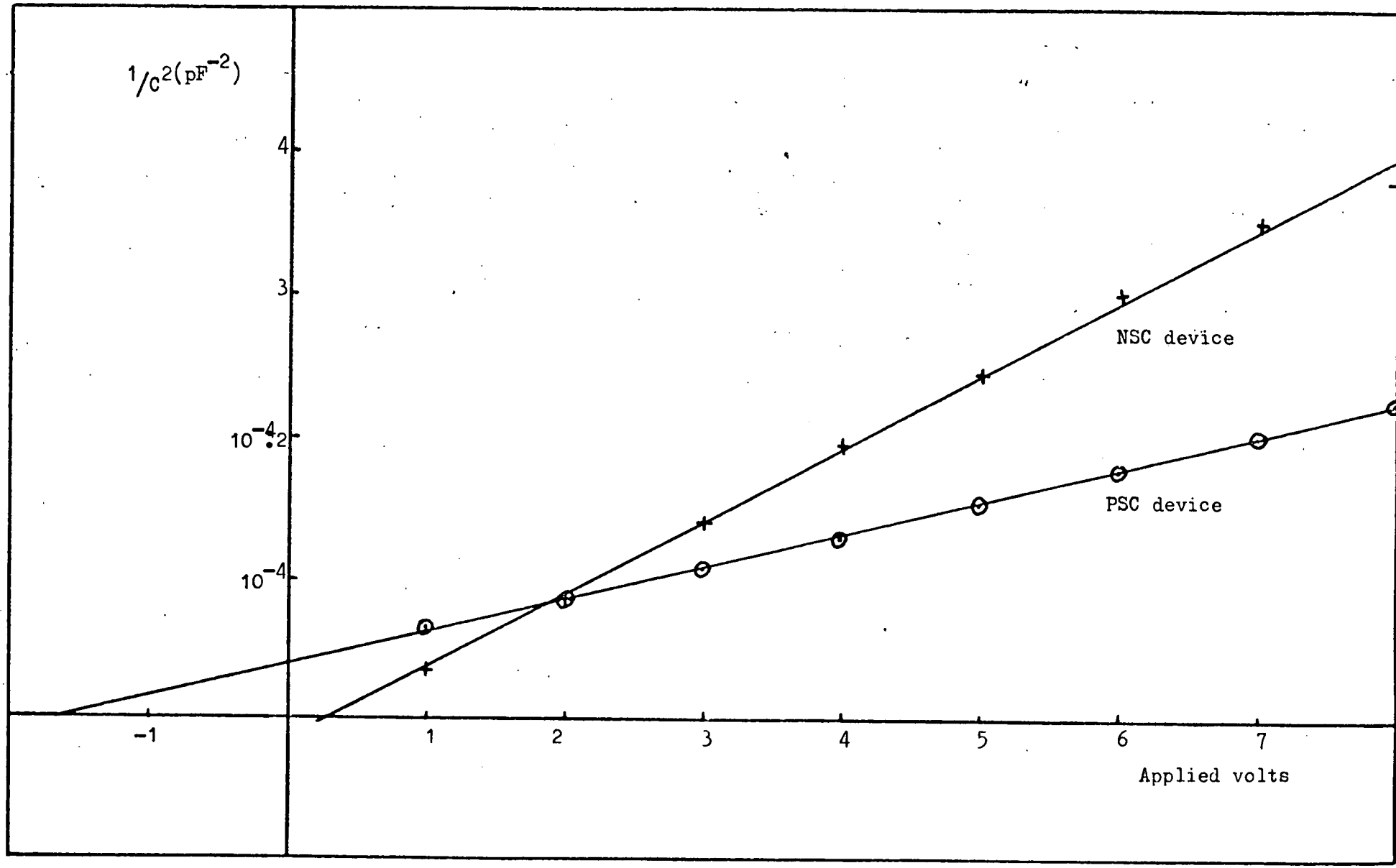

Figure 9.10 $1/C^2$ vs V characteristics of PSC and NSC devices of Figures 9.8 and 9.9.

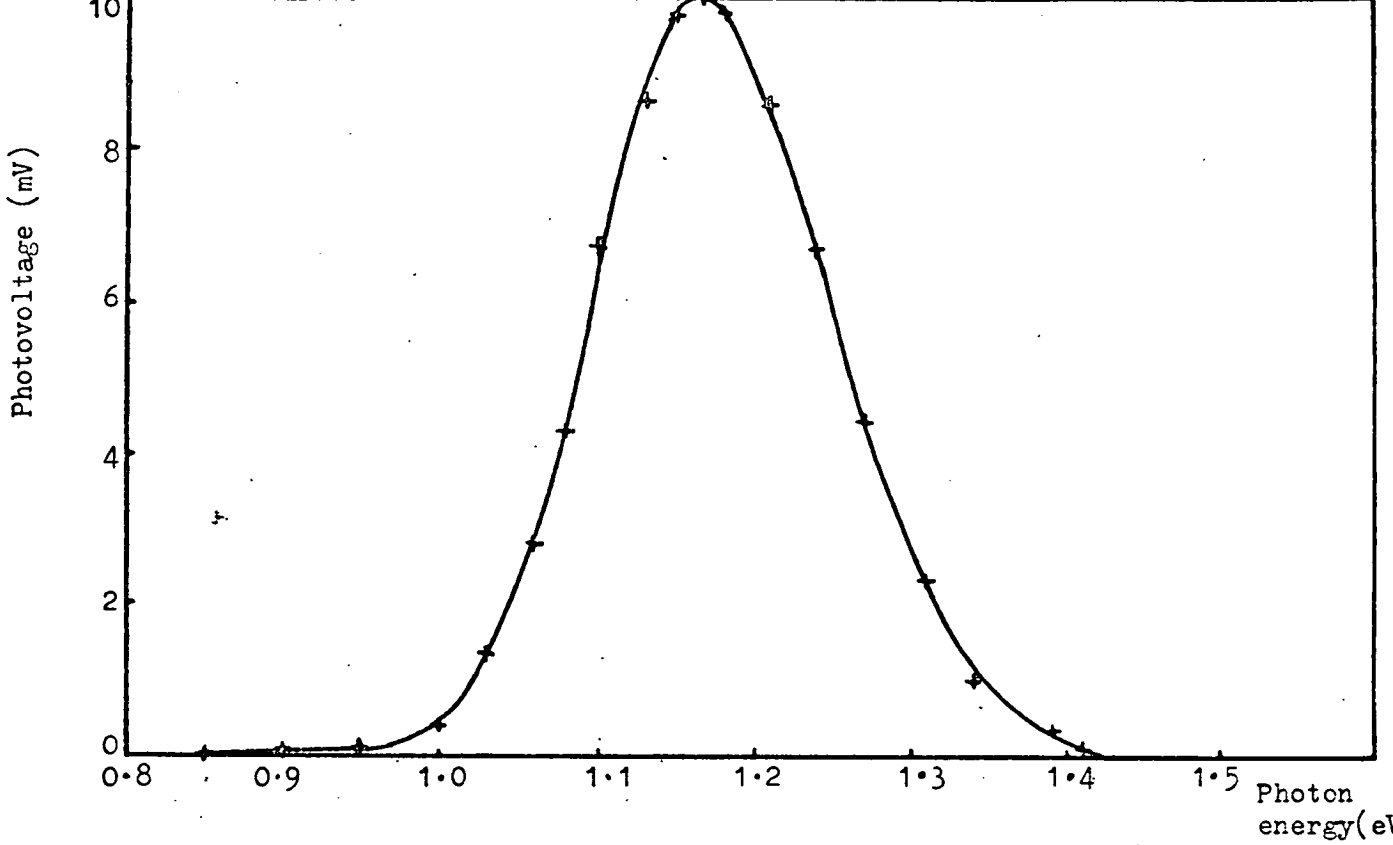

Figure 9.11 Photovoltaic response of PSC device to light incident on electrode adjacent to chalcogenide surface. Resistivity (Si), 0·01250hm.m. $Ge_{10}As_{40}Te_{50}$ thickness = 1·2um. Spot diameter = 0·23cm. Temperature = 293 K.

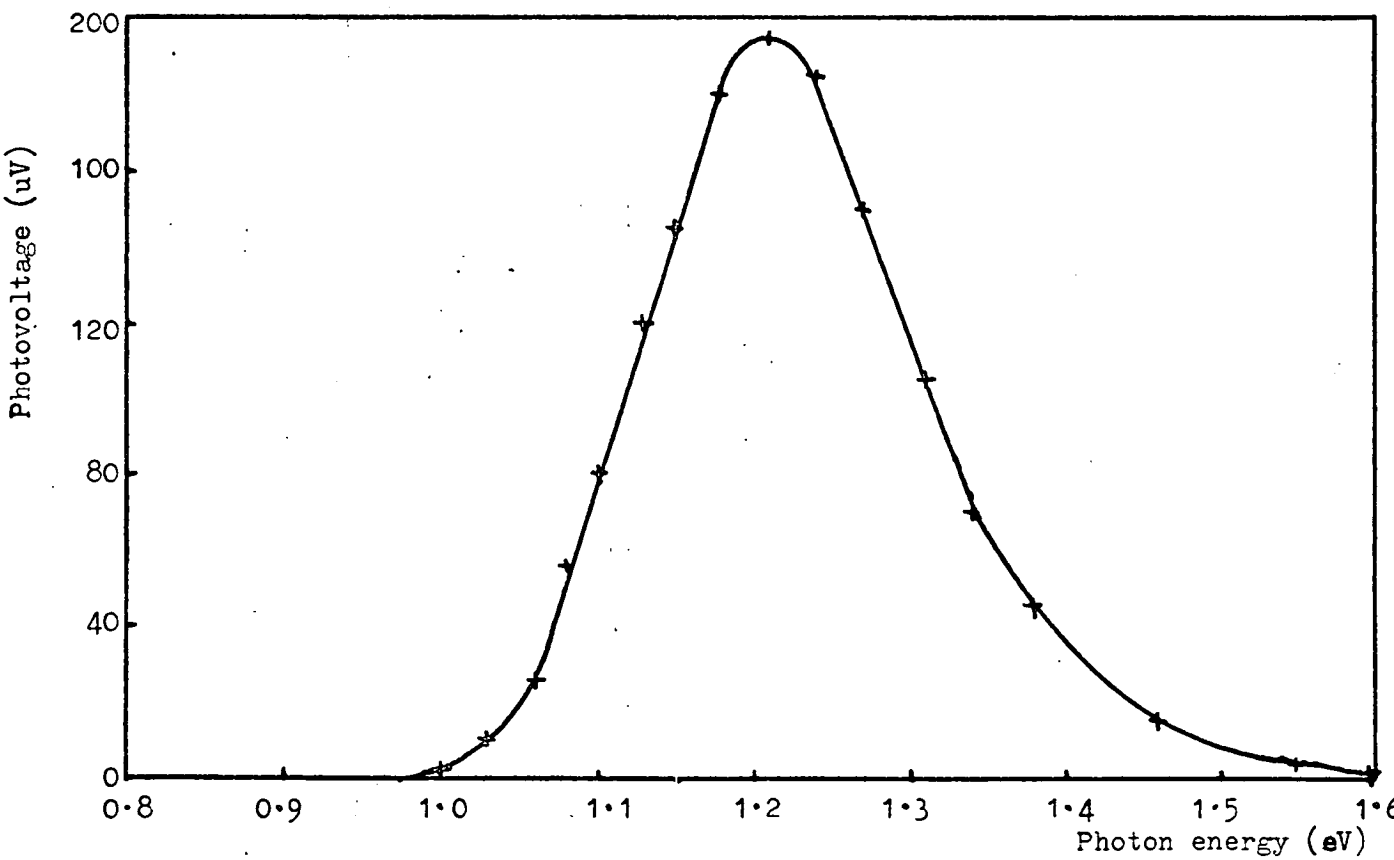

Figure 9.12 Photovoltaic response of NSC device to light incident on electrode adjacent to chalcogenide surface. Resistivity (Si), 0·0250hm.m. $Ge_{10}As_{40}Te_{50}$ thickness = 1·2um. Spot diameter = 0·23cm. Temperature = 293 K.

as near identical as possible. The quasi-symmetrical responses, peaking at around $h\upsilon$ = 1.2eV, are similar in sense and shape, but the response in the PSC case is considerably larger than that of the NSC device. It is also interesting to note that the relative effect of high intensity white light on the reverse characteristic of the PSC device, illustrated in Figure (9.6), is also much greater than its NSC counterpart, illustrated in Figure (9.7).

Much of the data presented here corresponds closely to that of other authors relating to heterojunctions formed between crystalline silicon and other chalcogenide materials, though there are some discrepancies which can lead to a slightly different interpretation of the results. Dunn et al.[11,12] report qualitatively similar current-voltage and capacitance-voltage characteristics on junctions formed between p- and n-type silicon substrates and amorphous $Ge_{25}Se_{10}Te_{65}$, $Ge_{33}Se_{33}Te_{34}$, and $As_{40}Se_{15}Te_{45}$, all chalcogenides in which, like $Ge_{10}As_{40}Te_{50}$, the dominant conduction mechanism is hole transport. In addition, the effect of light on the reverse characteristics of the relevant heterojunctions is also similar. The data of Reinhard, Adler et al.[7,8] on p-type silicon-amorphous $Te_{40}As_{35}Si_{15}Ge_7P_3$ devices is also very similar, but they notice some evidence of a blocking barrier in the forward direction for n-type silicon-amorphous $Te_{40}As_{35}Si_{15}Ge_7P_3$ devices. Unfortunately, no capacitance-voltage data is available from this source, but the photoelectric data is very similar; firstly, in the sense, magnitude and range

of the measured zero-bias photocurrent as a function of photon energy, and secondly, with regard to the effect of white light on the reverse characteristic.

9.3 Theory and Formulation of Heterojunction Model

The weight of experimental evidence presented in previous chapters indicates that it is highly unlikely that the reverse characteristics of these heterojunctions are dominated by a blocking barrier in the chalcogenide surface region. Therefore, it is logical to suppose that the principal controlling factor is the reverse biased silicon depletion region. The theoretical avalanche breakdown voltage, V_B, has been deduced from the equation for a one-sided abrupt junction,[16]

$$V_B = \frac{\varepsilon_s \cdot E_m^2}{2q} \cdot \frac{1}{N_B} \qquad (9.6.1)$$

where ε_s is the dielectric constant of silicon, N_B is the background carrier concentration, and E_m the maximum field. In practise, E_m varies very slowly with background doping concentration, and a good approximation is obtained by assuming E_m is a constant. An approximate expression for the breakdown voltage in abrupt junctions is thus obtained,[16]

$$V_B = 60.\left[\frac{E_g}{1.1}\right]^{3/2}.\left[\frac{N_B}{10^{22}}\right]^{-\frac{3}{4}} \qquad (9.6.2)$$

where E_g is the energy gap in eV, and N_B is now in m^{-3}. The calculated values of V_B, tabulated in Table (9.1), are in good agreement with the experimental data for PSC devices illustrated in Figures (9.1) to (9.3), but the soft characteristic and prior switching of the NSC devices makes

Table 9.1

Silicon type	Resistivity (Ohm.m.)	Nominal N_B calculated from Resistivity (m^{-3})	V_B, calculated from junction Equation (V)	N_B calculated from $1/C^2$ v. V_g data (m^{-3})	Negative Intercept (V)
p	0·0125	10^{22}	60	$1·8.10^{22}$	-4·2
p	0·025	$5·5.10^{21}$	88	$6·0.10^{21}$	-3·6
p	0·15	10^{21}	322	$1·1.10^{21}$	-1·8
n	0·025	2.10^{21}	190	$1·65.10^{21}$	0
n	0·08	6.10^{20}	400	$4·9.10^{20}$	+0·15

a comparison more difficult.

The fact that the open circuit photovoltaic response is of the same sense in both PSC and NSC devices is at first sight rather puzzling. Optical data on metal-$Ge_{10}As_{40}Te_{50}$-metal sandwich devices, presented in Chapter 8, indicated that one would not expect a measurable response from the chalcogenide film at room temperature, thus the photovoltaic response is most probably principally due to interband transitions within the silicon space charge region, as illustrated schematically in Figure (9.13) for a PSC device. As stated previously, the optical gaps of $Ge_{10}As_{40}Te_{50}$ and Si at room temperature are 0.94eV and 1.1eV respectively, thus at low photon energies, $h\nu < 1.0$eV, say, these transitions are not observed, while at high photon energies, $h\nu > 1.3$eV, say, the chalcogenide film is opaque, and light does not penetrate to the junction region. The measured response of Figures (9.11) and (9.12) indicates that, at equilibrium, the bands bend downwards considerably in the p-type silicon, producing a wide depletion region, whereas the bands bend down only slightly in the n-type silicon, producing a near flat-band or slight accumulation surface region. Consider the expanded, low-field characteristics illustrated in Figures (9.6) and (9.7). When the devices are under forward bias, light has little or no effect on the characteristic, as no barrier is presented to the majority carriers in the silicon and the fractional increase in the majority carrier concentration due to the light is small. Under reverse bias, however, the photogeneration of excess minority carriers results in a

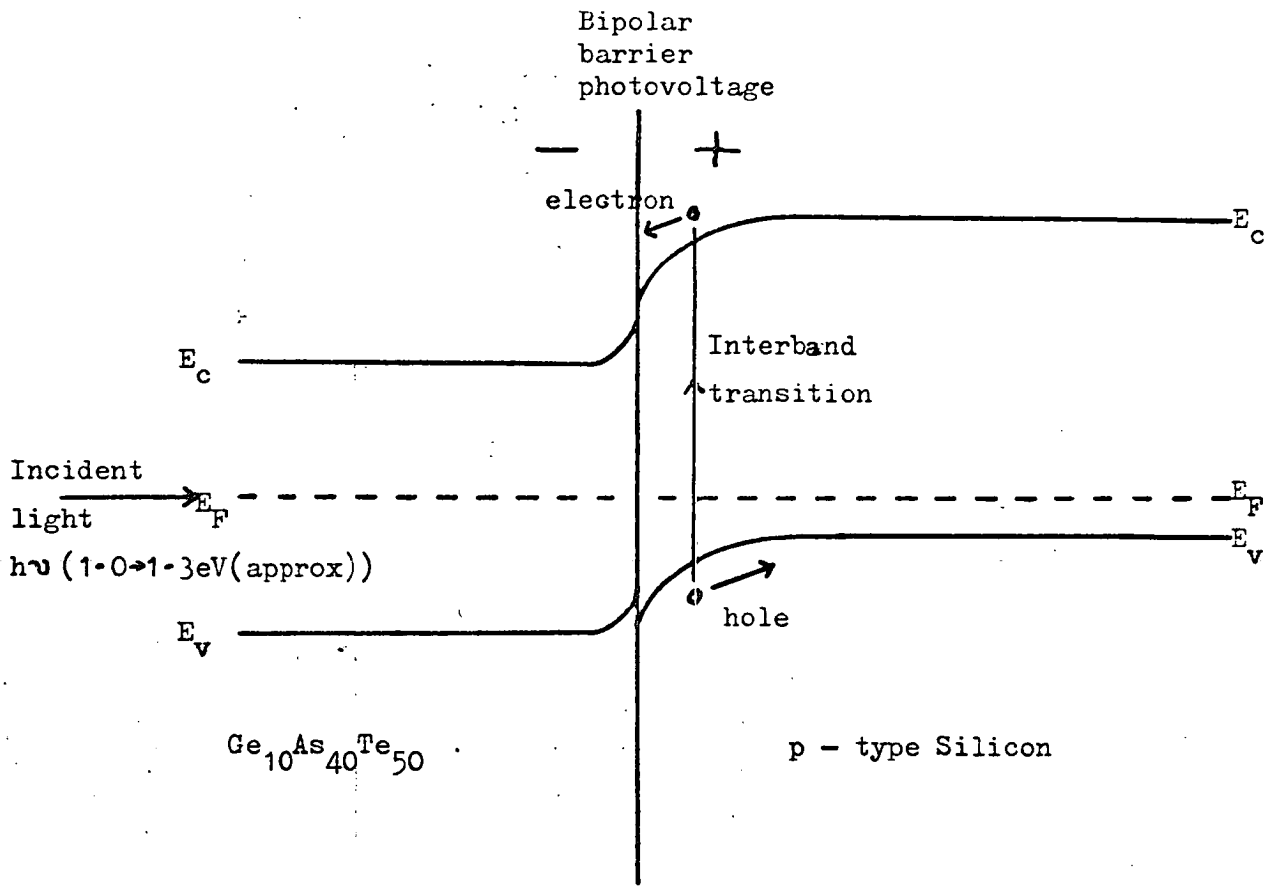

Figure 9.13 Photovoltaic response of $Ge_{10}As_{40}Te_{50}$ – silicon heterojunction to incident light of photon energy between 1·0 and 1·3eV.

significantly larger current.

Further confirmation that the dominant blocking resistance of the reverse characteristic is that of the silicon depletion region is obtained from the capacitance-voltage measurements by comparing the nominal value of the carrier concentration in the silicon, calculated from the resistivity value,[17] with the carrier concentration calculated from the data of Figures (9.8) and (9.9), and similar data on other devices. The standard expression for the bias modulated capacitance of an abrupt junction is used,[18]

$$N_B = \frac{dV}{d(1/C^2)} \cdot \frac{2}{q\varepsilon_s} \cdot \frac{1}{A^2} \qquad (9.6.3)$$

where $\frac{dV}{d(1/C^2)}$ is the measured gradient, and A is the device area. Table (9.1) indicates the good agreement obtained between the calculated values. The values of the negative intercepts obtained for these devices are also tabulated. A value for the built-in potential in the silicon, V_{bi}, approximately equal to zero in the NSC devices is in good agreement with the photovoltaic data, indicating a near flat-band/slight accumulation situation at the silicon surface. The values for V_{bi} in PSC devices are high, as expected qualitatively from the photovoltaic data, but quantitatively are anomalously high (the lowest value obtained for the negative intercept on any device was -1.0V). If the bands were bent downwards by this amount, the surface region in the p-type silicon would be so highly inverted that the Fermi level would cross the

conduction band. Therefore, the exact value of the negative intercept remains problematic.

Figures (9.14) and (9.15) illustrate the band models for PSC and NSC devices which explain the experimental data of this chapter. The equilibrium situations illustrated are similar to the models of Petersen and Adler[9] for $Te_{39}As_{36}Si_{17}Ge_7P_1$ - silicon heterojunctions, but the interpretation of the current transport is somewhat different. The downward band bending in the silicon surface region has been discussed previously and the upward bending of the bands within the chalcogenide surface layer is arbitrary. A high density of localised states is shown within the surface region of the chalcogenide, accompanied by a high density of interface states, but the density of localised states within the silicon space charge region is assumed low.

Under forward bias, the major component of current in the PSC devices is hole transport from the silicon to the chalcogenide (though there may be an additional small generation component), limited by the bulk chalcogenide film resistance, as observed in the current-voltage data. It is improbable, however, that a similar situation exists for electrons (the majority carrier) in the NSC devices, as the electron mobility in $Ge_{10}As_{40}Te_{50}$ and other chalcogenide glasses is much smaller than the hole mobility. In order to explain the observed forward characteristic, in which the limiting factor is the normal chalcogenide resistance, transport must be by holes in the $Ge_{10}As_{40}Te_{50}$ film and by electrons in the silicon, accompanied by a

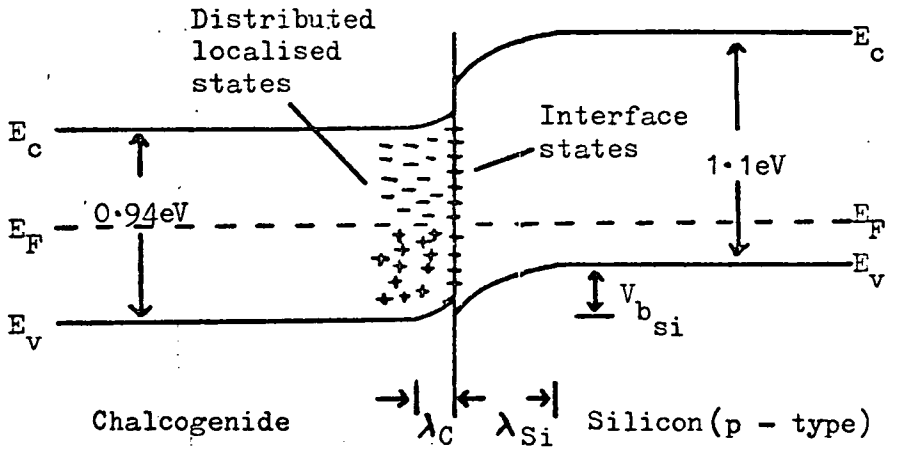

(i) Equilibrium

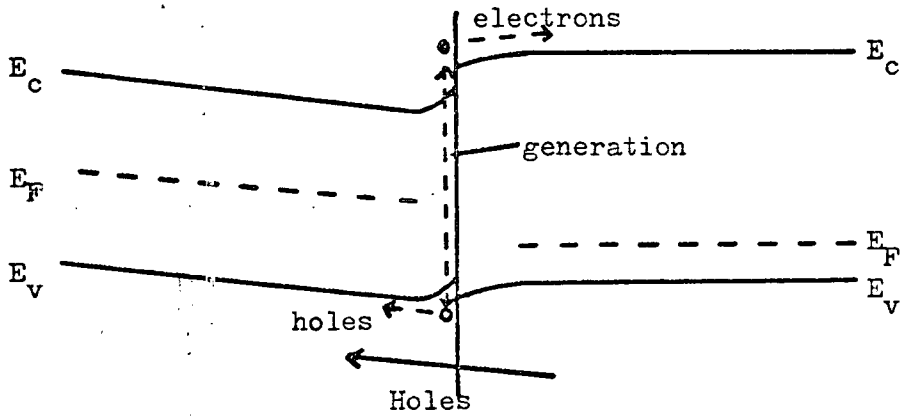

(ii) Forward bias

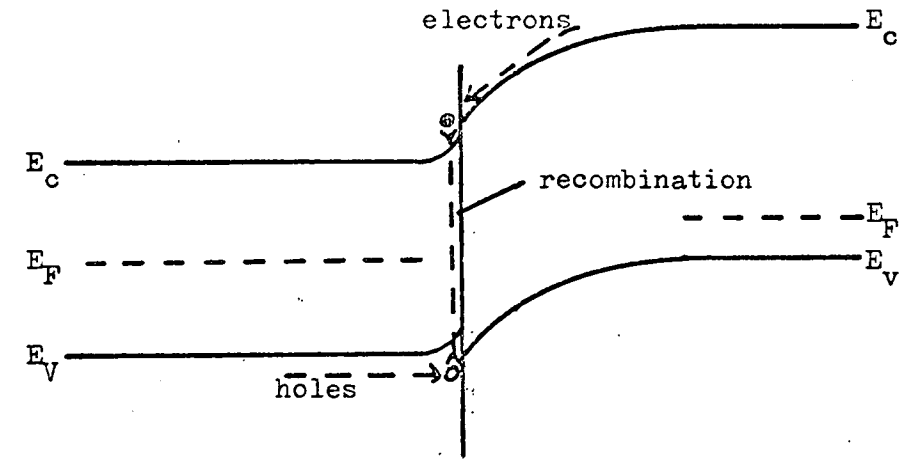

(iii) Reverse bias

Figure 9.14 Band model for PSC heterojunction

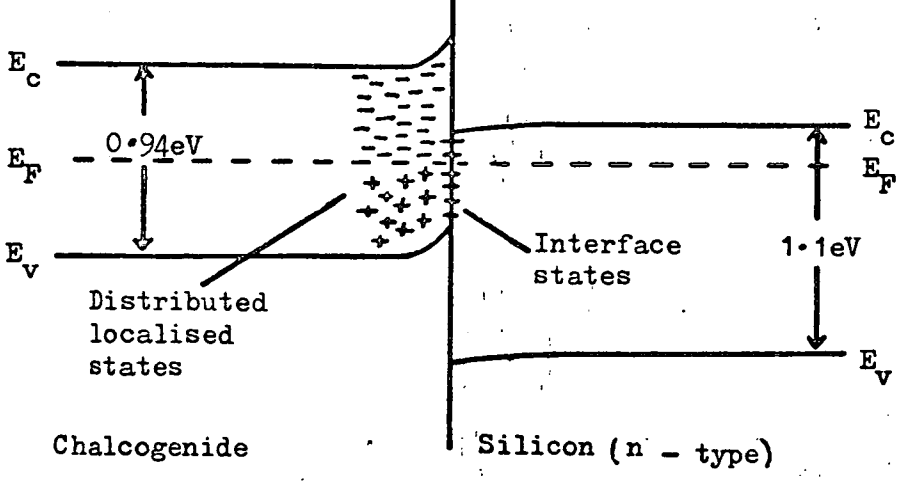

(i) Equilibrium

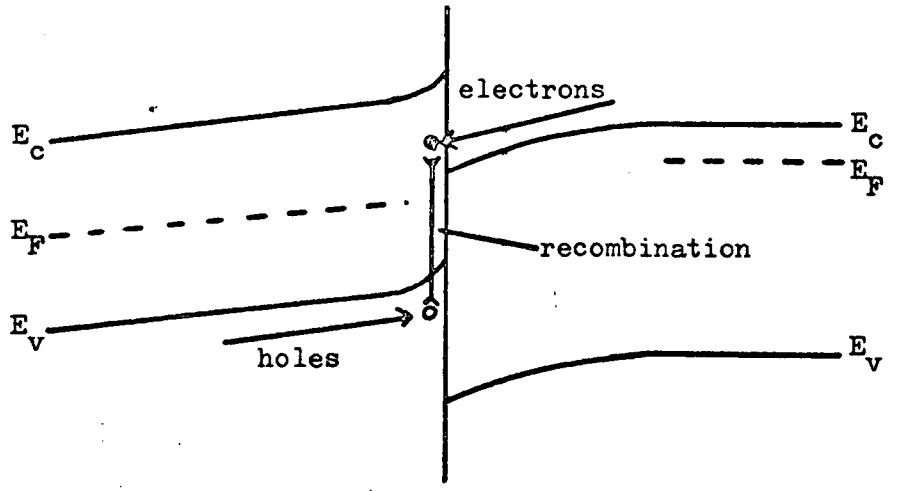

(ii) Forward bias

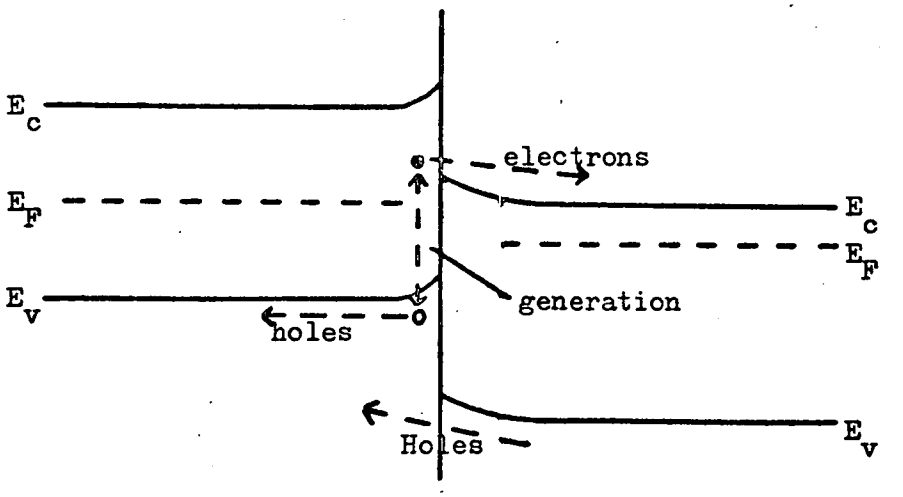

(iii) Reverse bias

Figure 9.15 Band model for NSC heterojunction.

recombination process at the junction via localised states in the chalcogenide surface layer and/or interface states. This situation differs from the PSC device generation current, because the recombining electrons are the silicon majority carriers, whereas in PSC devices the generated electrons are minority carriers. In all cases the actual rate of recombination/generation in the junction region is analogous to the metal-amorphous semiconductor junction discussed in Chapter 6; i.e. it is high enough to provide charge continuity.

Under reverse bias, similar arguments apply to carrier transport through the chalcogenide:- thus the principal transport mechanism in PSC device is probably minority electron flow in the silicon towards the junction, where recombination takes place with holes from the chalcogenide. The reverse bias saturation current increases with applied voltage because, firstly, the depletion layer widens and carriers are collected from a larger volume, and because, secondly, at high fields avalanching of minority carriers in the depletion layer occurs leading to eventual breakdown. The situation for the NSC devices is more complex. The high reverse offset voltage ($\simeq$0.5V) before a saturation current is apparent is reasonable, as the surface space charge region is initially in a slight accumulation condition. Minority hole flow across the junction, from the silicon to the chalcogenide, is expected to contribute to the current transport, and is a function of increasing depletion region width in the same way as the minority electron current in PSC devices. However, a contribution

from electron-hole pairs generated in the surface region of localised states and at the interface must also be considered, and may account for the "softness" of the characteristic. Quantitatively it is difficult to assess the exact magnitude of this contribution, but qualitatively it increases with applied voltage. As the device bias is increased, the generated electrons are subjected to a field of increasing strength across the silicon depletion region. However, as the bulk of the applied bias is dropped across the silicon depletion region, rather than the chalcogenide surface layer, the quasi-Fermi levels in the chalcogenide may not be initially sufficiently separated to provide adquate charge generation. Thus a rectifying characteristic is observed in NSC devices, but the reverse characteristic is much softer than in the PSC case.

9.4 Discussion

Heterojunctions formed between $Ge_{10}As_{40}Te_{50}$ films and crystalline silicon substrates manifest many of the properties of one-sided abrupt junctions, but PSC devices are more strongly rectifying than NSC devices, which exhibit a soft reverse characteristic with a strongly voltage dependent saturation current, which is perhaps due to significant generation of electron-hole pairs at the interface in addition to the conventional minority carrier flow. In both cases, the forward characteristics are limited by the series resistance of the chalcogenide film, after a slight offset voltage. Both PSC and NSC devices give linear $^1/_{C2}$ vs. V characteristics, and doping densities

are in good agreement with those calculated from silicon resistivity values. No quantitative estimate of the amount of band bending at the interface is attempted, as certain problems remain over the negative intercept of $^1/_{C^2}$ vs. V characteristics, but photoelectric measurements indicate that the bands in the silicon bend downwards in both cases. In order to produce a more exact model, and perhaps resolve anomalies in the capacitance data, an investigation of the reverse saturation current as a function of temperature could prove useful.[2,9]

CHAPTER 10 CONCLUDING REMARKS

10.1 Summary

In the preceding chapters, a wide variety of sample configurations and experimental techniques have been used in order to obtain a clearer understanding of the electrical contact and surface properties of chalcogenide thin films, in particular of the relatively conducting alloys, $Ge_{10}As_{40}Te_{50}$ and $Si_{12}Te_{48}As_{30}Ge_{10}$. As a preliminary to this, the conductivity of thin-films of $Ge_{10}As_{40}Te_{50}$ was studied as a function of temperature and applied field, and found to be typical of a wide range of chalcogenide glasses, as reported in the literature. Further experimental work on coplanar and sandwich devices revealed the absence of any blocking layer adjacent to the metal contact; this was particularly evident in the similarity of the current-voltage and capacitance-voltage characteristics of sandwich devices using a wide variety of metallic electrodes.

However, studies of the photovoltaic response of thin-film sandwich devices indicated that space charge regions do exist adjacent to the electrodes, yet there was no evidence of a rectifying Schottky barrier analogous to the metal-doped crystalline semiconductor case. An explanation for this was suggested by studies of the field-effect modulated conductance of thin films of $Ge_{10}As_{40}Te_{50}$ and $Si_{12}Te_{48}As_{30}Ge_{10}$. These indicated that a high density of localised states exists within the forbidden gap of the semiconductor, at or near the surface. The exact nature of these states is uncertain, and computed results from

field-effect data cannot be considered as representative of the bulk, but an approximate value of $10^{25} m^{-3} . eV^{-1}$ for the density of localised states at the Fermi level in the surface layer, or an equivalent surface state density of $10^{17} m^{-2} . eV^{-1}$ was deduced. From these values, the width of the chalcogenide depletion regions was calculated to be less than 100Å.

The existence of a high density of localised states within a narrow depletion region is crucial in the formulation of a model for the transport processes in the metal-amorphous semiconductor contact, as presented in Chapter 6. At low contact voltages, transport through the barrier can be accounted for in terms of band-to-band recombination/generation via localised states within the gap and/or a tunnelling process from the metal Fermi level to adjacent deep states in the semiconductor, or vice versa, coupled with a similar recombination/generation process. At high contact voltages, direct tunnelling through the narrow depletion region into extended states may provide an additional contribution. A quantitative comparison of the approximate magnitudes of the various transport processes in the contact region with the series bulk transport indicates that the current-voltage characteristics are bulk limited, a conclusion borne out by the experimental evidence. Further to this an equivalent circuit model is developed for metal-chalcogenide-metal sandwich devices which accounts for the experimentally observed frequency-independence of the device capacitance and A.C. conductance, as well as the I-V and C-V characteristics.

When the bottom electrode of a metal-chalcogenide-metal device is an oxidising metal, such as Al, a different situation prevails. A large low-field resistance was observed, and a rise in the capacitance and a fall in the A.C. conductance at low frequencies was also noticed. These features are explained in terms of a different equivalent circuit which takes into account the existence of a thin oxide layer adjacent to the bottom electrode. The D.C. current voltage characteristics are interpreted in terms of a tunnelling process from the metal, through the oxide layer, to adjacent localised states within the forbidden gap of the semiconductor, at or near the interface. These states are in equilibrium with extended states in the chalcogenide film via recombination/generation statistics, and this mechanism is also responsible for transport through the bulk film, at least in the temperature range considered.

Studies of heterojunctions formed between thin films of $Ge_{10}As_{40}Te_{50}$ and both p- and n-type silicon substrates did show strongly rectifying characteristics, but a close examination of current-voltage, capacitance-voltage and photo-electric data indicated that the high reverse junction resistance was dominated by a conventional Schottky barrier in the silicon, rather than by any blocking layer within the chalcogenide. However, the n-type heterojunctions displayed much softer reverse characteristics than the p-type counterparts. Qualitative models of the two heterojunction types are proposed, and an interpretation of the transport mechanisms under forward

and reverse bias conditions is presented to account for the observed experimental data.

Finally, the justification for using a two-dimensional approximation to a three-dimensional situation must again be raised. The existence of potential fluctuations across the plane of the interface between an amorphous and another material, whether metal, oxide or crystalline semiconductor, may result in greatly increased charge transport in certain localised "weak spots". This does not contradict the arguments presented here, but rather raises the possibility of other processes occurring in parallel, thus having important consequences with regard to any quantitative model.

10.2 Applications

When discussing applications of amorphous materials in general, or indeed applications of the junction properties of amorphous materials in particular, it is necessary to consider two factors. Firstly, is it possible to manufacture a reliable device; and secondly, does it fulfil a need which is not already adequately and perhaps better serviced by existing, long-established technologies? It is not the author's intention to provide a complete review here, but rather to refer the reader to a recent paper by Bosnell.[1] In general, interest in amorphous semiconductors has centred chiefly around their switching and optical properties. An example of a commercially available storage array is the 256-bit read-mostly memory produced by ICL in 1972,[2] employing memory switches manufactured

by Energy Conversion Devices Inc., which has one advantage over its competitors in its radiation "hardness".[3] Further applications for memory or threshold glass switches may include telephone systems, displays (leading to the flat screen TV?), logic circuits, amplifiers, temperature sensors, and so on. In many of these fields, however, it remains unlikely that amorphous materials will achieve a viable share of the market.

One application of amorphous materials which has achieved commercial success is the Xerox process, which utilises the optical properties of vitreous Se. In fact this provides an example of an application of technology preceding a full physical understanding of the material involved. Another example of an optical device is the vidicon, a term used for an "image to video signal converter or transducer used in television-like systems", sensitive to radiation of a particular wavelength. For example, amorphous films of Sb_2S_3 might be used in the visible range, while Sb_2Se_3 is more suitable for infra-red requirements.

When considering applications of amorphous semiconductor junctions, it is the heterojunction device which excites the most interest, as yet unrealised in commercial terms. For example, Petersen and Adler[4] have recently fabricated an amorphous-emitter transistor using amorphous films of $Te_{39}As_{36}Si_{17}Ge_7P_1$, but this has a small signal gain of only 3-5. They suggest that the device has possible logic and control circuitry applications. Alternatively, the simple heterojunction device might be

considered as a switch and rectifier in series, with an asymmetric switching characteristic, perhaps leading to a ternary-based logic system. Finally, solar cells present a further possibility.[5] By selecting an amorphous semiconductor of appropriate energy band gap, the glass may act as a window to a certain spectral range of incident radiation, creating carriers near the hetero-junction as desired.

10.3 Recent Developments

In recent months, several papers have been published which have a considerable relevance to the work presented in this thesis, but which were not available in time for a full consideration. The first of these is a summary of previous theoretical work by Rideout[6] on the relative importance of thermionic, thermionic field and field emission in transport through Schottky barriers. This paper reviews the theories developed in the papers by the same author and others referred to in Chapter 6, compares these theories with experimental data on group III - V semiconductors, and goes on to discuss relevant device technology. A second theoretical paper of considerable interest has been published by Gupta and Overstraeten[7], considering conduction through amorphous insulating barriers with a high density of localised states. They develop a theory of trap-assisted charge injection, by which mechanism a charge first tunnels into a vacant trap and is then either thermally excited into extended states, or tunnels directly into extended states, concluding that this mechanism is very important where the trap density is

$10^{24} m^{-3}$ or more. This paper has considerable relevance to the arguments relating to transport through barriers at the metal-amorphous semiconductor contact, as discussed in Chapter 6.

The studies of a group of German authors on amorphous GeSe sandwich devices with aluminium[8,9] and molybdenum[10,11] contacts are also of interest. Braun[10,11] discusses Mo-amorphous GeSe-Mo sandwich devices in terms of a simple equivalent circuit in order to explain the observed frequency-dependence of the capacitance and A.C. conductance. The treatment is similar to that presented in the latter part of Chapter 7, but the data of Braun resembles that of Wey and Fritzsche[12], and the data presented here on sandwich devices with Al contacts, rather than the results on simple Au/Mo-$Ge_{10}As_{40}Te_{50}$-Au/Mo sandwich devices. Finally Leimer[8,9] et al. discuss the transient response of the current through Al-amorphous GeSe-Al devices to an applied voltage pulse. In view of the nature of Al contacts discussed here, and the importance of preparation conditions, no comment is made on this work. However, the authors do conclude that "if depletion regions do exist near the electrode interfaces, there may be conditions making the influence of these barriers negligible, i.e. for appropriate values of bias, frequency, and temperature bulk properties can predominate".

10.4 Future Work

Rather than discuss specific experiments, it is more useful to discuss some of the immediate issues that need to

be clarified, as they have arisen from the work of this thesis:-

(i) It would be desirable to achieve a greater degree of control over the device preparation conditions, and to determine what effect these conditions have on the interface properties. Following on from this, a more exact determination of the energy distribution of localised states at the interface is required; to what extent is this typical of the bulk and what are the relative magnitudes of bulk and interface states?

(ii) The photovoltaic effect in these materials has been discussed in qualitative terms only. Further careful control of the experimental conditions, and a quantitative assessment of the response in order to determine such parameters as interfacial barrier height would be useful.

(iii) From (i) and (ii) a more complete picture of the metal-amorphous semiconductor interface would be obtained, and this could in turn lead to a quantitative assessment of the relative magnitudes of the transport mechanisms discussed in Chapter 6. However, experimental verification might remain problematic, in view of the high series bulk resistance of the chalcogenide, unless a different experimental configuration can be developed.

(iv) The nature of the heterojunction structures should be quantitatively determined, in turn leading to a more exact assessment of the relative importance of the various current contributions. In view of the unique properties of these junctions, greater emphasis could be placed on the potential applications of heterojunction devices.

CHAPTER 1 - References

1. MacKenzie, J.D. J. Vac. Sci. Tech. 6, 658 (1969).
2. Tanaka, M., Mukai, O. and Kamicke, O. J.Ceram. Assoc. Johan. 73, 51 (1965).
3. Savage, J.A. J. Non-Cryst. Sol. (J.N.C.S.) 11, 121 (1972).
4. Savage, J.A. J. Materials Science 6, 964 (1971).
5. Hilton, A.R., Jones, C.E. and Brau, M. Phys. Chem. Glasses, 7, 105 (1971).
6. Panus, V.R. and Borisova, Z.U. J. Appl. Chem. (USSR), 39, 937, (1966).
7. Maghrabi, C. et al. "Structural Studies of Glasses in the Ge-As-Te and Si-As-Te systems" (Annual report July (1972).
8. Tanaka, K. et al. Sol. Stat. Comm., 8, 1333, (1970).
9. Kaplow, R., Rowe, T.A. and Averbach, B.L. Phys. Rev. 168, 1068, (1968).
10. Lucovsky, G. et al. Solid. Stat. Comm., 5, 113, (1967).
11. Grigorivici, R. Chapter 5 in "Electronic and Structural Properties of Amorphous Semiconductors". (Academic Press 1973).
12. Ast, J.G. J. Vac. Sci. Tech., 10, 748, (1973).
13. Vaipolin, A.A. and Porai-Koshits, E.A. Soviet Phys. Solid State, 5, 178, (1963).
14. Vaipolin, A.A. and Porai-Koshits, E.A. Ibid., 5, 186, (1963).
15. Fitzpatrick, J.R. and Maghrabi, C. Phys. Chem. Glasses. 12, 105, (1971).

16. Vaipolin, E.A. and Porai-Koshits, E.A. Sov. Phys. Solid State, 5, 197 (1963).

17. Thornburg, D.D. Journal of Electronic Materials, 2, 495 (1973).

18. Renninger, A.L., Rechtin, M.D. and Averbach, B.L., J.N.C.S., 16, 1 (1974).

19. Bosnell, J.R. and Savage, J.A. J. Mat. Sci., 7, 1235, (1972).

20. Pinto, R. J.N.C.S., 6, 187 (1971).

21. Quinn, R.K. and Johnson, R.T. J.N.C.S., 7, 53, (1972).

22. Iizima, S., Sugi, M., Kikuchi, M. and Tanaka, K. Proc. 2nd Conf. on Solid State Devices. (Tokyo 1970).

23. Uttecht, R., Stevenson, H. et al. J.N.C.S., 2, 358 (1970).

24. Main, C. "Characteristics and Mechanisms of amorphous semiconductor Devices", SRC Report May (1974).

25. Savage, J.A. J. Mat. Sci., 7, 67, (1972).

26. Marshall, J.M. and Miller, G.R. Phil. Mag., 27, 1151, (1973).

27. Marshall, J.M. "Electronic Processes in semiconducting glasses and glass switches" 3rd Report (November 1973).

28. Marshall, J.M. Ibid, 4th Report (November 1974).

CHAPTER 2 - References

1. McKelvey, J.P. "Solid State and Semiconductor Physics" (Harker and Row, 1969).

2. Ioffe, A.F. and Regel, A.R. Progr. in semiconductors, 4, 239, (1960).

3. Cohen, M.H. J.N.C.S., 4, 391, (1970).
4. Cohen, M.H., Fritzsche, H. and Ovshinsky, S.R. Phys. Rev. Lett., 22, 1065, (1969).
5. Marshall, J.M. and Owen, A.E. Phil. Mag., 24, (1971).
6. Davis, E.A. and Mott, N.F. Phil. Mag. 22, 903, (1970).
7. Adler, D. "Amorphous Semiconductors" (CRC, Cleveland, Ohio 1971).
8. Mott, N.F. and Davis, E.A. "Electronic Processes in Non-Crystalline Materials" (Clarendon Press 1971), Section 7.4.
9. Many, A., Goldstein, Y. and Grover, N.B. "Semiconductor Surfaces" (North Holland 1971) Chapter 5.
10. Fritzsche, H. J.N.C.S., 6, 49, (1971).
11. Spear, W.E. Advances in Phys., 23, 523, (1974).
12. Brenig, W. Proc. of 5th International Conf. on Amorphous and Liquid Semiconductors (Garnisch 1973),31.
13. Mott, N.F. Phil. Mag., 22, 1, (1970).

CHAPTER 3 - References

1. Sze, S.M. "Physics of Semiconductor Devices" (Wiley, 1969).
2. McKelvey, J.P. "Solid State and Semiconductor Physics" (Harper, 1969).
3. Gossick, B.R. "Potential Barriers in Semiconductors" (Academic, 1964).
4. Many, A., Goldstein, Y. and Grover, N.B. "Semiconductor Surfaces" (North Holland, 1971).
5. Editor Pepper, M. Proc, of Conf. on Metal-Semiconductor Contacts (Manchester, 1974).

6. Henisch, H.K. "Rectifying Semiconductor Contacts" (Clarendon Press, 1957).
7. Schottky, W. Naturwiss, 26, 843, (1938).
8. Rhoderick, E.H. Proc. of Conf. on Metal-Semiconductor Contacts (Manchester 1974), 3.
9. Bethe, M.A. MIT Radiation lab reports 43, 12 (1942).
10. Crowell, C.R. and Sze, S.M. Solid State Electronics, 9, 1035, (1966).
11. Crowell, C.R., Sarace, J.C. and Sze, S.M. Trans. Met. Soc. A.I.M.E., 233, 478, (1965).
12. Andrews, J.M. and Lepselter, M.P. Solid State Electronics, 13, 1011 (1970).
13. Miller, S.L. Phys. Rev., 105, 1246, (1957).
14. Anderson, R.L. Sol. Stat. Electron., 5, 341, (1962).
15. Chang, L.L. Sol. Stat. Electron., 8, 721, (1965).
16. Oldham, W.G. and Milnes, A.G. Sol. Stat. Electronics, 7, 153 (1964).
17. Chang, L.L. J. Appl. Phys., 37, 3908 (1966).
18. Donnelly, J.P. and Milnes, A.G. IEEE Trans. Elect. Dev. ED-20, 63 (1967).

CHAPTER 4 - References

1. Tanaka, K. et al. Jap. Journal Appl. Phys., 40, 73, (1971).
2. Savage, J.A. Journal Mat. Sci., 6, 964, (1971).
3. These analyses were carried out within the department by Mr. D. Reynolds.
4. These analyses were carried out in the Geology Dept. (U. of E.) by Mr. G.R. Angell.

5. Preparation of masks by G. Borzucki.

6. Lynch, A.C. Proc. IEE, 104B, 363 (1957).

7. Robertson, J.M. and Owen, A.E. Proc. 4th Conf. on Am. and Liq. Semiconductors (Ann Arbor, 1971), 439.

CHAPTER 5 - References

1. Main, C. Private Communication.

2. Owen, A.E. and Robertson, J.M. J.N.C.S. 2, 40 (1970).

3. Fagen, A.E. and Fritzsche, M. J.N.C.S., 2, 170 (1970).

4. Marshall, J.M. and Miller, G.R. Phil. Mag., 27, 1151, (1973).

5. Barbe, D.F. and Saks, N.S. J. Appl. Phys., 44, 1666, (1973).

6. Arnoldussen, T.C. et al. Phys. Rev. B, 9, 3377 (1974).

7. Bube, R.H. et al. Appl. Phys. Lett., 25, 419 (1974).

8. Mott, N.F. and Davis, E.A. Chapter 7 in "Electronic processes in non-crystalline materials" (Clarendon Press 1971).

9. Tanaka, K. et al. Jap. J. Appl. Phys., 40, 73 (1971).

10. Fritzsche, M. Chapter 2 in "Electronic and Structural Properties of Amorphous Semiconductors". (Academic Press, 1973).

11. Spear, W.E. Proc. 5th Conf. on Amorphous and Liquid Semiconductors. (Garnisch), 1 (1973).

12. Fritzsche, M. Chapter 3 in "Amorphous and Liquid Semiconductors". (Plenum Press 1974).

13. de Wit, H.J. and Crevecouer, C. JNCS, 8-10, 787 (1972).

14. Frenkel, J. Phys. Rev., 54, 647, (1938).

15. Croituru, N. and Vescan, L. Thin Solid Films, 3, 269 (1969).

16. Servini, A. and Jonscher, A.K. Thin Solid Films, 3, 341 (1969).

17. Stubb, T., Suntola, T. and Tisinen, O.J.A. Sol. Stat. Electronics, 15, 611 (1972).

18. Hill, R.M. Phil. Mag., 23, 59 (1971).

19. Hartke, J.L. J. Appl. Phys., 39, 4871 (1968).

20. Mott, N.F. Phil. Mag., 24, 911 (1971).

21. Shimakawa, K. et al. Jap. Journal Appl. Phys., 12, 1043 (1973).

22. Suntola, T. Sol. Stat. Electronics, 14, 933 (1971)

23. Pinto, R. Thin Solid Films, 7, 391 (1971).

24. Croituru, N., Vescan, L., Popescu, C. and Lazurescu, M., J.N.C.S., 4, 493 (1970).

25. Thomas, D.L. and Warren, A.C. Electronics Letters, 6, 62 (1970).

26. Male, J.C. Ibid, 91 (1970).

27. Warren, A.C. and Male, J.C. Ibid, 567 (1970).

28. Thomas, D.L. and Male, J.C. J.N.C.S., 8-10, 522 (1972).

29. Warren, A.C. IEEE Trans. in Electron. Devices, ED-20, 123 (1973).

30. Main, C. S.R.C. Report B/SR/9889 (May, 1974).

CHAPTER 6 - References

1. Rose, A. Helv. Phys. Acta., 29, 199 (1956).

2. Mott, N.F. Phil. Mag., 24, 911 (1971).

3. Fritzsche, H.E. Chapter 2 in "Electronic and structural properties of amorphous semiconductors".

4. Barbe, D.F. J. Vac. Sci. & Tech., 8, 102 (1971).

5. Egerton, R.F. Appl. Phys. Lett., 19, 203 (1971).

6. Spear, W.E. Proc. 5th Conf. on Amorphous and Liquid Semiconductors (Garnisch-Partenkirken), 1 (1973).

7. Vezzoli, G.C. and Pratt, I.H. Thin Solid Films, 14, 161 (1972).

8. Altunyan, S.A. and Stafeev, V.I. Sov. Phys. Semiconductors, 4, 431 (1970).

9. Petrillo, G.A. and Kao, K.C. J.N.C.S., 16, 247 (1974).

10. Farooq, M.U. and Hirsch, J. Sol. Stat. Comm., 15, 1417 (1974).

11. Nielsen, P. Thin Solid Films, 15, 309 (1973).

12. Freeman, L.A., Shaw, R.F. and Yoffe, A.D. Thin Solid Films, 3, 367 (1969).

13. Osmun, J.W. and Fritzsche, H. App. Phys. Lett., 16, 87 (1970) and Osmun, J.W. Phys. Rev. B., 11 (12), 5008 (1975).

14. Osmun, J.W. and Fritzsche, H.E. Conf. on Tetrahedrally Bonded Semiconductors, (Yorktown Heights, 1974), 333.

15. Smith, C.W. and Clark, A.H. Thin Solid Films, 9, 207 (1972).

16. Hauser, J.J. C.T.B.S., 338 (Yorktown Hts. 1974).

17. Sauvage, J.A., Mogab, C.J. and Adler, D. Phil. Mag., 25, 1305 (1972).

18. Konak, C. and Stuke, J. Phys. Stat. Sol., 9, 333 (1972).

19. Osmun, J.W. Sol. Stat. Comm., 13, 1035 (1973).

20. Yamashita, K., Fujiyasu, H., Koboyashi, I. and Itoh, S. Jap. Journal App. Phys., 13, 290 (1974).

21. Nwachuku, A. and Kuhn, M. Appl. Phys. Lett., 12, 163, (1968).

22. Schewchun, J., Waxman, A. and Warfield, G. Sol. St. Electronics, 10, 1165 (1967).

23. Schewchun, J., Waxman, A. and Warfield, G. Ibid, 1187 (1967).

24. Hauser, J.J. Phys. Rev. B, 9, 2544 (1974).

25. Mott, N.F. Phil. Mag., 19, 835 (1969).

26. Hill, R.M. Thin Solid Films, 12, 367 (1972).

27. Crowell, C.R. and Rideout, V.L. Sol. Stat. Electronics, 12, 89 (1969).

28. Stratton, R. J. Phys. Chem. Solids, 23, 1177 (1962).

29. Sze, S.M. Physics of Semiconductor Devices (Wiley 1969).

30. Padovani, F.A. and Stratton, R. Sol. Stat. Electronics, 9, 695 (1966).

31. Cohen, M.H., Fritzsche, H. and Ovshinsky, S.R. Phys. Rev. Lett., 22, 1065 (1969).

32. Marshall, J.M. and Owen, A.E. Phil. Mag., 24, 1281 (1971).

33. Owen, A.E. and Robertson, J.M. J.N.C.S., 2, 40 (1970).

34. Padovani, F.A. "Semiconductors and Semi-metals" ed. Williamson and Beer (New York Academic), 75 (1971).

35. Kemble, E.E. "The Fundamental Properties of Quastum Mechanics with Elementary Applications", (Dover, New York 1958).

36. Rideout, V.L. and Crowell, C.R. Sol. St. Electronics, 13, 993 (1970).

37. Chang, C.Y. and Sze, S.M. Sol. St. Electronics, 13, 727 (1970).

38. Kottwitz, A. and Stotzel, H. Wiss. Z. Tech. Dresden, 22, 1043 (1973).

39. Stotzel, H. and Kottwitz, A. Wiss. Z. Tech. Dresden, 23, 365 (1974).

40. Sah, C.T., Noyce, R.N. and Shockley, W. Proc. IRE, 45, 1228 (1957).

41. Yu, A.Y.C. and Snow, E.H. Journal App. Phys., 39, 3008 (1968).

42. Main, C. "Electrical and Structural Properties of Amorphous Semiconductors" (Ed. Le Comber and Mort, Academic 1973), 527.

43. Vogel, R. and Walsh, P. App. Phys. Lett. 14, 216 (1969).

44. Allison, J., Dawe, V.R. and Robson, P.N. J.N.C.S., 8-10, 563 (1972).

45. Sheng, W.W. and Westgate, C.R. Sol. Stat. Comm., 9, 287 (1971).

46. Allison, J. and Dawe, V.R. Electronics Letters, 7, 706 (1971).

47. Warren, A.C. IEEE Trans. Electron Devices, ED-20, 123 (1973).

CHAPTER 7 - References

1. Egerton, R.F. Appl. Phys. Lett., 19, 203 (1971).

2. Arnoldussen, T.C. et al. Phys. Rev. B, 9, 3377 (1974).

3. Marshall, J.M. Electronic processes in semi-conducting Glasses. M.O.D. 3rd Report (1973).

4. Bube, R.H. et al. App. Phys. Lett., 25, 419 (1974).

5. Tick, D.A., Watson, J.H.P. and Hindley, N.K. J.N.C.S., 13, 229 (1974).

6. Marshall, J.M. and Owen, A.E. Private Comm. (1975).

7. Spear, W.E. and Le Comber, P.G. J.N.C.S., 8-10, 727 (1972).
8. Malhotra, A.K. and Neudeck, G.W. App. Phys. Lett., 24, 557 (1974).
9. Neudeck, G.W. and Malhotra, A.K. J. Appl. Phys., 46, 239 (1975).
10. Neudeck, G.W. and Malhotra, A.K. Ibid, 2662 (1975).
11. Malhotra, A.K. and Neudeck, G.W. J. Appl. Phys., 46, 2690 (1975).
12. Barbe, D.F. J. Vac. Sci. and Tech., 8, 102 (1971).
13. Egerton, R.F. Sol. Stat. Comm., 10, 1081 (1972).
14. Many, A., Goldstein, Y. and Grover, N.B. "Semiconductor Surfaces." (North Holland, Amsterdam 1971).
15. Wey, M.Y. and Fritzsche, H. J.N.C.S., 8-10, 336 (1972).
16. Fritzsche, H. Chapter 2 in "Electronic and Structural properties of Amorphous Semiconductors" (Academic Press 1973).
17. Gosney, W.M. and Muller, R.S. Thin Solid Films, 14, 255 (1972).
18. Nicollian, E.H. and Goetzberger, A. Bell Syst. Tech. J., 46(6), 1055 (1967).
19. Sze, S.M. "Physics of Semiconductor Devices" (Wiley 1969).

CHAPTER 8 - References

1. Andreichin, R. and Kolomiets, B.T. Fiz. Tverdago. Tela,,4, 814 (1962).
2. Wey, H.Y. and Fritzsche, H. J.N.C.S., 8-10, 336 (1972).

3. Reinhard, D.K., Adler, D. and Arntz, F.O. Proc. of 5th Internation Conf. on Amorphous and Liquid Semiconductors, 745 (Garnisch,1973).

4. Adler, D. J. Vac. Sci. and Tech., 10, 728 (1973).

5. Hayashi, T. and Ono, Y. Jap. J. Appl. Phys., 14, 719 (1975).

6. Moss, T.S., Burrell, G.J. and Ellis, B. "Semiconductor Optoelectronics" (Bullerworths, 1973).

7. Tsu, R., Howard, W.E. and Esaki, L. Physical Review, 172, 779 (1968).

8. Davis, E.A. Chapter 13 in "Electronic or Structural Properties of Amorphous Semiconductors" (Academic Press, 1973).

9. Fagen, E.A. quoted in Reference 8.

10. Dember, H. Phys. Z., 32, 554 (1932).

11. Moss, T.S., Pincherle, L. and Woodward, A.M. Proc. Phys. Soc. Cond., 66, 743 (1953).

12. Ryvkin, S.M. "Photo-electric effects in Semiconductors" (New York, 1969).

13. Buimistrov, V.M., Gorban, A.P. and Litovchenko, V.G., Surface Science, 3, 445 (1965).

14. Frankl, D.R. and Ulmer, E.A. Surface Science, 6, 115 (1966).

15. Heilmeier, G.H. and Zanoni, L.A. J. Phys. Chem. Solids, 25, 603 (1964).

16. Owen, A.E. and Robertson, J.M. J.N.C.S., 2, 40 (1970).

17. Fritzsche, H. Chapter 2 in "Electronic and Structural Properties of Amorphous Semiconductors" ed. Le Comber and Mort (Academic Press, 1973).

CHAPTER 9 - References

1. Jayadevaiah, T.S. and Busmundrud, O. Electronics Lett., 8, 77 (1972).
2. Busmundrud, O. Phys. Stat. Sol. 'A', 28, 255 (1975).
3. Mei, L. and Greene, J.E. J. Vac. Sci. and Tech., 11, 145 (1974).
4. Fuhs, W., Niemann, K. and Stuke, J. Conference on Tetrahedrally Bonded Semiconductors (Yorktown Heights, 1974), 345.
5. Dohler, G.H. and Brodsky, M.H. Ibid, 351 (1974).
6. Adler, D. J. Vac. Sci. and Tech., 10, 728 (1973).
7. Adler, D., Arntz, F.O., Flora, L.P., Mathur, B.P. and Reinhard, D.K. Proc. of 5th Internation Conference on Amorphous and Liquid Semiconductors (Garnisch, 1973), 859.
8. Reinhard, D.K., Arntz, F.O. and Adler, D. Appl. Phys. Lett., 23, 186 (1973).
9. Petersen, K.E. and Adler, D. Appl. Phys. Lett., 25, 211 (1974).
10. Petersen, K.E., Adler, D. and Shaw, M.P. Appl. Phys. Lett., 25, 585 (1974).
11. Dunn, B. Ph. D. Thesis (University of California, 1974.)
12. Dunn, B., Mackenzie, J.D., Clifton, J.K. and Masi, J.V. Appl. Phys. Lett., 26, 85 (1973).
13. Henisch, H.K. and Vendura, G.J. Appl. Phys. Lett., 19, 363 (1971).
14. Vendura, G.J. and Henisch, H.K. J.N.C.S., 11, 105 (1972).

15. Komura, H., Yoneyama, O., Morioka, K. and Mitsuhashi, H. Jap. J. Appl. Phys., 9, 1546 (1970).

16. Sze, S.M. and Gibbons, G. Appl. Phys. Lett., 8, 111 (1966).

17. Wolf, E. Semiconductor Data Handbook.

18. Sze, S.M. Physics of Semiconductor devices (Wiley 1969).

CHAPTER 10 - References

1. Bosnell, J.R. Physics in Technology, 4, 113 (1973).

2. ICL Electronics, 45, 56 (1972).

3. Ovskinsky, S.R., Evans, E.J., Nelson, D. and Fritzsche, H. IEEE, NS-15, 311 (1968).

See also Table 6 of Reference 1 for fuller comparison of existing technologies.

4. Petersen, K.E. and Adler, D. Appl. Phys. Lett., 25, 585 (1975).

5. Dunn, B.S. Ph.D. Thesis (University of California 1974).

6. Rideout, V.L. Sol. Stat. Electronics, 18, 541 (1975).

7. Gupta, H.M. and Overstraeten, R.J. van. J. Appl. Phys. 46, 2675 (1975).

8. Leimer, F., Stotzel, H. and Kottwitz, A. Phys. Stat. Sol 'A', 29, K129 (1975).

9. Kottwitz, A., Leimer, F. and Stotzel, H. Ibid, 24, K49 (1974).

10. Braun, F. Ibid, 23, K99 (1974).

11. Braun, F. Ibid, 21, K17 (1974).

12. Wey, H-Y. and Fritzsche, H. J.N.C.S., 8-10, 336 (1972).

INSTITUTE OF PHYSICS CONF. SER. NO. 22

Contacts to chalcogenide glasses

A Wallace and J Robertson
Electrical Engineering Department, University of Edinburgh, UK

Abstract. A useful experimental feature of most amorphous semiconductors is that it is easy to make ohmic contacts. This may be explained in terms of conventional theory if there is a very high density of states in the gap and these give rise to quasi-intrinsic semiconductor behaviour and a narrow ($\ll 0{\cdot}1$ μm) contact depletion region. Barriers which may be present are thin enough to allow high tunnel currents to flow and therefore appear transparent to both electrons and holes.

Our results also describe more complex configurations where there are interface layers (eg Al_2O_3 on Al) or chemical reaction between metal and glass. The contrast with crystalline semiconductors is shown by I–V relations for crystalline silicon–chalcogenide glass heterojunctions and C–V measurements made with metal–oxide–glass structures. Values of surface state densities deduced from metal and semiconductor contact measurements are self-consistent.

1. Introduction

A study has been made of the properties of junctions between amorphous chalcogenide films and other materials, showing to what extent the contact is dominated by the high density of gap states within the barrier region. Current–voltage and capacitance–voltage characteristics show a marked contrast to those for crystalline semiconductors in various device configurations. First, however, it is convenient to discuss briefly the bulk properties of amorphous solids in general, and the composition used here in particular.

In amorphous solids, the regular periodic structure characteristic of a crystal is absent. The disorder can be structural, due to distortion of bond angles or lengths, or where multi-component glasses are considered, compositional. Despite the absence of long range order, however, a degree of short range order is present. As long as short range order exists, the main features of electronic band structure are retained; namely, there will be allowed energy bands in which carriers may propagate freely, subject to the usual scattering processes, separated by regions in which such electronic states as do exist have wavefunctions that decrease exponentially from the states. Various models have been put forward to represent the distribution of these localized states within the gap (Cohen *et al* (1969), Mott 1971)). The best model depends on the features of the glass concerned. In all cases, a density of localized states, N_F, of the order of $10^{25}\ m^{-3}\ eV^{-1}$ is present at the Fermi level. Carrier transport between these localized states can take place by variations of two principal mechanisms, either by excitation from a trap so that the carrier can move in extended (Bloch) states similar to a crystalline semiconductor, or by quantum mechanical tunnelling between adjacent localized states—a 'hopping' mechanism.

The glass used for the experiments detailed here was a germanium–arsenic–tellurium composition ($Ge_{10}As_{40}Te_{50}$), a memory switching glass of the chalcogenide group. The bulk glass was prepared by melting together weighed amounts of the constituent elements in a rocking furnace (900°C for 24 h), followed by rapid quenching in a water bath. The resulting glass has a transition temperature around 180°C, and a melting point of 357°C. Preliminary measurements of the bulk characteristics showed a low

field resistivity, $\rho = 1\text{–}3 \times 10^3\ \Omega m$ and an activation energy, $\Delta E = 0{\cdot}47\text{–}0{\cdot}48$ eV, in good agreement with published data (Tanaka *et al* 1970).

2. Metal–chalcogenide contacts

To examine the metal–chalcogenide contact, simple devices were fabricated in a sandwich configuration on glass substrates, with the chalcogenide alloy RF sputtered between a top and bottom metal contact. The contact area (0·25 mm^2) was defined by the crossover of the two electrodes, while the glass thicknesses ranged from 1 μm to 5 μm. Metals with widely varying electrical and physical characteristics were used; gold, aluminium, silver, tin, lead, indium, nickel, iron, platinum and molybdenum. The devices were prepared in batches, each batch having four electrode combinations, gold–gold, gold–metal, metal–gold, and metal–metal. A typical example of the current–voltage characteristic is shown in figure 1, plotted on a log–log scale. The characteristic is completely symmetrical and apparently ohmic at low fields (less than $10^6\ Vm^{-1}$). At higher fields it is still symmetrical but a supra-ohmic dependence is evident. This non-ohmic behaviour

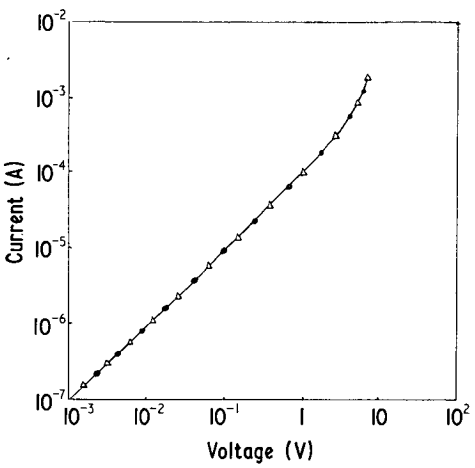

Figure 1. Current–voltage characteristic for a thin film of $Ge_{10}As_{40}Te_{50}$ sandwiched between gold electrodes. ● top electrode positive, △ top electrode negative.

has been widely observed (Fagen and Fritzche 1970, Robertson and Owen 1972, Marshall and Miller 1973, de Wit and Crevecoeur 1970), and can be expressed in the form

$$\sigma(E) = \sigma(0) \exp\left(\frac{E}{E_0}\right)$$

where σ is the conductivity, E is the applied field, $\sigma(0)$ is the conductivity at zero field and E_0 is a constant, approximately $3 \times 10^6\ Vm^{-1}$.

At higher power levels, joule heating occurs, which can cause thermal turnover and a negative resistance region in some cases. In general, all metals appear to form good ohmic contacts with the chalcogenide glass.

One would expect space charge regions to be formed in amorphous semiconductors, as they are in crystalline semiconductors. In the absence of interface states, the relative electron affinities of the amorphous semiconductor and the metal in contact determine the polarity of the contact dipole layer; where an appreciable density of interface states

is present, the amorphous semiconductor and the metal come into equilibrium with the interface layer essentially independently. Figure 2 shows the metal–amorphous semiconductor interface compared with a typical rectifying contact between a metal and an n-type crystalline semiconductor. In the amorphous semiconductor the Fermi level is

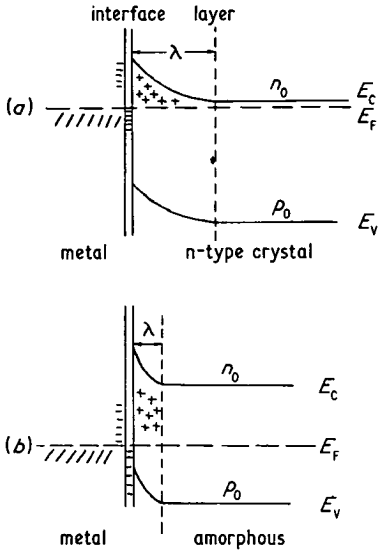

Figure 2. Potential distribution near metal–semiconductor contacts for (*a*) n-type crystalline semiconductor, (*b*) amorphous semiconductor.

near the centre of the gap, unlike its crystalline counterpart, and a large density of gap states exists within the space charge layer of the amorphous semiconductor. Calculations for the screening length, λ, in the amorphous semiconductor have been performed for various densities and distributions of states (Mott 1971, Barbe 1971, Fritzche 1973a, Egerton 1971). Using the standard expression:

$$\lambda = \left(\frac{K\epsilon_0}{q^2 N_F}\right)^{1/2}$$

where N_F is the density of localized states at Fermi level, K the dielectric constant, $\epsilon_0 = 8{\cdot}85 \times 10^{-12}\ \mathrm{Fm}^{-1}$ and q is the electronic charge. The screening length in the amorphous semiconductor is much shorter than that in the crystalline semiconductor. If the gap state density, N_F, is sufficiently high, of the order of $10^{26}\ \mathrm{m}^{-3}\ \mathrm{eV}^{-1}$, then this screening length could be short enough to allow easy tunnelling, so the barrier is essentially transparent. Even at larger screening lengths (of the order of 300 Å) low contact resistances are possible, on account of one of the following factors (Fritzche 1973b).

(i) The reverse bias saturation current is very much larger and the bulk conductivity much smaller when E_F is close to the gap centre. Considering an n-type crystalline semiconductor, the bulk conductivity is determined by the electron density n_0 which is large because E_F is close to E_c. The contact resistance in that case is high because (*a*) the hole density p_0 is exceedingly small and (*b*) the electron current in the barrier region is exponentially limited by the barrier height. Consequently, the contact resistance is large compared to the bulk resistance and a high rectification ratio is observed. On the

other hand, if the material is an amorphous semiconductor with the same barrier height and band gap, the Fermi level E_F is then close to the gap centre. As a consequence, n_0 is decreased by a factor exp $[(E_c - E_v)/2kT]$ and p_0 is increased by the reciprocal of this factor relative to the respective values in the n-type crystal. The electron current in the bulk has therefore no greater conductance than the hole current in the space charge region except for the difference in electron and hole mobilities, With a barrier thickness small compared with the electrode separation, even an appreciable difference in mobilities can exist before a barrier resistance becomes noticeable. In this case the generation and recombination rates have to be sufficiently large near the onset of the barrier region so that the conduction takes place in one band in the barrier region and in the other band in the bulk.

(ii) The high field across the space charge region delocalizes the states adjacent to the mobility edges and moves these edges towards the gap centre, lowering the effective blocking barrier.

(iii) The space charge region in some amorphous semiconductos may be too narrow for a conventional description of contacts to be valid, that is a uniform charge distribution and equipotential surfaces parallel to the interface. Discrete localized charges in the barrier may cause strong potential fluctuations across the plane of the contact, allowing charge carriers to pass preferentially at certain spots. With 10^{24} centres/m^3 the average separation of sites is approximately 100 Å; not too different from the screening length, λ.

While acknowledging the apparent ohmic nature of metallic contacts to chalcogenide glass, it was noticeable that when aluminium was used as a bottom contact, a high contact resistance was evident at low voltages (figure 3). As it is known that alu-

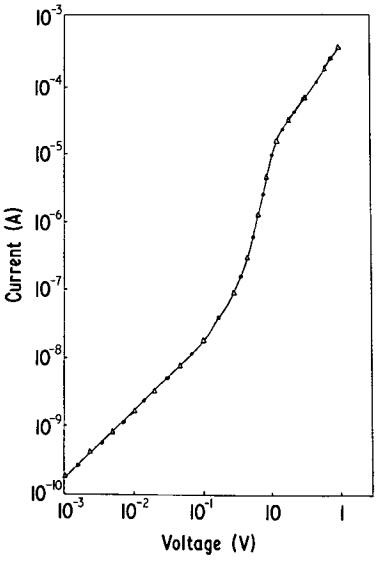

Figure 3. Current–voltage characteristic for a thin film of $Ge_{10}As_{40}Te_{50}$ sandwiched between aluminium electrodes. ● top electrode positive, △ top electrode negative.

minium oxidizes readily, and as no corresponding effect was noticed with top aluminium electrodes, it was suspected that a thin insulating layer was present between the metal and the chalcogenide glass. This was confirmed by the nature of the current–voltage charac-

teristic. A sharp rise in conductance occurred between 100 mV and 1 V, related to the onset of direct tunnelling into extended states. This sharp rise was shown to occur at a fixed voltage and was independent of temperature and glass thickness. The form of the characteristic can be compared to those obtained by Nwachuku and Kuhn (1968), and Osmun and Fritzche (1970) for tunnelling into amorphous germanium through deliberately fabricated insulating layers. Some tunnelling into localized states may also occur, but it is unlikely that this would contribute significantly to the bulk conduction in the semiconductor. For this reason the symmetrical nature of such a characteristic does not necessarily imply a symmetrical distribution of localized states, either in the bulk or at the surface of the amorphous semiconductor.

In addition, a series of capacitance–voltage characteristics were obtained for the same specimens, at a temperature of 235 K, and a constant test frequency of 140 kHz. The thermal time constant, τ, of these devices was measured by a pulsed technique to be in excess of 100 μs, so that $\omega\tau \gg 1$ for the test frequency. A typical characteristic is shown in figure 4. The high field pre-switching drop in capacitance has been observed

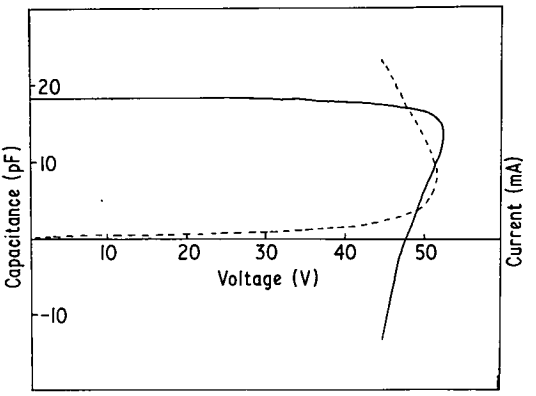

Figure 4. Capacitance–voltage and current–voltage characteristics of a thin film sandwich sample of $Ge_{10}As_{40}Te_{50}$ at a temperature of 235 K. Test frequency 140 kHz. Full curve: capacitance. Broken curve: current.

elsewhere (Vogel and Walsh 1969) and can probably be explained by means of a thermal model (Sheng and Westgate 1971, Allison and Dawe 1971), based on small signal analysis of the heat conduction equation. Over the major part of the characteristic the capacitance of the device remains essentially constant and equal to the geometric capacitance of the chalcogenide, confirming the absence of wide Schottky barriers at the interface.

Problems with metallic contacts may arise where compound formation and diffusion occur at the electrode–glass interface. This has been reported on selenium (Nielson 1973) and arsenic selenide (Freeman, Shaw and Yoffe 1969), but not to our knowledge on chalcogenides similar to the composition used here. The current–voltage characteristics for these samples were re-tested after a three month period, and were not found to have changed significantly.

3. Metal–oxide–chalcogenide devices

Metal–SiO_2–$Ge_{10}As_{40}Te_{50}$–metal structures were prepared on glass substrates in small area (0·25 mm^2) and large area (9 mm^2) configurations. The silica and chalcogenide layers were RF sputtered between top and bottom evaporated gold electrodes. Capaci-

tance–voltage characteristics show no apparent variation of capacitance with applied voltage, in sharp contrast to an MOS device where a crystalline semiconductor is used. Considering the equivalent circuit shown in figure 5, we can deduce an equivalent capacitance (Barbe 1971, Egerton 1971)

$$C_{eq} = \frac{(C_{sc} + C_{ss})C_O}{C_{sc} + C_{ss} + C_O} \tag{1}$$

where C_{sc}, space charge capacitance $= q\epsilon_s^{1/2}N^{1/2}$; C_{ss}, interface state capacitance $= q^2N_s$; C_O, oxide capacitance $= \epsilon_O A/d$; N is the density of bulk states in the space charge region and N_s is the density of interface states. ϵ_s, ϵ_O are the semiconductor and oxide dielectric constants respectively A is the device area and d is the oxide thickness.

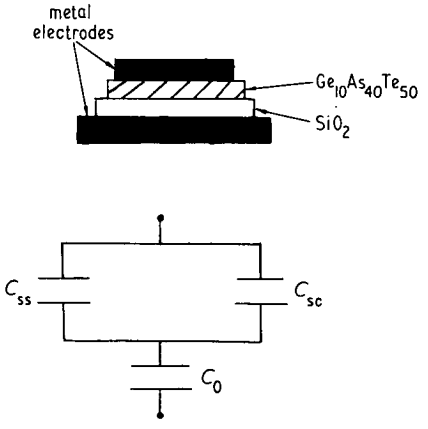

Figure 5. Equivalent circuit for an MOS device. C_{sc}, space charge capacitance; C_{ss}, interface state capacitance; C_O, oxide capacitance.

Taking typical values, $C_O = 6$ pF for a 1 μm oxide film, and $C_{sc} = 23$ μF for a bulk state density, $N = 6 \times 10^{25}\ m^{-3}\ eV^{-1}$. Substitution of these values into equation (1) gives $C_{eq} = C_O$.

If the oxide layer were made sufficiently thin, the oxide capacitance could be made significant with respect to the space charge capacitance. In this case any variation of capacitance with applied voltage could be related to a variation of the density of bulk states across the gap in the space charge layer (Egerton 1972). However, a thin insulating layer of the order of 500 Å would be required, and this would be difficult to achieve with existing equipment.

4. Silicon–chalcogenide heterojunctions

A number of chalcogenide–silicon heterojunctions were prepared on both p and n-type silicon substrates of various resistivities. The silicon slices were chemically cleaned to remove any surface impurities, then etched in HF to remove the surface oxide. A metal contact was evaporated on to the rear of the substrate, followed by a sintering process in a nitrogen atmosphere. Aluminium was used for p-type silicon, and antimony-doped gold for n-type. The chalcogenide alloy was then RF sputtered on to the front face of the silicon, followed by a thick top electrode of either gold or molybdenum to produce a

sandwich configuration. The area of the device was defined by the top contact. As well as the metal–chalcogenide–silicon–metal sandwiches, a number of metal–silicon–metal devices were fabricated on the same slice to check the non-blocking nature of the bottom contact.

The current–voltage characteristic for a heterojunction between the chalcogenide and p-type silicon is shown in figure 6. This characteristic appears similar in form to that

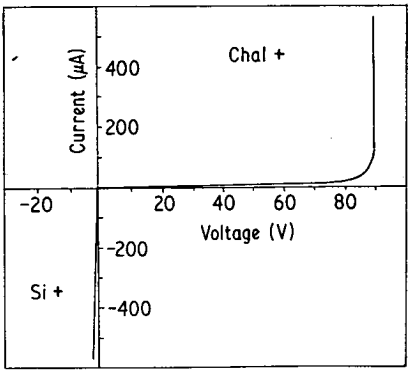

Figure 6. Current–voltage characteristic for a heterojunction between $Ge_{10}As_{40}Te_{50}$ and 0·025 Ωm p-type silicon. The chalcogenide is biased positively in the first quadrant.

of an n–p silicon junction. The forward current is determined by the resistance of the chalcogenide layer, while the reverse current saturates above 0·12 V, the current being limited by the reverse biased heterojunction. As the voltage is increased, junction breakdown is observed. The expected avalanche breakdown voltage may be derived from the one-sided abrupt junction equation (Sze and Gibbons 1966)

$$V_B = \left(\frac{\epsilon E_m^2}{2q}\right)\frac{1}{N_B} \tag{2}$$

where E_m is maximum field, ϵ is the silicon dielectric constant and N_B is the background carrier concentration in the silicon. The predicted values are in good agreement with the experimental results, for example for the characteristic shown in figure 6 with a p-type 0·025 Ωm silicon substrate, the observed breakdown voltage is 90 V, in good agreement with the calculated value. Local potential fluctuations may cause a slight lowering of the breakdown voltage.

Further evidence for a one-sided abrupt junction was obtained from capacitance–voltage characteristics on the various silicon substrates. A plot of $1/C^2$ against V is shown in figure 7 giving an almost perfect straight line. Values for the background carrier concentration were derived from the standard expression for an abrupt junction:

$$N_B = \frac{dV}{d(1/C^2)}\ \frac{2}{q\epsilon_s}\ \frac{1}{A^2} \tag{3}$$

The results are in close agreement with the nominal values of the carrier concentration in the silicon.

One would expect the situation for an n-type silicon–chalcogenide heterojunction to be complementary, in other words the chalcogenide appears n-type to p-type silicon, and p-type to n-type silicon. Therefore one expects a similar characteristic but with bias conditions reversed. This is shown in figure 8, but the reverse bias saturation current is

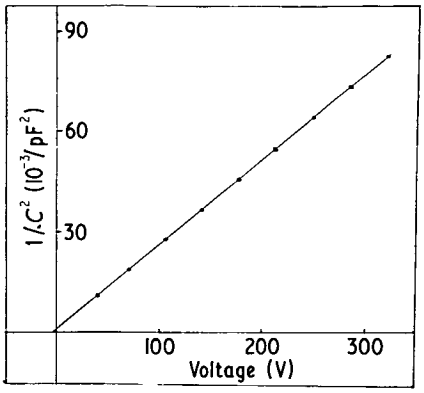

Figure 7. $1/C^2$ against V characteristic for a heterojunction between $Ge_{10}As_{40}Te_{50}$ and 0·115 Ωm p-type silicon. The chalcogenide is biased positively.

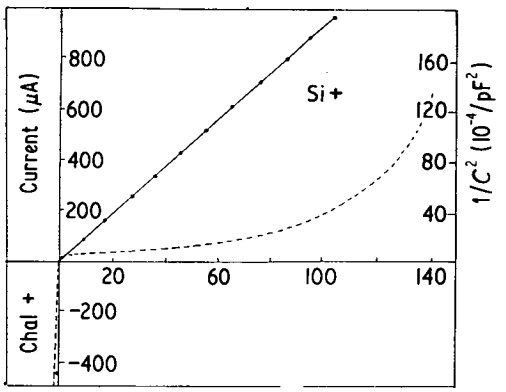

Figure 8. Current–voltage and $1/C^2$ against V characteristics for a heterojunction between $Ge_{10}As_{40}Te_{50}$ and 0·025 Ωm n-type silicon. The silicon is biased positively in the first quadrant.

higher, and the breakdown point appears less sharp and is generally at a lower voltage than predicted. Under forward bias, the determining factor is again the chalcogenide resistance. A $1/C^2$ against V plot, also shown in figure 8, gives a very good straight line, signifying an abrupt junction, and the calculated value for the background carrier concentration is again in close agreement with the nominal value for the various silicon substrates tested.

5. Conclusions

The characteristics of contacts to chalcogenide glasses are governed by the high density of gap states within the space charge layer for metal–glass, metal–oxide–glass–metal, and metal–silicon–glass–metal structures. To assess the distribution of these states, more advanced techniques have to be used, for example measurement of surface photovoltage or the fine structure of characteristics of very thin glass films.

References

Allison J and Dawe V R 1971 *Solid St. Commun.* **9** 387
Barbe D F 1971 *J. Vac. Sci. Technol.* **8** 102
Cohen M H, Fritzche H and Ovshinsky S R 1969 *Phys. Rev. Lett.* **22** 1065
Egerton R F 1971 *Appl. Phys. Lett.* **19** 203
——1972 *Solid St. Commun.* **10** 1081
Fagen E A and Fritzche H 1970 *J. Non-Cryst. Solids* **2** 170
Fritzche H 1973a *Electronic and Structural Properties of Amorphous Semiconductors* ed P G Le Comber and J Mort (New York: Academic) chapter 2
——1973b *Amorphous and Liquid Semiconductors* ed J Tauc (New York: Plenum) chapter 5
Freeman L A, Shaw R F and Yoffe A D 1969 *Thin Solid Films* **3** 30
Marshall J M and Miller G R 1973 *Phil. Mag.* **27** 1151
Mott N F 1971 *Phil. Mag.* **24** 911
Nielson P 1973 *Thin Solid Films* **15** 309
Nwachuku A and Kuhn M 1968 *Appl. Phys. Lett.* **12** 163
Osmun J W and Fritzche H 1970 *Appl. Phys. Lett.* **16** 87
Robertson J M and Owen A E 1972 *J. Non-Cryst. Solids* **8–10** (*Proc. Ann Arbor Conf. Amorphous Semiconductors*) p 439

Sheng W W and Westgate C R 1971 *Solid St. Commun.* **9** 387
Sze S M and Gibbons G 1966 *Appl. Phys. Lett.* **8** 111
Tanaka K *et al Proc. Second Conf. Solid State Devices (Tokyo, 1970)* p 73
Vogel R and Walsh P J 1969 *Appl. Phys. Lett.* **14** 216
de Wit H J and Crevecoeur C 1970 *J. Non-Cryst. Solids* **2** 170